Transport and dynamics of nanostructured graphene

Gunst, Tue

Publication date:
2013

Document Version
Publisher's PDF, also known as Version of record

Transport and dynamics of nanostructured graphene

Ph.D. Thesis by Tue Gunst

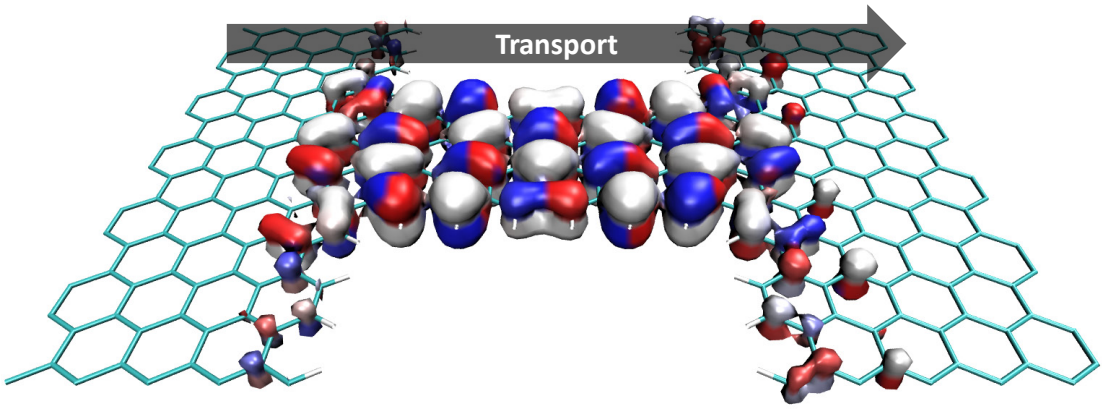

DTU Nanotech
Technical University of Denmark
Supervisor: Mads Brandbyge
2013

Preface

This thesis is submitted in candidacy for the Ph.D. degree at the Technical University of Denmark (DTU). The work was carried out between October 2010 and September 2013 at the Department of Micro- and Nanotechnology (DTU Nanotech). The project was financed by DTU.

The project was supervised by Associate Prof. Mads Brandbyge. I would like to thank Mads for his participation in developing novel and inspiring ideas, which has made this project exciting work for me for the past three years. I would also like to thank Jing-Tao Lü and Troels Markussen for the fruitful collaboration and sharing of technical experience and knowledge. Additionally, I would like to thank Prof. Antti-Pekka Jauho for sharing his great overview, which has helped me putting my work into context. I also thank Prof. Per Hedegård for always asking the necessary questions, and Jesper G. Pedersen, Rasmus B. Christensen, Peter Bøggild, Thomas G. Pedersen and Thomas Frederiksen for previous and ongoing collaboration.

It has been a great pleasure working in the 'Theoretical Nanoelectronics and Nanotechnology' group, where many fruitful discussions have been invaluable in the progress of this project. Therefore, a great thanks to all the guys for creating a pleasant working environment and for assistance, in particular by Nick P. Andersen, when puzzling linux or latex problems occurred.

I also wish to thank Prof. Jian-Sheng Wang for generously hosting a short research stay at the National University of Singapore. I thank Branislav K. Nikolic, Kristian S. Thygesen and Kurt Stokbro for serving on the evaluation committee of my thesis, and Jesper T. Rasmussen and Mikkel Settnes for helpful comments on the thesis manuscript. Finally, I would like to thank my girlfriend, my family and the guys in office no. 022 for making it a pleasant time and for supporting me during the project.

- Tue Gunst, Lyngby, 2013
DTU Nanotech

Abstract

This thesis is concerned with the heating and electronic properties of nanoscale devices based on nanostructured graphene. As electronic devices scale down to nanometer dimensions, the operation depends on the detailed atomic structure. Emerging carbon nano-materials such as graphene, carbon nanotubes and graphene nanoribbons, exhibit promising electronic and heat transport properties.

Much research addresses the electron mobility of pristine graphene devices. However, the thermal transport properties, as well as the effects of e-ph interaction, in nanoscale devices, based on nanostructured graphene, have received much less attention. This thesis contributes to the understanding of the thermal properties of nanostructured graphene. The computational analysis is based on DFT/TB-NEGF. We show how a regular nanoperforation of a graphene layer - a graphene antidot lattice (GAL) - may be a solution for making graphene a versatile material for electronics, as well as thermal management. One of the main results is that both electronic and thermal transport properties converge fast with the number of antidot rows between the leads. Increasing the antidot dimensions is found to reduce the thermal conductance relatively more than the electronic conductance. This trend may, together with other thermal scattering mechanisms such as disorder or isotopes, lead to fair thermoelectric performance of graphene with an otherwise high ability to conduct heat.

We also propose two novel materials that can lead to pseudo 1D transport in graphene. These systems may be a favorable way of realizing electronic wires in integrated graphene circuits. Firstly, GAL waveguides, where a region of pristine graphene is sandwiched between GAL regions, utilize the electronic band gaps to obtain localized waveguide modes. Secondly, the increased chemical reactivity of graphene with a bend may be used to electronically isolate pseudo-ribbons by absorption of hydrogen along the bends.

When a large current is passed through such nanostructures they will heat up due to the excitation of the local vibrations. This thesis further addresses effects of having a large finite bias voltage. In particular, we find that the electronic spectrum of nanostructured graphene features sharp variations in energy. Electronic resonances with a broadening on the scale of the phonon frequencies need a special treatment beyond the common praxis in theoretical modelling. There is a strong tendency to enter this regime in graphene technology due to the large phonon frequencies approaching 0.2 eV. The aim is to develop atomistic simulation methods that incorporate the effect from the electronic energy variation on the phonon energy scale in electronic conductance and local heating modelling. The methods we have developed are applied to graphene devices but are of much more general validity. We find a strongly nonlinear heating of phonons in a graphene nanoconstriction (GNC) with bias when the Fermi level is tuned close to a resonance in the electronic structure. The behavior is traced back to the presence of negatively damped phonons driven by the current. This effect may limit the stability and capacity of GNCs to carry high currents. Carbon nanosystems bridging electrically gated graphene electrodes may offer an interesting test-bed for these effects.

Resumé (Danish translation)

Denne afhandling omhandler opvarmning og elektroniske egenskaber for nanoskala komponenter baseret på nanostruktureret grafen. Efterhånden som elektroniske komponenter nedskaleres til nanometer dimensioner, vil virkemåden afhænge af den detaljerede atomare opbygning. Fremspirende carbon nanomaterialer, som fx grafen, nanotuber og grafen nanoribbons, besidder lovende elektroniske og varmeledende egenskaber.

Meget forskning undersøger elektron-mobiliteten for uberørte grafen komponenter. De termiske egenskaber, og effekter relateret til e-ph vekselvirkning, er derimod stadig et relativt nyt forskningsområde for nanoskala-komponenter baseret på nanostruktureret grafen. Denne afhandling bidrager til forståelsen af de termiske egenskaber af nanostruktureret grafen. Den beregningsmæssige analyse er baseret på DFT/TB-NEGF. Vi viser, hvordan en systematisk nanogennemhulning af grafen - et grafen antidot gitter (GAL) - kan være med til at gøre grafen til et alsidigt materiale for elektronik, såvel som til kontrol af termisk energi. Et hovedresultat er, at både de elektroniske og varmeledende egenskaber konvergerer hurtigt med antallet af hul-rækker mellem kontakterne. Vi finder, at en opskalering af hullerne kan reducere den termiske ledningsevne relativt mere end den elektroniske ledningsevne. Denne tendens kan sammen med andre spredningsmekanismer, som fx uorden eller isotoper, medvirke til gode termoelektriske egenskaber af grafen med en ellers høj varmeledningsevne.

Vi foreslår også to nye systemer til at opnå pseudo 1D transport i grafen. Disse systemer kan være en favorabel måde at realisere elektroniske ledninger i integrerede grafen kredsløb. GAL bølgeledere, hvor en region af uberørt grafen indeklemmes imellem GAL regioner, udnytter det elektroniske båndgab til at opnå lokaliserede bølgeledende tilstande. Endvidere kan man anvende den øgede kemiske reaktionsevne af bøjet grafen til elektronisk at isolere pseudo-ribbons vha. hydrogen absorption langs med bukket.

Når en stærk strøm passerer igennem sådanne nanostrukturer, vil de opvarmes pga. energitilførsel til lokaliserede vibrationer. Denne afhandling undersøger endvidere effekter relateret til at påføre en høj spænding. Specifikt finder vi, at det elektroniske spektrum for nanostruktureret grafen indeholder skarpe variationer med energi. Elektroniske resonanser, med en forbredning i størrelsesordenen af fonon frekvenserne, kræver en beskrivelse udover den sædvanlige praksis i teoretisk modellering. Der er en kraftig tendens til at ramme dette parameterområde i grafen-teknologi pga. de høje fonon frekvenser, som nærmer sig 0.2 eV. Målsætningen er at udvikle atomistiske simuleringsmetoder, som inkorporerer effekten fra den elektroniske energivariation på fonon energiskalaen i modellering af den elektroniske ledningsevne og den lokale opvarmning. Metoderne vi har udviklet anvendes på grafen komponenter, men er af langt mere generel gyldighed. Vi finder en stærkt ulineær opvarmning af fononer i en grafen nanoindsnævring (GNC) med spænding, når Fermi niveauet tunes til en resonans i elektronstrukturen. Dette fænomen kan føres tilbage til fremkomsten af negativt dæmpede fononer drevet af strømmen. Denne effekt kan begrænse stabiliteten og kapaciteten for GNC'er til at trække en stærk strøm. Carbon nanosystemer, som forbinder elektrisk gatede grafen elektroder, kan være et bud på en interessant testbænk for disse effekter.

List of publications

Paper I:
Thermoelectric properties of finite graphene antidot lattices
Tue Gunst, Troels Markussen, Antti-Pekka Jauho and Mads Brandbyge
Phys. Rev. B **84**, 155449 (2011)

Paper II:
Current-induced dynamics in carbon atomic contacts
Jing-Tao Lü, Tue Gunst, Antti-Pekka Jauho and Mads Brandbyge
Beilstein Journal of Nanotechnology **2**, 814-823 (2011)

Paper III:
Thermoelectric properties of disordered graphene antidot devices
Tue Gunst, Jing-Tao Lü, Troels Markussen, Antti-Pekka Jauho and Mads Brandbyge
IEEE Xplore Conf. Proc. 10.1109/IWCE.2012.6242835 (2012)

Paper IV:
Graphene antidot lattice waveguides
Jesper G. Pedersen, Tue Gunst, Troels Markussen and Thomas G. Pedersen
Phys. Rev. B **86**, 245410 (2012)

Paper V:
Electronic and transport properties of kinked graphene
Jesper T. Rasmussen, Tue Gunst, Peter Bøggild, Antti-Pekka Jauho and Mads Brandbyge
Beilstein Journal of Nanotechnology **4**, 103-110 (2013)

Paper VI:
Phonon excitation and instabilities in biased graphene nanoconstrictions
Tue Gunst, Jing-Tao Lü, Per Hedegård and Mads Brandbyge
Phys. Rev. B, Rapid Comm., **88**, 161401(R) (2013)

Contents

Preface ii

Abstract iii

Resumé iv

List of publications v

Symbols ix

1 Introduction 1
- 1.1 Nanoelectronics . . . 1
- 1.2 Nanophononics . . . 3
- 1.3 Thermoelectric energy conversion . . . 4
- 1.4 Heating on the nanoscale . . . 5
- 1.5 Outline of the thesis . . . 7

2 Atomistic modelling of thermoelectric properties 9
- 2.1 Quantum transport theory . . . 9
- 2.2 Thermoelectric properties of an electron-phonon interacting nanojunction 11
- 2.3 Modelling of electronic structure . . . 14
  - 2.3.1 Density Functional Theory . . . 15
  - 2.3.2 SIESTA . . . 15
  - 2.3.3 Tight Binding . . . 16
  - 2.3.4 Beyond Born-Oppenheimer . . . 16
- 2.4 DFT-NEGF - TranSIESTA . . . 17
- 2.5 Modelling of vibrations . . . 17
- 2.6 Thermoelectric properties of a GNC . . . 18

3 Thermoelectric properties of finite GALs 20
- 3.1 Electronic properties . . . 21
- 3.2 Phonon transport . . . 25
- 3.3 Thermoelectric properties . . . 26
- 3.4 Topology optimization of the thermoelectric properties of graphene . . . 30
  - 3.4.1 The model . . . 30
  - 3.4.2 Sensitivity analysis and reintroducing recursion . . . 31
  - 3.4.3 Simulations . . . 34

3.5 Summary and discussion . . . 36

4 Designing the conduction properties in graphene 37
4.1 Graphene antidot lattice waveguides . . . 37
4.1.1 Dirac model . . . 39
4.1.2 Simulations . . . 40
4.2 Kinked graphene . . . 45
4.2.1 Curvature-directed process for templated chemical functionalization 46
4.2.2 Kink formation and electronic transmission through kinks . . . 47
4.3 Summary and discussion . . . 49

5 Inelastic signals in graphene nanoconstrictions 51
5.1 IETS from exLOE . . . 51
5.2 IETS for a graphene nanoconstriction . . . 54
5.3 Summary and discussion . . . 58

6 Phonons in the presence of electronic current 59
6.1 Semiclassical Langevin equation . . . 60
6.1.1 Phonon forces and reservoir . . . 61
6.1.2 Average electronic forces . . . 62
6.1.3 Electronic noise . . . 63
6.1.4 SCLE . . . 64
6.2 Wide-band approximation . . . 64
6.3 Applications in carbon atomic contacts . . . 65
6.4 Spectral expansion - beyond the WBA . . . 67
6.4.1 Relation between the $\mathbf{\Lambda}$ function and the MAMA integrals . . . 69
6.4.2 Eigenexpansion of Green's function and the MAMA integrals . . . 71
6.5 Current-induced instabilities in nanoconstrictions . . . 73
6.5.1 Origin of the resonances and potential drop . . . 73
6.5.2 Modelling the phonon bath . . . 75
6.5.3 Harmonic stability analysis . . . 76
6.5.4 A and B coefficients . . . 80
6.5.5 Negative friction mechanism . . . 81
6.6 Summary and discussion . . . 87

7 Molecular dynamics in the presence of current 88
7.1 QMD methodology . . . 88
7.1.1 Generating colored noise . . . 89
7.2 QMD applied to GALs . . . 90
7.3 Molecular dynamics including Joule heating . . . 92
7.4 The origin of thermal expansion in current-carrying graphene nanoconstrictions . . . 95
7.4.1 Thermal contraction in graphene and GNCs . . . 95
7.4.2 A two-temperature quasiharmonic model . . . 98
7.4.3 Nonsuspended graphene . . . 99
7.4.4 Thermal expansion and local heating of the GNC from QMD . . . 100
7.5 Summary and discussion . . . 101

8 Summary and outlook 103

List of figures **104**

Bibliography **107**

9 Appendix A: Derivations and technical information **122**
9.1 DFT settings . . . 122
9.2 Transport cheat sheet: Symmetries and technical relations . . . 122
9.2.1 Mathematical relations - distribution functions . . . 123
9.2.2 Relations for the noninteracting system . . . 123
9.2.3 Symmetry relations . . . 124
9.3 Ballistic thermoelectric properties . . . 124
9.4 Thermoelectric properties of an electron-phonon interacting nanojunction 125
9.4.1 Electron current . . . 125
9.4.2 Thermal current . . . 127
9.5 Derivation of the exLOE . . . 128
9.5.1 Fock selfenergy . . . 128
9.5.2 Transmission correction by Fock diagram . . . 128
9.5.3 Symmetric part . . . 129
9.5.4 Asymmetric part . . . 129
9.6 Sensitivity analysis . . . 130
9.7 Recursive relations . . . 130
9.8 Löwdin transformation . . . 132

10 Appendix B: List of conference contributions **134**

11 Appendix C: Publications **135**
Paper I . . . 136
Paper II . . . 148
Paper III . . . 159
Paper IV . . . 165
Paper V . . . 174
Paper VI . . . 183

General notation and constants

Symbol	Description	Value
h	Plancks constant	$6.63 \cdot 10^{-34}$J·s
$\hbar$	$\frac{h}{2\pi}$	$1.05 \cdot 10^{-34}$J·s
k_B	Boltzmann's constant	$8.617 \cdot 10^{-5}$eV/K
e	Elementary charge (positive)	$1.602 \cdot 10^{-19}$C
m_e	Electron mass	$9.11 \cdot 10^{-31}$kg
1 amu	atomic mass unit	$1822.889 \cdot m_e$
I	Unit matrix with dimension to fit in context.	Ones in diagonal.
β	Inverse temperature factor in energy	$\frac{1}{k_B \cdot T}$
A^T	Matrix Transpose of A	$[A]$
$A^\dagger$	Hermitian Conjugate of matrix A	$[A]$
Tr[A]	Trace of a matrix	$[A]$
Re(A)	Real part of matrix	$[A]$
Im(A)	Imaginary part of matrix	$[A]$

Typical abbreviations:

Abbreviation	Description
2DEG	2-dimensional electron gas
BP	Berry-Phase
BTE	Boltzman Transport Equation
c.c.	complex conjugate
CEID	Correlated electron-ion dynamics
CNT	Carbon Nanotube
CPU	Central Processing Unit
CVD	Chemical vapor deposition
DOS	Density of states
DFT	Density Functional Theory
EBL	Electron beam lithography
EVP	Eigenvalue problem
exLOE	Extended lowest order expansion
FBZ	First Brillouin Zone
FGR	Fermi's Golden Rule
FWHM	Full Width Half Maximum
GALs	Graphene antidot lattices
GALWG	Graphene antidot lattice waveguide
GGA	Generalized Gradient Approximation
GLE	Generalized Langevin equation
GNRs	Graphene nanoribbons
HOMO	Highest Occupied Molecular Orbital
IETS	Inelastic tunneling spectroscopy
LDA	Local Density Approximation
LDOS	Local density of states
LJ	Lennard-Jones
LOE	Lowest order expansion
LUMO	Lowest Unoccupied Molecular Orbital
MD	Molecular Dynamics
MFP	Mean free path
MMA	Method of moving asymptotes
N2	Newton's second law
NC	nonconservative
NEGF	Nonequilibrium Green's functions
NEMS	Nano Electro-Mechanical Systems
NNTB	Nearest Neighbor Tight Binding
PAO	pseudoatomic orbital
PBCs	Periodic boundary conditions
QMD	Quantum molecular dynamics
SCLE	Semiclassical generalized Langevin equation
SIESTA	Spanish Initiative for Electronic Simulations with Thousands of Atoms
TB	Tight Binding
TEM	Transmission electron microscopy
WBA	Wide-band approximation

Chapter 1

Introduction

Graphene has been a focus of attention within many research branches since it was first isolated in 2004[33, 137], an achievement for which A. Geim and K. Novoselov were awarded the Nobel price in 2010. This two-dimensional layer of carbon can sustain current densities six orders of magnitude larger than copper, has a measured record high stiffness, and is foreseen to have numerous applications ranging from nanoelectronics, spintronics and nanoelectromechanical devices[33, 62]. It has an extremely high carrier mobility[63, 128] and additionally it is one of the best thermal conductors known[10, 163]. In many ways graphene seems to be a material where the gap between engineering applications and groundbreaking basic research is exceedingly small. Methods that enable large-scale production of graphene[5] for fast graphene-based transistor applications[104] and transmission electron microscopy (TEM) "nano-sculpting" with close to atomic precision[196], see Fig. 1.1a, are emerging simultaneously. Therefore, graphene may become a joint focus area where theoretical predictions are helpful in designing and understanding experiments and new applications.

One example of this is the graphene antidot lattice (GAL) which was suggested to offer an attractive approach to band-gap engineering in graphene[59, 141, 148, 151]. Recent experimental studies provide indications of a transport gap in GALs fabricated by electron beam lithography(EBL)[53, 64]. EBL provides a precise nanostructuring tool with hole distances down to 5-10 nm. However, another emerging procedure named block copolymer lithography[6, 91] also provides a promising method to obtain periodic perforation with hole distances down to 5 nm, see Fig. 1.1b.

This thesis discusses theoretical modelling of the electronic, thermal and thermoelectric properties of nanostructured graphene. The analysis is based on nonequilibrium Green's functions from an atomistic description of the graphene devices. Fig. 1.1c illustrates some areas of device applications where graphene technology is fast-growing. We will now discuss some recent developments in the branches touched upon in this thesis.

1.1 Nanoelectronics

A major driving force of nanotechnology is the continued miniaturization of electronics in modern smart phones and laptops powered by more than a billion transistors[1]. This downscaling is characterized by Moore's law[127], stating that the number of transistors

[1]The first Central Processing Unit (CPU) on one chip (Intel 4004) had 2300 transistors. A modern standard core i7 quad-cpu has 731,000,000. A low number still compared to the high-end 8-Core Xeon Nehalem-EX with 2,300,000,000 transistors.

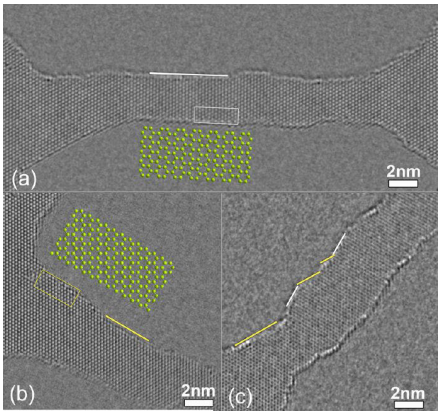

(a) *GNCs fabricated by in situ transmission electron microscopy. Image from [196].*

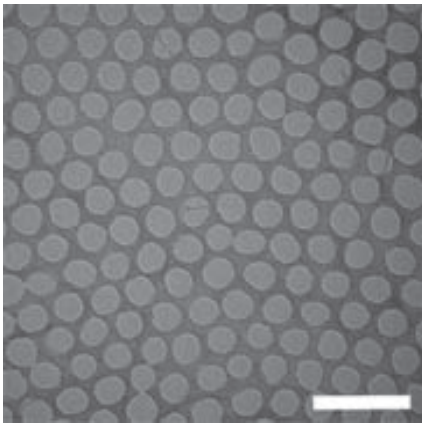

(b) *GAL device fabricated by block copolymer lithography with an antidot periodicity of* 39 *nm and neck widths of* 7.1 *nm. Scale bar is* 100 *nm. Image from [6].*

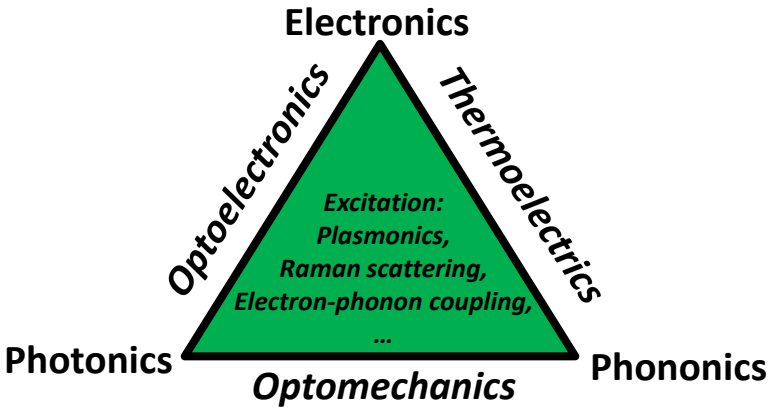

(c) *Areas in which many device applications of graphene are developing.*

Figure 1.1: *Techniques for nanostructuring graphene are developing rapidly. This thesis discuss theoretical modelling of the electronic, thermal and thermoelectric properties of such devices.*

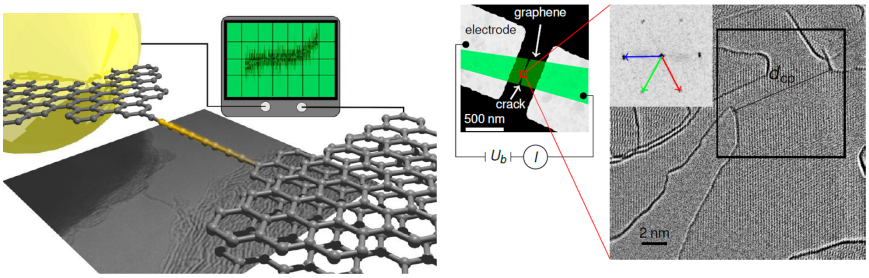

(a) Electrical transport measured in atomic carbon chains. Taken from [40].

(b) Electrical transport and thermal expansion measured in bilayer GNCs. Taken from [23].

Figure 1.2: *Transport measurements in nanostructured graphene.*

per area fitted into integrated circuits doubles every $1.5 - 2$ years. By now transistors vastly outnumber even the proverbial ants[2], each with an active region that is barely a few hundred atoms long (with conventional $22 - 45$ nm processes). We are therefore at a point where a bottom-up approach is needed, to obtain a deeper understanding of the influence of quantum effects in the current-flow, energy-exchange and device operation.

This may be particularly important in graphene where electrons due to the linear dispersion behave as mass-less Dirac fermions that can travel for micrometers. Within state-of-the-art graphene research one can realize devices consisting of single atomic carbon chains by "direct writing" in TEM[85]. A very recent experiment[40] was further able to measure the electrical transport across such carbon chains bridging graphene, see Fig. 1.2a. In another experiment Börrnert *et al.* were able to electrically characterize a GNC while at the same time observing the structural response of the device[23], Fig. 1.2b. They find a highly localized anomalously large lattice expansion inside the constriction, which will be discussed further in chapter 7. One can envision constrictions and nanoribbons to provide semi-conducting interconnects in graphene nano-circuitry[4, 24], and as a central building block of graphene based nanoelectronics. They are potentially cheap and have a flexibility in design and functionality opening up an avenue of applications.

1.2 Nanophononics

Heat flow at the atomic scale is described by the phonon modes, or quanta of lattice vibrations, in the device. Nanostructuring opens up exciting possibilities for controlled modification of the phonon spectrum and transport[8]. Acoustic phonons carry the most heat in graphene, while optical phonons can be used for determining the number of atomic planes in few-layer graphene by Raman spectroscopy. An ultimate exemplification of phonon engineering was the first experimental realization of a thermal rectifier in 2006[35], see Fig. 1.3. The device was based on an asymmetric nanotube structure with one end submerged in a deposited $C_9H_{16}Pt$ layer of increasing size. As a result the system yields an asymmetric axial thermal conductance depending on the direction of the heat flow. Many analogies between phononics and electronics are developing such as thermal logic components[100] and quantum interference effects, such as phononic Fano resonances, in carbon nanojunctions[116, 198].

[2]Biologists have estimated that the approximate number of individual ants, alive in the world at any one time, is $10^{15} - 10^{16}$[76].

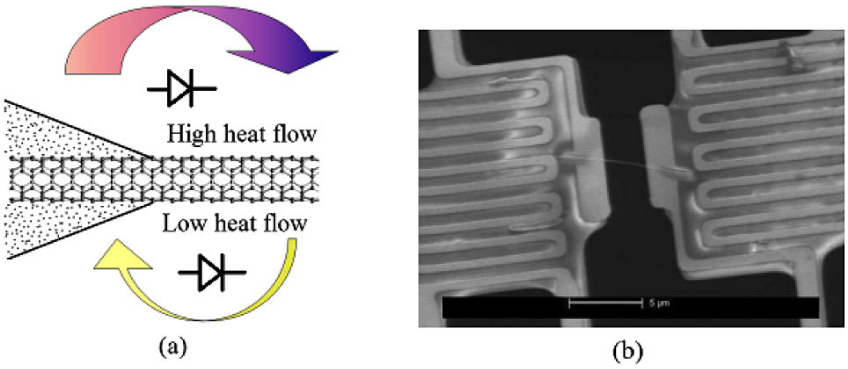

Figure 1.3: *Thermal rectification in axial asymmetric carbon nanotube. Taken from [35, 100].*

Until recently most modelling of phonons used Boltzmann transport equations[31] or classical molecular dynamics (MD). However, atomistic NEGF[80, 124, 191] or Kubo methods[101] are needed in the case of nanojunctions. Marzari *et al.* have included anharmonic interactions in a quasiharmonic model of the vibrational free energy to explain a negative thermal expansion coefficient (contraction) of graphene originating from the out-of-plane vibration[21, 129]. The quantum nature of phonons can also be treated within quantum MD simulations (QMD)[188, 190]. QMD is a recently developed semi-classical Langevin method that reconcile thermal transport properties in the low-temperature ballistic and high-temperature diffusive regimes. This is possible due to a replacement of the phonon bath with a set of random colored noises, obeying quantum Bose-Einstein statistics.

Atomic scale simulations are essential in the interpretation of heat flow in nanodevices. Phonon engineering has applications for diverse thermal management problems, ranging from nanoscale calorimeters and refrigerators to microelectronic processors and macroscopic energy-saving buildings[192].

1.3 Thermoelectric energy conversion

Thermoelectric devices can be used for waste-heat harvesting, solid-state generators or active cooling in electronics[74]. A good thermoelectric material should have a high electrical conductance but low thermal conductance. One approach to good thermoelectrics is to increase the Seebeck coefficient by reducing the dimensionality of the system[47, 92, 152]. However, one often finds that the efficiency in transforming heat into charge current is limited by the ability to conduct heat. Therefore, much research investigates how one can decrease heat conduction in nanostructured materials using nanomesh structures, surface-disorder and -decoration, passivation, or by other means. Promising nanostructured thermoelectric materials include passivated Si nanowires[117], Si antidot lattices[174, 202], chevron-type graphene nanoribbons (GNRs)[38], and connected capped carbon nanotubes[54]. An alternative idea comes from the field of molecular electronics. Here one utilizes the low thermal conductance, together with a sharp resonance in the electronic conductance, of molecular junctions[48, 144, 154, 159].

Graphene cannot by itself be used for thermoelectric applications, despite a giant Seebeck coefficient when gated by a sequence of metal electrodes[46]. Its efficiency in transforming heat into charge current is limited by its very high ability to conduct heat,

exceeding that of copper. Ways to reduce the superior thermal conductivity of graphene are needed if one looks for thermoelectric applications[9]. One idea is to apply edge roughness to long GNRs[164]. In the diffusive limit edge disorder was theoretically predicted to suppress heat conductance of GNRs by orders of magnitude[101, 102, 161]. A second idea has been to utilize edge currents in zigzag or chiral GNRs perforated with an array of nanopores[36]. In that case the electronic and thermal conductance is partly decoupled, i.e. the electronic conductance is almost not affected by the nanoperforation in the center of the ribbon. A third idea is to utilize interface mismatching between graphene and nanoribbons[80, 81]. Thermoelectric devices based on graphene could be applied as integrated elements for thermoelectric cooling in future graphene nanoelectronics.

1.4 Heating on the nanoscale

As we scale down electronics, while keeping the voltage constant, one eventually has to face the problem of a bottleneck for heat transfer away from the system. E.g. the total heat dissipation to the surroundings is decreasing, reducing the capability to transfer energy away from the device. At the same time the local current density is increasing and at some point the current-induced forces are of crucial importance for the atomic motion. The energy transfer mechanism is described by the electron-phonon (e-ph) coupling, i.e. the nonadiabatic coupling between electronic and nuclear vibrational motion. In equilibrium a system is described by the effective conservative confining potential together with a friction and noise. The competition between the latter two enables the system to equilibrate with the bath. Out-of-equilibrium five principal current-induced forces describe how a flow of electrons in the atomic bonds excite and couple the local vibrations[20, 50, 109, 111]. Four have been put forth as deterministic (not noise-like) mechanisms of energy transfer from the current to the atomic motion: The electronic friction force, nonconservative (NC) wind force, renormalization force (correction to the confining potential) and Berry-phase (BP) force. The fifth primary way for excited electrons to excite atomic vibrations is related to spontaneous phonon emission and describes the stochastic Joule heating out-of-equilibrium.

Dundas *et al.* have shown that the NC wind force can continually pump energy into the nuclear motion by driving the nuclei around closed paths in configuration space[50], see Fig. 1.4a. The net work done is nonzero along closed paths through regions of different current-density. The current flow hereby induces motion akin to atomic waterwheels[26, 50] with an increasing kinetic energy, also termed 'runaway' motion. Since the circular motion involves the coupling of the motion of two independent linear-oscillations, this force is maximized for systems with several nearly equal frequencies. The runaway phenomena was later generalized to cooperative mode displacements in which case the BP force was found to strengthen the runaway condition[108]. Another runaway mechanism was illustrated to exist due to population inversion between two levels of a donor-acceptor(DA) system, Fig. 1.4b. This results in a nonequilibrium negative friction that was theoretically predicted for low conductance tunneling transport through asymmetric molecules[111, 158]. It was argued to require that the two molecular states are independently tunable by the bias voltage due to a asymmetric coupling to the two leads, i.e. the low hopping parameter, t, and high bias limit, see Fig. 1.4b. Electromigration, where electrical current drives atomic diffusion and rearrangements, is traditionally thought of as activated by local Joule heating, but NC and BP forces provide an alternative activation mechanism.

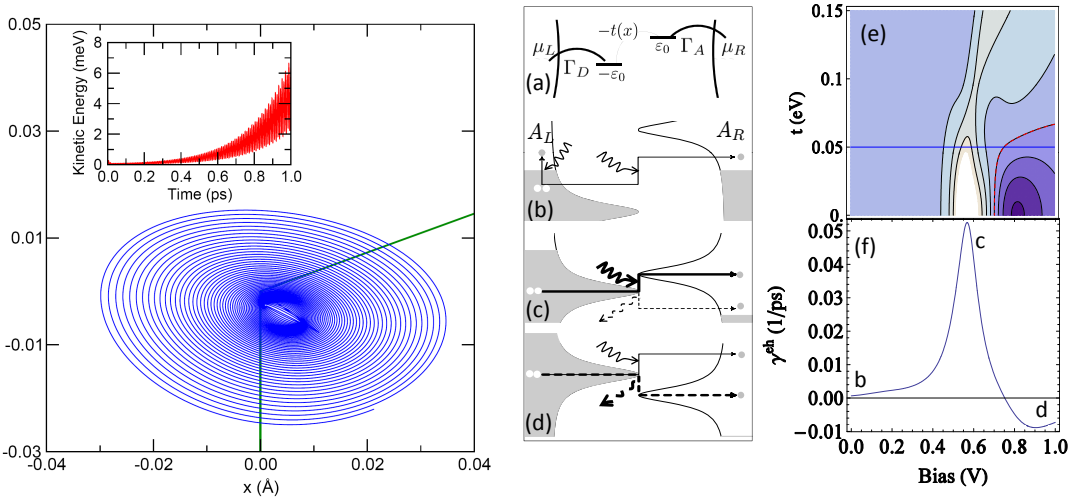

(a) *Design of a single-atom "waterwheel" driven by the nonconservative force. The trajectory is calculated for the center atom of a long bend chain at a bias voltage $V_a = -1$ V. The onsite energy is 2 eV at the center atom, 1 eV at its neighbors and zero otherwise. Taken from [50].*

(b) *"Laser-like" population inversion in a two-level model for the donor-acceptor(DA) system illustrated in (a). (b-d)D- and A-DOS and filling(grey) at $T = 0$. The D(A)-levels follow the chemical potential, $\mu_L\,(\mu_R)$ of the closest L(R) electrode. (b) For zero voltage only absorption around $\mu_L = \mu_R$ is possible. Similar excitations from the right electrode are not shown. (c) Absorption dominates for a voltage where $\varepsilon_A - \varepsilon_D \approx \hbar\Omega$ and the friction γ_{eh} is maximal. (d) Population inversion for larger voltage when, $\varepsilon_D - \varepsilon_A \approx \hbar\Omega$: Emission dominates and $\gamma_{eh} < 0$. (e) Contours of $\gamma_{eh}(V)$ for varying hopping t (dark is negative), $\varepsilon_0 = 0.35eV$, lead couplings $\Gamma_1 = 0.3eV$, $\Gamma_2 = 0.1eV$, e-ph interaction $m = 0.005eV$, frequency $\hbar\Omega = 20meV$, $\mu_0 = -0.2eV$. (f) $\gamma_{eh}(V)$ for $t = 0.05eV$ showing the generic behavior (maximum followed by negative values). Taken from [111].*

Figure 1.4: *Two types of current-induced instabilities different from local Joule heating.*

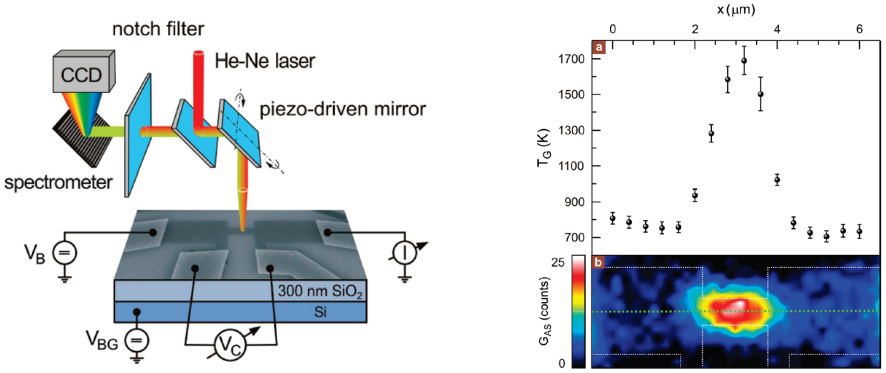

(a) *Measurement setup for Raman spectroscopic studies of electrically biased graphene constrictions. Taken from [34].*

(b) *Effective temperature distribution along a graphene constriction of width 0.6μm and length 1.5μm. The maximal temperature at a dissipated electrical power of 2.4mW (corresponding to a bias of $V_a = 5$ V) is above 1600K. The white lines indicate the etched constriction. The authors observe a breakdown of the constriction in the region $V_a = 7 - 10$ V. Taken from [34].*

Figure 1.5: *Measured local Joule heating in molecular junctions and graphene constrictions.*

In graphene, the structural response to a high bias can be studied by *in situ* TEM. This makes graphene nanoconductors a good test-bed for current-induced phenomena[15, 52, 83]. Additionally, Raman spectroscopy was used to measure the spatially resolved current-induced heating of graphene nanoconstrictions[18, 34, 86], Fig. 1.5.

Leaving aside the aspect of local heating, the phenomena of e-ph coupling is also observable in the IV-characteristics of nanosystems. The IV-characteristics can provide a spectroscopic fingerprint of a molecular junction. This is due to the dramatic conductance changes at bias voltages, where electron-phonon coupling enables additional conducting channels. It seems realistic that measurements, such as the ones depicted in Fig. 1.2, can be refined to low temperature characterization of inelastic signals in the future.

1.5 Outline of the thesis

The purpose of this thesis is to provide further details on the methods and simulations besides to summarize the main findings of the published articles. This includes the published results of thermoelectric performance of GALs, conduction properties of GAL waveguides and hydrogen passivated bends in graphene and the current-induced dynamical effects in GALs and graphene nanoconstrictions. Additionally, several results will be presented that are still unpublished. This includes a developed methodology and simulations for topology optimization of the thermoelectric performance of graphene and the inelastic signals, drag effect and current-induced thermal expansion in graphene nanoconstrictions. The remaining of this thesis is organized as follows (with related papers in parentheses):

- In **Chapter 2:**
  We describe the electronic structure models and NEGF theory of quantum transport for phonons and electrons. The NEGF-formalism is applied to the general case of thermoelectric energy conversion in an e-ph interacting nanojunction.

- In **Chapter 3 (Paper I, III):**
  Simulations of the ballistic thermoelectric properties of finite GAL devices are presented. The transport properties are shown to converge fast with increasing length of the perforated device. We find a sizable thermoelectric figure of merit considering the very excellent thermal transport of graphene. Additionally, a reduced thermoelectric performance of GALs with zigzag edges is traced back to the splitting of GAL minibands representing quasi-localized antidot edge states. Furthermore, alternative ways to manipulate thermoelectric performances, such as isotope scattering and an atomistic topology optimization method, are discussed.

- In **Chapter 4 (Paper IV, V):**
  Two alternative routes, named GAL waveguides and kinked graphene devices, to quantum confinement of charge carriers in graphene are illustrated. GAL waveguides are shown to support modes which are highly confined to the waveguide region, and are robust against structural disorder and kinks in the waveguide. Bending graphene may provide a curvature-directed process for hydrogenation, which is used to electronically isolate pseudo-ribbons between two stable kinks.

- In **Chapter 5 (Manuscript in preparation):**
  We outline the theoretical modelling of inelastic tunneling spectroscopy for systems where the electronic structure is changing on the scale of the phonon frequencies. The spectrum for the GNC obtained from the novel extended LOE method is compared to that of the original wideband LOE. Additionally, we find that a Li adatom on the constriction weakly modifies the IETS whereas a slightly heavier Zn adatom gives rise to a fingerprint signal.

- In **Chapter 6 (Paper II, VI):**
  We present a theoretical framework based on a semiclassical generalized Langevin equation. Two applications are used to illustrate how one can perform a harmonic stability analysis of a nanosystem. We find that nonconservative wind forces can form runaway modes in graphene chains. Additionally, we observe a strongly nonlinear heating with bias of a GNC, rooted in a breakdown of the harmonic approximation due to unstable, negatively damped phonons driven by the current. The effect is related to the "phonon-laser" instability, but is generalized to systems in the contact regime.

- In **Chapter 7 (Paper II, manuscript in preparation):**
  We describe the methodology of quantum molecular dynamics, which is applied to obtain the ballistic thermal conductance of a short GAL device. In the presence of bias a significant difference in the current-induced heat dissipation between the harmonic and anharmonic simulations is demonstrated. Additionally, it is shown that a GNC expands as optical modes are excited with increasing bias voltage, in contrast to raising the temperature.

- In **Chapter 8:**
  We evaluate the progress made in the thesis and summarize the main results. Furthermore, we discuss some possible next steps to take in the future.

Chapter 2

Atomistic modelling of thermoelectric properties

In this chapter the basic theoretical framework of quantum transport for phonons and electrons is introduced. Most transport methods for molecular electronics are either based on the mutually related scattering wave functions or single particle Green's functions. Both being attractive as a common language to address open boundary problems and a strongly interacting central part. The treatment here is based on nonequilibrium Green's functions (NEGF) which in a systematic way includes many-body interactions, e.g. from electron-phonon coupling, perturbatively[72]. Furthermore, methods exist that allow for a potential drop to be applied between the semi-infinite leads as described in the TranSIESTA method[27]. We will apply the NEGF-formalism to the general case of thermoelectric energy conversion in an electron-phonon interacting nanojunction. The corrections to the ballistic thermoelectric properties are related to the novel current-induced forces which will be the main focus in later chapters. Furthermore, the results will serve as foundation of the analysis of inelastic signals in graphene related nanostructures in chapter 5.

2.1 Quantum transport theory

We take an approach where more complex many-body variables are expanded in the single-particle Green's function. We will consider systems that can be partitioned into a central device region (D) connected to two semi-infinite electrodes (L and R). Such partitioning is straight-forward in the case of a Tight-Binding (TB) and SIESTA Kohn-Sham Hamiltonian, $\mathbf{H}_{ij} = \langle\phi_i|H|\phi_j\rangle$, and overlap matrix, $\mathbf{S}_{ij} = \langle\phi_i|\ \phi_j\rangle$, expressed in a localized basis, $\{\phi_i\}$. The single particle retarded Green's function of the full system is defined from

$$\begin{pmatrix} (\varepsilon+i\eta)\mathbf{S}_L-\mathbf{H}_L & \mathbf{S}_{LD}^\dagger-\mathbf{V}_{LD}^\dagger & \mathbf{0} \\ \mathbf{S}_{LD}-\mathbf{V}_{LD} & (\varepsilon+i\eta)\mathbf{S}_D-\mathbf{H}_D & \mathbf{S}_{RD}-\mathbf{V}_{RD} \\ \mathbf{0} & \mathbf{S}_{RD}^\dagger-\mathbf{V}_{RD}^\dagger & (\varepsilon+i\eta)\mathbf{S}_R-\mathbf{H}_R \end{pmatrix} \mathbf{G}_0^r(\varepsilon) = \mathbf{I}\,, \tag{2.1}$$

where $\mathbf{V}_{LD}$ and $\mathbf{V}_{RD}$ describes hopping from the contacts to the central region and η is a positive infinitesimal. The Green's function for indices restricted to the device region is found from the three equations obtained from the Green's function matrix center

column:

$$\mathbf{G}^r_{0,D} = [(\varepsilon + i\eta)\mathbf{S}_D - \mathbf{H_D} - \mathbf{\Sigma}_L - \mathbf{\Sigma}_R]^{-1}\,, \tag{2.2}$$

where the self-energies are defined as

$$\mathbf{\Sigma}_\alpha = (\mathbf{V}_{\alpha D} - \varepsilon\mathbf{S}_{\alpha D})\mathbf{g}^r_\alpha(\mathbf{V}_{\alpha D} - \varepsilon\mathbf{S}_{\alpha D})^\dagger\,,\ \ \alpha = L, R\,, \tag{2.3}$$

describing the finite life-time (nonzero imaginary part) of when the electron escapes from device into the semi-infinite leads. In case of a periodic structure of the electrodes, the electrode surface Green's function, $\mathbf{g}^r_\alpha$, can be determined using an iterative procedure[160].

The Green's function describes how excitations propagates through the system. It is related to the transmission probability, $\mathcal{T}_e$, in the famous Landauer-Büttiker formula[44]:

$$I_e = \frac{G_0}{e}\int d\varepsilon \mathcal{T}_e(\varepsilon)[n_F(\varepsilon,\mu_L) - n_F(\varepsilon,\mu_R)]\,, \tag{2.4}$$

assuming a noninteracting spin degenerate system, with the conductance quanta $G_0 = \frac{2e^2}{h}$. The energy-dependent transmission function is:

$$\mathcal{T}_e(\varepsilon) \;=\; \frac{1}{N_k}\sum_{i=1}^{N_k}\mathrm{Tr}\left[\mathbf{G}^r_{0,D}(\varepsilon,k_i)\mathbf{\Gamma}_R(\varepsilon,k_i)\mathbf{G}^a_{0,D}(\varepsilon,k_i)\mathbf{\Gamma}_L(\varepsilon,k_i)\right]\,. \tag{2.5}$$

Here the broadening matrices due to the electrode coupling are defined as $\mathbf{\Gamma}_{L,R} = i[\mathbf{\Sigma}^r_{L,R} - \mathbf{\Sigma}^a_{L,R}]$. $n_F(\varepsilon,\mu_{L/R})$ is the Fermi-Dirac distribution at the chemical potential of the left/right lead. We have included a k-point dependence for the possibility of periodic repetition in the transverse direction. The following integrals can be evaluated from the electronic transmission,

$$L_n(\mu) = \frac{2}{\hbar}\int\frac{d\varepsilon}{2\pi}(\varepsilon-\mu)^n\mathcal{T}_e(\varepsilon)\left(-\frac{\partial n_F}{\partial\varepsilon}\right). \tag{2.6}$$

From these integrals several physical properties follow in the linear response limit[165], see Appendix A (Sec. 9.3); the electrical conductance $G_e(\mu) = \frac{\partial I}{\partial V} = e^2L_0$, the electron thermal conductance $\kappa_e(\mu) = \left[L_2 - \frac{L_1^2}{L_0}\right]/T$, and the Seebeck coefficient $S(\mu) = \frac{\Delta V}{\Delta T}|_{I_e=0} = \frac{L_1}{eL_0T}$. In the calculation of thermoelectric properties of graphene nanostructures we will assume that the chemical potential, $\mu = (\mu_L + \mu_R)/2$, can be changed by an external gate.

For phonons the Landauer formula takes an analogous form,

$$J_{ph} = \int_0^\infty d\omega\frac{\hbar\omega}{2\pi}\mathcal{T}_{ph}(\omega)\left[n_B(\omega,T_L) - n_B(\omega,T_R)\right]\,, \tag{2.7}$$

where $n_B(\omega)$ is the Bose distribution function. The phonon transport equations are equivalent to the electronic equations with the Hamiltonian replaced by the force constant matrix $\mathbf{H} \to \mathbf{K}$, and the energy replaced by $\varepsilon\mathbf{I} \to \omega^2\mathbf{M}$, ω and $\mathbf{M}$ being the frequency and diagonal mass matrix, respectively.

Both transmission functions, $\mathcal{T}_e$ and $\mathcal{T}_{ph}$, are obtained using a recursive Green's function $O(N)$ growth process[118]. In this very intuitive approach, that is simple in terms of bookkeeping, one divides the center region into subsystems and includes each

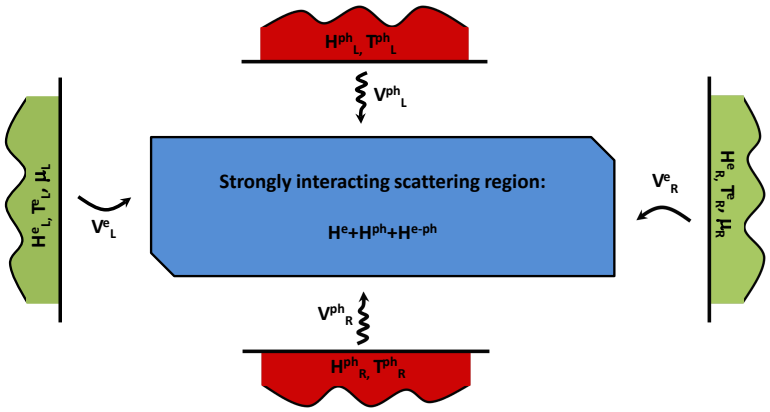

Figure 2.1: *Schematic of the general NEGF system setup.*

subsystem cell by cell, e.g. in the left lead. At the i'th step the matrices of the i'th cell will be written:

$$\mathbf{G}_{0,ii}(\varepsilon) = \left[\varepsilon\mathbf{S}_D^{(i)} - \mathbf{H}_D^{(i)} - \mathbf{\Sigma}_L^{(i)}(\varepsilon)\right]^{-1} \tag{2.8}$$

$$\mathbf{\Sigma}_L^{(i)}(\varepsilon) = (\mathbf{V}_{i-1,i} - \varepsilon\mathbf{S}_{i-1,1})\mathbf{G}_{0,ii}(\varepsilon)(\mathbf{V}_{i-1,i} - \varepsilon\mathbf{S}_{i-1,i})^\dagger \tag{2.9}$$

One then obtains both left and right self-energies in the last subsystem at the right side. From the full Green's function obtained at the last cell one can do a transmission calculation. This approach is used to obtain transmissions for long GAL devices in chapter 3.

2.2 Thermoelectric properties of an electron-phonon interacting nanojunction

The effect of electron-phonon interaction can be perturbatively included in the DFT-NEGF formalism. We consider a system consisting of an interacting central region connected to two noninteracting electron baths and two phonon baths, Fig. 2.1. We label the chemical potentials μ_L and μ_R, electronic temperatures T_L^e and T_R^e and the phonon bath temperatures T_L^{ph} and T_R^{ph}. The main assumptions are that electrons in the leads are free (electron-electron interaction described by mean-field DFT), we use the harmonic approximation for the phonons, there are no bath-bath interactions but only interactions in the central region and we assume the system to be spin-degenerate. The electron and phonon left or right could be the same electrode. However, one could imagine a more general case where control of T^e and T^{ph} is independent and tunable - e.g. a system which is conducting in one direction but insulating and thermal conducting in another. The full Hamiltonian is:

$$\mathbf{H} = \left(\mathbf{H}^e + \mathbf{H}^{ph} + \mathbf{H}^{eph}\right) + \sum_{\alpha=L,R}\left(\mathbf{H}_\alpha^e + \mathbf{V}_\alpha^e + \mathbf{V}_\alpha^{e,\dagger} + \mathbf{H}_\alpha^{ph} + \mathbf{V}_\alpha^{ph} + \mathbf{V}_\alpha^{ph,\dagger}\right), \tag{2.10}$$

where the first part describes the central region and the remaining terms describe the coupling to the baths. The electron-phonon coupling is given by

$$\mathbf{H}^{eph} = \sum_i \sum_{n,m} \mathbf{M}_{nm}^i \hat{c}_n^\dagger \hat{c}_m u_i\,, \tag{2.11}$$

where $\hat{c}_n^\dagger(\hat{c}_m)$ is the electron creation(annihilation) operator for the $n(m)$-th electronic state and $u_i = \sqrt{m_i} r_i$ is the (mass-normalized) displacement of the i'th degree of freedom. This matrix is obtained through a finite difference approximation as implemented in Inelastica[58][1]:

$$\mathbf{M}^i_{nm} \equiv \langle n| \frac{d\hat{H}}{d\mathbf{u}_i(t)} |m\rangle \,. \tag{2.12}$$

The particle current into the the central region from lead α is given by the famous Meir-Wingreen formula[72, 123]

$$I_\alpha = \sum_\sigma \frac{e}{\hbar} \int_{-\infty}^{\infty} \frac{d\varepsilon}{2\pi} \mathrm{Tr}\left[G^>(\varepsilon)\Sigma^<_\alpha(\varepsilon) - G^<(\varepsilon)\Sigma^>_\alpha(\varepsilon)\right] , \tag{2.13}$$

where σ is the spin index and $G^{>(<)}$ is the greater(lesser) Green's function. The derivation of the heat flux goes equivalently with a factor $(\varepsilon - \mu)$ measuring the energy transported by each electron. Hereby the thermal current due to electrons is

$$J^e_\alpha = \sum_\sigma \frac{e}{\hbar} \int_{-\infty}^{\infty} \frac{d\varepsilon}{2\pi} (\varepsilon-\mu) \mathrm{Tr}\left[G^>(\varepsilon)\Sigma^<_\alpha(\varepsilon) - G^<(\varepsilon)\Sigma^>_\alpha(\varepsilon)\right] . \tag{2.14}$$

The Meir-Wingreen formula for the thermal current due to phonons is given by[112, 189]:

$$J^{ph}_\alpha = -\int_{-\infty}^{+\infty} \frac{d\omega}{4\pi} \hbar\omega \mathrm{Tr}\left[D^>(\omega)\Pi^<_\alpha(\omega) - D^<(\omega)\Pi^>_\alpha(\omega)\right] . \tag{2.15}$$

The greater and lesser Green's functions are obtained through the steady state Keldysh equation

$$G^{>,<}(\varepsilon) = G^r(\varepsilon)\Sigma^{>,<}(\varepsilon)G^a(\varepsilon)\,, \tag{2.16}$$
$$D^{>,<}(\omega) = D^r(\omega)\Pi^{>,<}(\omega)D^a(\omega)\,, \tag{2.17}$$

for electrons and phonons, respectively. The electron and phonon self-energies here include contributions from the bath coupling as well as the electron-phonon coupling:

$$G^r(\varepsilon) = \left[(\varepsilon + i0^+)I - H^e - \Sigma^r(\varepsilon)\right]^{-1}, \tag{2.18}$$
$$D^r(\omega) = \left[(\omega + i0^+)^2 I - K - \Pi^r(\omega)\right]^{-1}, \tag{2.19}$$
$$\Sigma^{r,>,<}(\varepsilon) = \Sigma^{r,>,<}_L(\varepsilon) + \Sigma^{r,>,<}_R(\varepsilon) + \Sigma^{r,>,<}_{eph}(\varepsilon), \tag{2.20}$$
$$\Pi^{r,>,<}(\omega) = \Pi^{r,>,<}_L(\omega) + \Pi^{r,>,<}_R(\omega) + \Pi^{r,>,<}_{eph}(\omega). \tag{2.21}$$

The equations for the self-energies and Green's functions are coupled together. For the electronic part a typical route to solving this problem is to find a self-consistent solution by iteration. Here we will instead expand the Green's function to lowest order in the e-ph interaction matrix M:

$$\begin{aligned} G^r(\varepsilon) &= G^r_0(\varepsilon) + G^r_0(\varepsilon)\Sigma^r_{eph}(\varepsilon)G^r(\varepsilon) \approx G^r_0(\varepsilon) + G^r_0(\varepsilon)\Sigma^r_{eph}(\varepsilon)G^r_0(\varepsilon) \\ G^<(\varepsilon) &= G^r(\varepsilon)\Sigma^<(\varepsilon)G^a(\varepsilon) \\ &\approx G^<_0(\varepsilon) + G^r_0(\varepsilon)\Sigma^<_{eph}(\varepsilon)G^a_0(\varepsilon) \\ &+ G^r_0(\varepsilon)\Sigma^r_{eph}(\varepsilon)G^r_0(\varepsilon)\Sigma^<_{LR}(\varepsilon)G^a_0(\varepsilon) + G^r_0(\varepsilon)\Sigma^<_{LR}(\varepsilon)G^a_0(\varepsilon)\Sigma^a_{eph}(\varepsilon)G^a_0(\varepsilon) \end{aligned} \tag{2.22}$$

[1] This method takes into account the nonorthogonal basis of SIESTA to correct that one obtains $\frac{d\langle n|\hat{H}|m\rangle}{d\mathbf{u}_i(t)}$ instead of $\mathbf{M}^i_{nm}$ in a direct finite difference.

Here we have obtained a set of closed Dyson and Keldysh equations by replacing the full Green's function with the single-particle Green's function. This approach is termed the lowest order expansion (LOE) and has been shown to be current conserving when the Born approximation of the self-energies is used[145]. The original LOE assumes a diagonal e-ph coupling matrix and neglects the phonon subproblem. Furthermore, the wide-band approximation used in the original formulation assumes that the electronic structure is constant on the scale of the phonon frequencies ($\omega \to 0$). In graphene nanostructures the thermal conductance is large and phonon frequencies can exceed 0.2 eV. Therefore, we will see that the original formulation is not adequate for describing e-ph coupling in graphene nanostructures with electronic resonances.

Inserting the approximate Green's function in the Meir-Wingreen expression results in four terms for the current to second order in M:

$$I_\alpha = \frac{2e}{\hbar}\int_{-\infty}^{\infty}\frac{d\varepsilon}{2\pi}\sum_{n=1:3}\mathcal{T}_e^{(n)}\left[n_F^\alpha(\varepsilon)-n_F^{\bar{\alpha}}(\varepsilon)\right]+I_\alpha^{(4)}. \tag{2.23}$$

Where $\bar{\alpha}$ is the opposite lead to α and the three transmission terms are

$$\begin{aligned}
\mathcal{T}_e^{(1)} &= \mathrm{Tr}\left[\Gamma^\alpha(\varepsilon)G_0^r(\varepsilon)\Gamma^{\bar{\alpha}}(\varepsilon)G_0^a(\varepsilon)\right]=\mathrm{Tr}\left[\Gamma^\alpha(\varepsilon)A_{\bar{\alpha}}\right]\\
\mathcal{T}_e^{(2)} &= \mathrm{Tr}\left[\Gamma_\alpha(\varepsilon)G_0^r(\varepsilon)\Sigma_{eph}^r(\varepsilon)A_{\bar{\alpha}}(\varepsilon)\right]\\
\mathcal{T}_e^{(3)} &= \mathrm{Tr}\left[\Gamma_\alpha(\varepsilon)A_{\bar{\alpha}}(\varepsilon)\Sigma_{eph}^a(\varepsilon)G_0^a(\varepsilon)\right]
\end{aligned} \tag{2.24}$$

The detailed derivation is given in Appendix A (Sec. 9.4). We have defined the direct and time-reversed spectral functions of electrons and phonons originating from lead α as

$$\begin{aligned}
A_\alpha(\varepsilon) &= G_0^r(\varepsilon)\Gamma_\alpha^e(\varepsilon)G_0^a(\varepsilon)\\
\tilde{A}_\alpha(\varepsilon) &= G_0^a(\varepsilon)\Gamma_\alpha^e(\varepsilon)G_0^r(\varepsilon)\\
\mathcal{A}_\alpha(\omega) &= D_0^r(\omega)\Gamma_\alpha^{ph}(\omega)D_0^a(\omega)\\
\tilde{\mathcal{A}}_\alpha(\omega) &= D_0^a(\omega)\Gamma_\alpha^{ph}(\omega)D_0^r(\omega).
\end{aligned} \tag{2.25}$$

The first term is the noninteracting Landauer-Büttiker result. The next two terms is seen to originate from a correction to the electron DOS due to e-ph interaction. The fourth current term is not directly written with a difference of the lead Fermi functions and is given by

$$\begin{aligned}
I_\alpha^{(4)} &= \frac{2e}{\hbar}\int_{-\infty}^{\infty}\frac{d\varepsilon}{2\pi}\mathrm{Tr}\left[G_0^r\Sigma_{eph}^>G_0^a\Sigma_\alpha^< - G_0^r\Sigma_{eph}^<G_0^a\Sigma_\alpha^>\right]\\
&= \frac{2e}{\hbar}\int_{-\infty}^{\infty}\frac{d\varepsilon}{2\pi}i\mathrm{Tr}\left[G_0^r\Sigma_{eph}^>G_0^a\Gamma^\alpha n_F^\alpha - G_0^r\Sigma_{eph}^<G_0^a\Gamma^\alpha\left(n_F^\alpha-1\right)\right]
\end{aligned} \tag{2.26}$$

These four terms will give corrections to the thermoelectric moments in the linear response limit, $\mathcal{L}_n=\sum_{i=1}^4\mathcal{L}_n^{(i)}$. Here $\mathcal{L}_n^{(1)}=L_n(\mu)$ is the usual noninteracting moments. Furthermore, the forth current term gives rise to drag coefficients $\mathcal{Q}_n$ and $\tilde{\mathcal{Q}}_n$ due to a difference in phonon and electron temperatures[113]. These coefficients describe a situation where a temperature difference between the phonon baths drives an electronic current between the electron baths, and vice versa. This is a result of momentum transfer between electrons and phonons related to the nonconservative forces. Here we only outline main results relevant in the context of the later discussion of inelastic signals and current-induced forces. In Appendix A (Sec. 9.4) we derive the corresponding four corrections to the thermal current.

So far we have not assumed a specific form of the interaction self-energies. In Fig. 2.2 the lowest order Feynman diagrams included in the first Born approximation is sketched. The real time expressions of the electron self-energies are obtained according to the Feyn-

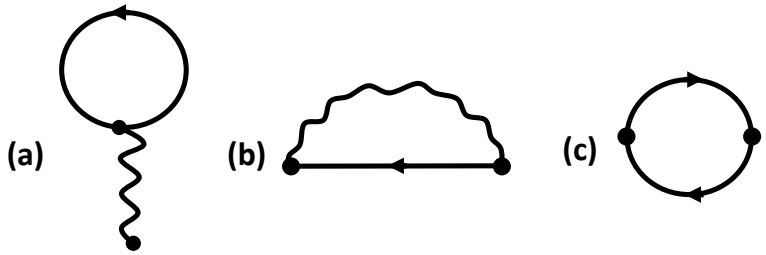

Figure 2.2: *Lowest order diagrams in the electron-phonon coupling self-energies of the perturbation expansion of the electron and phonon Green's function. For the electronic system the "Hartree" (a) and "Fock" (b) diagrams are included. For the phonon system the "polarization bubble" (c) is included.*

man rules. Performing analytic continuations according to the Langreth rules[72] and Fourier transforming (steady state) to energy space one obtains(see [56] and references therein):

$$\begin{aligned}
\Sigma^{H,</>}_{eph}(\varepsilon) &= 0 \\
\Sigma^{H,r/a}_{eph}(\varepsilon) &= -i\hbar \sum_{i,j,k,l} \mathbf{M}^i_{mn} \mathbf{D}^{r/a}_{0,ij} \mathbf{M}^j_{kl} \int \frac{d\varepsilon}{2\pi} \mathbf{G}^{<}_{0,lk}(\varepsilon) \\
\Sigma^{F,</>}_{eph}(\varepsilon) &= i\hbar \sum_{i,j,k,l} \mathbf{M}^i_{mk} \int \frac{d\omega}{2\pi} \left(\mathbf{G}^{</>}_{0,kl}(\varepsilon-\omega) \mathbf{D}_{0,ij}(\omega) \right) \mathbf{M}^j_{ln} \\
\Sigma^{F,r/a}_{eph}(\varepsilon) &= \pm \frac{1}{2} \left(\Sigma^{>}_{eph}(\varepsilon) - \Sigma^{<}_{eph}(\varepsilon) \right) - \frac{i}{2} \mathcal{H} \left(\Sigma^{>}_{eph}(\varepsilon') - \Sigma^{<}_{eph}(\varepsilon') \right)(\varepsilon) \,. \qquad (2.27)
\end{aligned}$$

The "Hartree" terms are energy independent and provides no signal near the phonon threshold. This term is neglected within the LOE method. The "Fock" retarded part was in eqn. 2.27 conveniently expressed through the greater and lesser self-energies through the Kramers-Kronig relations between real and imaginary part and the general relation $\mathbf{G}^r - \mathbf{G}^a = \mathbf{G}^> - \mathbf{G}^<$[56]. The "phonon polarization bubble" is given by[112]

$$\begin{aligned}
\Pi^{</>}_{eph}(\varepsilon) &= -i\hbar \sum_{l,k,p,q} \mathbf{M}^i_{lk} \int \frac{d\varepsilon}{2\pi} \mathbf{G}^{</>}_{0,kp}(\varepsilon) \mathbf{G}^{>/<}_{0,ql}(\varepsilon-\omega) \mathbf{M}^j_{pq} \qquad (2.28) \\
\Pi^{r/a}_{eph}(\varepsilon) &= -i\hbar \sum_{l,k,p,q} \mathbf{M}^i_{lk} \int \frac{d\varepsilon}{2\pi} \left(\mathbf{G}^{r/a}_{0,kp}(\varepsilon) \mathbf{G}^{<}_{0,ql}(\varepsilon-\omega) + \mathbf{G}^{<}_{0,kp}(\varepsilon) \mathbf{G}^{a/r}_{0,ql}(\varepsilon-\omega) \right) \mathbf{M}^j_{pq} \,.
\end{aligned}$$

In chapter 5 we will present the extended LOE method for the inelastic signals based on these approximations. Also the inelastic signal of a GNC as a function of gate voltage is discussed.

2.3 Modelling of electronic structure

The simulations in this project will be based on atomistic Density-Functional Theory (DFT) and semi-empirical tight-binding (TB) electronic structure calculations.

2.3.1 Density Functional Theory

The DFT simulations in this project are used to describe electron-phonon coupling in a GNC and adatoms on graphene nanostructures. By now DFT is a common framework for a large research community to address the quantum physics of condensed-matter[87, 122]. Its strength lies in it being *ab initio*, no fitting parameters are needed, and to accurately describe ground-state properties of systems with a number of atoms on the order of 10^3. Novel nanostructured materials are therefore within the grasp of DFT with the present computer resources.

The fundamental Schrödinger equation governing the full quantum mechanics of atoms and electrons has been well known since the 1920's[11, 162]. However, the task of solving these equations for realistic systems is tremendous. For electrons and nuclei interacting through the Coulomb force the Hamiltonian is:

$$\begin{aligned}\hat{H} = & - \sum_i \frac{\hbar^2}{2m_e}\nabla_i^2 - \sum_A \frac{\hbar^2}{2m_A}\nabla_A^2 \\ & + \sum_{i\neq j} \frac{e^2}{2|\vec{r}_i - \vec{r}_j|} + \sum_{A\neq B} \frac{Z_A Z_B e^2}{2|\vec{R}_A - \vec{R}_B|} - \sum_{i,A} \frac{e^2 Z_A}{2|\vec{r}_i - \vec{R}_A|}\end{aligned} \tag{2.29}$$

where $\vec{r}_i$, m_e and $-e$ is the position, mass and charge of the i'th electron, and A labels the corresponding nucleus parameters. Within the Born-Oppenheimer approximation[22] one decouples the electrons and nuclei by neglecting the nuclei kinetic energy. Due to the large mass difference ($m_A/m_i \approx 1823 Z_A$) the nuclei move on a much longer time scale and the electronic structure only depends parametrically on the nuclear coordinates. Hence one thinks of the Coulomb repulsion between electrons and nuclei together with external fields as an external potential. The solid success of DFT lies in the possibility of a complete description of a many-body ground state from the density of an noninteracting system with an effective potential. This is the essence of the Hohenberg-Kohn theorems[75] applied in the KS-theory due to Kohn and Sham[94, 122]. According to the theorem by Hohenberg and Kohn a system's external potential and the corresponding ground state energy is a unique functional of the ground state density. Therefore, the full Hamiltonian and all properties, including excited states, can be regarded as a functional of the ground state density. In the Kohn-Sham procedure one replaces the Hamiltonian of the interacting many-body problem with that of a noninteracting auxiliary system with an effective potential reproducing the correct ground state energy. In this way one reduce the problem to having to solve a sequence of single-particle equations self-consistent with a generally unknown exchange-correlation potential describing all quantum many-body interactions. A variety of different exchange-correlation functionals exist. In this project only the most common Local Density Approximation (LDA) or Generalized Gradient Approximation (GGA-PBE) are used for exchange and correlations[122, 150].

2.3.2 SIESTA

The SIESTA package[167] is a DFT implementation solving the KS-equations with periodic boundary conditions (PBCs) in a finite basis set of pseudoatomic orbitals (PAOs). It utilizes norm-conserving pseudo potentials[70, 181] to replace the chemically inert core electrons and reduce the basis size. The basis consists of a number of free atomic orbitals specified by the multiple-ζ nomenclature, and possible polarization orbitals generated from a polarizing electric field, localized at each atomic site. The minimal single-ζ (SZ) basis has a single radial function per angular momentum for those angular momenta

with substantial electronic population in the valence of the free atom. The strict locality imply a highly sparse Hamiltonian ideal for $O(N)$ calculations on large systems and the system partitioning needed in the NEGF setup. The electron wavefunctions and density are projected onto a real-space grid with a fineness specified by an energy "mesh-cutoff". The detailed settings used in this project are outlined in Appendix A, Sec. 9.1.

2.3.3 Tight Binding

To model transport in large all carbon GAL devices considered in the project we will apply a minimal TB model. Carbon has four valence orbitals, conveniently modeled by the tight binding sp^3-orbital model. The sp^2-hybrids, or σ-orbitals[171], in the graphene plane are responsible for the bonding. This is modeled by the more accurate empirical Brenner potential[29]. The electrons in the sp^2-hybrids are strongly bound and occupy lower energies than the remaining out of plane $\pi-$orbital. Furthermore, the $\pi-$orbital with odd z-parity decouple from the σ-orbitals with even z-parity. Therefore, one can accurately describe transport properties of planar graphene by the nearest-neighbor orthonormal tight binding $\pi-$model.

The tight-binding Hamiltonian is constructed for a specific configuration from a distance dependent hopping integral, $t(a) = t_0 \left(\frac{a_0}{a}\right)^2$, with[2] $t_0 = 2.7$ eV. Here $a_0 = 1.42$ Å is the equilibrium nearest neighbor distance of graphene. Extended TB models are available for graphene following the general Slater-Koster Scheme[25, 36, 166]. Strain and relaxation is incorporated through Harrisons scaling law[71] accounting for the decreasing probability of electron jumps when atoms move away from each other. Based on this model Guinea and co-workers[68] have shown how strain in graphene can lead to a pseudo-magnetic field affecting the electronic properties. It has proven itself to be a good model for the electronic transport properties rooted in the fact that the $\pi-$electrons occupy the states near the Fermi level. Being a very accurate model for planar graphene systems, more sophisticated DFT simulations are needed if the structure is not planar or other atoms are present such as adsorbates or passivation.

2.3.4 Beyond Born-Oppenheimer

We express the Hamiltonian, $\tilde{\mathbf{H}}^e = \mathbf{H}^e + \mathbf{H}^{eph}$, of the non-interacting electrons in the PAO or TB basis as

$$\tilde{\mathbf{H}}^e = \sum_{\sigma} \sum_{n,m} \hat{c}_n^\dagger(t) \hat{c}_m(t) H_{nm}(\mathbf{u}) \,. \tag{2.30}$$

It adiabatically includes the electron-phonon interaction through a parametrically dependence on the atomic displacements with time, $\vec{u} = \vec{u}(t)$. To go beyond the uncoupled Born-Oppenheimer description we Taylor expand the matrix elements to first order around the equilibrium positions denoted $\vec{x}_0$:

$$\begin{aligned} H_{nm}(\mathbf{u}) &\approx H_{nm}(\mathbf{x}_0) + \sum_i \frac{\partial}{\partial x_i} H_{nm}(\mathbf{x})|_{\mathbf{x}=\mathbf{x}_0} (\mathbf{x}_i - \mathbf{x}_0) \\ &= H_{nm}(\mathbf{x}_0) + \sum_i \mathbf{M}^i_{nm}(\mathbf{x}_0) \cdot \mathbf{u}_i \end{aligned} \tag{2.31}$$

[2] This value reproduces low-energy band structures of graphene obtained by DFT calculations and was shown to predict conducting properties of GAL devices consistent with SIESTA[59]. Another value often occurring in literature is $\beta_0 = 3.033$eV fitted to the Fermi velocity obtained by experiments.

hereby $\tilde{\mathbf{H}}^e$ is explicitly split into a free electron part and a term describing the electron-phonon interaction to lowest order.

2.4 DFT-NEGF - TranSIESTA

The single-particle KS energies and eigenstates cannot be rigorously interpreted as true excitations. However, they have proven themselves as a reasonable approximation for *ab initio* quantum transport[147, 197]. This pragmatic approach has successfully been applied to study electronic properties of e.g. molecular wires[28, 136, 175], C_{60} on metallic surfaces[132], quantum interference in carbon molecules[67, 121], inelastic scattering in Au-chains[57], spintronics[155] and thermoelectric properties of single-molecule nanojunctions with graphene electrodes[135].

Benchmark studies have shown that the elastic SIESTA transmission converge toward more accurate plane-wave results as the SIESTA basis is enlarged[170]. An important deficit of the approach is that the common LDA and GGA functionals are known to underestimate the gap between the semiconductor valence and conduction bands and molecule HOMO-LUMO states. Especially for poorly conducting molecules more sophisticated methods are needed for describing exchange-correlation interactions - e.g. the GW method, time-dependent DFT and the Kubo formula[42, 45, 97, 178, 179]. In this project the focus will be on highly conducting nanosystems in which the shape of the bands are often well described as compared to the considerably more demanding methods.

Several DFT-NEGF schemes further includes a potential drop between the semi-infinite leads within the self-consistent procedure[27, 176]. In this project we apply the TranSIESTA method[27] to study finite bias phenomena in graphene nanostructures.

2.5 Modelling of vibrations

For short molecular junctions or nanodevices it is reasonable to use the harmonic approximation, thus neglecting anharmonic phonon-phonon scattering. The fully decoupled (Born-Oppenheimer) Hamiltonian is then written as

$$\mathbf{H}^{ph} = \frac{1}{2}\dot{\vec{u}}^T\dot{\vec{u}} + \frac{1}{2}\vec{u}^T\mathbf{K}\vec{u}\,. \tag{2.32}$$

The force constant matrix, $\mathbf{K}$, contains spring constants between atoms i and j in directions μ and ν (labeling $\{x, y, z\}$). Following a structural relaxation, we calculate $\mathbf{K}$ using either DFT or, in case of TB calculations, the semi-empirical Brenner interatomic potential[29]. In case of TB+Brenner simulations, we will perform the structural relaxation through the 'General Utility Lattice Program' (GULP)[60] or by ad-hoc MD. In case of DFT we use the equilibrium lattice constant that minimize the total energy. The nearest neighbor distance depend on the basis size, as illustrated in Fig. 2.3. For the Brenner potential one obtain the experimental result of $a_0 = 1.42$ Å. The force constants and electron-phonon coupling are then calculated with the *frozen phonon* method. Here each ion is displaced $Q_{i\mu} \approx 0.002$ Å one by one to obtain the forces, $F_{j\nu}(Q_{i\mu})$, on atom $j \neq i$ in direction ν. From the finite difference calculation we evaluate the elements of $\mathbf{K}$ as

$$\mathbf{K}_{i\mu,j\nu} = \frac{\partial^2 E}{\partial r_{i\mu}\partial r_{j\nu}} = \frac{F_{j\nu}(Q_{i\mu}) - F_{j\nu}(-Q_{i\mu})}{2Q_{i\mu}}\,, \tag{2.33}$$

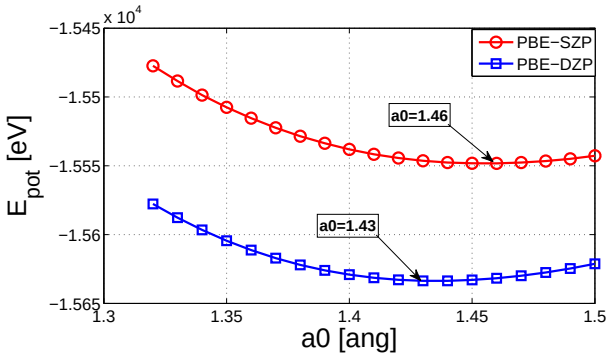

Figure 2.3: *Different nearest neighbor distances obtained from SIESTA. As the basis is increased the nearest neighbor distance approach the value, $a_0 = 1.42$ Å, measured in experiments.*

where E is the total energy. The intra-atomic elements are calculated by imposing momentum conservation, such that $\mathbf{K}_{i\mu,i\nu} = -\sum_{j\neq i}\mathbf{K}_{i\mu,j\nu}$. When the atomic masses are included in the force constants it is usually called the dynamical matrix, $\mathbf{D}_{i\mu,j\nu} = \mathbf{K}_{i\mu,j\nu}/\sqrt{m_i m_j}$. The phonon eigenfrequencies, ω_i, and eigenmodes, v_i, are defined from the equation of motion

$$\mathbf{D}v_i \quad = \quad \omega_i^2 v_i \,. \tag{2.34}$$

The phonon NEGF calculations can be performed by calculating the force constants of a super cell, i.e. repeating the unit cell in the transverse direction.

2.6 Thermoelectric properties of a GNC

To validate the TB+Brenner model for the elastic thermoelectric properties of planar graphene nanostructures we compare the transmission functions with DFT for a small GNC. The following DFT settings will be used throughout this project unless otherwise stated (further details are given in Appendix A, Sec. 9.1). The generalized gradient approximation (GGA-PBE) is used for exchange and correlations. To accurately describe the phonon modes we use a single-ζ polarized basis set and a mesh-cutoff of 210 Ry. Similar settings were previously used to accurately describe phonon modes of carbon nanotubes[126]. With these parameters the optimal nearest neighbor distance of graphene is approximately 1.46 Å.

The phonon transmission for both graphene and the constriction is illustrated in Fig. 2.4. The DFT results are shown as solid lines, while the Brenner results are indicated with a dashed line. For the ab initio calculation a cutoff radius smaller than the lead dimension was used to apply Green's function techniques. The momentum conservation was imposed by adjusting the diagonal elements of the dynamical matrix to secure physical transmissions also at acoustic frequencies. No changes in the symmetrized result were observed when increasing the cutoff radii. The figure highlights the importance of using ab initio approaches in the description of especially optical phonon modes. In the context of current-induced heating it is these high frequency phonon modes that are excited the most. However, discrepancies are small in the low frequency part that dominates the thermal conductance at 300K.

The electron transmission and resulting ZT is shown in Fig. 2.5. Despite a shift in peak positions, the shapes of the transmission curves generally agree well. Additionally,

the maximal ZT obtained by the two different approaches are in good agreement. It is mentioned that the GNC is H-passivated in the DFT calculation. There is no explicit passivation in the TB calculation. Within the π-model we assume that all atoms are sp_2 bonded. Therefore, the model neglects the dangling bond near the edges. As a result the edges are in some sense effectively H-passivated. We conclude that the TB+Brenner model will be adequate for transport simulations across planar nanostructured graphene devices. In the next chapter we will apply this model in simulations of the thermoelectric performance of GAL devices.

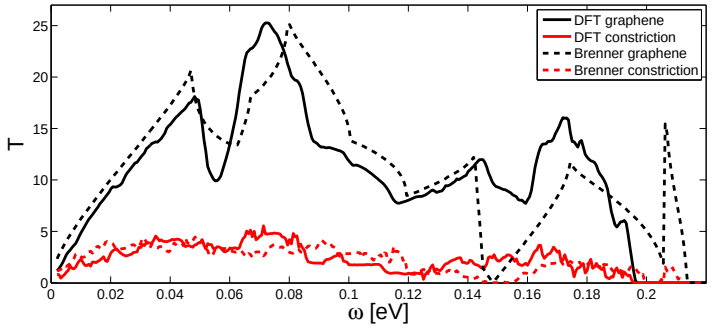

Figure 2.4: *Phonon transmission as a function of frequency across ideal graphene and the GNC. The result from the DFT calculations is compared to that of the empirical Brenner potential.*

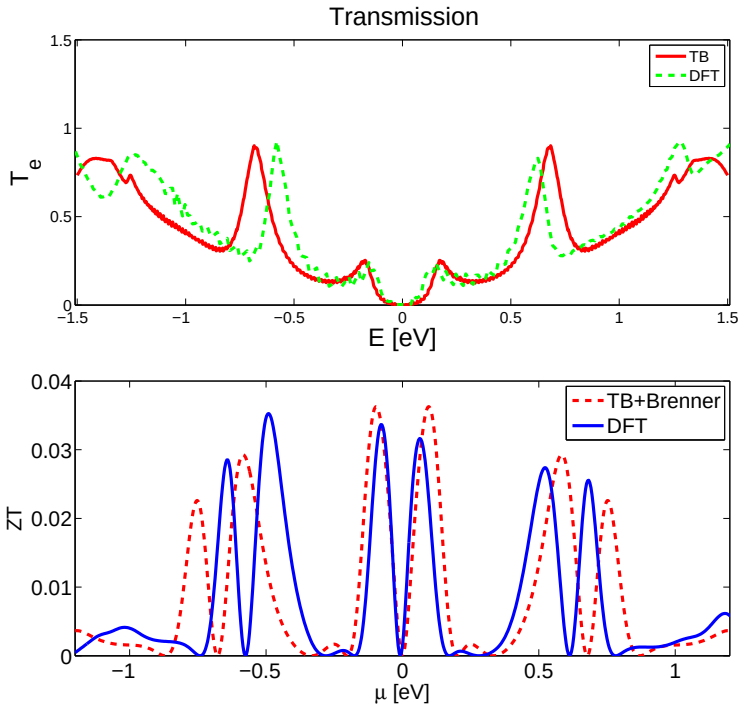

Figure 2.5: *Thermoelectric figure of merit for the GNC. The simpler TB+Brenner model compares well to the more accurate DFT description. The temperature is $T = 300\,K$.*

Chapter 3

Thermoelectric properties of finite GALs

This chapter provides a review of paper I and III and discusses some additional unpublished results regarding topology optimization of the thermoelectric properties of graphene. For the time being we neglect the effect of e-ph interaction but instead consider the ballistic thermoelectric properties of large nanostructured graphene flakes. All simulations are based on the TB+Brenner model.

So far the electronic properties of infinite GALs have attracted attention due to the band-gap opening[59, 141, 148, 151]. Here we complement those studies and show how an electron transport-gap appears already for a few repetitions of dots. We also consider phonon transport and find a similar fast convergence with number of repetitions. Combining both transport calculations we are able to report on the thermoelectric figure of merit which is sizable considering the very excellent thermal transport of graphene.

A selection of different fabrication techniques exists for creating this nanostructured system, e.g. by electron beam lithography[53, 64] or block copolymer lithography[6, 91]. The latter method results in a highly regular hexagonal lattice of holes. Inspired by these experiments we consider devices with a periodic perforation in a hexagonal lattice, see Fig. 3.1.

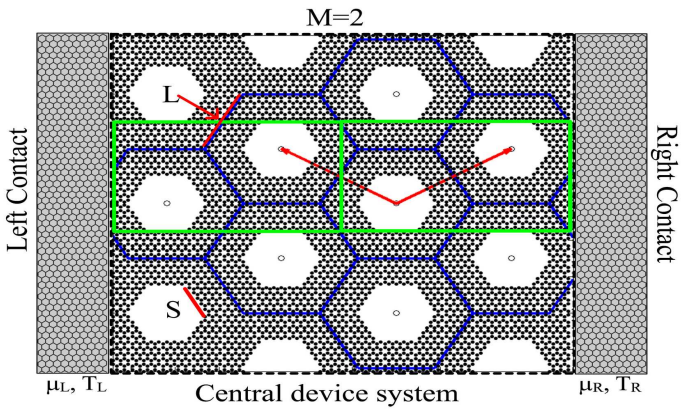

Figure 3.1: *GAL system setup and the computational rectangular unit cell (green rectangle). Two graphene leads are connected by the finite GAL. The depicted system is a {10,5zz} GAL with a length of 2 ($M = 2$) corresponding to 4 holes in the direction of transport. From Paper I.*

We use the nomenclature introduced in Ref. [148] and specify the GAL by $\{L,Ss_2\}$, where the L is the length of the side of a hexagonal Wigner-Seitz cell, and S is the side length of the antidot(see Fig. 3.1), both in units of the lattice constant $\sqrt{3}a_0$, with $a_0 = 1.42\,\text{Å}$ being the carbon-carbon distance. $s_2 = \{\text{zz}, \text{arm}, \text{cir}\}$ labels the edge type. We will assume the device to be of finite length, labeled by the number of unit cells M, between two pristine graphene leads. The infinite direction perpendicular to the transport direction is treated using periodic boundary conditions and corresponding k-point sampling. In another experiment hexagonal holes were obtained with very pure edge chirality by anisotropic etching[96]. The shape will be hexagonal with either armchair

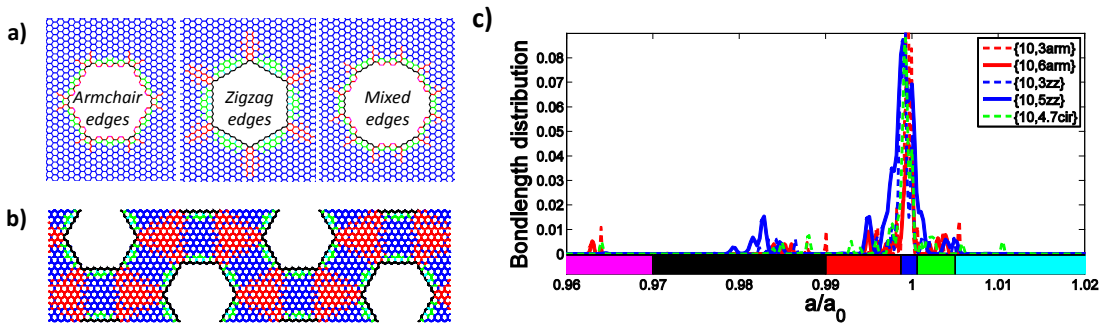

Figure 3.2: *Antidot shapes and resulting strain fields. a) We consider antidots with hexagonal or circular shapes. The hexagonal antidots results in either pure armchair or zigzag edges depending on the hexagon rotation. b) Resulting local change in bond lengths after a structural relaxation of a {10,5zz} GAL. The coloring scheme for the bond lengths is illustrated in (c), that gives the distributions of bond lengths for varying sizes and shapes of antidots. As the hole size is increased the spectrum broadens and peaks occur at different bond lengths that are characteristic of different hole types. Partially from Paper I.*

or zigzag edges inspired by the experiment, or simply circular with mixed edges resulting from a given hole radius, Fig. 3.2a. Following a structural relaxation, we find that the changes in the bond lengths compared to a_0 are below 4%, Fig. 3.2c. Compression of bonds at the edge is followed by a region with elongation of bonds and the relaxation is confined in small regions in space. Matching of edge relaxations can result in longer-ranged relaxations (small compressions) emanating from the corners. This occurs mainly for zigzag edges of large antidots, Fig. 3.2b. We include the strain effect in the electronic transport calculations through the Harrison scaling. We find that the modulation of the hopping elements is of minor importance for the present applications.

It is interesting to examine how the electron and phonon transport properties are affected by an embedded GAL, e.g. in terms of thermoelectric applications. To this end, we investigate how the thermoelectric properties depend on antidot shapes and sizes.

3.1 Electronic properties

The electron transmission for a varying length, determined by the number of unit cell repetitions (M), is shown in Fig. 3.3. As can be seen the electronic transmission $\mathcal{T}_e$ converges fast toward a length independent result. We define a transport gap as the energy range where the transmission is below a certain small value. On the semi-logarithmic scale the transmission goes toward zero in a region corresponding to the band gap of the

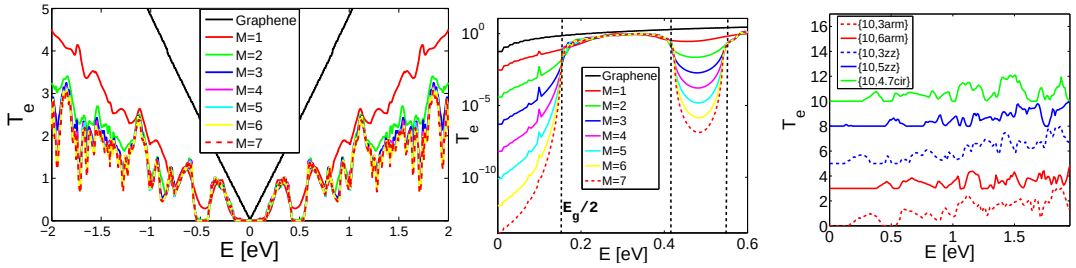

Figure 3.3: *Left: Convergence with length (M, the number of unit cells with two holes along the device) of transmission for a {10,3arm} antidot lattice. Middle: Zoom at the transport gap for the {10,3arm} GAL. The leftmost vertical dashed line marks the value of the band gap obtained from the band structure of an infinite GAL. Right: Transmissions close to the Fermi level. The transmission curves were shifted by an integer to ease the comparison. From Paper I.*

infinite GAL within a very few repetitions of antidots between the leads. We conclude that the transport gap converges to the band gap of the infinite antidot lattice, found from the band structure, and the system behaves 'bulk-like' after only six to seven unit cell repetitions. This was found to hold true for the more than 20 GAL configurations considered in Paper I.

It is interesting to examine how much of the transmission reduction, compared to transmission of pristine graphene $\mathcal{T}_0$, that can be attributed to the effective width reduction from W_0 to the minimal width along the device, W. To this end, we define a set of envelope lines that approximate the transmission versus energy as linear curves corresponding to a simple reduction of the pristine transmission, $\mathcal{T}_{\text{eff}} = R_{\text{eff}}\,\mathcal{T}_0$. Here the effective width reduction $R_{\text{eff}} = W/W_0$ describes the amount of pristine transmission that survives the lattice perturbation in terms of a regular perforation. The hole dimension was varied between 1.2 nm and 2.6 nm giving an effective width reduction between 71% and 26%. We take two approaches. Firstly, if we define the actual reduction factor as the average reduction found at each energy point. It decreases linearly with hole dimension from 24% to 5%, i.e. a much lower transmission than expected. Example curves are shown in the transmission plots of Fig. 3.4. Therefore, only a minor part of the average transmission reduction can be ascribed to the narrowing of the conducting plane. Secondly, we instead examine if the peak transmission is limited by the effective width. The peak transmission reduction factor is found to be decreasing from 65% to 21%, and fits the effective width reduction very well for small holes. As the hole size increases, the effective width is overestimated due to the triangular lattice structure of the perforation, and the reduction factor approaches the averaged value.

In Fig. 3.4 we compare the electronic transmission and the band structures for two GALS with large holes with zigzag and armchair edges, respectively. The figure illustrates how the transmission can be directly traced back to the band structure of the GAL. Additionally, we find that there is an important difference between holes of different atomic arrangements at the edges. Systems with zigzag edges leads to an additional splitting into flat minibands around the Fermi level. From the simplest NNTB model of a 1D chain we know that the energy width of a band is a measure of the strength of the given atomic states' interaction with nearest neighbor states[1]. Therefore, if the

[1]The energy width obtained from the 1D bands, $E(k) = E_0 + 2tcos(ka)$, is $W_E = 4t$, e.g. it is

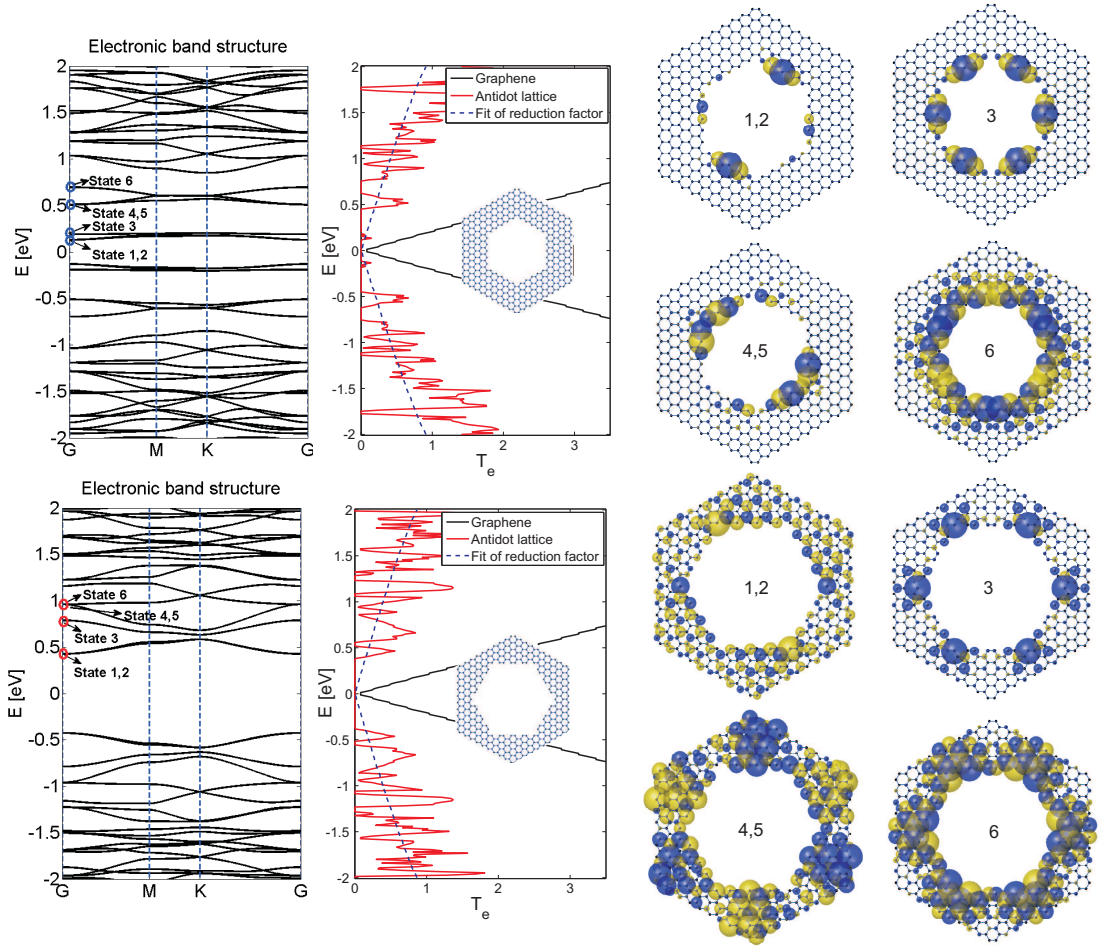

Figure 3.4: *Left: Band structure for {10arm,5zz} (top) and {10arm,6arm} (bottom) antidot lattices respectively. Middle: Corresponding electronic transmission around the Fermi level. The energies of the states illustrated and compared further are marked with circles. Right: Eigenstates 1, 3, 4 and 6 at the Γ-point with energies as marked in the corresponding band structures. The eigenstates of the {10,5zz} antidot lattice (top) are very localized at the edges. The eigenstates of the {10,6arm} antidot lattice (bottom) are less localized at the edges, but resemble corner states. A phase of zero and π is colored blue and yellow, respectively. From Paper I.*

bands are very flat (low dispersion), the interaction is small, and we expect to have quasi-localized states in the system. This feature can be understood in terms of localized states due to a local excess of atoms of one of the two sublattices in the graphene bipartite lattice[183]. The local imbalance of A and B type atoms at the edges leads to the corresponding number of defect states. In hexagonal holes with zigzag edges each side consists of a segment of either type A or B atoms. The hybridization will be small between these defect states which are partially separated in space. As illustrated at the rightmost of Fig. 3.4, the flat minibands are highly localized at the edges. In the case of hexagonal holes with armchair edges each side consists of an alternating sequence of A and B atoms. Therefore, these defect states hybridize more resulting in a larger shift from the Fermi level and a reduced flatness of the bands. As can be seen from Fig. 3.4 the first bands with minimal dispersion are mainly localized in the small zigzag corner region between two AB sequences. We expect the localized states to be sensitive to disorder destroying the pristine edge chirality of the antidots. However, as is indicated by the {10,6arm} corner states, one can always expect to have some degree of localization at zigzag edge segments, which we have also found to be true in the mixed edges.

One could also expect that the nature of the localized states at the hole edges depends heavily on the presence of passivation. For the purpose of examining the effect of passivation we have performed calculations of the band structures with a model including two *d*-orbitals for each C-atom and an explicit model for the carbon-hydrogen interaction[25]. The qualitative features of the band diagram, and the edge states, de-

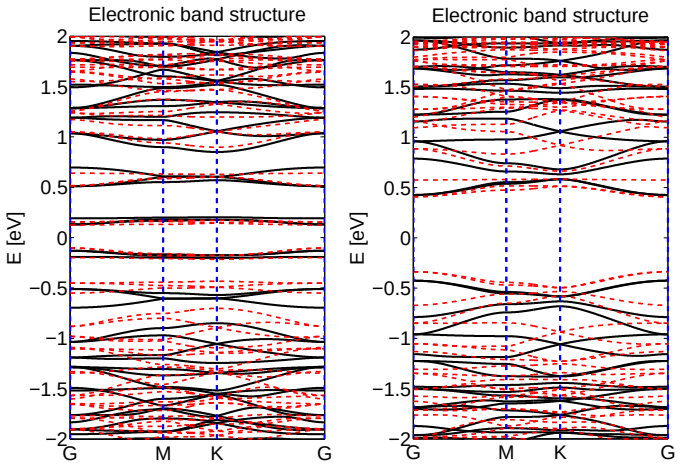

Figure 3.5: *Comparison of band structures with and without passivation of a {10arm,5zz} (left) and {10arm,6arm} (right). Black solid lines are calculated with the conventional $\pi-$model and red dashed lines includes hydrogen passivation at the hole edges using the p/d-model. The passivation is positioned at the same bond angle as in graphene.*

pend surprisingly little on the presence of hydrogen passivation, Fig. 3.5. However, the effect of passivation might be more important in antidot lattices with localized zero energy states such as in the triangular antidots considered in Ref. [183].

We conclude that the flat minibands of the zigzag antidots are more localized than the corresponding states of an antidot lattice with armchair edges. This has the important consequence that localization in armchair antidots is due to a decreasing hole-hole distance, whereas it is due to edge states for zigzag antidots. Therefore, the band gaps

proportional to the nearest neighbor hopping element.

of GALs with armchair edges are determined by the confinement, as opposed to the case of zigzag edges where it is governed by edge state formation.

3.2 Phonon transport

We now turn to the thermal transport properties of finite GALs. The most time-consuming part of the thermoelectric calculations is the evaluation of the force constant matrices and the recursive phonon NEGF calculation. The relaxation is performed with Gulp[60]. The calculation of the transport matrices are evaluated directly by the Brenner potential[29] enabling a fewer repetitions of the system (only three repetitions are needed in the transverse direction for transport calculations) and more freedom in parallelization. We further speed up simulations by subsequently repeating the dynamical matrix and Hamiltonian of the center unitcell (2 holes) for longer systems. The first cell is close to the fixed contact region. Using three unitcells (M=3, 6 holes) was found to be sufficient.

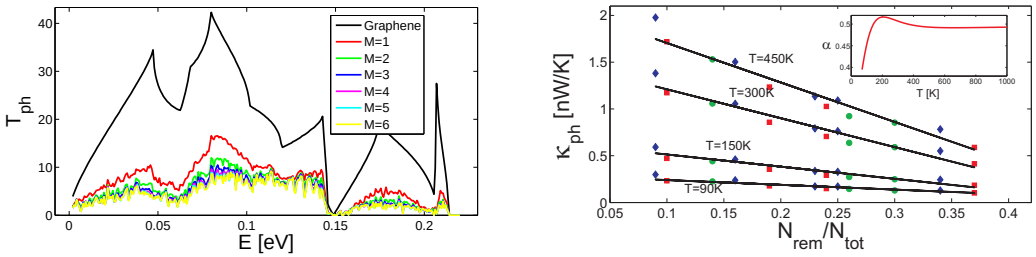

Figure 3.6: *Left: Convergence with length of phonon transmission for a {10,3arm} antidot lattice. Right: Thermal conductance from phonons as a function of hole dimension. The red squares, blue diamonds and green circles label holes with armchair, zigzag and circular/mixed edges respectively. Four different temperatures are plotted for each system. From top to bottom the thermal conductance is found at a temperature [450,300,150,90] K. The thermal conductance at these four temperatures is for pristine graphene found to be [8.5,6.1,2.6,1.2]$\frac{nW}{K}$. Inset: fitted dimensionless parameter α describing the scaling with hole size of the thermal conductance. From Paper I.*

In Fig. 3.6 we show the phonon transmission as a function of M, the number of repeated unit cells. As it was the case for the electrons we find that the thermal properties converge at a short length scale. The phonons behave 'bulk-like' after six to seven unit cell repetitions, and hereafter have properties equivalent to the periodic superlattice phonons.

The resulting thermal conductance is shown for a sequence of different antidot sizes and shapes, Fig. 3.6(right). We will typically examine temperature from slightly above the boiling point of liquid nitrogen, $T_{bn} = 77.2$K, to above room temperature. The thermal conductance due to phonons in pristine graphene at 300 K can be compared to a measured partially diffusive thermal conductivity[10] of $\sigma_{ph}^{\rm exp} \approx 4.5 - 5.5 \times 10^3\,{\rm W/(m\,K)}$. We find that the reduced ballistic thermal conductance, $\kappa_{ph}^{\rm pri}/(W_0 h) \approx 4.27 \times 10^9\,{\rm W/(m^2K)}$, is much larger than the experimentally extracted result $\sigma_{ph}^{\rm exp}/(L^{\rm exp}) \approx 0.39 - 0.48 \times 10^9\,{\rm W/(m^2K)}$. Here $h = 3.35\,$Å and $L^{\rm exp} \approx 11.5\,\mu$m are the graphite interlayer distance and traveled distance by the phonons in the experiment by Balandin *et al.*[10],

respectively. This result is consistent with other theoretical calculations[84] and the main difference from the experiments can probably be attributed to isotopes, defect scattering and especially anharmonicity being important for long devices.

Turning to the antidot results we have calculated an average reduction factor for the phonon transmission as we did for the electrons. The transmission of the lowest acoustic and especially the highest optical modes is in general reduced more than the remaining of the phonon spectrum. There is a tendency that the phonons are scattered more than the electrons by the nanoperforation for small antidot concentrations. For large hole dimensions both the electrons and phonons are scattered to an extent where the transmission is reduced by more than 80% on average for the systems considered. For the largest holes up to 36% of the atoms was removed from the pristine graphene plane.

Fig. 3.6(right), illustrates how the thermal conductance decreases almost linearly with the number of removed atoms (for perforation ratios larger than 5%). Furthermore, the graph shows that the thermal conductance has a tendency to be slightly larger for holes with zigzag edges (shown as diamonds in Fig. 3.6). A similar behavior has been found for graphene nanoribbons with zigzag edges[78]. However, compared to the electronic case the thermal transport features are less sensitive to the exact shape and edge of the holes. Only the amount of removed material is of significant importance. As a consequence we can extract an empirical expression relating the GAL thermal conductance to that of pristine graphene. In the regime where the thermal conductance is linear in the hole dimension one can parameterize the thermal conductance as

$$\kappa_{ph} \approx \left(-\alpha(T)\frac{N_{rem}}{N_{tot}} + \beta\right)\kappa_{ph}^{\mathrm{pri}}(T)\,. \tag{3.1}$$

From this approximation we fit the 'linear regime offset' $\beta \approx 0.25$ and the dimensionless parameter $\alpha(T)$, given in the inset of Fig. 3.6. Above room temperature $\alpha \approx 0.5$ is almost constant. The lines in Fig. 3.6 are illustrating this parametrization. Only the variation of absolute hole size is plotted in Fig. 3.6, for a fixed unitcell dimension L. No qualitative difference is found regarding antidot concentration dependence of the thermal conductance keeping the hole geometry fixed and varying the unitcell parameter L. Again, this illustrates that the phonon properties are less sensitive to the exact nature of the holes as compared to the corresponding electronic properties.

3.3 Thermoelectric properties

The efficiency of a material in converting temperature gradients into an electric voltage, at an average temperature T, is quantified by the dimensionless figure of merit $ZT = S^2 G_e T/\kappa$. Thermoelectric materials with $ZT \approx 1$ have an efficiency in the range of available thermoelectric components based on nanostructered bulk materials, whereas $ZT > 3$ is needed to compete with conventional refrigerators and generators[115, 185]. We thus seek a high electronic power factor, $S^2 G_e$, and minimal thermal conductance $\kappa = \kappa_{ph} + \kappa_e$ which includes contributions both from phonons and electrons.

Maximal thermoelectric figure of merit, ZT, is obtained after length convergence due to the increased band gap and decreased thermal conductance. It becomes independent of length at the same scale as the electron and phonon transmissions ($M \geq 7$) as the superlattice properties settle in. I.e. since our system consists of two graphene leads connected by a perfect superlattice of holes it never reaches a diffusive transport limit.

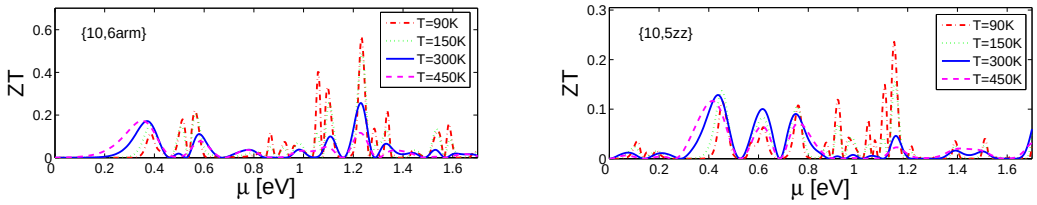

Figure 3.7: *ZT for {10,6arm} and {10,5zz} lattices at the four temperatures [450,300,150,90] K. At low temperature the pure electronic figure of merit, ZT_{el}, can be very large due to a vanishing thermal conductance from electrons and sharp features in the transmission spectrum. At low temperature many sharp transmission features also becomes visible in the actual ZT. From Paper I.*

Fig. 3.7 shows the estimated ZT as a function of chemical potential for two representative GALs. ZT has a number of peaks corresponding to a large variation of the transmission with energy. The Seebeck coefficient is a measure of these changes and their robustness to temperature smoothening, and displays peak values of the order of 0.1-1.5 mV/K, which is similar to what has been obtained for other carbon based nanosystems and molecular contacts[13, 142, 159].

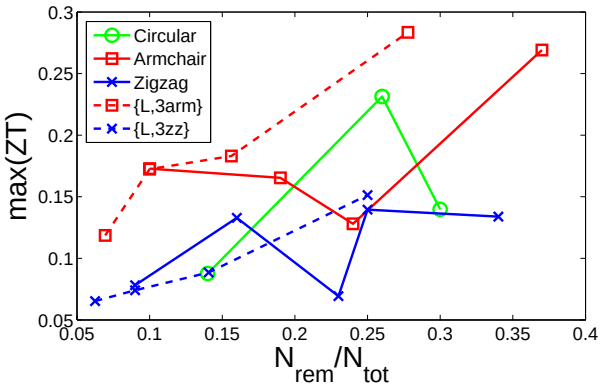

Figure 3.8: *ZT dependence on the ratio of removed atoms in the nanoperforation at $T = 300\,K$. Systems included in the figure are {10,Szz} with S=3,4,4.5,5,5.5, {10,Sarm} with S=3,4.5,5,6 and {10,Scir} with S=3.5,4.7,5 (full lines) and furthermore two set of systems with a fixed hole {L,3arm} and {L,3zz} with L=6,8,10,12 (dotted lines). From Paper I.*

The Seebeck coefficient is highly sensitive to the variations in the electronic transmission resulting from different hole edges, sizes and so forth. In Fig. 3.8 we collect the maximum ZT values we have found for a selection of GALs. We can extract a set of design guidelines from this result. First of all it seems possible to obtain larger ZT from GALs based on hexagonal holes with armchair edges. The presence of highly splitted flat-minibands reduce the power factor of GALs with pure zigzag edge chirality. The Seebeck coefficient can be larger for zigzag edges. However, the power factor is significantly lower due to the lower transmission from the isolated energy levels with low dispersion. There is also a weak trend that the hole dimension compared to the system size should be maximized. By increasing the hole dimension we actually reduce the electronic fig-

ure of merit ($\kappa_{ph} = 0$ result) but increase the obtained fraction of it due to a reduced phonon conductance. We also examine if the antidot concentration should be varied by changing the hole size, while keeping the lattice parameter L fixed, or by keeping the hole size fixed under L variation. The latter examination is computationally possible only for small antidot dimensions. Therefore, it is possible to see if the thermoelectric properties depend on the absolute hole size or only on the antidot concentration. For the examined systems we find that antidots with smaller absolute sizes seem to result in better thermoelectric performance for holes with armchair edges. For holes with zigzag edges the exact nature of the localized states comes into play and seems to keep the thermoelectric performance less sensitive to the absolute hole size. We conclude that it is possible to obtain fair thermoelectric properties of GALs. ZT can exceed 0.25 and is highly sensitive to the atomic arrangement at the hole edges.

As mentioned one could expect several effects to further reduce the thermal conductance relatively more than the electronic conductance. Isotope scattering, anharmonic interactions, defect scattering in the diffusive limit and graphene-substrate interactions could all contribute to a reduction of the phonon thermal conductance. In Fig. 3.9 we

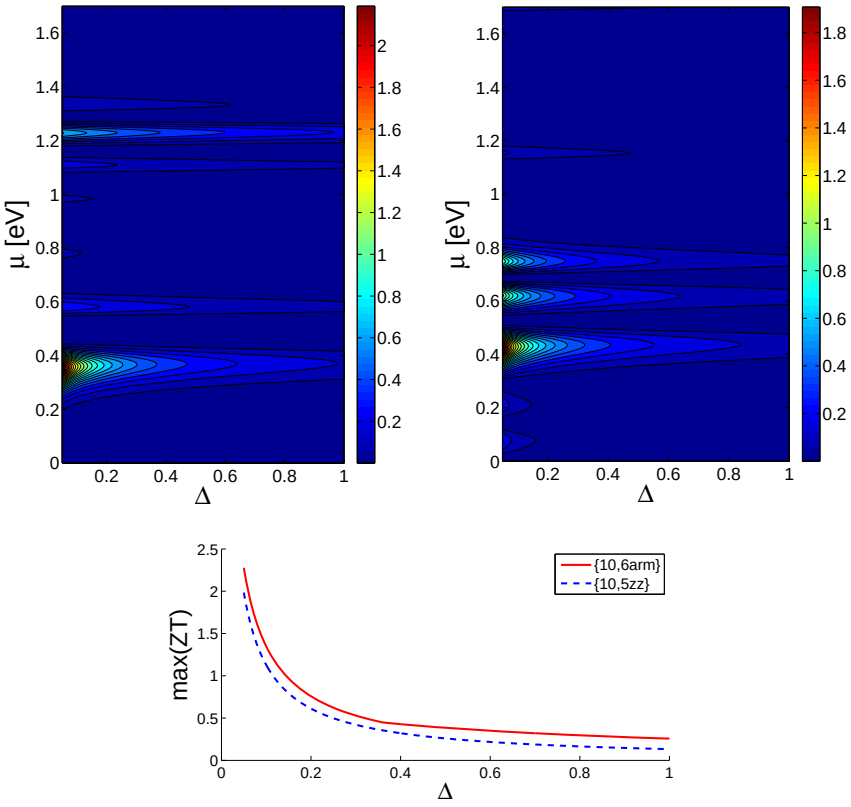

Figure 3.9: *ZT variation with a decrease of the phonon thermal conductance at $T = 300\,K$. Δ describes the fraction of the original thermal conductance used in the calculation. Top: ZT as a function of the chemical potential and the phonon thermal conductance for the {10,6arm} (left) and {10,5zz} (right) GAL. Bottom: Peak ZT as a function of the variation of the phonon thermal conductance. From Paper I.*

illustrate the effect of a reduction of the phonon thermal conductance. The parameter Δ gives the fraction of the original phonon thermal conductance kept in the calculation.

For the {10,6arm}GAL the first peak ($\mu \approx 0.37\,\mathrm{eV}$) increases more rapidly than the high energy peaks. The peak position crossover happens around $\Delta \approx 0.35$. When the phonon thermal conductance dominates, the figure of merit variation goes as ZT/Δ, clearly present in the low energy ZT variation (see Fig. 3.9, bottom) even when the phonon thermal conductance is reduced below 5% of its original value. This illustrates two important points. At high chemical potential the main limitation is the power factor and not a further reduction of the phonon heat conductance. On the contrary one could obtain a significant ZT enhancement at low chemical potential by further reducing the thermal conductance. The main difference between the {10,6arm}GAL and {10,5zz}GAL is that the first mentioned is limited by the power factor while the latter is limited by the phonon conductance.

One interesting scattering mechanism that solely reduce the thermal conduction is the effect of isotopes. The effect of isotopes on the thermal conductivity of graphene has recently attracted much attention due to the advances in graphene synthesized by chemical vapor deposition (CVD). By using sequential input of $^{13}CH_4$ and $^{12}CH_4$ several groups have managed to fabricate graphene with regions of different isotopes[103]. The local thermal conductivity of the regions with different isotopes has been measured by Raman spectroscopy[37]. The isotope effect has been addressed theoretically for graphene[125, 206] and nanoribbons[79].

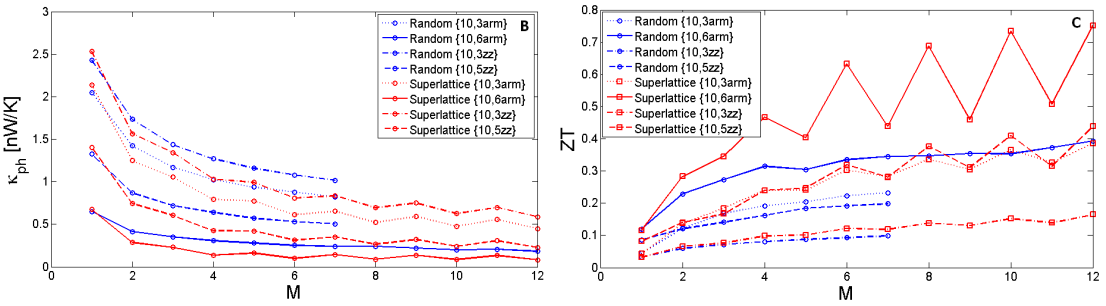

Figure 3.10: *The effect of isotopes is considered for a long system (up to $M = 12$). The random isotopes of ^{13}C atoms are distribution at random positions at each M with a concentration of 50%. For the supercell pattern every second unit cell consist of ^{13}C isotopes. The temperature is 300K. From Paper III.*

In Fig. 3.10 we see how isotope scattering give rise to a significant reduction in the thermal conductance of two GAL systems with different hole shape and size, as a function of length of GAL-device. Comparing the reduction from the random isotope distribution to that of a pattern (alternating isotopes for every 2-hole supercell), it is clear that the "clustering" of isotopes leads to an extra reduction for especially the acoustic modes in the GAL region. With random isotopes the thermal conductance of the $M = 12$-{10,6arm}-device is reduced by 55%, compared to 88% with the ordered isotope pattern. For devices of longer lengths we enter the diffusive region and cannot neglect phonon-phonon scattering as considered here.

Since isotopes only affect the thermal properties we get a significant increase in ZT, especially at low gate bias where thermal transport is dominated by phonons. A peak $max(ZT) \approx 0.8$ is observed for the supercell pattern of isotopes at 300K, compared to $max(ZT) \approx 0.26$, 0.17, 0.07 and 0.13 for the ideal {10,6arm}, {10,3arm}, {10,9zz} and {10,3zz} GALs without isotopes. The oscillations in ZT with M stems from the choice of patterning where we only have $50\% - 50\%$ isotopes for even M. With random isotopes

we can exceed $max(ZT) \approx 0.4$ for the {10,6arm} lattice. This illustrates that one can benefit from a further reduction of the heat conductance in GAL devices to increase the thermoelectric efficiency.

We conclude that nanopatterning of isotope distributions can be more efficient in scattering phonons than a random distribution. This holds true up to a certain cluster size, where all frequencies are not affected equally anymore. In general isotopes, both randomly distributed or not, seems very efficient in reducing the thermal conductance. Other scattering mechanism related to disorder are discussed in Paper III, but will not be mentioned here.

3.4 Topology optimization of the thermoelectric properties of graphene

The GAL may be a good guess for a thermoelectric device based on graphene. Certainly, it allows one to manipulate the thermal properties and band gap in a direct way. However, modern computer technology allows for optimization routines where one can scan through a large set of promising configurations. Topology optimization address the general problem of "where to put the holes" to optimize a physical parameter of interest. Within production industries there is a heavy demand for obtaining high quality at a low material cost. Topology optimization methods were initially developed within continuum mechanics, but has now found applications in a wide range of engineering fields[3, 16]. For instance, recently developed applications are within nano-scale heat transfer[55], thermoelectric generators[172], piezoelectric actuators[93, 201], photonic waveguides[186] and steady-state Navier-Stokes flow in microfluidics[138]. In this section we develop a methodology for atomistic topology optimization of transport properties. The result is mainly the method and implementation by itself, but we aim at topology optimization of ZT for graphene and graphene nanoribbons and discuss some potential issues with application of the machinery to atomic structures.

3.4.1 The model

In this section we introduce the mathematical model of how the design variable (or density), ρ, is varied locally in the atomistic transport calculation. We furthermore perform the sensitivity analysis of how to obtain the change in thermoelectric behavior with variation of the local density.

The optimization problem can be formulated as

$$\underset{\rho}{\text{Maximize}} \quad ZT(\rho) = \frac{S^2(\mu_0, T, \rho) G_e(\mu_0, T, \rho)}{\kappa_e(\mu_0, T, \rho) + \kappa_{ph}} T \tag{3.2}$$

$$\text{subject to:} \tag{3.3}$$

$$\text{Volume constraint: } \int_\Omega \rho(\mathbf{r}) d\mathbf{r} - f \cdot |\Omega| \leq 0 \tag{3.4}$$

$$\text{Design variable bounds: } 0 < \rho_{min} \leq \rho(\mathbf{r}) \leq 1 \tag{3.5}$$

$$\text{Equilibrium equations: } \mathbf{G}^{r/a} \left[E - \mathbf{H} - \mathbf{\Sigma}^{r/a} \right] = \mathbf{I} \tag{3.6}$$

To simplify the calculation we keep the phonon thermal conductance fixed and optimize the electronic part at a specific chemical potential μ_0. Instead of performing a phonon calculation at each iteration we apply a volume constraint. This may reduce the power factor globally, but to lowest order a larger fraction hereof is obtained when the phonons

are included correctly. From the previous section we know that the thermal conductance scales linearly with the removed amount of material. For instance eqn. 3.1 suggest a good initial guess for the thermal conductance at a volume constraint f >60%. An optimization strategy could therefore be: First optimize ZT with a fixed estimated thermal conductance, which will be a very fast single orbital problem. Then perform a single phonon calculation with the dynamical matrix of graphene modified by the density field and optimize ZT with fixed thermal conductance during some optimization iterations. This procedure can be repeated so that the thermal conductance eventually do not need to be updated anymore. Lastly one could do a full optimization where both electron and phonon properties are modified during each iteration. The main problem will in this approach be if the relaxation matters, so we are in principle restricted to f >60% in any case.

We define a density field adjusting the local density of carbon at each site between 'white' and 'black', $0 < \rho < 1$. We compare the performance of two different transport models that both describes the effect of removing individual atomic sites, $\rho_i = 0$ for site 'i'.

- ***Onsite model:*** The onsite energy is defined as $H_{ii} = \epsilon_0 + (1 - \rho_i)^p \epsilon_{max}$. The derivative of the Hamiltonian is $\frac{\partial H_{ii}}{\partial \rho_i} = -p(1 - \rho_i)^{p-1}\epsilon_{max}$.
- ***Hopping model:*** The hopping integral is modified as $H_{ij} = (\rho_i \rho_j)^p t$. The derivative is $\frac{\partial H_{ij}}{\partial \rho_i} = p(\rho_i)^{p-1}(\rho_j)^p t = p\frac{H_{ij}}{\rho_i}$.

The onsite model is frequently used to model point defects and edge disorder in graphene nanostructures. The hopping model combines the density at the two atomic sites in a parametrization of the hopping element of a bond. The panelization parameter, p, is adjusted to obtain as "black-white" configurations as possible.

To illustrate the models we consider the transmission across a minimal armchair ribbon, where we gradually remove 3 atoms at one edge, Fig. 3.11. In (a) we show the transmission as a function of energy for varying density at the defect sites. Interestingly, we find that the transmission peaks, when developed, are fairly stable positioned at the final peak energy. This is not the case for the onsite model, where we find the transmission peak position to converge slowly to the correct position. In (b) and (c) we show the transmission at the defect peak position, $\mu_0 = -0.6$ eV, as a function of design variable. The transmission should be 1 in both limiting cases (from perfect ribbon at $\rho = 1$, to defected ribbon at $\rho = 0$). For the onsite model $\epsilon_{max} \geq 10^2$ for the barrier to actually act like a defect. $\epsilon_{max} = \infty$ corresponds to the defected GNR while $\epsilon_{max} = 0$ corresponds to graphene. This model seems to trap itself between a smooth variation and wrong T_e at low ϵ_{max} versus an abrupt variation and correct T_e at high ϵ_{max}. Therefore, the onsite model seems more sensitive, with a very nontrivial interpolation between transmission and density. On the contrary, the hopping model shows a change in transmission with density that seems quite smooth and easy to fine tune with a p in between 1/2 and 5. If we increase the p above 1 a low density will very fast be equal to a true defect, promoting highly contacted devices. The hopping model therefore seems the most promising, despite the additional complexity in bookkeeping of the elements.

3.4.2 Sensitivity analysis and reintroducing recursion

The difficult problem of iteratively minimizing a function on the basis of a series of constraints and information from previous iterations is performed with the licensed math-

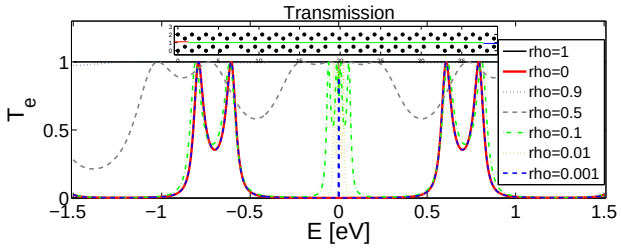

(a) Transmission from the hopping model at different designed density at three atomic sites. Insert: The transport setup of a minimal GNR between two leads. The 3 missing atoms illustrates the sites where the density ρ_i is gradually reduced from one.

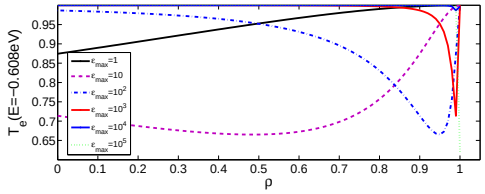

(b) Transmission for the onsite model at the peak position $\mu_0 = -0.6$ eV as a function of design variable.

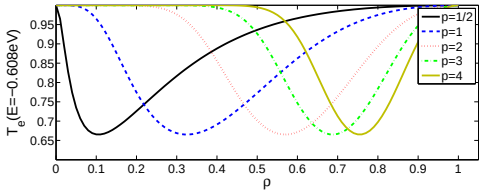

(c) Transmission for the hopping model at the peak position $\mu_0 = -0.6$ eV as a function of design variable.

Figure 3.11: *Transmission across a minimal GNR as a function of the design variable, which illustrates how smooth the transition from perfect to defected ribbon is within the two models.*

ematical Method of Moving Asymptotes (MMA) developed by K. Svanberg[16]. The essential ingredients is a previous and present set of densities, object functions and sensitivities to changes in the local densities. In our case, the fundamental parameter is the energy dependent transmission. We now evaluate the sensitivity of the transmission to a change in the design variable. Direct derivatives of the Green's functions are rather expensive to calculate. Applying the adjoint method, see appendix 9.6, we find that

$$\frac{\partial \mathcal{T}_e(E)}{\partial \rho_i} = 2\mathrm{Re}\left(\mathrm{Tr}\left[\mathbf{G}^{\mathrm{r}}\frac{\partial \mathbf{H}}{\partial \rho_{\mathrm{i}}}\mathbf{G}^{\mathrm{r}}\mathbf{\Gamma}_{\mathrm{R}}\mathbf{G}^{\mathrm{a}}\mathbf{\Gamma}_{\mathrm{L}}\right]\right). \tag{3.7}$$

The remaining $\frac{\partial \mathbf{H}}{\partial \rho_i}$ factor is evaluated according to the chosen models in the previous section. Eqn. 3.7 is consistent with a lowest order Dyson equation, i.e. replacing the Green's function in the Landauer formula with $\mathbf{G}^{r/a} + \mathbf{G}^{r/a}\frac{\partial \mathbf{H}}{\partial \rho_i}\mathbf{G}^{r/a}$.

We apply a recursive method for evaluating the part of the Green's function relevant to the transmission and sensitivity calculation. We slice our system in subsystems from one lead to the other only interacting with the neighbor cells, see Fig. 3.12A. The equation for the system consisting of (n+1) subsystems is

$$\begin{bmatrix} (E+i\eta)\mathbf{I} - \mathbf{H}^{(n)} & [0\cdots -\mathbf{V}_n]^T \\ \left[0\cdots -\mathbf{V}_n^\dagger\right] & (E+i\eta)\mathbf{I} - \mathbf{H}_{n+1} \end{bmatrix} \times \begin{bmatrix} \mathbf{G}_n^{(n+1)} & \mathbf{G}_{lr}^{(n+1)} \\ \mathbf{G}_{rl}^{(n+1)} & \mathbf{G}_{n+1,n+1}^{(n+1)} \end{bmatrix} = \begin{bmatrix} \mathbf{I} & \mathbf{0} \\ \mathbf{0} & \mathbf{I} \end{bmatrix}$$

where the Green's function at the previous step and the coupling parts are written in

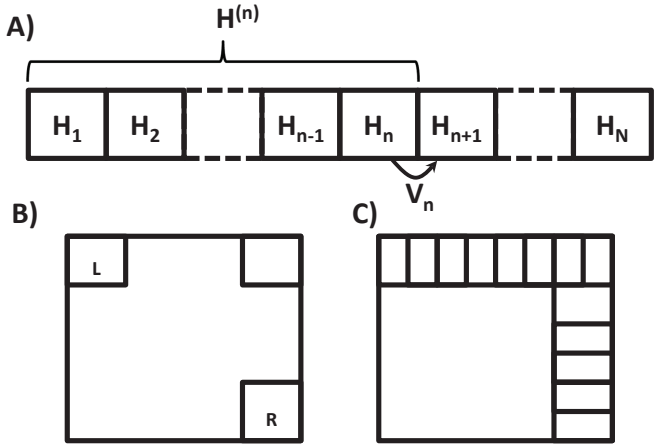

Figure 3.12: *A) The full Hamiltonian is partitioned in N subsystems, described by H_n, only connected by nearest neighbor coupling matrices, V_n. B) Part of full Green's function needed to perform transmission calculation. The L and R regions describes the part connected to the lead self-energies. Only the corner part with the lead dimensions is needed for the transmission calculation. C) Part of full Green's function needed to perform the calculation of the sensitivity. The full first block row and the last block column contributes.*

terms of subsystem blocks as

$$\mathbf{G}_n^{(n+1)} = \begin{bmatrix} \mathbf{G}_{1,1}^{(n+1)} & \cdots & \mathbf{G}_{1,n+1}^{(n+1)} \\ \vdots & \ddots & \vdots \\ \mathbf{G}_{n,1}^{(n+1)} & \cdots & \mathbf{G}_{n,n}^{(n+1)} \end{bmatrix},$$

$$\mathbf{G}_{lr}^{(n+1)} = \begin{bmatrix} \mathbf{G}_{1,n+1}^{(n+1)} \\ \vdots \\ \mathbf{G}_{n,n+1}^{(n+1)} \end{bmatrix}, \mathbf{G}_{rl}^{(n+1)} = \begin{bmatrix} \mathbf{G}_{n+1,1}^{(n+1)} & \cdots & \mathbf{G}_{n+1,n}^{(n+1)} \end{bmatrix}.$$

We operate with two sets of indices: the lower block indices and the upper iteration step (length of system). The recursive procedure for obtaining the relevant blocks of the Green's function is described in Appendix A, Sec. 9.7.

Considering the transmission, we rewrite the trace in the Landauer formula in terms of blocks:

$$\begin{aligned} \mathcal{T}_e &= \mathrm{Tr}\left[\mathbf{G}^{r,(N)}\mathbf{\Gamma}^R\mathbf{G}^{a,(N)}\mathbf{\Gamma}^L\right] = \sum_{j'}\left(\mathbf{G}_{1,N}^{r,(N)}\mathbf{\Gamma}_{N,N}^R\mathbf{G}_{N,1}^{a,(N)}\mathbf{\Gamma}_{1,1}^L\right)_{j',j'} \\ &= \mathrm{Tr}\left[\mathbf{G}_{1,N}^{r,(N)}\mathbf{\Gamma}_{N,N}^R\mathbf{G}_{1,N}^{\dagger r,(N)}\mathbf{\Gamma}_{1,1}^L\right] \end{aligned} \tag{3.8}$$

Due to the trace and the local nature of the coupling matrices (only nonzero in first and last block respectively), only the corner part of the full Green's functions is required, see Fig. 3.12B.

The trace in the sensitivity is simplified as

$$\begin{aligned}\frac{\partial \mathcal{T}_e}{\partial \rho_n} &= 2\mathrm{Re}\left(\mathrm{Tr}\left[\mathbf{G}^{\mathrm{r,(N)}}\frac{\partial \mathbf{H}}{\partial \rho_{\mathrm{n}}}\mathbf{G}^{\mathrm{r,(N)}}\mathbf{\Gamma}^{\mathrm{R}}\mathbf{G}^{\mathrm{a}}\mathbf{\Gamma}^{\mathrm{L}}\right]\right) \\ &= 2\mathrm{Re}\sum_{\mathrm{j}'}\sum_{\mathrm{p,q}}\left(\mathbf{G}^{\mathrm{r,(N)}}_{\mathrm{1,p}}\left(\frac{\partial \mathbf{H}}{\partial \rho_{\mathrm{n}}}\right)_{\mathrm{p,q}}\mathbf{G}^{\mathrm{r,(N)}}_{\mathrm{q,N}}\mathbf{\Gamma}^{\mathrm{R}}_{\mathrm{N,N}}\mathbf{G}^{\mathrm{a,(N)}}_{\mathrm{N,1}}\mathbf{\Gamma}^{\mathrm{L}}_{\mathrm{1,1}}\right)_{\mathrm{j}',\mathrm{j}'} \\ &= \sum_{p,q}2\mathrm{Re}\left(\mathrm{Tr}\left[\mathbf{G}^{\mathrm{r,(N)}}_{\mathrm{1,p}}\left(\frac{\partial \mathbf{H}}{\partial \rho_{\mathrm{n}}}\right)_{\mathrm{p,q}}\mathbf{G}^{\mathrm{r,(N)}}_{\mathrm{q,N}}\mathbf{\Gamma}^{\mathrm{R}}_{\mathrm{N,N}}\mathbf{G}^{\dagger\mathrm{r,(N)}}_{\mathrm{1,N}}\mathbf{\Gamma}^{\mathrm{L}}_{\mathrm{1,1}}\right]\right) \end{aligned} \tag{3.9}$$

Therefore, we only need one block row and column of the full Green's function, each with a dimension of the lead, see Fig. 3.12C. By performing the calculations specified by 9.63-9.66 with the restriction $i = 1$ we obtain the first and last block rows correctly. The last block column is related to the last block row by a transpose since the Green's function is symmetric. Furthermore, $\frac{\partial \mathbf{H}}{\partial \rho_n}$ is only nonzero in a single block, and possible its two neighbor blocks, further reducing the sum over p, q for each n. The recursive approach has been implemented in Fortran and a speedup is obtained of many orders of magnitude (compared to the full inversion). However, this is also needed for systems with more than 10^2 atoms since on the order of 10^3 transport calculations are needed in the optimization.

3.4.3 Simulations

To optimize the algorithm we will not follow the estimated f >60% restriction, but apply the method to the extreme case of a six unitcell wide GNR with f =0.3 (corresponding to 3-4 chains between two contacts). The purpose is to illustrate that the method can be tuned to give ideal atomistic structures. To simplify the analysis we apply a fixed thermal conductance of 0.25 nW/K. This artificial value is significantly more than what should be expected for such a narrow ribbon. The drawback of the topology optimization techniques is large gray transition regions between solid and void parts that can be hard to interpret. The tendency to gray transition areas is alleviated by using various projection methods[187]. Without going into details we apply a threshold projection filter where one gradually project gray densities above or below 1/2 towards 1 and 0, respectively. These filtering techniques also impose a characteristic length scale, r_{min}, within which sensitivities are obtained as a weighted average. In the examples shown here, we set r_{min} equal to the nearest neighbor distance, but for larger structures, it can be used to define the limit of manufacturability. I.e. structural variation below the dimensional limits in the fabrication process is removed. As a proof of principle we illustrate an optimized configuration for a narrow GNR in Fig. 3.13a. A density of one is displayed as black, while a removed atom, corresponding to a density of zero, is white. The optimized structure is in this case a constriction with atoms removed in a periodic fashion along the edge and two point defects. Note that the four disconnected atoms do not contribute to the transport result. They occur as a result of the projection technique because the intermediate connecting density at some point was projected to zero. Additional constraints will be imposed in the future to remove disconnected atoms. The dramatic change in configuration with projection is also visible as oscillations in the objective function (ZT) as a function of iteration number, displayed in Fig. 3.13b. The objective function is gradually increased during the iterations. As a stable configuration is found the projection toward zeros and ones is increased, resulting in a reduced objective function. The reduction eventually becomes less pronounced and a physical

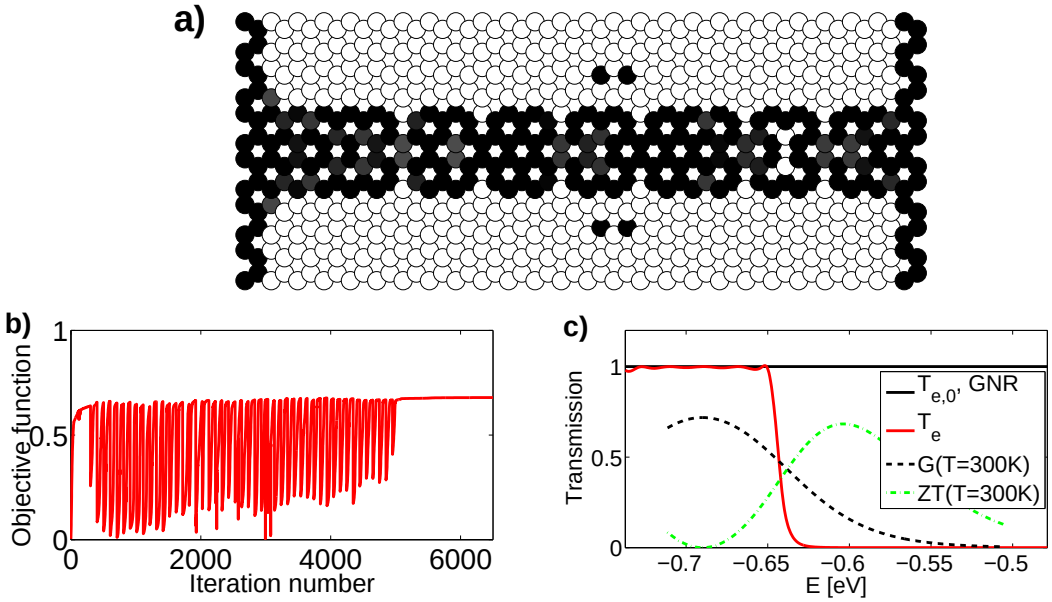

Figure 3.13: *Topology optimization of a GNR. a) Configuration consisting of the initial sites marked by circles. The site density of the final configuration is displayed as the filling color from white (void) to black (density of one). The total volume is 0.3 of the configuration space. The breaking of the left-right symmetry is due to the additional row of atoms used to have leads with the same geometry. b) Objective function (ZT with an artificial thermal conductance) as a function of iteration number. Oscillation occur when gray transition densities are projected further toward zero and one. c) Conductance and ZT, with an artificial thermal conductance, of the final configuration.*

configuration emerges. The transmission before and after optimization and ZT is illustrated in Fig. 3.13c. The transmission of the ideal ribbon (full line black), with a density of one everywhere, is unity in the shown energy range. We arbitrarily try to optimize the ZT at a specific chemical potential, $\mu_0 = -0.6$ eV. This is achieved in the final configuration by introducing a band edge at a slightly lower energy, $E \approx -0.65$ eV, see the final transmission (red full line) in Fig. 3.13c. At $T = 300$ K a nonvanishing conductance, high power factor and resulting optimized ZT is achieved at the requested chemical potential. We conclude that topology optimization methods are applicable in engineering of transport properties to obtain desired features. It is noted that the method developed here applies equally well in the thermal transport problem. However, this is a less sensitive problem that requires longer computations. Topology optimization could become a promising tool for optimizing the thermoelectric properties on the basis of atomistic simulations. Possibly, with additional fine tuning of the projection techniques to remove gray densities and disconnected atoms.

3.5 Summary and discussion

In this chapter we presented simulations of the ballistic thermoelectric properties of finite GAL devices. We showed that the transport properties converge fast toward the bulk limit with increasing length of the perforated device. GALs with different antidot shapes and sizes allows one to manipulate the thermal properties and band gap in a direct way, making graphene a versatile material in electronic as well as thermal management problems. Specifically, hexagonal holes with pure armchair edges lead to an order-of-magnitude larger ZT as compared to pure zigzag edges. This behavior was traced back to the localization of states, which predominantly occurs for zigzag edges, and to an increased splitting of the electronic minibands, which reduces the power factor of GALs with zigzag edges.

The simulations were based on the TB+Brenner model. A recent proposal was to utilize edge currents and antidots in zigzag and chiral graphene nanoribbons[36] to obtain thermoelectric energy conversion. It is noticed that the precise description of these edge currents relies on extended TB models. However, we believe that the minimal π-model is accurate for the periodic structures considered here. Additional phonon scattering mechanisms such as isotopes, substrate interaction and anharmonic interaction may further reduce the excellent thermal transport of graphene to manipulate thermoelectric performances. The latter was theoretically found to severely suppress the thermal conductivity of graphene systems longer than 600Å[190].

Furthermore, we illustrated how topology optimization techniques may be a promising tool for generating a set of prototype structures to be tested in more advanced simulations. This may be a promising route toward atomistic engineering of transport properties of graphene, as well as other systems, where simple tight-binding simulations are able to capture many geometrical trends. This was exemplified by optimization of the thermoelectric performance of a narrow GNR.

Chapter 4

Designing the conduction properties in graphene

A key aspect of future graphene-based electronics is the ability to localize carriers in graphene wires[65], e.g. in order to facilitate electronic graphene networks and interconnects[4, 24]. The most immediate way of realizing such wire structures is by cutting graphene into so-called graphene nanoribbons (GNRs). Quantum confinement will in general induce a band gap in such structures, with a magnitude that scales with the inverse of the width of the GNR[30, 130]. However, the exact atomistic configuration of the edge of the ribbon greatly influences the magnitude of this gap, with particular edge configurations resulting in vanishing gaps or localized edge states.

In this chapter, we review two alternative suggestions to confining charge carries in graphene published in Paper IV and V. Firstly, in GAL electron waveguides we utilize the large band gap of GAL structures to guide carriers in graphene in a way closely analogous to photonic crystal waveguide structures[39]. Secondly, bending graphene may offer a unique approach towards templated chemical functionalization, which we use to electronically isolate pseudo-ribbons.

4.1 Graphene antidot lattice waveguides

The previous chapter illustrated how an embedded GAL can be an efficient way of tuning the electronic and thermal properties of graphene. While bulk GALs are interesting in their own right, there is a rich opportunity for developing graphene-based devices based on combinations of GALs and pristine graphene. One such combination, named GAL waveguides, was suggested in Paper IV.

The basic idea is to sandwich a region of pristine graphene between surrounding GAL regions with a large band gap, Fig. 4.1. Hereby, one can achieve localized guided modes in the central graphene region. The periodic perforation induces a band gap in graphene, rendering it semi-conducting, and the resulting band structure closely resembles that of gapped graphene[149] in the low-energy limit with a parabolic dispersion $E_{gg} \approx \pm\sqrt{\Delta^2 + (\hbar v_F k)^2} \approx \pm\Delta\left(1 + \frac{1}{2}\left(\frac{\hbar v_F k}{\Delta}\right)^2\right)$. Here we defined the Fermi velocity, $v_F = 10^6$ m/s, of graphene and the effective gap, 2Δ.

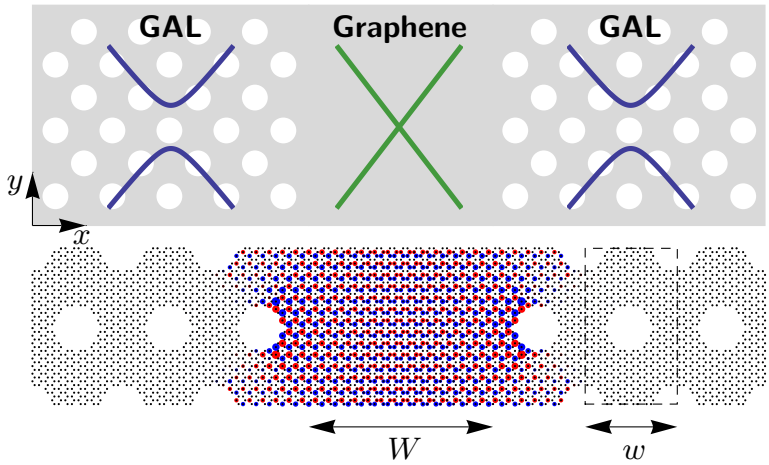

Figure 4.1: *(upper panel) Conceptual illustration of a GAL waveguide. A central region of pristine graphene is surrounded by GAL regions, the band gaps of which confine states to the waveguide region. Translational symmetry is assumed in the y–direction, which is along the longitudinal direction of the waveguide. (lower panel) The geometry of a* $\{7,3\}_2^{\mathrm{zz}}$ *GAL waveguide. Black dots show the location of carbon atoms. Bloch boundary conditions are imposed on all boundaries. The dashed lines illustrate the enlarged GAL unit cell, the width of which we denote by* w*. The lowest-energy waveguide mode at the* Γ *point, calculated via the tight-binding model, is illustrated with circles, the size of which shows the absolute value* $|\psi(x,y)|$ *of the (real-valued) eigenstate, while the color indicates the sign. From Paper IV.*

4.1.1 Dirac model

In this section we employ the simple Dirac continuum model of graphene to derive analytical expressions for the band structure and eigenstates of the localized modes. This enables us to extract simple scaling laws for extrapolating results to larger structures and will be used for benchmarking against the atomistic TB calculation in the next section.

Near the Dirac K point one can linearize the TB Hamiltonian of graphene. The effective Dirac equation for the two ϕ_A and ϕ_B spinor eigenstates reads[30, 90]

$$\begin{bmatrix} m(\chi) & -i\left(\partial_\chi - i\partial_\gamma\right) \\ -i\left(\partial_\chi + i\partial_\gamma\right) & -m(\chi) \end{bmatrix} \begin{bmatrix} \phi_A(\chi,\gamma) \\ \phi_B(\chi,\gamma) \end{bmatrix} = \epsilon \begin{bmatrix} \phi_A(\chi,\gamma) \\ \phi_B(\chi,\gamma) \end{bmatrix}, \tag{4.1}$$

where we introduced dimensionless coordinates $(\chi,\gamma) = 2/W \times (x,y)$ and dimensionless energies $\epsilon = E/E_0$, with $E_0 = 2\hbar v_F/W \simeq 1.278$ eV·nm$\times W^{-1}$. We model the GAL regions by introducing a position-dependent dimensionless mass term, $m(\chi)$. It is nonzero, $m(\chi) = \delta = E_g/(2E_0)$ for $|\chi| > 1$ and zero in the waveguide region, $|\chi| < 1$. Here E_g is the band gap of the GAL region. One should pay careful attention to the alternating sign between the two sublattices in the diagonal of eqn. 4.1. This sign difference between the diagonal elements has two important consequences. Firstly, it secures electron-hole symmetry in the GAL regions. This should be so since the original linearized dispersion of graphene is symmetric and the scattering from missing atoms is equivalent for electrons and holes. We can explicitly illustrate the electron-hole symmetry by acting twice with the Dirac Hamiltonian on an eigenstate:

$$\begin{bmatrix} m(\chi)^2 - \left(\partial_\chi^2 + \partial_\gamma^2\right) & 0 \\ 0 & m(\chi)^2 - \left(\partial_\chi^2 + \partial_\gamma^2\right) \end{bmatrix} \begin{bmatrix} \phi_A(\chi,\gamma) \\ \phi_B(\chi,\gamma) \end{bmatrix} = \epsilon^2 \begin{bmatrix} \phi_A(\chi,\gamma) \\ \phi_B(\chi,\gamma) \end{bmatrix}. \tag{4.2}$$

From this we see that we have obtained two decoupled ordinary Schrödinger equations. The two spinors are coupled solely through the boundary conditions. Furthermore, the eigenvalue is now the *square* of the energy leading to the electron-hole symmetry around the Fermi energy. This is in contrast to gating graphene in a local area which should be modelled as a potential term, $V(\chi)$, with the same sign in the diagonal of eqn. 4.1. Gating graphene breaks the electron-hole symmetry by creating a barrier for one carrier and a well for the other. Secondly, Klein tunneling[90] makes it difficult to achieve carrier localization in graphene via ordinary gating. The Klein paradox describes the phenomenon that an relativistic electron can pass through a high barrier perfectly in contrast to the conventional tunneling. Guiding of electrons via electrostatic gating was demonstrated experimentally[194] and theoretically[106, 203, 205] albeit with the caveat that guiding is restricted to a specific range of wave vectors for which Klein tunneling is negligible. In contrast, the *mass term* in graphene provides confinement that is a much closer analogue of gate-defined localization and quantum point contacts in ordinary two-dimensional electron gases (2DEGs)[177]. This is seen from the fact that eqn. 4.2 resembles that of a 2DEG, but with the squared energy originating from the linear dispersion of graphene.

We now discuss the nature of bound states in the waveguide, and thus take $\epsilon^2 < \delta^2$. The Hamiltonian commutes with the y-component of the momentum operator and we take spinor components of the form $\phi_A(\chi,\gamma) = f(\chi)e^{i\kappa\gamma}$ and $\phi_B(\chi,\gamma) = g(\chi)e^{i\kappa\gamma}$, where $\kappa = kW/2$ is the dimensionless Bloch wave vector along the longitudinal direction of the waveguide. Inserting this in eqn. 4.2 we obtain an ordinary differential equation for the first spinor

$$\frac{\partial^2 f(\chi)}{\partial \chi^2} = -\left(\epsilon^2 - m(\chi)^2 - \kappa^2\right) f(\chi). \tag{4.3}$$

The normalizable solutions for the first spinor component thus read $f(\chi) = A_{\pm}e^{\pm\beta\chi}$ for $|\chi| > 1$ and $f(\chi) = B\cos(\alpha\chi) + C\sin(\alpha\chi)$ for $|\chi| < 1$. Here, we have defined $\alpha = \sqrt{\epsilon^2 - \kappa^2}$ and $\beta = \sqrt{\delta^2 + \kappa^2 - \epsilon^2}$. It is convenient to express the second spinor in terms of the first through the second vector equation in eqn. 4.1:

$$g(\chi) = i\frac{(\kappa - \partial_\chi)f(\chi)}{\epsilon + m(\chi)}\,. \tag{4.4}$$

In the waveguide region we obtain the solution $g(\chi) = i/\epsilon(B\kappa - C\alpha)\cos(\alpha\chi) + (C\kappa + B\alpha)\sin(\alpha\chi)$ for $|\chi| < 1$. The general solution is found from the requirement of continuity of both spinor components at the boundaries of the central waveguide region, see Paper IV. Here we restrict the discussion to the infinite mass limit, $\delta \to \infty$, were one can apply the billiard boundary condition

$$\phi_B(\chi, \gamma) = -ie^{i\theta(\chi,\gamma)}\phi_A(\chi, \gamma)\,, \tag{4.5}$$

securing that the local particle current into an infinite mass region is zero[19]. In our case this results in the conditions that $g(\pm 1) = -ie^{\pm pi/2}f(\pm 1) = \mp f(\pm 1)$, and after some algebra (requiring the determinant in coefficient space to be zero) one arrive at an analytical solution for the energies,

$$\epsilon^{\infty}_{ns}(\kappa) = s\sqrt{\kappa^2 + \frac{\pi^2}{4}\left(n + \tfrac{1}{2}\right)^2},\ n = 0, 1, 2\ldots \tag{4.6}$$

or, reverting to ordinary units,

$$E^{\infty}_{ns}(k) = s\sqrt{E_b^2(k) + \frac{\hbar^2 v_F^2 \pi^2}{W^2}\left(n + \tfrac{1}{2}\right)^2}, \tag{4.7}$$

where $E_b(k) = \hbar v_F k$ is the bulk graphene dispersion relation and $s = \pm 1$. The solution of the problem is thus closely reminiscent of that of an ordinary one-dimensional square well potential, albeit with the crucial difference that for graphene $E \propto \alpha$ rather than $E \propto \alpha^2$, as a consequence of the linear dispersion relation of graphene. The dispersion relations of the waveguide modes thus resemble those of gapped graphene[149] with a mass term of $\Delta_{\text{eff}} = (\hbar v_F \pi/W)(n + \frac{1}{2})$.

We stress that while we focus on GALs for generating a band gap, the Dirac approximation used here is not restricted to this application. The concept of a GAL waveguide depends only on the existence of a band gap in the GAL region and not on the specific details.

4.1.2 Simulations

In this section we use the TB model to illustrate how waveguiding modes can be obtained in GAL waveguides. We extend the GAL notation from the previous chapter to a waveguide geometry as $\{L, R\}^{\text{zz/ac}}_N$. Here L and R are the GAL unit cell and hole dimensions, respectively. The width W of the waveguide is defined via $N \equiv W/w$, where w is the width of the enlarged GAL unit cell, as illustrated in the lower panel of Fig. 4.1. The superscript 'zz' ('ac') denotes a waveguide with the longitudinal direction along the zigzag (armchair) orientation of the graphene lattice.

The band structure of a $\{7, 3\}^{\text{zz}}_5$ GAL waveguide reveals tightly confined states in the gapped energy range of the GAL, Fig. 4.2. We take a slightly larger width of the waveguide, $W_{\text{eff}} = (N + \frac{1}{2})w$, than used in the geometry nomenclature, in lack of

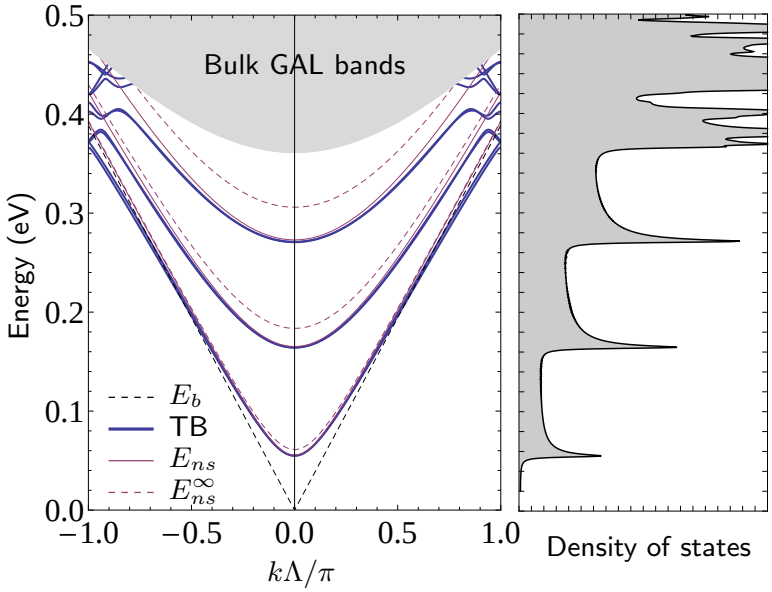

Figure 4.2: *(left) Dispersion relation of a* $\{7,3\}_5^{\mathrm{zz}}$ *GAL waveguide. The tight-binding result (thick blue line) is compared to the analytical Dirac results in the infinite mass-limit results,* E_{ns}^{∞} *(dashed red) and numerical solution of the transcendental equation with a finite mass,* E_{ns} *(full red). For comparison, the bulk graphene band structure,* E_b*, is also shown. The shaded gray area shows the projected bands of the surrounding GAL regions, below which localized states exist. Note that* $\Lambda = 3\sqrt{3}La_0$ *(*$\Lambda = 3La_0$*) denotes the lattice constant of the ZZ (AC) waveguide. (right) Corresponding DOS for the TB model. Note the clear van Hove singularities characteristic of one-dimensionality. From Paper IV.*

well-defined sharp edges. There is an excellent agreement between the analytical Dirac results and the TB atomistic calculations. Deviations between the two models mainly occur for energies close to the projected bands of the GAL, and near the Brillouin zone edges. The shaded, gray region illustrates the projected bands of the GAL, which define the region below which localized waveguide states are expected to appear. This particular waveguide structure supports several localized states. It is worth stressing that localized waveguide modes exist for all wave vectors in the first Brillouin zone. This is in contrast to the case of waveguides defined via electrostatic gating, where guided modes generally exist only for a limited range of wave vectors. The DOS calculated from the TB model is shown in the right panel of Fig. 4.2. As expected from the Dirac approximation, the DOS closely resembles one-dimensional gapped graphene, i.e. $g(E) \propto \Theta(E - \Delta_{\text{eff}})E/(\hbar v_F \sqrt{E^2 - \Delta_{\text{eff}}^2})$ with the van-Hove singularities characteristic of one-dimensionality clearly evident in the figure.

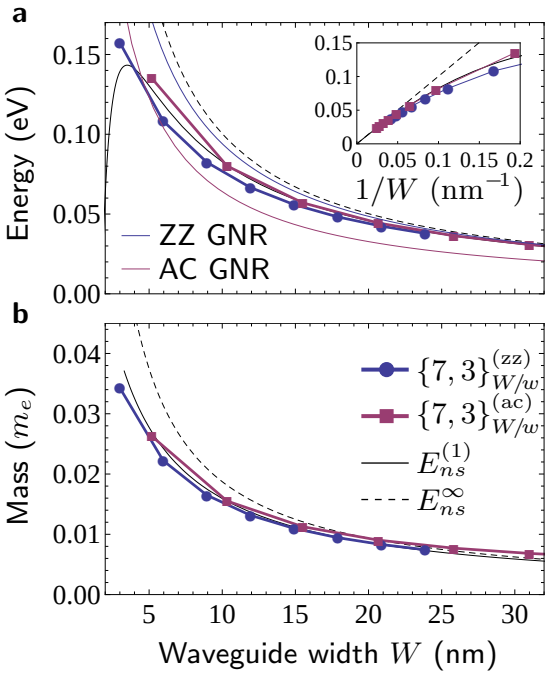

Figure 4.3: *(a) Energy as a function of waveguide width of the lowest localized waveguide state (Γ-point), for the $\{7,3\}_N$ family of GAL waveguides. The band gap is twice this value due to electron-hole symmetry. We compare the TB model (points) of waveguides oriented along the zigzag (ZZ) and armchair (AC) directions, respectively, to the analytical results obtained via the Dirac model in the infinite mass limit and including the first-order correction (black lines). See the legends in panel b. The inset illustrates the $1/W$ dependence of the energy for wide waveguides. For comparison, the thin colored lines show the energies for ZZ and AC GNRs, if certain edge dependencies are ignored. (b) Corresponding effective masses in units of the free electron mass, m_e. In both panels, note the close resemblance of the results obtained for AC and ZZ oriented waveguides. From Paper IV.*

In Fig. 4.3a, we show the energy of the lowest localized waveguide state at the Γ-point as a function of the width of a $\{7,3\}^{(\text{zz,ac})}_N$ waveguide. Again, the analytical results

are benchmarked against the atomistic model, and we see that the results are overall in excellent agreement between the two methods. The inset of the figure illustrates that both ZZ and AC orientations exhibit a clear $1/W$ dependence of the energies, as predicted from the Dirac approximation, provided the waveguide is sufficiently wide. The rather small differences between ZZ and AC orientations are attributed to a slightly different effective width of the waveguides in the two cases. GAL waveguides are always semiconducting in contrast to GNRs, where the NNTB model predicts armchair GNRs alternate between metallic[1] and semiconducting behavior depending on the exact width of the ribbon, while zigzag GNRs display dispersionless midgap states, localized on the edges[30]. Therefore, one finds a width dependence of the energy of the guided modes that are simpler than for GNRs, and may be easier to control in experiments. The figure shows that the energy scaling is in good agreement with that of semiconducting AC GNRs and ZZ GNRs where the dispersionless midgap states are neglected. GAL waveguides thus resemble ribbons without the particulars resulting from edge effects.

The effective masses of the subbands is obtained from the infinite mass Dirac result as

$$m_{\text{eff}}^{\infty} = \hbar^2 \left(\frac{\partial^2 E_{ns}^{\infty}(k)}{\partial k^2}\bigg|_{k=0} \right)^{-1} = \frac{\hbar\pi(n+\frac{1}{2})}{v_F W} \,. \tag{4.8}$$

This result is compared to the numerical simulations in Fig. 4.3b for the lowest waveguide state. Again, we note that there is excellent agreement between the results obtained in the Dirac approximation and those from a TB model, for both orientations of the waveguide. While electrons in pristine graphene have vanishing effective masses, guided modes obtain a non-zero, albeit still very small effective electron mass, which tend to zero in the limit of infinitely wide waveguides.

Using the recursive Green's function method we calculate the transmission through a GAL waveguide attached to semi-infinite graphene leads, Fig. 4.4a. The conductance of the ZZ- and AC oriented GAL waveguides is similar in the energy range of the waveguide mode (shaded area). This is compared to the transmission through a GNR of comparable dimensions, Fig. 4.4b. We see that the transmission is higher through the GAL waveguide compared to the GNRs in the energy range for the confined waveguide mode. The figures also illustrate the conductances with a relatively high level of disorder, for which edge atoms (at the antidots and GNR edges) are removed with a 5% probability. We observe that the GAL waveguides retain relatively high conductances. The ZZ and AC orientations show comparable reductions in the conductance due to disorder. The ZZ-GNR is less affected by disorder, while the AC-GNR conductance is significantly reduced except at the lowest energies. We conclude that the GAL waveguides appear to be relatively robust against structural disorder and in general have higher conductances than the corresponding GNR systems.

In analogy with photonic crystal waveguides, we expect GAL waveguides to have a high robustness to kinks along the waveguide. This is illustrated by the local bond current through the waveguide in Fig. 4.5. The electronic states are clearly localized in the waveguide and the current is nicely able to follow the guided path through the device. The left going bond current (per unit energy) in the presence of an infinitesimal bias voltage is calculated from the left scattering state spectral function, $A_{L,ij}$, and the hopping matrix elements H_{ij} from the TB Hamiltonian. Between atom i and j the local current is $A_{L,ij}\, H_{ij}$[180]. To visualize the current on the given scale the current running away from each atom was calculated and averaged over an applied mesh. The illustrated

[1] AC-GNRs are metallic for widths $W = (3p-1)\sqrt{3}a_0$, with p an integer.

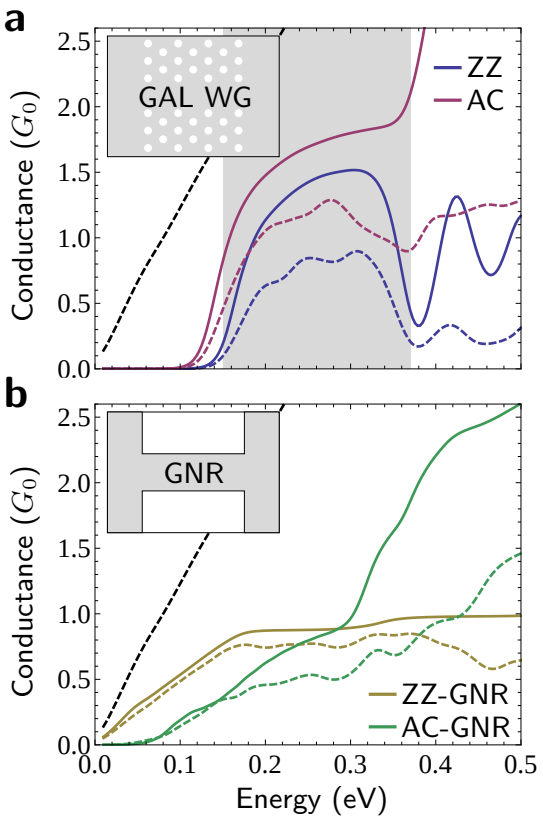

Figure 4.4: *Insets show the schematic transport setups for (a) a GAL waveguide and (b) a GNR, each connecting two semi-infinite graphene leads. Conductances for pristine (solid lines) and disordered systems (dashed lines) are shown for (a) GAL waveguides and (b) GNRs, in units of the conductance quantum G_0. The conductance is evaluated at a temperature of $T = 100$ K. The straight black dashed lines show the graphene conductance. In the disordered systems, edge atoms have been randomly removed with a 5% probability. The length of the waveguides and GNRs are $L = 89$ nm. The shaded area in (a) indicates the energy range of the confined waveguide mode. The transmission is averaged over 100 values of the transverse wave vector, and we further average over 10 samples with different realizations of the random disorder. From Paper IV.*

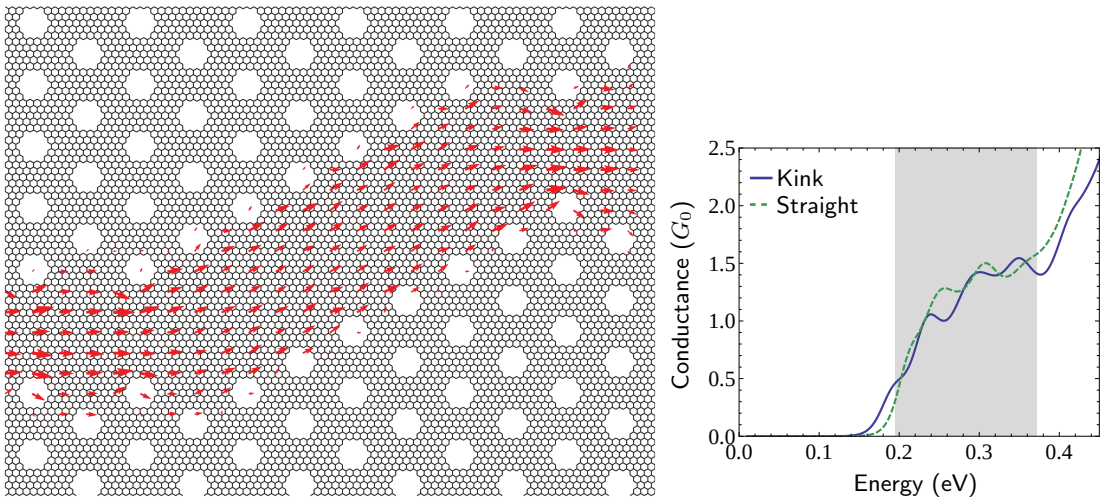

Figure 4.5: *(Left) Bond current through a 'kinked' $\{5,2\}_1^{(zz)}$ GAL waveguide. The current is calculated at energy $E = 0.25eV$ with a transmission of $\mathcal{T} = 1.9$. The current is highly confined to the waveguide region and no additional reflections are observed due to the kinks. (Right) Conductances of the 'kinked' waveguide (straight line) and of a straight waveguide of similar length (dashed line). The shaded area indicates the energy range of the confined waveguide mode of the straight waveguide. Note the nearly identical conductances of the two systems. From Paper IV.*

average current thus cannot be assigned to the individual atoms anymore, which is the reason why current appears to occur within the holes in the figure. Since the k-averaged transmission only changes slightly from the Γ-point result, we use the Γ-point scattering states. Fig. 4.5 clearly illustrates the confinement of the current to the waveguide region and the robustness against kinks.

The conductance of the waveguide with a bend is compared to that of a straight waveguide of similar length, right part of Fig. 4.5. We conclude that the conductance is nearly identical for the two systems, despite small differences between the two structures in the oscillations of the conductance. Very low reflection loss is thus introduced by the kink, despite the fact that the waveguide with a bend switches between zigzag and armchair orientations. This illustrates the promising prospect in guiding electrons in electronic wires in graphene.

4.2 Kinked graphene

Graphene consists entirely of surface atoms and it is thus appealing to think of nano-engineering by chemical modification. Here we discuss local curvature, or bending, of a graphene sheet as a mean of increasing the chemical reactivity. This presents an opportunity for templated chemical functionalization as an alternative way to confine charge carriers in graphene wires.

4.2.1 Curvature-directed process for templated chemical functionalization

Recent experiments show that graphene curvature is a mean of hydrogen adsorption, which may be used for hydrogen storage devices[66] or selective bandgap engineering in graphane[51]. Graphene exhibits an intrinsic curvature owing to the interaction with the substrate, but bending graphene could be a feature of the substrate fabrication. For instance, the bending may be a result of substrate-induced nanomodulation[99, 105, 143] or thermally generated strains in graphene suspended over a trench[12].

In paper V we suggested to use bending to obtain site-selective adsorption of atomic hydrogen on convexly curved regions. All simulations are based on SIESTA, with parameters outlined in the paper. The three step process is illustrated in Fig. 4.6a. Firstly,

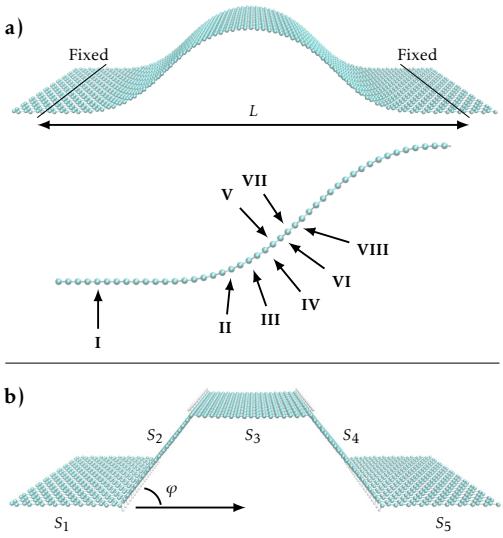

Figure 4.6: *Rippling and kink formation by hydrogen absorption. (a) Smooth ripple-like structure where the first and last six rows of carbon-dimers are surface-clamped regions with a separation of $L = 90$ Å. Atomic hydrogen is adsorbed at positions I–VIII. (b) The resulting kinked graphene structure after hydrogen is adsorbed in lines at the most reactive position (II) corresponding to the smallest local radius of curvature. The four kinks divide the structure into five sections, S_1–S_5. From Paper V.*

one has to bend or ripple graphene by the means illustrated in the experiments, e.g. nanomodulation by a templated substrate, strain-engineering or thermal expansion of a sheet suspended over a trench. Secondly, one use curvature-directed linear alignment to absorb hydrogen along the bend. We examine hydrogen absorption at the I-VIII positions to predict favorable hydrogen absorption sites. Thirdly, the absorbed hydrogen modifies the local bonding from sp^2 to sp^3 giving a relaxation mechanism towards linear stable graphene kinks, Fig. 4.6b. In effect one obtains electronically isolated pseudo-ribbons with properties similar to that of ideal GNRs. Recently, a related process sequence was suggested to unzipping GNRs by oxidation[173].

Adsorption of hydrogen on graphene involves a reaction barrier which needs to be overcome before the single hydrogen atom sticks to the graphene sheet. DFT calculations have showed that atomic H adsorbs on-top on flat graphene with a barrier of 0.2 eV[77, 195], locally decreasing as more H atoms are added. In Fig. 4.7 we have

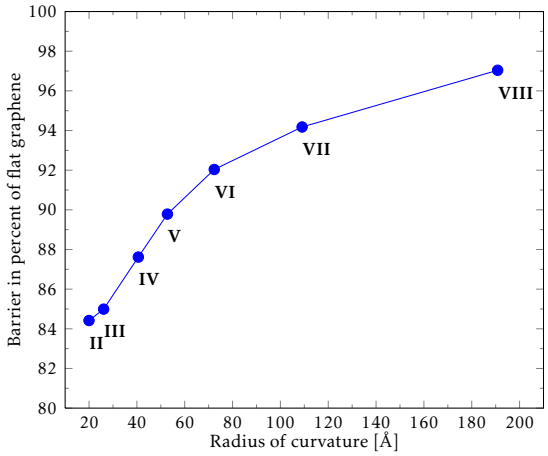

Figure 4.7: *Calculated reaction barriers for hydrogenation of bend graphene as a function of the local radius of curvature (II–VIII in Fig. 4.6a). Flat graphene (position I) has an infinite radius of curvature and is used to normalize the barriers. Calculations are spin-polarized due to unpaired electrons and allow for atomic relaxation. From Paper V.*

obtained adsorption barriers for reacting with single atomic H on the graphene bend at positions with different local radius of curvature (RoC) (positions I–VIII in Fig. 4.6a). The barrier is determined by calculating the total energy for each position of hydrogen above graphene as the hydrogen is moved successively closer to the graphene with the hydrogen-bonded carbon atom and its three nearest neighbours free to relax. The second least curved position (VIII), resulting in a large RoC, reduces the barrier by roughly 3% compared to flat graphene (position I). The most curved position (II) in our considered structure has a minimum RoC of $\sim$20 Å resulting in a barrier reduction of roughly 16%. For comparison, this RoC corresponds roughly to the radius of a (25,25) nanotube. Similar enhanced chemical reactivity with decreasing RoC was found in experiments for C_{60} molecules and carbon nanotubes (CNTs)[157, 169].

We may understand the reaction barrier and its change with curvature by considering the changes in carbon bond lengths. The barrier is due to the fact that the reacting carbon atom has to be pulled out of the graphene plane, stretching the strong carbon-carbon bonds, when reacting with the incoming hydrogen atom. When the graphene sheet is curved the carbon atom is already slightly out of the plane, and thus the energy required to pull the atom further out of plane is decreased compared to flat graphene.

We conclude that the considered system allows the adsorption of hydrogen atoms in single lines. The kink in the atomic structure due to the sp^3-binding of a single H makes the graphene curve even more in its vicinity which, in turn, preferentially lowers the barrier for absorption of a H along the linear bend. This suggests a mechanism for curvature-directed linear alignment and leads to the decoration of the entire linear bend turning it into a kink-line. It may be viewed as analogous to crack formation mechanisms, where the breaking of a bond increases the stress on neighbouring bonds - only in this case, the graphene is hydrogenated rather than broken or destroyed.

4.2.2 Kink formation and electronic transmission through kinks

Next, we examine the energetic and transport properties of kink-lines in the armchair-direction. We first consider a single kink with angle φ, e.g. between sections S_1 and S_2

in 4.6b. The kink-angle φ is varied in the range $0°\ldots90°$, while the three nearest unit cells on each side of the kink are allowed to relax. The total energy per H is shown as a function of φ in the inset of Fig. 4.8, showing a minimum energy for $\varphi\approx50°$. This angle roughly corresponds to the angle in a sp^3-configuration where $2\varphi=109.5°$. The adsorption of H causes local changes in the geometry, i.e. only the carbon atoms very close to the kink are moved, while the remaining structure remains unperturbed. For this reason, the adsorption of hydrogen atoms can be considered as a process which locally pins the bend in a kink formation.

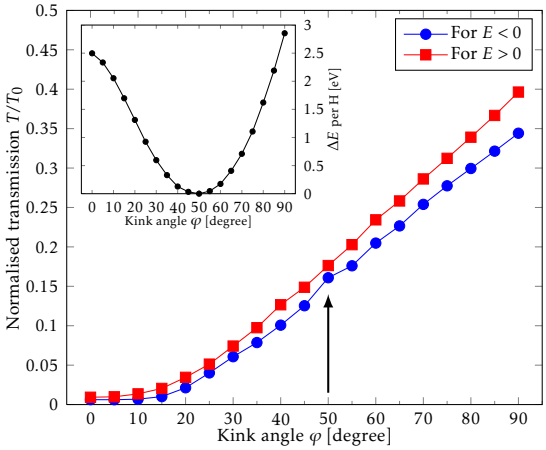

Figure 4.8: *Electronic transmission through a single kink normalized with the pristine graphene transmission (T_0) as a function of the kink angle, φ, for electrons ($E>0$) and holes ($E<0$). The arrow indicates the normalized transmission at the equilibrium angle determined from the total energy calculations shown in the inset. From Paper V.*

The electron transmission per unit-cell width is linear in energy for pristine graphene in an energy range around the charge neutrality point ($E=0$), e.g. $T_0\propto E$. We find similarly that the calculated kink-transmission curves also are linear, and therefore we express the results for the transmissions in terms of the roughly energy independent ratio $T/T_0=$const. The kink breaks the electron-hole symmetry and we fit $E>0$ and $E<0$ separately, as shown in 4.8. Larger kink-angles result in an increase in the overall transmission, which may be contributed to a better π-orbital overlap across the kink. For the equilibrium angle, $\varphi=50°$, the ratio T/T_0 is close to 0.17 in both regions (indicated by the arrow in 4.8), corresponding to a transmission reduction of 83%. Thus, we see that the hydrogen-induced kinks in graphene can be used to form effective electron barriers.

We now show how two parallel kinks lead to a local electronic structure which resembles that of an isolated GNR between the kinks. Hydrogen terminated armchair GNRs are semiconducting but have a small energy gap when the width in atomic lines is $N=3L-1$, where L is an integer[30]. In Fig. 4.9 we compare the electronic band-structure for armchair GNR (aGNR) (left panel) to the electronic transmission through two kinks separated by the corresponding aGNR width (right panel). In the present case the initial width (or, kink separation) is $N=17$ atomic lines of carbon, which shows a semi-metallic behaviour in the transmission spectrum with a small transport gap. In accordance with isolated aGNRs the next two widths $N=18$, 19 are semi-conducting, while the last investigated width $N=20$ is semi-metallic again (not shown). The close correspondence between the electronic band structure for the GNR and the transmission

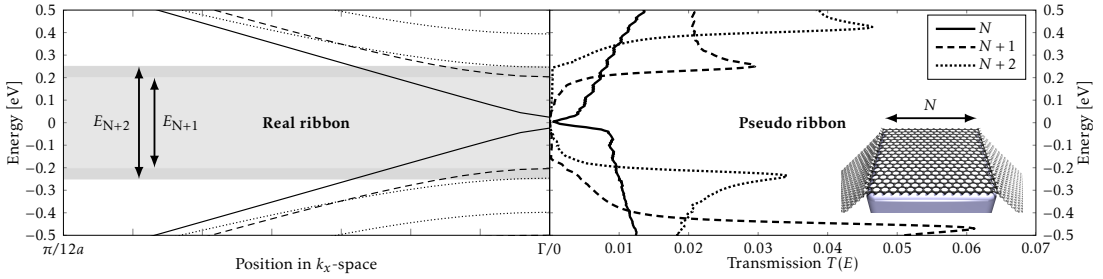

Figure 4.9: *(Left) Band structures for H-passivated armchair ribbons with varying width, N. The ribbons are a zero-gap semi-conductor, a semi-conductor with band gap E_{N+1}=0.4 eV, and a semi-conductor with band gap E_{N+2}=0.5 eV for widths N, $N+1$, $N+2$, respectively. All widths are based on the number of carbon atom lines N=17. The band gaps are indicated by arrows and highlighted. (Right) The electronic transmission functions for the corresponding pseudo-ribbons, i.e. across two parallel kinks of varied separation as shown in inset. From Paper V.*

gap for the double kink system allows us to consider the structure between two kinks as a pseudo-ribbon. For the semi-conducting pseudo-ribbons transport gaps surrounded by van Hove-type 1D behavior are seen in the transmission functions (4.9, right panel). The transport gaps, E_{gap}=0.4 eV and E_{gap}=0.5 eV, are in reasonable agreement with power-law scaling of E_{gap} with width found for aGNRs[30]. We note that the pseudo-ribbon breaks electron-hole symmetry. For the $N = 18$ case a larger van Hove resonance is seen at the valence band-edge, while for $N = 19$ a larger resonance is seen at the conduction band-edge. There are small transmission values within the electronic band gap due to leakage through the barriers, which we expect to introduce shifts in the energies between the real and pseudo aGNRs.

4.3 Summary and discussion

In summary, we have considered two approaches for confining charge carriers based on GAL waveguides and the functionalization of kinks in graphene.

GAL waveguides support modes which are highly confined to the waveguide region and are robust against structural disorder and kinks in the waveguide. They differ from electrostatic waveguides since confinement is not limited to a specific range of wave vectors where Klein tunneling is negligible. Furthermore, we were able to derive analytical results from the Dirac method. This was used to illustrate that while antidot lattices do provide means of achieving localization the concept relies on a general principle that goes beyond the specifics of how a band gap is generated. Additionally, the analytical results illustrates the scaling with geometrical parameters to larger devices. We found that GAL waveguides have higher conductances than corresponding GNRs but otherwise resemble GNRs without the complications related to edges.

Preliminary results for the thermoelectric performance of GAL waveguides suggest ZT to be limited by the presence of the surrounding GAL. In essence one reduces the electronic problem to a 1D problem, while the phonons, being less sensitive to the atomic arrangements, still behave as part of a 2D system. Therefore, ZT is limited by the nonzero thermal conductance of the surrounding GAL. An advantage of the surrounding GAL may instead be that it will mechanically stabilize the structure and be able to carry

some of the generated Joule heat away from the device. GAL waveguides may thus be an attractable way of realizing electronic wires in integrated graphene circuits.

Additionally, we discussed a curvature-directed process for templated chemical functionalization of graphene. This may result in a pinned kink formation where pseudoribbons are electronically isolated by effective electron barriers in the form of atomic hydrogen absorbed along the bend. Both the GAL waveguides and kinked graphene illustrate the richness in utilizing nano-engineering and quantum confinement in designing the conducting properties of graphene to specific applications.

Chapter 5

Inelastic signals in graphene nanoconstrictions

This chapter is concerned with the theoretical modeling of inelastic tunneling spectroscopy (IETS). The IV-characteristics can provide a spectroscopic fingerprint of a molecular junction. We present the newly developed extended LOE (exLOE) method applicable to systems where the electronic structure is changing on the scale of the phonon frequencies. This occurs, for instance, in graphene nanostructures where phonon frequencies can exceed 0.2 eV. Additionally, the results from the exLOE is presented and compared to that of the original wide-band LOE where all electronic parameters are evaluated at the equilibrium chemical potential.

5.1 IETS from exLOE

Molecule vibrations are hard to access by experiments in a direct way. However, molecules can be contacted to metallic leads within state-of-the-art molecular electronics. Therefore, it is interesting to gain as much information as possible from the IV-characteristics. In inelastic tunneling spectroscopy one evaluates the second derivative of the current with bias voltage, d^2I/dV_a^2. When studying molecules the signal $IETS = \frac{d^2I/dV_a^2}{dI/dV_a}$ is often used, since the current scales with the number of molecules in the junction. At bias voltages where electrons are able to lose (gain) energy by emission (absorption) of a phonon a new transmission channel opens or closes. This results in a peak (dip) in the second derivative if a channel is opened (closed). Hereby, the spectrum can be used to identify characteristic vibrations of the molecule that are interacting with the electrons. The LOE model for inelastic transport has successfully predicted inelastic scattering in Au-chains[57] and hydrocarbon molecules[146]. One can envision that inelastic measurements could be performed for graphene nanostructures as well. Recent low temperature scanning tunneling spectroscopy measurements on graphene, epitaxially grown on a Ru substrate, did find inelastic fingerprint features in the IV[32]. To our knowledge, there are currently no measurements available of the inelastic features in nanostructured graphene devices. Nanostructuring graphene may give rise to Lorentzian-like resonances such as the one depicted in Fig. 5.1. When phonon frequencies are much smaller than the variations in the electron transmission (dashed line, FWHM$>>\omega$) the WBA can be applied. In the WBA one evaluates the electronic variables at the equilibrium chemical potential, $(\mu_L + \mu_R)/2$. This is often a good model for metals. With a peak broadening

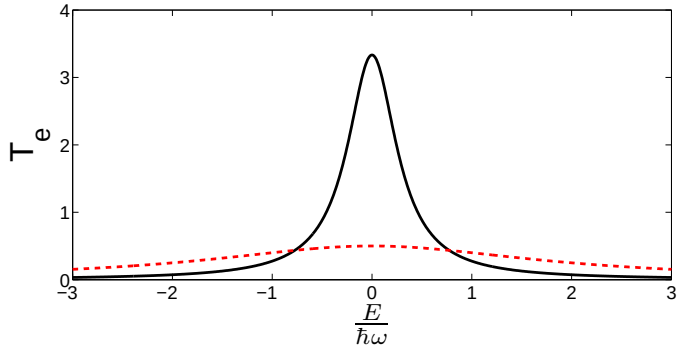

Figure 5.1: *Model transmissions with variations on different energy scales. The shown example is a Lorentzian resonance with a broadening comparable to the phonon frequencies (full line) and one where the frequencies are much smaller than the broadening (dashed line). The exLOE procedure extends the method to model a system with such dramatic variations. Tuning away from the resonance energy the original LOE and exLOE are equivalent.*

comparable to the phonon frequencies (full line, FWHM$< \omega$) it is clearly not accurate to assume a constant electronic structure.

The success of the original LOE lies partially in the transparency of the equations that are fairly easy to implement in a DFT-NEGF setup. We here provide a very convenient extension that takes care of strong variations in the electronic structure but at the same time keeps the equations in a form very similar to the original formulation. To illustrate the assumptions that goes into the model we derive the fourth correction to the current below. The remaining terms are derived in appendix 9.5. For equal electron and phonon temperatures of the two baths we have (see eqn. 9.34)

$$\begin{aligned}\mathbf{I}_\alpha^{(4)} &= 2e\int_{-\infty}^{\infty}\frac{d\varepsilon}{2\pi}\left(\mathrm{Tr}\left[G_0^r\Sigma_{ph}^{>}G_0^a\Sigma_\alpha^{<}-G_0^r\Sigma_{ph}^{<}G_0^a\Sigma_\alpha^{>}\right]\right) \qquad (5.1)\\ &= e\int_{-\infty}^{\infty}\frac{d\varepsilon}{2\pi}\int_{-\infty}^{\infty}\frac{d\omega}{2\pi}\mathrm{Tr}\left[M_{\lambda_n}\tilde{A}_\alpha(\varepsilon)M_{\lambda_n}A_{\bar\alpha}(\varepsilon-\omega)\mathcal{A}(\omega)\right]C^{\bar\alpha\alpha}(\omega)(n_F^\alpha(\varepsilon)-n_F^{\bar\alpha}(\varepsilon-\omega)).\end{aligned}$$

We used the relation between the $\coth(x)$ and Bose-Einstein distribution (cf. eqn. 9.5) and defined $C^{\bar\alpha\alpha}(\omega)\equiv\left(\coth\frac{\omega}{2k_BT}-\coth\frac{\omega+\mu_{\bar\alpha}-\mu_\alpha}{2k_BT}\right)$ and $M_{\lambda_n}=\sqrt{\hbar/2\omega_n}M^n$. At zero temperature the phonon spectral density is $\mathcal{A}(\omega)=2\pi\sum_n(\delta(\omega-\omega_n)-\delta(\omega+\omega_n))$. For a bias polarity with $\mu_\alpha>\mu_{\bar\alpha}$ only the term from $\delta(\omega-\omega_n)$ contributes to emission. This gives

$$\begin{aligned}&C^{\bar\alpha\alpha}(\omega_n)e\int_{-\infty}^{\infty}\frac{d\varepsilon}{2\pi}\mathrm{Tr}\left[M_{\lambda_n}\tilde{A}_\alpha(\varepsilon)M_{\lambda_n}A_{\bar\alpha}(\varepsilon-\omega_n)\right](n_F^\alpha(\varepsilon)-n_F^{\bar\alpha}(\varepsilon-\omega_n))\\ &\approx C^{\bar\alpha\alpha}(\omega_n)e\int_{\mu_{\bar\alpha}+\omega_n}^{\mu_\alpha}\frac{d\varepsilon}{2\pi}\mathrm{Tr}\left[M_{\lambda_n}\tilde{A}_\alpha(\varepsilon)M_{\lambda_n}A_{\bar\alpha}(\varepsilon-\omega_n)\right]\\ &\approx C^{\bar\alpha\alpha}(\omega_n)\frac{e}{2\pi}(\mu_\alpha-\mu_{\bar\alpha}-\omega_n)\,\mathrm{Tr}\left[M_{\lambda_n}\tilde{A}_\alpha(\mu_{\bar\alpha}+\omega_n+\Delta/2)M_{\lambda_n}A_{\bar\alpha}(\mu_{\bar\alpha}+\omega_n+\Delta/2-\omega_n)\right],\end{aligned}$$

where we assumed a zero electronic temperature in the Fermi functions and in the last line approximated $\int_a^{a+\Delta}f(x)dx\approx\Delta f(a+\Delta/2)$. Near the threshold we can assume that the trace part is varying slowly ($\Delta\to0$). Inserting $\mu_{\alpha/\bar\alpha}=\mu_0\pm\omega_n/2$ we have

$$C^{\bar\alpha\alpha}(\omega_n)\frac{e}{2\pi}(\mu_\alpha-\mu_{\bar\alpha}-\omega_n)\,\mathrm{Tr}\left[M_{\lambda_n}\tilde{A}_\alpha(\mu_0+\omega_n/2)M_{\lambda_n}A_{\bar\alpha}(\mu_0-\omega_n/2)\right] \qquad (5.2)$$

At strictly zero phonon temperature $C^{\bar{\alpha}\alpha}(\omega_n) \to 2\theta(\mu_\alpha - \mu_{\bar{\alpha}} - \omega_n)$. This gives the threshold condition, i.e. phonon emission is possible only when $eV_a \equiv \mu_\alpha - \mu_{\bar{\alpha}} \geq \omega_n$. This results in a step function in dI/dV_a, and a delta peak or dip in d^2I/dV_a^2. For the opposite bias polarity $\mu_{\alpha/\bar{\alpha}} = \mu_0 \mp \omega_n/2$ the other term from $-\delta(\omega + \omega_n)$ will contribute to phonon emission.

The final expressions for the exLOE is

$$I(V_a) = G(V_a)V_a + \sum_n \{C_{sym}(\omega_n, V_a)I_{sym}(\omega_n, V_a) + C_{asym}(\omega_n, V_a)I_{asym}(\omega_n, V_a)\} \tag{5.3}$$

The difference from the original LOE lies in the frequency dependence of the $C_{sym/asym}$ coefficients. If the frequencies are set to zero in these coefficients the inelastic signal obtained is equivalent to that of the original LOE. In the exLOE the coefficients are

$$\begin{aligned} C_{sym}(\omega_n, V_a) &= \mathrm{Im}\{\mathrm{Tr}[\mathbf{M}_{\lambda_n}\mathbf{A}_{\bar{\alpha}}(\mu_\alpha)\mathbf{\Gamma}^{\alpha}(\mu_\alpha)\mathbf{G}^{\mathrm{r}}(\mu_\alpha)\mathbf{M}_{\lambda_n}\mathbf{A}_{\bar{\alpha}}(\mu_{\bar{\alpha}})] \\ &+ \mathrm{Tr}[\mathbf{M}_{\lambda_n}\mathbf{A}_{\bar{\alpha}}(\mu_{\bar{\alpha}})\mathbf{\Gamma}^{\alpha}(\mu_{\bar{\alpha}})\mathbf{G}^{r}(\mu_{\bar{\alpha}})\mathbf{M}_{\lambda_n}\mathbf{A}_{\alpha}(\mu_\alpha)]\} \\ &+ \mathrm{Tr}\left[\mathbf{M}_{\lambda_n}\tilde{A}_{\alpha}(\mu_\alpha)\mathbf{M}_{\lambda_n}\mathbf{A}_{\bar{\alpha}}(\mu_{\bar{\alpha}})\right], \\ C_{asym}(\omega_n, V_a) &= 2\mathrm{Re}\{\mathrm{Tr}[\mathbf{M}_{\lambda_n}\mathbf{A}_{\bar{\alpha}}(\mu_\alpha)\mathbf{\Gamma}^{\alpha}(\mu_\alpha)\mathbf{G}^{\mathrm{r}}(\mu_\alpha)\mathbf{M}_{\lambda_n}\mathbf{A}_{\bar{\alpha}}(\mu_{\bar{\alpha}})] \\ &- \mathrm{Tr}[\mathbf{M}_{\lambda_n}\mathbf{A}_{\bar{\alpha}}(\mu_{\bar{\alpha}})\mathbf{\Gamma}^{\alpha}(\mu_{\bar{\alpha}})\mathbf{G}^{r}(\mu_{\bar{\alpha}})\mathbf{M}_{\lambda_n}\mathbf{A}_{\alpha}(\mu_\alpha)]\}, \end{aligned} \tag{5.4}$$

and the generic functions $I_{sym}(\omega_n, V_a)$ are (in units of G_0/e) given by

$$\mathcal{I}^{sym} = \frac{1}{2}\sum_{\sigma=\pm}\sigma(\omega_n + \sigma eV_a)\left(\coth\frac{\omega_n + \sigma eV_a}{2k_BT} - \coth\frac{\omega_n}{2k_BT}\right) \tag{5.5}$$

$$\mathcal{I}^{asym} = \int_{-\infty}^{+\infty}\frac{d\varepsilon}{2\pi}\mathcal{H}\{n_F(\varepsilon' - \omega_n) - n_F(\varepsilon' + \omega_n)\}(\varepsilon)\left(n_F(\varepsilon - eV_a) - n_F(\varepsilon)\right). \tag{5.6}$$

The Hilbert transform is defined as $\mathcal{H}\{g(x')\}(x) = \frac{1}{\pi}\mathcal{P}\int\frac{g(x')}{x'-x}dx'$, where P is the principal value[1]. These functions are illustrated in Fig. 5.2. The symmetric term, $\mathcal{I}^{sym}$,

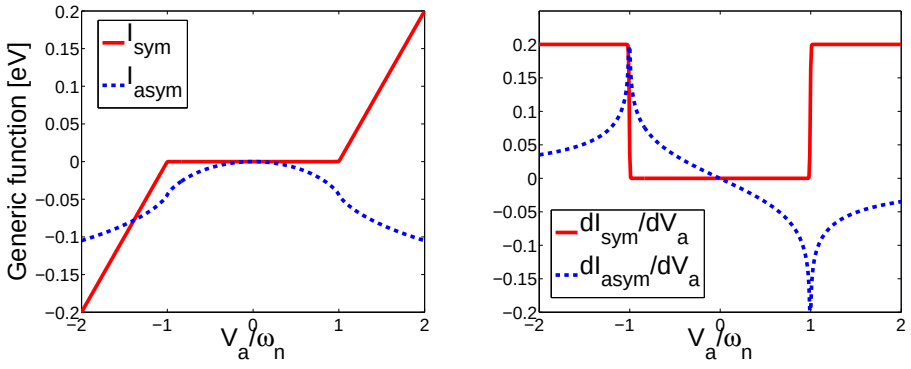

Figure 5.2: *Generic functions in the LOE expression describing the universal variation of* $\frac{dI}{dV_a}$ *with bias.*

corresponds to symmetric conductance steps at the vibrational energies whereas the asymmetric term, $\mathcal{I}^{asym}$, corresponds to conductance peaks and dips which are asymmetric with voltage inversion.

[1]For the Fermi function difference the integral can be solved analytically by contour integration, whereby we get: $\mathcal{I}^{sym} = -k_BT\left[h(\frac{eV_a+\omega_n}{2\pi k_BT}) - h(\frac{eV_a-\omega_n}{2\pi k_BT}) - 2h(\frac{\omega_n}{2\pi k_BT})\right]$, where $h(x) = x\psi(ix)$ and $\psi(x)$ is the digamma function.

5.2 IETS for a graphene nanoconstriction

This section presents SIESTA calculations of the inelastic signals obtained from both the original LOE and novel exLOE. The system is illustrated in Fig. 5.3 along with the Γ-point transmission. Besides shifting the position of the second peak all main features

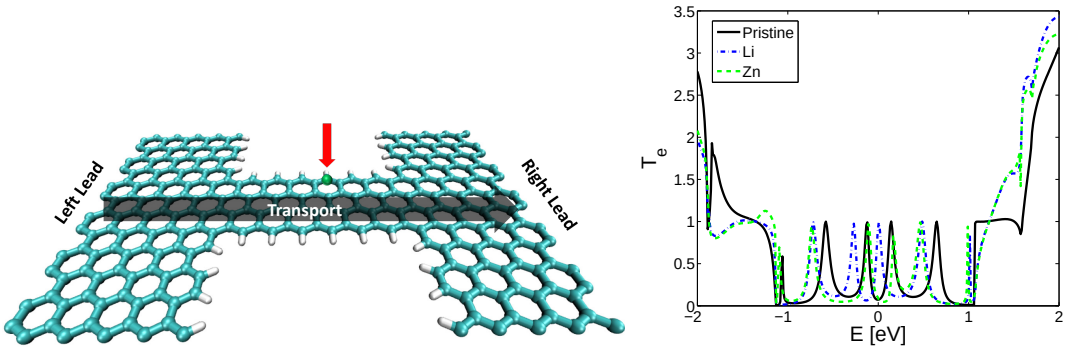

Figure 5.3: *Transport across a GNC passivated by hydrogen between two pristine graphene leads. The effect on inelastic transport of the presence of a Li or Zn adatom at the indicated H-site is examined. Left: System setup. Right: Transmission function from a Γ-point calculation for the three systems.*

in the peak neighborhood are unchanged by the presence of the adatoms. In Fig. 5.4 the IV-characteristic of the pristine GNC is illustrated. For now the GNC is gated to the second peak at $\mu_0 = -0.57$eV (cf. Fig. 5.3). The main point is that the results from LOE and the exLOE are remarkably different. Therefore, we can conclude that the original LOE formalism breaks down for systems where the electronic structure is changing on the scale of the phonon frequencies. Within the LOE the electron-phonon coupling seems artificially strong, i.e. the change of conductance is larger than a few percents. This exaggerated effect of e-ph interactions is ascribed to the WBA assumption of a constant electronic structure. An additional option is the inclusion of the heating[145], where the nonequilibrium phonon numbers are obtained from a steady state rate equation, within the WBA. From this we see that if one exploits the wide-band calculation to a maximum unphysical results may return. Specifically we can obtain a negative differential conductance in a bias region where no phonon modes can give rise to the change.

Figure 5.5 shows the inelastic tunneling spectrum for the GNC. Five distinct peaks show up. The strongest interacting modes are located around 170 meV. We will later analyze how these modes contribute to the local heating of the system. The eight phonon modes with the largest inelastic signal are also illustrated. A finite broadening is included in the signal from the finite temperature of $T = 4.2$K (boiling temperature of helium). Other broadening mechanisms exist that are not included, e.g. originating from a lock-in modulation voltage[56, 146] or coupling to the surrounding phonon baths.

Table 5.1 contains the linear frictions, giving the broadening due to the phonon bath, for the characteristic modes. The friction is calculated from the phonon self-energy due to the coupling with the leads, $\eta_{ph} = -\frac{\partial}{\partial\omega}\left(\mathrm{Im}[\Pi^{\mathrm{r}}_{\mathrm{ph}}]\right)|_{\omega=0}$. It will be smallest for modes localized in the center of the constriction (e.g. M3 and M6) and larger for modes with displacements near the contacts (e.g. M1, M5 and M7). The largest phonon friction in

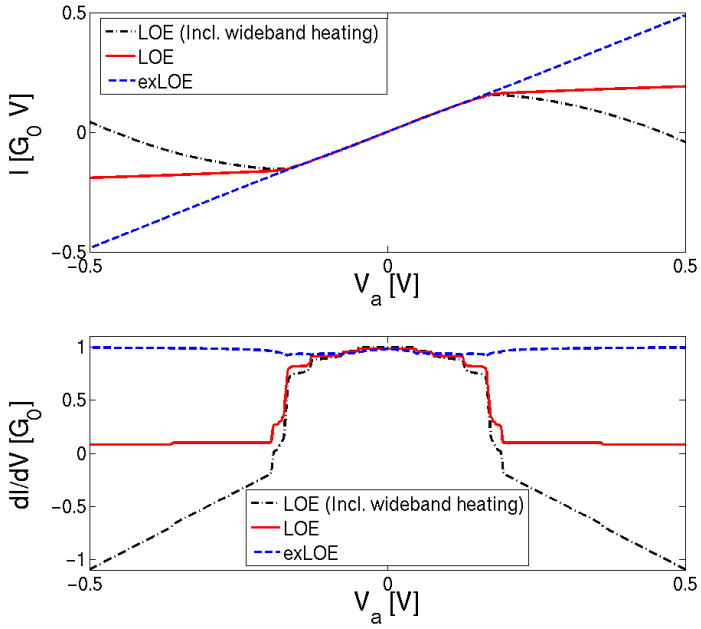

Figure 5.4: *Inelastic current and conductance for the GNC. Top: IV-characteristics of the GNC at a chemical potential of $\mu_0 = -0.57eV$. Bottom: $dI/dV_a(\mu_0 = -0.57eV)$ curves within the different approximations; LOE including the wide-band heating effect[145], original LOE and exLOE. The LOE result shown here including the wide-band heating is used to stress that if the wide-band result is used for the present system unphysical results may occur - e.g. the negative conductance observed here. The LOE results is strongly modified in the new exLOE signal including the finite phonon frequencies.*

Table of damping

	M1	**M2**	**M3**	**M4**	**M5**	**M6**	**M7**	**M8**
ω [meV]	193	192	172	171	168	128	76	49
η_{ph} [meV]	16.2	3.0	0.6	5.2	6.3	0.2	6.4	2.6
η_e [meV]	12.9	8.0	15.1	7.9	26.0	5.8	1.8	1.0

Table 5.1: *The friction from phonon and electron baths for the eight characteristic modes.*

the system is found to be $\eta_{ph} = 77.1\,\text{meV}$ for comparison. The table also contains the electronic friction[2]. The electronic friction is notable large for mode 5 by comparison with the phonon friction. This mode also leads to the largest peak in the d^2I/dV_a^2 and will from hereon be labeled the IETS mode. It is very close in frequency to a runaway mode heated by a nonlinear mechanism examined in the next chapter.

The Hamiltonian is the same for planar graphene nanostructures whether we move atoms up or down in the out-of-plane direction. Therefore, the out-of-plane electron-phonon coupling elements between π-orbitals will be zero since these are also symmetric about the out-of-plane direction. Since the current is mainly running through the π-orbitals we should expect the current to interact the strongest with longitudinal modes

[2]In the next chapter the details of the calculation of the friction due to the electron bath will be given.

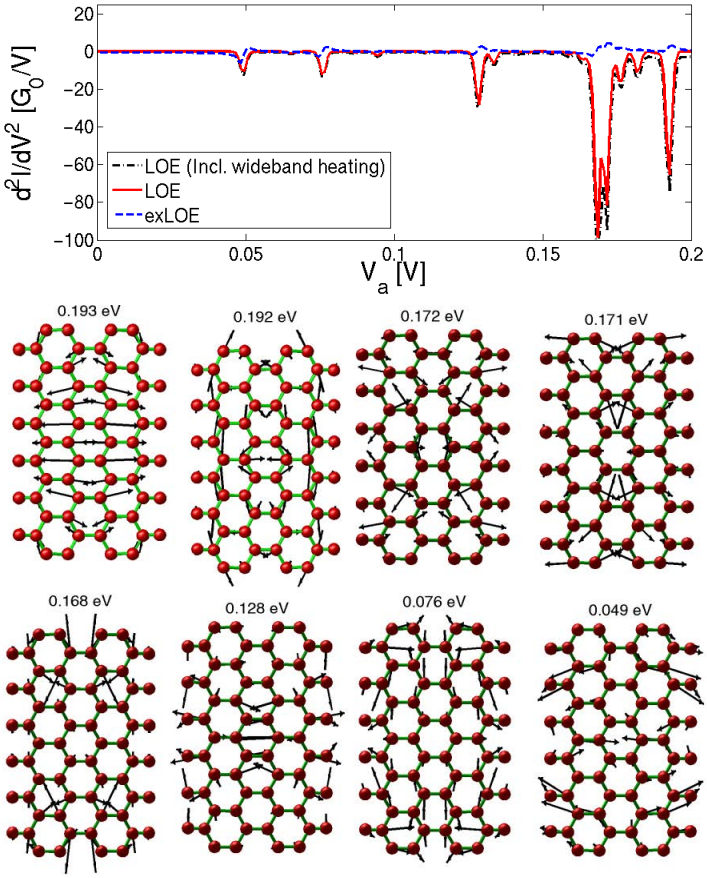

Figure 5.5: *Inelastic signal for the GNC. Top: $d^2I/dV_a^2(\mu_0 = -0.57eV)$ curves within the different approximations. The LOE result is compared to the new exLOE signal including the finite phonon frequencies. Bottom: Main contributing modes to the five main peaks. The contributing modes are the same within both LOE and exLOE although the exLOE signal is clearly different.*

in the device plane. The characteristic vibrations found for the GNC are all in-plane as expected.

In Fig. 5.6 we examine the effect of gating the GNC away from the second peak. Three scenarios are considered: Gating to the peak position as above, gating slightly away to where the transmission slope is the largest and gating away from the peak. We conclude that as one move the chemical potential away from the resonant transmission features we gradually reduce the overall inelastic signal. Especially the low bias features are initially decreased when gating to the chemical potential where the transmission slope is largest. The signal originating from optical modes is also suppressed when gating further away from the peak. Far away from the peak the LOE and exLOE results agree much better than near the resonance, as expected due to the slower energy variation.

It is also interesting to examine the influence of the adatoms on the inelastic signals. This will enable one to evaluate the robustness of the results but also to see if new fingerprint features occur. Fig. 5.3 shows that the main effect of the adatoms on the electronic structure is to shift the position of the second transmission peak. Therefore, modifications mainly originate from the change in the local vibrations of the GNC. Both

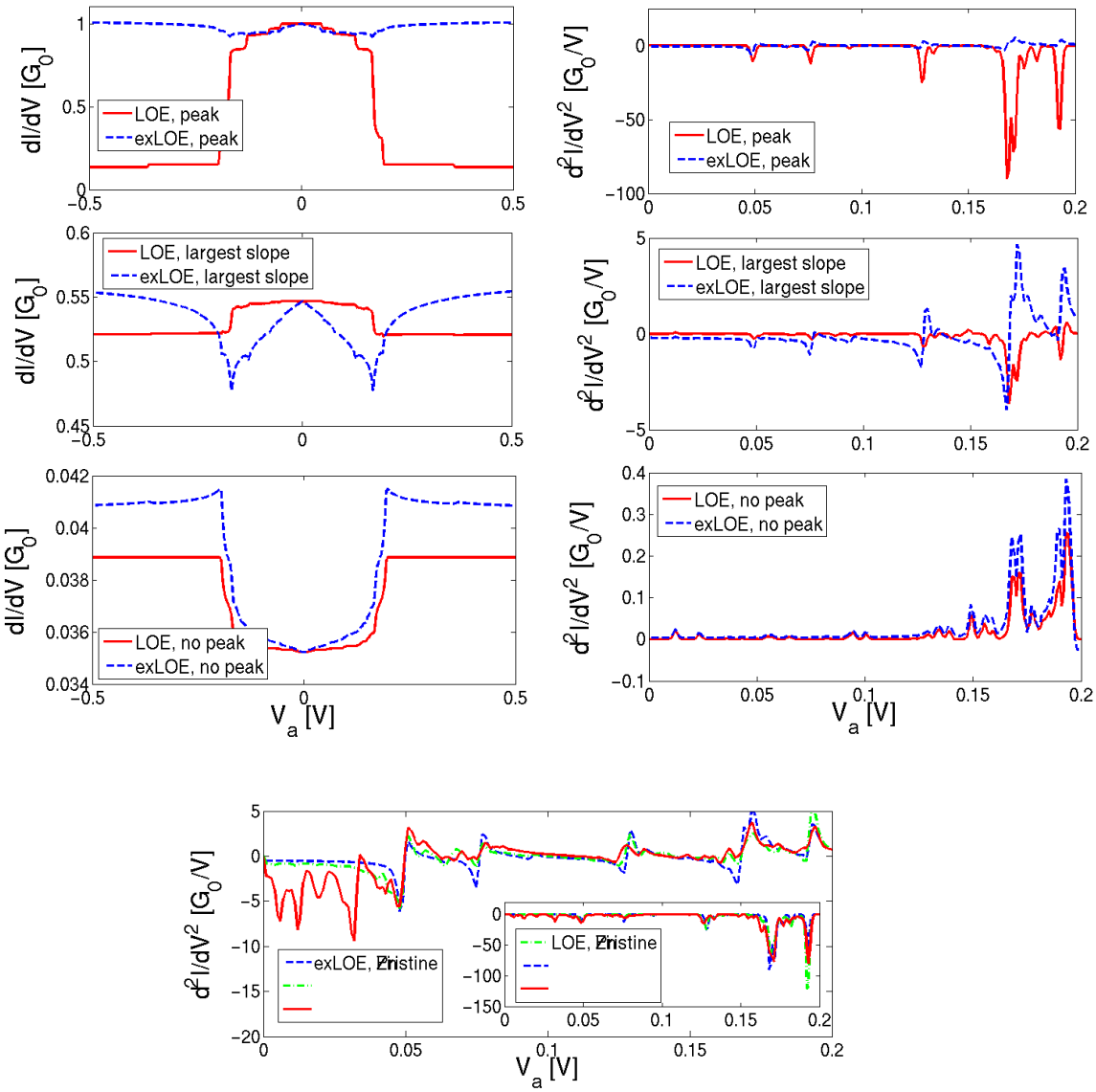

Figure 5.6: *Inelastic signal for the GNC gated or with adatoms. Left column: $dI/dV_a(\mu_0)$ curves for the GNC gated to the peak ($\mu_0 = -0.57eV$), at the largest transmission slope ($\mu_0 = -0.62eV$) and away from the peak ($\mu_0 = -0.86eV$). Right column: Corresponding $d^2I/dV_a^2(\mu_0)$ curves for the GNC gated to the same three different chemical potentials. Bottom: Inelastic signals for the pristine GNC and with a Li and Zn adatom on top the center of a hexagon in the GNC.*

Li and Zn are positioned at the H-site (above the center of a hexagon)[3]. The main effect of these light adatoms is a small reduction in the GNC peaks, as shown in Fig. 5.6. For the Zn adatom additional low frequency peaks occurs whereas no such additional features are observed for Li. The low frequency of the vibrations of these light adatoms also supports that the adatoms are weakly bonded. Additionally, we see that the Li adatoms may be promising candidates for doping of GNCs due to the large shift in transmission peak without any additional scattering or structural modification. Even when positioned inside the GNC its effect on the local vibrations and the scattering of electrons is minimal. We conclude that the main features of the IETS of GNCs seem fairly robust to a low degree of disorder such as the presence of light adatoms. In general the developed extension makes it possible to include the effect of electronic resonances while still being computationally tractable even for larger systems like the GNC.

5.3 Summary and discussion

The new exLOE method is summarized in eqn. 5.3-5.4. One obtains significantly modified results as compared to the original LOE for a GNC gated to a resonance. Gating the GNC away from the resonant transmission features gradually changes the exLOE inelastic signal to that of the LOE. We also showed that high bias features of the IETS of GNCs are robust to a low scattering disorder. Especially for a Li adatom the IETS is weakly modified whereas a fingerprint signal may be found for slightly heavier adatoms such as the Zn adatom considered. A manuscript describing the exLOE method is in preparation.

As mentioned in Sec. 2.2, we can derive corresponding corrections to the phonon transmission from the first Born approximation applied in the LOE. We will not show the results for the GNC here, but mention that both transmission corrections and drag coefficients are significant. The exLOE method may provide a first step towards evaluating the change in thermoelectric performance due to e-ph coupling of realistic devices, such as a GNC. Graphene nanostructures are particular interesting in this aspect due to the adjustability of the electronic structure by an external gate.

[3]The computational settings for the GNC with adatoms are the same as in Appendix A (Sec. 9.1) except that a DZP basis is used for the adatoms.

Chapter 6

Phonons in the presence of electronic current

From many experiments on graphene it is known that unstable device behavior occur when an applied voltage exceeds a certain threshold. For instance, this is observed as contact disruption in experiments and is used for current-annealing of nanostructured graphene[52, 83]. With graphene research now at a point where the structural response to a high bias is being studied by *in situ* transmission electron microscopy[15, 83], there may be a unique possibility in understanding the fundamental mechanisms behind current-induced instabilities at the atomic scale, which takes place far from equilibrium. Typical explanations are "inelastic scattering" or "Joule heating", but we show here that other mechanisms should be considered as well.

This chapter presents the theoretical framework for current-induced dynamics based on a semiclassical generalized Langevin equation (SCLE). We apply this method in studies of current-induced dynamics of graphene nanoscale devices. It is essential to be able to predict the stability of nanoscale devices in the design phase of nano-circuitry. On the basis of the SCLE we can model how the current excites and couples local vibrations of a nanosystem and perform a harmonic stability analysis of a nanosystem.

Several mechanisms are at play in the presence of an electric current that can induce a breakdown of the harmonic approximation. A force given as a derivative of a scalar potential (Hellmann-Feynmann definition) will always describe conservative forces, i.e. the dynamical matrix will always be symmetrical and have real eigenfrequencies. However, this is not necessarily the case in nonequilibrium conditions. Todorov *et al.* have shown that nonconservative forces can lead to complex frequencies and exponential growing motion[17, 20, 50]. The current flow hereby induces motion akin to atomic waterwheels[26] with an increasing kinetic energy. This motion is related to electromigration which is a central problem in integrated circuits due to the breakdown of electrical interconnects[168]. It was argued that the nonconservative forces from a "wind" of electrons may serve as an ignition key for atomic-scale motors[49]. On a macroscopic scale wind forces can lead to a nonconservative energy pumping in bridges, as it was the case of the famous collapse of the Tacoma bridge. An important issue regarding the electronic wind force is its magnitude compared to other energy-exchange mechanisms that involve electrons, such as Joule heating and frictional damping. From an electronic point of view, Head-Gorden and Tully generalized MD to include the equilibrium electronic friction[73] in their studies of adsorbate dynamics at metal surfaces. We aim at extending the description of nonadiabatic energy exchange between nuclear and elec-

tronic degrees of freedom to current-carrying systems[108, 109, 110]. It is essential to include the damping due to electrode phonons to describe the local heating accurately. An extension of the SCLE to include the quantum distribution of the phonon baths was developed by Wang *et al.*[188, 190]. The generalized Langevin framework constitute a unified description of the aforementioned mechanisms on equal footing with local Joule heating.

This chapter reviews the SCLE method and the applications to carbon-chain molecular junctions and a GNC published in Paper II and VI. We perform a harmonic stability analysis to predict current-induced instabilities. The two applications illustrate how two different mechanisms can lead to a breakdown of the harmonic approximation and runaway modes in graphene devices. Instabilities arise due to the water-wheel effect rooted in the nonconservative wind force for the carbon-chain system. However, for the GNC, we show how a phonon "laser"-effect gives rise to negatively damped phonons. Both of these phenomena may limit the stability of graphene devices and are important compared to local Joule heating.

6.1 Semiclassical Langevin equation

In this section we present a derivation of the generalized Langevin equation based on NEGF theory, providing more details than in Paper II. For a more rigorous derivation based on influence functional theory, see [109]. The starting point is the equation of motion for the displacements[1]

$$\ddot{u} = \left\langle \hat{F} \right\rangle, \tag{6.1}$$

where the force operator is defined from the full Hamiltonian as

$$\hat{F} = -\frac{\partial \hat{H}(u)}{\partial u}. \tag{6.2}$$

The expectation value of the force can be expressed in terms of the lesser Green's function, $\mathbf{G}^<_{nm}(t,t_+) = \frac{i}{\hbar}\langle \hat{c}^\dagger_m(t_+)\hat{c}_n(t)\rangle$,

$$\left\langle \hat{F}_k \right\rangle = -\sum_{n,m} \mathbf{M}^k_{nm} \left\langle \hat{c}^\dagger_n \hat{c}_m \right\rangle = i\hbar \mathrm{Tr}\left[\mathbf{M}^k \mathbf{G}^<(t,t_+)\right]. \tag{6.3}$$

The corresponding contour ordered Green's function defined on the Keldysh contour has a well-defined perturbation expansion obtained from the Dyson equation[72]:

$$\mathbf{G}(\tau,\tau') = \mathbf{G}_0(\tau,\tau') + \int_C \mathbf{G}_0(\tau,\tau')\mathbf{V}(\tau')\mathbf{G}(\tau,\tau')d\tau' \tag{6.4}$$

with $\mathbf{V} = \sum_k \mathbf{M}^k u_k(t)$. We perform analytical continuation according to Langreths theorem[72] and obtain

$$\begin{aligned} \mathbf{G}^<(t,t_+) &= \mathbf{G}^<_0(t,t_+) \\ &+ \sum_k \int_{-\infty}^{\infty} \left[\mathbf{G}^r_0(t,t')\mathbf{M}^k\vec{u}_k(t')\mathbf{G}^<(t',t_+) + \mathbf{G}^<_0(t,t')\mathbf{M}^k\vec{u}_k(t')\mathbf{G}^a(t',t_+)\right] dt' \end{aligned} \tag{6.5}$$

[1] This follows from the Heisenberg equation of motion with a replacement of the ionic position operators by its classical expectation values and is often termed the Ehrenfest approach.

We then replace the full Green's function, as in the LOE, by its noninteracting equivalent to model the effect of electrons to second order in the e-ph interaction. Inserting this in the equation of motion together with the definition of the e-ph coupling self-energy,

$$\mathbf{\Pi}^r_{e,ij}(t,t') = -i\hbar\left(\mathrm{Tr}\left[\mathbf{M}^i\mathbf{G}^r_0(t,t')\mathbf{M}^j\mathbf{G}^>_0(t,t')\right] + \mathrm{Tr}\left[\mathbf{M}^i\mathbf{G}^<_0(t,t')\mathbf{M}^j\mathbf{G}^a_0(t,t')\right]\right)\,, \quad (6.6)$$

we obtain

$$\ddot{u}_k \;=\; i\hbar\mathrm{Tr}[\mathbf{M}^k\mathbf{G}^<_0(t,t_+)] - \int \mathbf{\Pi}^r(t,t')u(t')dt' + f^e\,, \quad (6.7)$$

where we in addition to the average force have added a noise term, f^e, with a zero average. We define it from a noise operator, $\hat{f}^e \equiv \hat{F} - \left\langle \hat{F} \right\rangle$, and it contains a term up to second order in the e-ph interaction originating from Joule heating. In this semiclassical approach we replace the full electronic force by the average value plus the deviation term to second order in the e-ph interaction. In the following sections we will discuss the separate terms one by one.

6.1.1 Phonon forces and reservoir

We start by considering the first term, $i\hbar\mathrm{Tr}[\mathbf{M}^k\mathbf{G}^<_0(t,t_+)]$, describing the equilibrium forces. It is rewritten as a harmonic force

$$F^{ph} \;=\; -\mathbf{K}u - \sum_{\alpha=L,R}\mathbf{V}^{ph}_\alpha u_\alpha \quad (6.8)$$

The first term describes the harmonic forces due to the local springs in the device region. The forces in the device region could include the full anharmonicity as it is done in MD simulations. The second term describes the connection to the bath oscillators in the electrodes. We will assume that the bath degrees of freedom fulfill a harmonic equation of motion

$$\ddot{u}_\alpha(t) \;=\; -\mathbf{K}_\alpha u_\alpha(t) - \mathbf{V}^{ph,\dagger}_\alpha u(t)\,. \quad (6.9)$$

Thus, the device displacements, in eqn. 6.7, depends on the unknown initial conditions and displacements of the bath oscillators. The explicit dependence on the initial conditions of the infinite number of bath atoms was, in the 1970's, suggested to be interpreted as a result of a stochastic process[1, 2, 88, 89]. Here, we take an approach proposed by Wang *et al.*[190], where one assumes that the bath-device interactions are adiabatically turned on. One can express the bath solution in terms of the free bath solution $u^0_\alpha(t)$, satisfying the bath equation of motion with no bath-system interactions:

$$u_\alpha(t) \;\approx\; u^0_\alpha(t) + \int \mathbf{g}^r_\alpha(t,t')\mathbf{V}^{ph}_\alpha u_\alpha(t')dt'\,. \quad (6.10)$$

The phonon force, in eqn. 6.8, is then expressed as

$$F^{ph} \;=\; -\mathbf{K}u - \sum_{\alpha=L,R}\int \mathbf{\Pi}^r_\alpha(t,t')u(t)dt' + \sum_{\alpha=L,R} f^{ph}_\alpha(t) \quad (6.11)$$

The second term describes the damping force due to the connection with the bath. The third term is given by $f^{ph}_\alpha = -V^{ph}_\alpha u^0_\alpha(t)$. It is interpreted as a noise term since it has a zero average, $\left\langle f^{ph}_\alpha \right\rangle = \langle u^0_\alpha \rangle = 0$ (undisplaced harmonic oscillators in the leads), and

is Gaussian distributed if the unknown initial conditions and displacements of the bath atoms are Gaussian distributed[1, 88]. The noise correlation function in the adiabatic limit is

$$\begin{aligned} < f_\alpha^{ph}(t) f_\alpha^{ph,\dagger}(t') > &= V_\alpha^{ph} < u_\alpha^0(t) u_\alpha^{0,\dagger}(t') > V_\alpha^{ph,\dagger} \\ &= V_\alpha^{ph} i\hbar \mathbf{g}_\alpha^>(t-t') V_\alpha^{ph,\dagger} = i\hbar \mathbf{\Pi}_\alpha^>(t-t') \end{aligned} \tag{6.12}$$

The opposite correlation function is

$$< f_\alpha^{ph}(t') f_\alpha^{ph,\dagger}(t) > = i\hbar \mathbf{\Pi}_\alpha^<(t-t') \tag{6.13}$$

In the semiclassical approximation one replaces all operators by numbers and uses a symmetrized noise spectral density:

$$\begin{aligned} \mathbf{S}_f^{ph}(\omega) &\equiv \sum_{\alpha=L,R} \int_{-\infty}^{\infty} \frac{d\omega}{2\pi} \left[\frac{< f_\alpha^{ph}(t) f_\alpha^{ph,\dagger}(t') > + < f_\alpha^{ph}(t') f_\alpha^{ph,\dagger}(t) >}{2} \right] e^{-i\omega t} \\ &= \sum_{\alpha=L,R} i\hbar \frac{\mathbf{\Pi}_\alpha^>(\omega) + \mathbf{\Pi}_\alpha^<(\omega)}{2} = \sum_{\alpha=L,R} \hbar \left(n_B(\omega) + \frac{1}{2} \right) \mathbf{\Gamma}_\alpha(\omega) \end{aligned} \tag{6.14}$$

where $\mathbf{\Gamma}_\alpha(\omega) = i\left(\mathbf{\Pi}_\alpha^r(\omega) - \mathbf{\Pi}_\alpha^a(\omega)\right)$. Eqn. 6.14 is called the quantum fluctuation-dissipation theorem and is the basis of QMD simulations[188, 190]. We are thus left with solving a stochastic differential equation. The expression in eqn. 6.11, with noise distributed according to eqn. 6.14, gives the final result for the first term in eqn. 6.7.

6.1.2 Average electronic forces

The remaining part of the average electronic force, second term in eqn. 6.7, is related to the retarded e-ph interaction self-energy. In equilibrium the electronic friction was related to the interaction-weighted electron-hole pair density of states, $\mathbf{\Lambda}$, by Head-Gorden and Tully[73]. In nonequilibrium we define $\mathbf{\Lambda} = \sum_{\alpha,\beta} \Lambda^{\alpha\beta}$, with contributions from left/right leads ($\alpha = L, R$), as

$$\begin{aligned} \Lambda^{\alpha\beta}(\omega) &\equiv 2 \int \frac{d\epsilon}{4\,\pi^2} \mathrm{Tr}\left[\mathbf{M}^k \mathbf{A}_\alpha(\epsilon+\omega) \mathbf{M}^l \mathbf{A}_\beta(\epsilon) \right] \\ &\times \left[n_F(\epsilon+\omega-\mu_\alpha) - n_F(\epsilon-\mu_\beta) \right] . \end{aligned} \tag{6.15}$$

We can relate it to the self-energies as

$$\tilde{\mathbf{\Pi}}(\omega) = \mathbf{\Pi}^{e,r}(\omega) - \mathbf{\Pi}^{e,a}(\omega) = \mathbf{\Pi}^{e,>}(\omega) - \mathbf{\Pi}^{e,<}(\omega) = i2\pi \mathbf{\Lambda}(\omega) \tag{6.16}$$

In steady state, $\mathbf{\Pi}^r$ only depends on the time difference, $\tau = t - t'$, and it is therefore convenient to work in the frequency(energy) domain. The retarded self-energy is

$$\mathbf{\Pi}^{e,r}(\tau) = \theta(\tau) \tilde{\mathbf{\Pi}}(\tau) = i2\pi \int \frac{d\omega}{2\pi} e^{-i\omega'\tau} \mathbf{\Lambda}(\omega') \theta(\tau) \tag{6.17}$$

By Fourier transformation we obtain

$$\mathbf{\Pi}^{e,r}(\omega) = i2\pi \int_0^\infty d\tau \int \frac{d\omega}{2\pi} e^{-i(\omega' - (\omega+i\eta))\tau} \mathbf{\Lambda}(\omega') = \int \frac{d\omega}{2\pi} \frac{\mathbf{\Lambda}(\omega')}{\omega' - \omega - i\eta} \tag{6.18}$$

for $\eta \to 0^+$. Applying the Sokhatsky-Weierstrass theorem(cf. eqn. 9.3), the expression in eqn. 6.18 gives four deterministic contributions to the atomic forces:

$$\begin{aligned} \mathbf{\Pi}^{e,r}(\omega) &= i\pi \mathrm{Re}\Lambda(\omega) - \pi \mathrm{Im}\Lambda(\omega) \\ &+ \pi\mathcal{H}\{\mathrm{Re}\Lambda(\omega')\}(\omega) + i\pi\mathcal{H}\{\mathrm{Im}\Lambda(\omega')\}(\omega)\,. \end{aligned} \tag{6.19}$$

The four terms in this expression yields the electronic friction force, nonconservative wind force, renormalization force and Berry-phase force in the presence of current, respectively[109, 110]. The friction term is imaginary and symmetric in mode index m, n and relates to the generation of electron-hole pairs in the electronic environment by the ionic motion. The term related to the nonconservative wind force is real and anti-symmetric, which means that the general curl of this force is not zero as discussed by Dundas and co-workers[50]. This force describes the angular momentum transfer between electrons and phonons and involves two separate, often nearly degenerate, phonon modes. The third term is real and symmetric and can be considered a renormalization of the dynamical matrix. The Berry-phase term is imaginary, anti-symmetric and proportional to ω for small frequencies. It was originally discussed by Lü *et al.*[108], who showed that it resembles a Lorentz-like force due to an effective magnetic field, since the direction of the Berry-phase force is always normal to the velocity in the phase space.

6.1.3 Electronic noise

To obtain all forces to second order in the e-ph coupling we need to include an additional term describing the Joule heating, i.e. f^e in eqn. 6.7. We will interpret this as a stochastic force with a Gaussian distribution determined by the second order (in M) correlation function[2],

$$\begin{aligned} \langle \hat{f}_i^e(t)\hat{f}_j^e(t')\rangle &= \hbar^2 \mathrm{Tr}[\mathbf{M}^i \mathbf{G}_0^{>}(t,t')\mathbf{M}^j \mathbf{G}_0^{<}(t',t)] \\ &= i\hbar \mathbf{\Pi}_{ij}^{>}(t,t')\,, \end{aligned} \tag{6.20}$$

and at the opposite time

$$\langle \hat{f}_j^e(t')\hat{f}_i^e(t)\rangle = i\hbar \mathbf{\Pi}_{ij}^{<}(t,t')\,. \tag{6.21}$$

Once again we apply the semi-classical approximation to replace the noncommuting quantum correlation functions by a single semi-classical spectral density:

$$\begin{aligned} S_f^e(\omega) &= \int_{-\infty}^{\infty} e^{-i\omega\tau}\frac{d\omega}{2\pi}\frac{1}{2}(\langle \hat{f}_i^e(t)\hat{f}_j^e(t+\tau)\rangle + \langle \hat{f}_j^e(t+\tau)\hat{f}_i^e(t)\rangle) \\ &= S_{f,0}^e(\omega) + \Delta S_f^e(\omega) \\ &= -\pi\Lambda(\omega)\coth\left(\frac{\hbar\omega}{2k_BT}\right) - \pi\sum_{\alpha\beta}\Lambda^{\alpha\beta}(\omega)\left[\coth\left(\frac{\hbar\omega - (\mu_\alpha - \mu_\beta)}{2k_BT}\right) - \coth\left(\frac{\hbar\omega}{2k_BT}\right)\right]. \end{aligned} \tag{6.22}$$

This semiclassical noise spectrum predicts a real time correlation function, that can be used in a semiclassical MD setup. Importantly, the quantum zero-point fluctuation is

[2]Here we apply Wick's theorem[114, page 95-99] for the time-ordered product

$$\left\langle \mathrm{T}_c\left[\hat{c}_n^\dagger(t)\hat{c}_m(t)\hat{c}_k^\dagger(t')\hat{c}_l(t')\right]\right\rangle = \left\langle \mathrm{T}_c\left[\hat{c}_n^\dagger(t)\hat{c}_m(t)\right]\right\rangle\left\langle \mathrm{T}_c\left[\hat{c}_k^\dagger(t')\hat{c}_l(t')\right]\right\rangle + \left\langle \mathrm{T}_c\left[\hat{c}_n^\dagger(t)\hat{c}_l(t')\right]\right\rangle\left\langle \mathrm{T}_c\left[\hat{c}_m(t)\hat{c}_k^\dagger(t')\right]\right\rangle$$

Where we have defined the time ordering operator T_c. For $t > t'$ the four operator combination is expressed in terms of Green's functions as:
$i^2/\hbar^2 < \hat{c}_n^\dagger(t)\hat{c}_m(t)\hat{c}_k^\dagger(t')\hat{c}_l(t') >= \mathbf{G}_{0,mn}^{<}(t,t)\mathbf{G}_{0,lk}^{<}(t',t') - \mathbf{G}_{0,ln}^{<}(t',t)\mathbf{G}_{0,mk}^{>}(t,t')$.

encoded in the coth function. We emphasize the ability of the semiclassical approximation to evaluate the correct quantum mechanical average of two displacement operators at equal time, $\langle u_i(t)u_j(t)\rangle$. Since the equal time correlation functions commute it is still possible to describe the quantum mechanical vibrational energy and steady-state heat transport from the SCLE. The force from the electron bath, the last two terms in eqn. 6.7, is hereby reduced to five principal forces. Four deterministic in eqn. 6.19 and the stochastic Joule heating in eqn. 6.22. They are all related to the interaction-weighted electron-hole pair density of states, $\mathbf{\Lambda}$, defined in eqn. 6.15.

6.1.4 SCLE

In summary, we have eliminated the bath degrees of freedom due to electrons and electrode phonons in sec. 6.1.1-6.1.3. Collecting the different terms, one only has to consider the dynamics in the device part described by the SCLE:

$$\ddot{u}(t) = -Ku(t) - \int^t \Pi^r(t-t')u(t')dt' + f(t)\,. \tag{6.23}$$

The coupling to the electron and phonon baths are described by the total retarded phonon self-energies $\Pi^r = \Pi^r_e + \Pi^r_{ph}$, and the random noise force, $f(t) = f^{ph}(t) + f^e(t)$. The SCLE in eqn. 6.23 is the fundamental equation that describes the dynamics of a device in the presence of electronic current. However, we still need ways to evaluate $\mathbf{\Lambda}$ to obtain the forces in nonequilibrium. We next describe two approaches that are applicable in first-principles calculations. We start with the wide-band approximation, which afterwards is applied in a study of the dynamics of a carbon chain, and continue with a spectral expansion technique, that is used to study dynamics of a GNC.

6.2 Wide-band approximation

Earlier studies have successfully employed the wide-band approximation (WBA) to include the effect of the electronic environment on the atomic motion of realistic molecular junctions[108]. Within the WBA one assumes that the electronic spectrum varies slowly not only within the vibrational energy spectrum, but also within the bias window. The equations governing the atomic forces are dramatically simplified by evaluating all electronic properties at the Fermi level (μ_0). Within this approximation the SCLE reads:

$$\begin{aligned}\ddot{u}(t) &= -Ku(t) - (\eta_0 + \eta_{ph})\dot{u}(t) + \mathcal{N}_0 u(t) \\ &- \zeta_0 u(t) - \mathcal{B}_0\dot{u}(t) + f(t)\,,\end{aligned} \tag{6.24}$$

with the electronic friction, nonconservative, renormalization and Berry-phase forces given by

$$\eta_0 = \sum_\sigma \frac{\hbar}{4\pi}\mathrm{Tr}\left[MA(\mu_0)MA(\mu_0)\right], \tag{6.25}$$

$$\mathcal{N}_0 = eV\chi^-, \tag{6.26}$$

$$\zeta_0 = \sum_\sigma \frac{eV}{2\pi}\mathrm{ReTr}\left[M\Delta A(\mu_0)MR(\mu_0)\right], \tag{6.27}$$

$$\mathcal{B}_0 = \sum_\sigma \frac{\hbar eV}{2\pi}\mathrm{ImTr}\left[M\Delta A(\mu_0)M\partial_\varepsilon R(\mu_0)\right], \tag{6.28}$$

respectively. We have introduced

$$\chi^{-} = \sum_{\sigma} \frac{1}{2\pi} \mathrm{ImTr}[MA_L(\mu_0)MA_R(\mu_0)]\,, \tag{6.29}$$

$$\chi^{+} = \sum_{\sigma} \frac{1}{2\pi} \mathrm{ReTr}[MA_L(\mu_0)MA_R(\mu_0)]\,, \tag{6.30}$$

$$R(\varepsilon) = -\frac{1}{2}\mathcal{H}\{A(\varepsilon')\}(\varepsilon) = \frac{G_0^r(\varepsilon)+G_0^a(\varepsilon)}{2} = \mathrm{Re}(\mathrm{G}_0^{\mathrm{r}}(\varepsilon))\,, \tag{6.31}$$

and $\Delta A(\mu_0) = A_L(\mu_0) - A_R(\mu_0)$. The noise correlation function, in eqn. 6.22, simplifies to

$$S^e_{f,0}(\omega) = (\omega\eta_0 - ieV_a\chi^{-})\coth\left(\frac{\hbar\omega}{2k_BT}\right), \tag{6.32}$$

and

$$\begin{aligned}\Delta S^e_f(\omega) &= \frac{1}{2}\sum_{\tilde{\sigma}=\pm1}\left(\chi^{+} - i\tilde{\sigma}\chi^{-}\right)(\hbar\omega + \tilde{\sigma}eV_a) \\ &\times \left[\coth\left(\frac{\hbar\omega+\tilde{\sigma}eV_a}{2k_BT}\right) - \coth\left(\frac{\hbar\omega}{2k_BT}\right)\right].\end{aligned} \tag{6.33}$$

We next apply the WBA to study current-driven dynamics of a carbon chain from first-principles.

6.3 Applications in carbon atomic contacts

This section discusses the application of the SCLE to the carbon-chain junction published in Paper II. All simulations were performed with SIESTA DFT and the detailed settings are described in the paper. The application illustrates the role current-induced forces can have on local vibrations. The four-atom carbon chain system between graphene leads is illustrated in Fig. 6.1. We evaluate the dynamical matrix and e-ph interaction matrix at zero bias, whereas the finite bias is included in the electronic structure otherwise. The equal potential drop at the left and right electrodes reflects the electron-hole symmetry for $V_g = 0\,\mathrm{V}$. From the transmission we see, that as long as the gate voltage is kept below $0.6\,\mathrm{V}$, we can assume the WBA to be a fairly good model. We hereby employ the SCLE within the WBA, but neglect the coupling to the electrode phonons. This is of secondary importance for the highest frequency optical modes involved in the following discussion. We will later elaborate on the effect of the electrode phonon damping for the GNC.

We can analyze the effect of deterministic current-induced forces by looking at the eigenmodes of the system. A set of orthogonal normal modes are defined by diagonalizing K by a unitary transformation; Fig. 6.2(a) illustrates two nearly degenerate modes for the chain system. The corresponding eigenvalues are the diagonal matrix elements ω_i^2. These normal modes are effectively coupled to each other via the interaction with electrons and the coupling to the environment by a damping. The current is found to interact most strongly with the two longitudinal modes depicted in Fig. 6.2(a). We can calculate the new eigenmodes, with eigenfrequencies $\tilde{\omega}_i$, by including the current-induced coupling. They are a linear combination of the normal modes, but are not orthogonal anymore.

We obtain the modes from the set of coupled differential equations for displacements defined by the WBA SCLE in eqn. 6.24 and the Fourier transforms, $\dot{u}(\omega) = -i\omega u(\omega)$

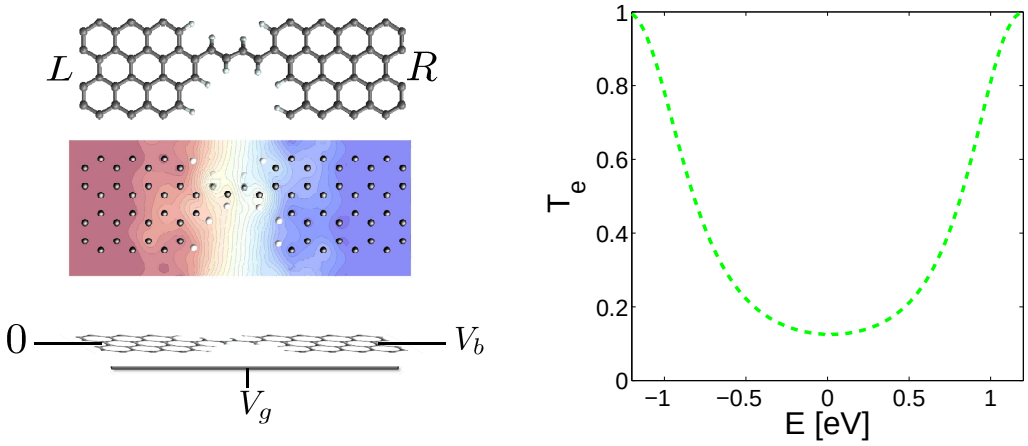

Figure 6.1: *Transport setup for the carbon chain system. Left: The system consists of a four-atom carbon chain bridging two graphene electrodes. The dangling bonds are passivated by Hydrogen atoms. We consider the effect of both an external applied bias voltage (V_b) between the L and R electrodes and a gate voltage (V_g) perpendicular to the graphene surface. The contour plot illustrates the electrostatic potential drop across the junction at $V_g = 0\,V$, and $V_b = 1\,V$. Right: Transmission function as a function of energy for the carbon chain system. Partly from Paper II.*

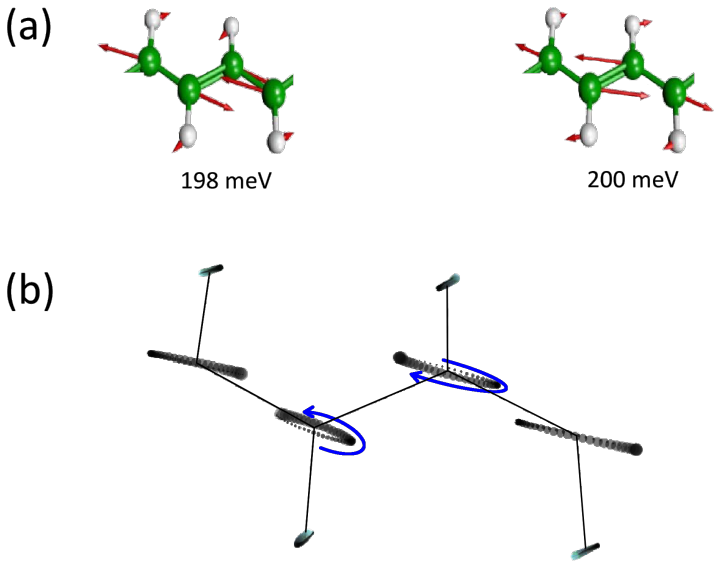

Figure 6.2: *Modes in and out of equilibrium. (a) Motion of the two phonon modes around 200 meV. The main effect of the nonconservative wind force is to couple these two modes. (b) Motion of the runaway mode at $V_g = 0.6\,V$, and $V_b = 1\,V$. We depict the motion using a number of discrete time steps roughly corresponding to a full oscillation period. The position of each atom is depicted as a circle for a sequence of time steps indicated by an increasing radius with time. The motion is a phase-shifted linear combination of the two modes in (a). We can see the elliptical motion of the carbon atoms from the plot. The enclosed area indicates a nonzero work done by the current-induced wind force. From Paper II.*

and $\ddot{u}(\omega) = -i\omega\dot{u}(\omega)$. The new set of eigenmodes are defined from the double-sized eigenvalue problem expressed from these equations:

$$\begin{bmatrix} 0 & -I \\ K+\zeta_0+\mathcal{N}_0 & \eta_{ph}+\eta_0+\mathcal{B}_0 \end{bmatrix} \begin{bmatrix} u(\omega) \\ \dot{u}(\omega) \end{bmatrix} = i\omega \begin{bmatrix} u(\omega) \\ \dot{u}(\omega) \end{bmatrix}. \tag{6.34}$$

This SCLE dynamical matrix is in general nonhermitian if the damping or electronic forces are nonzero. Therefore, one obtains complex eigenfrequencies, $\tilde{\omega}_i$, and we can define the Q-factor from the relative change in energy per time unit:

$$\frac{1}{Q} \equiv \left(2\pi\frac{\Delta E}{E_{tot}}\right)^{-1} = -\frac{2\mathrm{Im}(\tilde{\omega}_\mathrm{i})}{\mathrm{Re}(\tilde{\omega}_\mathrm{i})}. \tag{6.35}$$

If the system is connected to a bath the eigenmodes can describe an elliptical motion in contrast to the isolated circular motion described by a linear combination of the normal modes. The new eigenmodes are phase-shifted linear combinations of the normal modes with a change in amplitude described by the Q-factor, see Fig. 6.2(b).

In the simplest case of a phonon damping/friction the $1/Q$-factor will be positive and the motion damped. In nonequilibrium the motion can be growing in amplitude, depending on the imaginary part of the eigenfrequency. This important effect, related to the nonconservative force, was theoretically described by a current-induced change in the inverse Q-factor by tuning of the bias[108]. The inverse Q-factor is illustrated for the carbon-chain system in Fig. 6.3. Above a certain threshold bias, it may become negative, which means the energy stored in the mode gets larger with time until the amplitude of the motion gets so large that the harmonic approximation breaks down, and the molecular contact may disrupt. This is also illustrated in the phonon number in Fig. 6.3, which is calculated from the displacement correlation function:

$$N_i + \frac{1}{2} \approx \mathrm{Re}\{\omega_i\} \int \langle u_i u_i \rangle(\omega) \frac{d\omega}{2\pi}\,. \tag{6.36}$$

Near the threshold bias the occupation diverges as the harmonic approximation breaks down. We conclude that the bias and gate voltage can be used to tuning the excitation and life time of the local vibrations of such molecular junctions bridging graphene leads. After the threshold is reached the system will enter a highly anharmonic regime where the preceding eigenanalysis formally breaks down.

6.4 Spectral expansion - beyond the WBA

The chain system considered in the previous section is a good example of a system where it is reasonable to apply the WBA to perform a mode analysis in the presence of current. We do not examine the chemical potential directly at a transmission peak, since the peak is outside the experimental reachable potential by gating, see Fig. 6.1. All electronic variations are reasonably slow as long as the gate voltage is $< 0.6\,\mathrm{V}$. However, for the GNC system the transmission function has peaks at much lower chemical potentials. Additionally, the peak width is of the order of the phonon frequencies ($0.1 - 0.2\,\mathrm{eV}$, cf. Fig. 5.3) for the GNC, where it was much larger ($1\,\mathrm{eV}$) for the chain-system. Clearly, the WBA will break down in that case. The remaining of this chapter is therefore devoted to discussing the spectral expansion method applicable to systems where the electronic structure is changing on the scale of the phonon frequencies, as it is the case for the GNC.

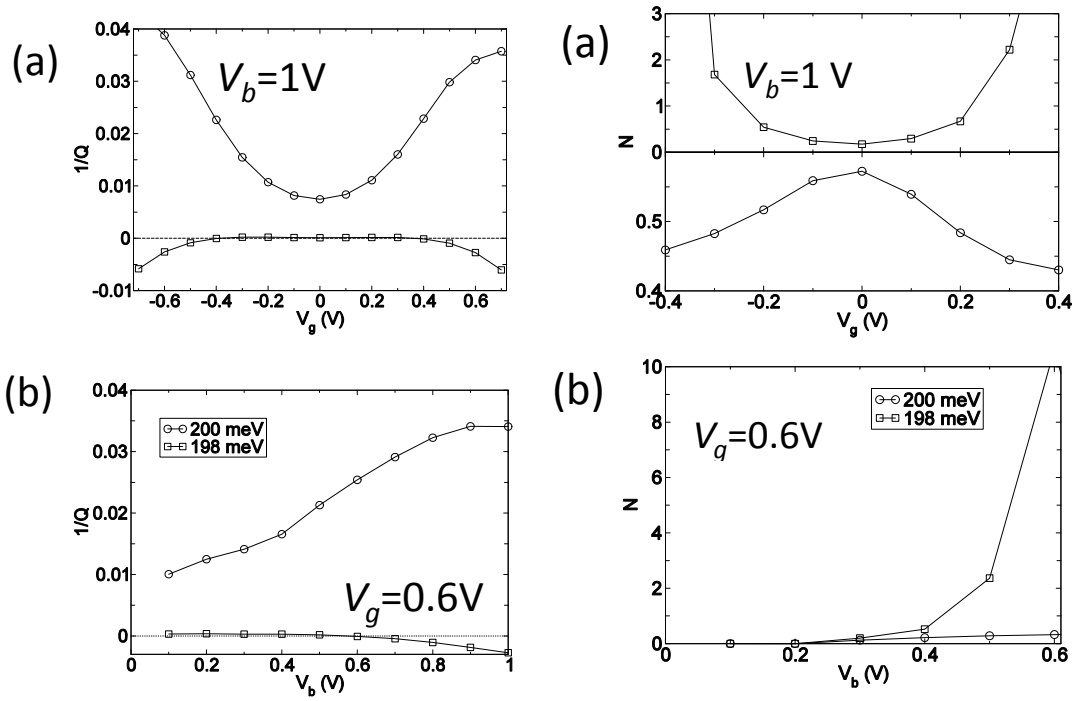

Figure 6.3: *Harmonic stability analysis of the carbon chain system. Left: (a) Inverse Q-factor* $(1/Q)$ *as a function of gate voltage,* V_g*, at* $V_b = 1\,V$ *for the two modes around* $200\ meV$*. (b)* $1/Q$ *as a function of bias voltage,* V_b*, at fixed gate voltage* $V_g = 0.6\,V$*, for the same pair of phonon modes. Right: (a) Effective phonon number (*N*) for the two phonon modes around* $200meV$ *as a function of gate voltage,* V_g*, at fixed bias voltage,* $V_b = 1\,V$*. (b)* N *as a function of bias voltage,* V_b*, at fixed gate voltage* $V_g = 0.6\,V$*. Note that it diverges at the critical point when the damping (1/Q) goes to zero. From Paper II.*

To go beyond the WBA, we perform an eigenexpansion of the retarded Green's function and the spectral density functions. The idea is twofold. Once we have developed a tool for calculating the effective electron-hole pair density of states within this space we can try to reduce the number of eigenstates to include. We will show that mainly the ones with energy around the bias window will contribute. Furthermore, this method will enable us to go beyond the WBA, which as mentioned is needed to perform a more quantitative analysis for the GNC. The reason to do an eigenexpansion is that we within the eigenspace of $H+\Sigma_0$ can evaluate the energy integrals in the electron-hole pair DOS analytically. This method will therefore be both fast and more predictive for systems with Lorentzian-like resonances in the spectral function.

6.4.1 Relation between the Λ function and the MAMA integrals

The five principal current-induced forces in eqn. 6.19 and eqn. 6.22 can all be related to a sequence of integrals with a special form. We define a non equilibrium field

$$\mathbf{I}_{kl}^{\alpha,\beta}(\omega,\epsilon_l,\epsilon_h) \equiv \int_{\epsilon_l}^{\epsilon_h} \mathrm{Tr}\left[\mathbf{M}^{\mathrm{k}}\mathbf{A}_\alpha(\epsilon+\omega)\mathbf{M}^{\mathrm{l}}\mathbf{A}_\beta(\epsilon)\right]\frac{\mathrm{d}\epsilon}{4\,\pi^2}\,. \tag{6.37}$$

In terms of this field we can calculate the Λ function, eqn. 6.15, in the following way. For the equilibrium part we obtain:

$$\begin{aligned}
\mathbf{\Lambda}_{0,kl}(\omega) &= \int \frac{d\epsilon}{4\,\pi^2}\mathrm{Tr}\left[\mathbf{M}^{\mathrm{k}}\mathbf{A}(\epsilon+\omega)\mathbf{M}^{\mathrm{l}}\mathbf{A}(\epsilon)\right]\,(\mathrm{n_F}(\epsilon+\omega-\mu_0)-\mathrm{n_F}(\epsilon-\mu_0))\\
&\approx \int_{\mu_0}^{\mu_0-\omega}\frac{d\epsilon}{4\,\pi^2}\mathrm{Tr}\left[\mathbf{M}^{\mathrm{k}}\mathbf{A}(\epsilon+\omega)\mathbf{M}^{\mathrm{l}}\mathbf{A}(\epsilon)\right]\\
&= \mathbf{I}_{kl}^{L,L}(\omega,\mu_0,\mu_0-\omega)+\mathbf{I}_{kl}^{R,R}(\omega,\mu_0,\mu_0-\omega)\\
&+ \mathbf{I}_{kl}^{L,R}(\omega,\mu_0,\mu_0-\omega)+\mathbf{I}_{kl}^{R,L}(\omega,\mu_0,\mu_0-\omega)\,,
\end{aligned} \tag{6.38}$$

where we have neglected the electronic temperature broadening ($T\to 0$).

For the nonequilibrium part we define $\Delta n_F^\alpha(\epsilon)\equiv n_F(\epsilon-\mu_\alpha)-n_F(\epsilon-\mu_0)$ and get:

$$\begin{aligned}
\underset{\mathrm{Re}}{\overset{\mathrm{Im}}{}}\mathbf{\Delta\Lambda}_{kl}(\omega) &= \sum_\alpha\int\frac{d\epsilon}{4\,\pi^2}\underset{\mathrm{Re}}{\overset{\mathrm{Im}}{}}\left(\mathrm{Tr}\left[\mathbf{M}^{\mathrm{k}}\mathbf{A}_\alpha(\epsilon)\mathbf{M}^{\mathrm{l}}\left(\mathbf{A}(\epsilon-\omega)\pm\mathbf{A}(\epsilon+\omega)\right)\right]\right)\,\Delta n_F^\alpha(\epsilon)\\
&= \sum_\alpha\int\frac{d\epsilon}{4\,\pi^2}\underset{\mathrm{Re}}{\overset{\mathrm{Im}}{}}\Big(\mathrm{Tr}\Big[\mathbf{M}^{\mathrm{k}}\mathbf{A}_\alpha(\epsilon+\omega)\mathbf{M}^{\mathrm{l}}\mathbf{A}(\epsilon)\Delta\mathrm{n}_{\mathrm{F}}^\alpha(\epsilon+\omega)\\
&\quad \pm\mathbf{M}^k\mathbf{A}_\alpha(\epsilon-\omega)\mathbf{M}^l\mathbf{A}(\epsilon)\Delta n_F^\alpha(\epsilon-\omega)\Big]\Big)\\
&\approx \underset{\mathrm{Re}}{\overset{\mathrm{Im}}{}}[\mathbf{I}_{kl}^{L,R}(\omega,\mu_0-\omega,\mu_L-\omega)+\mathbf{I}_{kl}^{L,L}(\omega,\mu_0-\omega,\mu_L-\omega)\\
&+ \mathbf{I}_{kl}^{R,R}(\omega,\mu_0-\omega,\mu_R-\omega)+\mathbf{I}_{kl}^{R,L}(\omega,\mu_0-\omega,\mu_R-\omega)\\
&\pm (\mathbf{I}_{kl}^{L,R}(-\omega,\mu_0+\omega,\mu_L+\omega)+\mathbf{I}_{kl}^{L,L}(-\omega,\mu_0+\omega,\mu_L+\omega)\\
&+ \mathbf{I}_{kl}^{R,R}(-\omega,\mu_0+\omega,\mu_R+\omega)+\mathbf{I}_{kl}^{R,L}(-\omega,\mu_0+\omega,\mu_R+\omega))]
\end{aligned} \tag{6.39}$$

Where Im and Re means the real and imaginary part, respectively (with the corresponding sign change in the equation). In the second line the integration variable was changed as $\epsilon\to\epsilon\pm\omega$ in each term, respectively.

For the Hilbert transformed part we define another nonequilibrium field,

$$\mathbf{J}_{kl}^{\alpha}(\omega,\epsilon_l,\epsilon_h) \equiv \int_{\epsilon_l}^{\epsilon_h} \mathrm{Tr}\left[\mathbf{M}^{\mathrm{k}}\mathbf{A}_\alpha(\epsilon+\omega)\mathbf{M}^{\mathrm{l}}\mathrm{Re}\left(\mathbf{G}(\epsilon)\right)\right]\frac{\mathrm{d}\epsilon}{2\,\pi}\,. \tag{6.40}$$

We then have

$$
\begin{aligned}
-\pi\mathcal{H}\{{}^{\mathrm{Im}}_{\mathrm{Re}}\mathbf{\Delta\Lambda}_{kl}\}(\omega) &= \pm\sum_\alpha\int\frac{d\epsilon}{4\,\pi^2}{}^{\mathrm{Im}}_{\mathrm{Re}}\mathrm{Tr}\left[\mathbf{M}^{\mathrm{k}}\mathbf{A}_\alpha(\epsilon)\mathbf{M}^{\mathrm{l}}\mathrm{Re}\left(\mathbf{G}(\epsilon+\omega)\mp\mathbf{G}(\epsilon-\omega)\right)\right]\,\Delta\mathrm{n}_{\mathrm{F}}^{\alpha}(\epsilon)\\
&= \pm\sum_\alpha\int\frac{d\epsilon}{4\,\pi^2}{}^{\mathrm{Im}}_{\mathrm{Re}}\mathrm{Tr}\Big[\mathbf{M}^{\mathrm{k}}\mathbf{A}_\alpha(\epsilon-\omega)\mathbf{M}^{\mathrm{l}}\mathrm{Re}\left(\mathbf{G}(\epsilon)\right)\Delta\mathrm{n}_{\mathrm{F}}^{\alpha}(\epsilon-\omega)\\
&\quad\mp\mathbf{M}^{k}\mathbf{A}_\alpha(\epsilon+\omega)\mathbf{M}^{l}\mathrm{Re}\left(\mathbf{G}(\epsilon)\right)\Delta\mathrm{n}_{\mathrm{F}}^{\alpha}(\epsilon+\omega)\Big]\\
&\approx \pm{}^{\mathrm{Im}}_{\mathrm{Re}}\left(\sum_\alpha\mathbf{J}^{\alpha}_{kl}(-\omega,\mu_0+\omega,\mu_\alpha+\omega)\mp\mathbf{J}^{\alpha}_{kl}(\omega,\mu_0-\omega,\mu_\alpha-\omega)\right)
\end{aligned}
\tag{6.41}
$$

where we in the second line have changed variables $\epsilon\to\epsilon\pm\omega$ in each term, respectively.

From the integrals we can evaluate the full $\Lambda(\omega)=\Lambda_0(\omega)+\Delta\Lambda(\omega)$ and e-ph polarization bubble:

$$
\begin{aligned}
\Pi_e^r(\omega) &= i\pi\mathrm{Re}\Lambda(\omega)-\pi\mathrm{Im}\Lambda(\omega)+\pi\mathcal{H}\{\mathrm{Re}\Lambda(\omega')\}(\omega)+\mathrm{i}\pi\mathcal{H}\{\mathrm{Im}\Lambda(\omega')\}(\omega)\\
&= i\pi\mathrm{Re}\left(\Lambda_0(\omega)+\Delta\Lambda(\omega)\right)-\pi\mathrm{Im}\left(\Lambda_0(\omega)+\Delta\Lambda(\omega)\right)+\pi\mathcal{H}\{\Delta\Lambda\}(\omega)
\end{aligned}
\tag{6.42}
$$

The term from $\mathcal{H}\{\Lambda_0\}$ is giving the dynamical matrix and is handled by itself.

As shown previously the nonequilibrium noise spectral density

$$
S_f(\omega) = -\pi\Lambda(\omega)\coth\left(\frac{\omega}{2k_BT}\right)-\pi\sum_{\alpha,\beta}\Lambda^{\alpha\beta}(\omega)\left[\coth\left(\frac{\omega-(\mu_\alpha-\mu_\beta)}{2k_BT}\right)-\coth(\frac{\omega}{2k_BT}\right)\Big]
\tag{6.43}
$$

includes the change to the friction due to the change in the electronic structure in nonequilibrium conditions and the additional nonequilibrium noise term due to the nonequilibrium friction and Joule heating. This second contribution can be related to the $\mathbf{I}^{\alpha,\beta}$ fields[3] as follows:

$$
\begin{aligned}
\Lambda^{\alpha\beta}(\omega) &\equiv \int\frac{d\epsilon}{4\,\pi^2}\mathrm{Tr}\left[\mathbf{M}^{\mathrm{k}}\mathbf{A}_\alpha(\epsilon+\omega)\mathbf{M}^{\mathrm{l}}\mathbf{A}_\beta(\epsilon)\right]\left[\mathrm{n_F}(\epsilon+\omega-\mu_\alpha)-\mathrm{n_F}(\epsilon-\mu_\beta)\right]\\
&= \int\frac{d\epsilon}{4\,\pi^2}\Big(\mathrm{Tr}\left[\mathbf{M}^{\mathrm{k}}\mathbf{A}_\alpha(\epsilon)\mathbf{M}^{\mathrm{l}}\mathbf{A}_\beta(\epsilon-\omega)\right]\mathrm{n_F}(\epsilon-\mu_\alpha)\\
&\quad-\mathrm{Tr}\left[\mathbf{M}^{\mathrm{k}}\mathbf{A}_\beta(\epsilon)\mathbf{M}^{\mathrm{l}}\mathbf{A}_\alpha(\epsilon+\omega)\right]^*\mathrm{n_F}(\epsilon-\mu_\beta)\Big)
\end{aligned}
\tag{6.44}
$$

where we in the second line have changed $\epsilon\to\epsilon-\omega$ in the term with the first Fermi function and in the second term we use the symmetry relation $\mathrm{Tr}\left[\mathbf{M}^{\mathrm{k}}\mathbf{A}^{\alpha}(\epsilon+\omega)\mathbf{M}^{\mathrm{l}}\mathbf{A}^{\beta}(\epsilon)\right]=\mathrm{Tr}\left[\mathbf{M}^{\mathrm{k}}\mathbf{A}^{\beta}(\epsilon)\mathbf{M}^{\mathrm{l}}\mathbf{A}^{\alpha}(\epsilon+\omega)\right]^*$. By adding and subtracting the equilibrium term we find

$$
\begin{aligned}
\Lambda^{\alpha\beta}(\omega) &= \int\frac{d\epsilon}{4\,\pi^2}\Big(\Big[\mathrm{Tr}\left[\mathbf{M}^{\mathrm{k}}\mathbf{A}_\alpha(\epsilon)\mathbf{M}^{\mathrm{l}}\mathbf{A}_\beta(\epsilon-\omega)\right]\mathrm{n_F}(\epsilon-\mu_0)\\
&\quad-\mathrm{Tr}\left[\mathbf{M}^{\mathrm{k}}\mathbf{A}_\beta(\epsilon)\mathbf{M}^{\mathrm{l}}\mathbf{A}_\alpha(\epsilon+\omega)\right]^*\mathrm{n_F}(\epsilon-\mu_0)\Big]\\
&\quad+\Big[\mathrm{Tr}\left[\mathbf{M}^{\mathrm{k}}\mathbf{A}_\alpha(\epsilon)\mathbf{M}^{\mathrm{l}}\mathbf{A}_\beta(\epsilon-\omega)\right]\Delta\mathrm{n}_{\mathrm{F}}^{\alpha}(\epsilon)-\mathrm{Tr}\left[\mathbf{M}^{\mathrm{k}}\mathbf{A}_\beta(\epsilon)\mathbf{M}^{\mathrm{l}}\mathbf{A}_\alpha(\epsilon+\omega)\right]^*\Delta\mathrm{n}_{\mathrm{F}}^{\beta}(\epsilon)\Big]\Big)\\
&= \int\frac{d\epsilon}{4\,\pi^2}\mathrm{Tr}\left[\mathbf{M}^{\mathrm{k}}\mathbf{A}_\alpha(\epsilon+\omega)\mathbf{M}^{\mathrm{l}}\mathbf{A}_\beta(\epsilon)\right]\left[\mathrm{n_F}(\epsilon+\omega-\mu_0)-\mathrm{n_F}(\epsilon-\mu_0)\right]\\
&\quad+\mathbf{I}^{\alpha,\beta}(\omega,\mu_0-\omega,\mu_\alpha-\omega)-\mathbf{I}^{*\beta,\alpha}(-\omega,\mu_0+\omega,\mu_\beta+\omega)\\
&= \mathbf{I}^{\alpha,\beta}(\omega,\mu_0,\mu_0-\omega)+\mathbf{I}^{\alpha,\beta}(\omega,\mu_0-\omega,\mu_\alpha-\omega)-\mathbf{I}^{*\beta,\alpha}(-\omega,\mu_0+\omega,\mu_\beta+\omega)
\end{aligned}
\tag{6.45}
$$

[3] NB: it is not just a summation of the terms from 6.39 as one maybe would expect. This is because of the mixing between left and right parts used in that expression.

To conclude we have related the different current-induced forces to integrals of the form $\mathbf{I}^{\alpha,\beta}$ and $\mathbf{J}^{\alpha}$ in eqn. 6.37 and eqn. 6.40, respectively.

6.4.2 Eigenexpansion of Green's function and the MAMA integrals

The remaining challenge in calculating the full $\mathbf{\Lambda}$ function is to find a way to evaluate integrals of the form $\mathbf{I}^{\alpha,\beta}_{kl}(\omega,\epsilon_l,\epsilon_h)$ and $\mathbf{J}^{\alpha}_{kl}(\omega,\epsilon_l,\epsilon_h)$ in a fast and efficient way. We do this by an eigenexpansion and by utilizing the matrix nature of the problem. Assuming a constant self-energy, $\mathbf{\Sigma}_0$, and a orthonormal basis set ($S=I$, by applying the Löwdin transformation discussed in Sec. 9.8) we can expand the Green's function as

$$\mathbf{G}_0(\varepsilon) \;=\; [\varepsilon\mathbf{I}-\mathbf{H}_D-\mathbf{\Sigma}_0(\mu_0)]^{-1}=\sum_i \frac{|\psi_i\rangle\,\langle\phi_i|}{\varepsilon-\varepsilon_i}\,, \tag{6.46}$$

where ε_i, $|\psi_i\rangle$ and $\langle\phi_i|$ are the complex eigenvalues, right and left eigenstates of $\mathbf{H}_D-\mathbf{\Sigma}_0$. We then obtain an eigenexpansion in Lorentzians for the spectral function as

$$\mathbf{A}^{\alpha}(\varepsilon) \;=\; \frac{|\psi_i\rangle\langle\tilde{\psi}^{\alpha}_i|}{\varepsilon-\varepsilon_i}+\frac{|\tilde{\psi}^{\alpha}_i\rangle\langle\psi_i|}{\varepsilon-\varepsilon^*_i}\,, \tag{6.47}$$

where we defined

$$\left\langle\tilde{\psi}^{\alpha}_i\right| \;=\; \sum_j \frac{\langle\phi_i|\mathbf{\Gamma}^{\alpha}|\phi_j\rangle}{\varepsilon_i-\varepsilon^*_j}\,\langle\psi_j| \tag{6.48}$$

The coefficients, in eqn. 6.47, were rearranged by using

$$\frac{1}{(\epsilon-\epsilon_i)(\epsilon-\epsilon^*_j)} \;=\; \frac{1}{\epsilon_i-\epsilon^*_j}\frac{(\epsilon-\epsilon^*_j)-(\epsilon-\epsilon_i)}{(\epsilon-\epsilon_i)(\epsilon-\epsilon^*_j)}=\frac{1}{\epsilon_i-\epsilon^*_j}\left(\frac{1}{\epsilon-\epsilon_i}-\frac{1}{\epsilon-\epsilon^*_j}\right). \tag{6.49}$$

The spectral function hereby retains some energy dependence, when assuming a constant self-energy, in contrast to the WBA were one assume a constant spectral function. We expect this procedure to work quite well for the Lorentzian-like resonance of the GNC as long as only a single peak lies within the bias window. Otherwise the assumption of a nearly constant self-energy will break down. How well the assumption works can be tested by comparison of the transmission function with the full and constant self-energy, see Fig. 6.4. The figure shows that the transmission is approximated well by the constant self-energy assumption in a large energy region around the resonances. This holds true even at high bias. Inserting the expansion in the interaction integral, eqn. 6.37, we get

$$\begin{aligned}
&\mathbf{I}^{\alpha,\beta}_{kl}(\omega,\epsilon_l,\epsilon_h)\equiv\int_{\epsilon_l}^{\epsilon_h}\mathrm{Tr}\left[\mathbf{M}^{\mathrm{k}}\mathbf{A}_{\alpha}(\epsilon+\omega)\mathbf{M}^{\mathrm{l}}\mathbf{A}_{\beta}(\epsilon)\right]\frac{\mathrm{d}\epsilon}{4\,\pi^2}\\
&=\frac{1}{4\,\pi^2}\sum_{i,j}\Big(\langle\tilde{\psi}^{\beta}_j|\mathbf{M}^k|\psi_i\rangle\langle\tilde{\psi}^{\alpha}_i|\mathbf{M}^l|\psi_j\rangle C_{1,ij}+\langle\psi_j|\mathbf{M}^k|\psi_i\rangle\langle\tilde{\psi}^{\alpha}_i|\mathbf{M}^l|\tilde{\psi}^{\beta}_j\rangle C_{2,ij}\Big)\\
&+\langle\tilde{\psi}^{\beta}_j|\mathbf{M}^k|\tilde{\psi}^{\alpha}_i\rangle\langle\psi_i|\mathbf{M}^l|\psi_j\rangle C^*_{2,ij}+\langle\psi_j|\mathbf{M}^k|\tilde{\psi}^{\alpha}_i\rangle\langle\psi_i|\mathbf{M}^l|\tilde{\psi}^{\beta}_j\rangle C^*_{1,ij}\Big)\,,
\end{aligned} \tag{6.50}$$

where the coefficients are obtained from the energy integrals over the inverse energy factors[4]:

$$\begin{aligned}
C_{1,ij} &\equiv \ln\left[\frac{(\varepsilon_{\mathrm{h}}+\omega-\varepsilon_{\mathrm{i}})(\varepsilon_{\mathrm{l}}-\varepsilon_{\mathrm{j}})}{(\varepsilon_{\mathrm{l}}+\omega-\varepsilon_{\mathrm{i}})(\varepsilon_{\mathrm{h}}-\varepsilon_{\mathrm{j}})}\right]\frac{1}{\varepsilon_{\mathrm{i}}-\varepsilon_{\mathrm{j}}-\omega}\\
C_{2,ij} &\equiv \left(\ln\left[\frac{\varepsilon_{\mathrm{h}}+\omega-\varepsilon_{\mathrm{i}}}{\varepsilon_{\mathrm{l}}+\omega-\varepsilon_{\mathrm{i}}}\right]\ln\left[\frac{\varepsilon_{\mathrm{l}}-\varepsilon_{\mathrm{j}}}{\varepsilon_{\mathrm{h}}-\varepsilon_{\mathrm{j}}}\right]^*\right)\frac{1}{\varepsilon_i-\varepsilon^*_j-\omega}
\end{aligned} \tag{6.51}$$

[4]It is here important to express the coefficients in a way that one obtain the retarded response. E.g. with complex part continuously in the same half-plane.

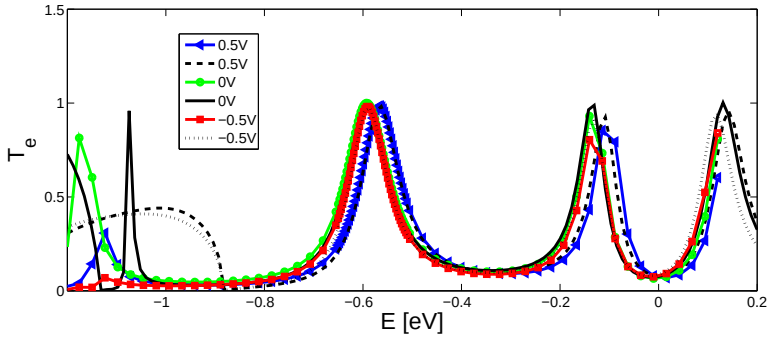

Figure 6.4: *Constant self-energy approximation. We compare the true transmission calculation (lines) with that of a constant self-energy evaluated at* $\mu_0 = -0.58\,eV$ *(lines with points).*

For the second interaction integral, eqn. 6.40, we insert the expansion of the spectral function and $\mathrm{Re}(\mathrm{G}_0^{\mathrm{r}}(\epsilon)) = 1/2\sum_{\mathrm{i}}\left(\frac{|\psi_{\mathrm{i}}\rangle\langle\phi_{\mathrm{i}}|}{\epsilon-\epsilon_{\mathrm{i}}} + \frac{|\psi_{\mathrm{i}}^*\rangle\langle\phi_{\mathrm{i}}^*|}{\epsilon-\epsilon_{\mathrm{i}}^*}\right)$ to get

$$\begin{aligned}
\mathbf{J}_{kl}^{\alpha}(\omega,\epsilon_l,\epsilon_h) &\equiv \int_{\epsilon_l}^{\epsilon_h} \mathrm{Tr}\left[\mathbf{M}^{\mathrm{k}}\mathbf{A}_{\alpha}(\epsilon+\omega)\mathbf{M}^{\mathrm{l}}\mathrm{Re}\left(\mathbf{G}(\epsilon)\right)\right]\frac{\mathrm{d}\epsilon}{2\,\pi} \\
&= \frac{1}{4\,\pi}\sum_{i,j}\Big(\langle\phi_j|\mathbf{M}^k|\psi_i\rangle\langle\tilde{\psi}_i^{\alpha}|\mathbf{M}^l|\psi_j\rangle C_{1,ij} + \langle\phi_j^*|\mathbf{M}^k|\psi_i\rangle\langle\tilde{\psi}_i^{\alpha}|\mathbf{M}^l|\psi_j^*\rangle C_{2,ij}\Big) \\
&+\langle\phi_j|\mathbf{M}^k|\tilde{\psi}_i^{\alpha}\rangle\langle\psi_i|\mathbf{M}^l|\psi_j\rangle C_{2,ij}^* + \langle\phi_j^*|\mathbf{M}^k|\tilde{\psi}_i^{\alpha}\rangle\langle\psi_i|\mathbf{M}^l|\psi_j^*\rangle C_{1,ij}^*\Big)\,. \qquad (6.52)
\end{aligned}$$

We notice that each factor, in eqn. 6.50 and eqn. 6.52, can be rearranged to a matrix with dimensions given by the collective index describing the orbitals (i,j) and the degrees of freedom (k,l). This allows for an efficient evaluation by matrix products for all degrees of freedoms in one calculation.

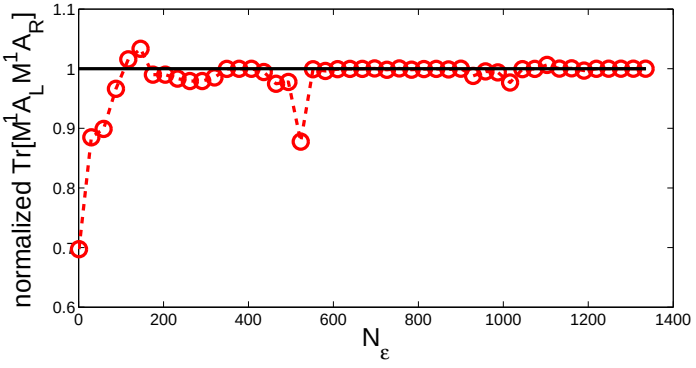

Figure 6.5: *Convergence with the number of included eigenvalues in the calculation of* $\mathrm{Tr}\left[\mathrm{M}^1\mathrm{A}_{\mathrm{L}}(\epsilon_0)\mathrm{M}^1\mathrm{A}_{\mathrm{R}}(\epsilon_0)\right]$ *for the first mode of the graphene constriction. Here* $\mu_0 = -0.58eV$ *corresponding to the second transmission peak. The full-line indicates the exact result obtained by a matrix multiplication of the full matrices.*

Fig. 6.5 compares the result of the spectral expansion formalism, with an increasing number of included eigenvalues, with that of a direct calculation for the energy independent interaction kernel. The spectral expansion result converge fast with number

of included eigenvalues sorted away from μ_0, but a smooth convergence is not guaranteed. In principle one can increase the number of included eigenvalues to get the exact result at the chosen chemical potential. The spectral expansion goes beyond the WBA since it extends to an energy dependent interaction kernel and includes the finite phonon frequency in the formalism.

6.5 Current-induced instabilities in nanoconstrictions

We now apply the developed spectral expansion method to a quite generic nanoconstriction, formed in graphene, conducting an electronic current. Many of the results are published in paper VI. We investigate the current-induced phonon excitation in the system using DFT calculations taking full account of the nonequilibrium and coupling to electrodes. The GNC has a significant greater number of optical modes interacting with the current as compared to the carbon chain system. Several runaway modes exist when applying a bias voltage higher than 0.4 V and we will mainly concentrate on the one ignited at lowest bias voltage. Our results show how the nonlinear heating effects and instabilities appear for systems with electronic resonances that cannot be quantitatively described by the WBA.

6.5.1 Origin of the resonances and potential drop

The GNC is illustrated in Fig. 6.6A. The current density is locally very high and we only include e-ph interaction in the narrow part. Fig. 6.6B shows how the electron transmission of the GNC has two resonance peaks originating from states presenting localized current along the edges(1st peak) and through the center(2nd peak) of the ribbon, respectively. Resonances occur due to the diffraction barrier at abrupt interfaces in graphene[43, 82]. In terms of the corresponding band structure of the infinite nanoribbon there will not be infinitely many states. Instead a discretized number of states exist due to quantum confinement between the edges. The resonances were shown to occur at the 'particle in a box' wavelengths/energies from the requirement that $\sin(k_z L + \tilde{\phi}) = 0$. Here L is the length of the ribbon and $\tilde{\phi}$ is the phase obtained by reflection at one interface[43, 199]. A detailed study of the geometry will not be presented here. However, we mention that by increasing the length one obtains a larger number of narrow resonances. Increasing the neck width reduces the interface resistance and the transmission eventually approaches that of graphene. The nonadiabatic transport across a constriction resembles that of a molecule and the coupling between motion and current is amplified by the local nature of both phonon and electron modes, increasing the time to interact.

To visualize the localized voltage drop we define a 2D and 1D potential as

$$\begin{aligned} \Delta V(x,z) &= \frac{1}{L_y}\int_0^{L_y} \left(V(x,y,z;eV_a) - V(x,y,z;0)\right) , \\ \Delta V(z) &= \frac{1}{L_x L_y}\int_0^{L_x}\int_0^{L_y} \left(V(x,y,z;eV_a) - V(x,y,z;0)\right) , \end{aligned}$$

where we integrate over the region of nonzero density for all applied bias voltages. The potential will be varying linearly along the transport direction far away from the device, where no screening takes place. Fig. 6.7 shows the 1D potential across the constriction at different bias voltages. The voltage drop takes place exclusively at the constriction region even at high bias voltage. The 2D localized voltage drop at 0.5 V and high current across

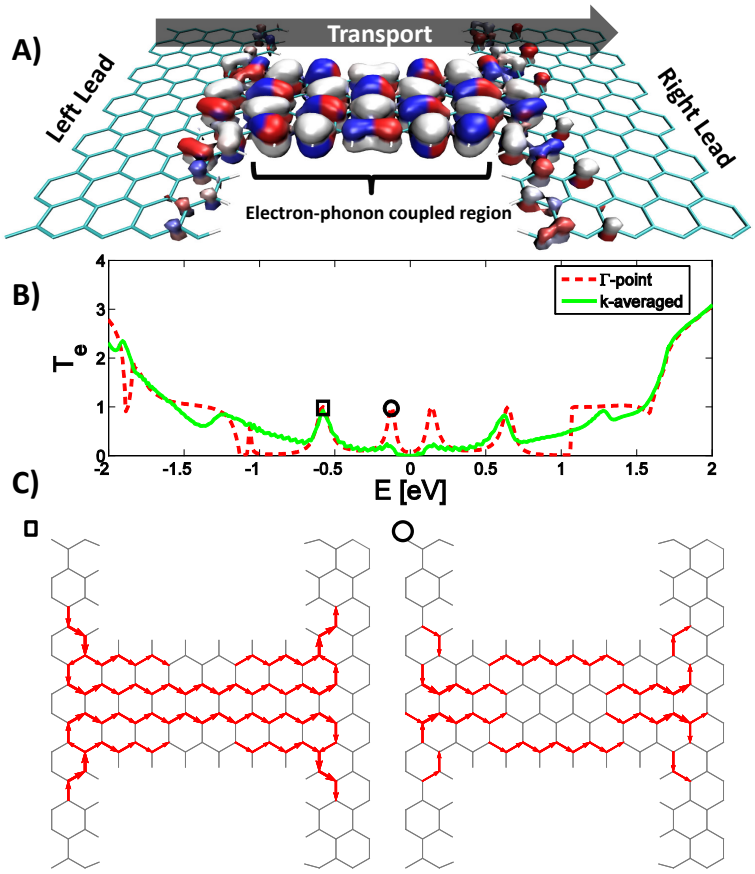

Figure 6.6: *A) Transport setup illustrating the hydrogen passivated GNC between two semi-infinite graphene leads. The left eigenchannel at zero bias and* $E \approx -0.58eV$ *(colored according to phase, red-white-blue from* $-\pi$ *to* π*). B)* Γ*-point and the k-averaged transmission function (*$E = 0$ *corresponds to the Dirac point). C) Bond-currents at the two peaks (*Γ*) marked in the transmission plot (*$E \approx -0.12eV$ *and* $E \approx -0.58eV$*). From Paper VI.*

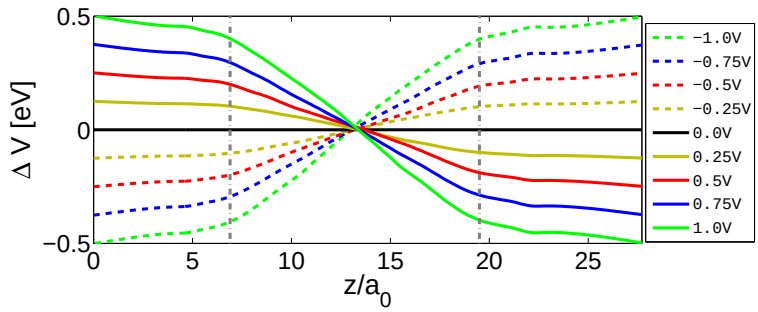

Figure 6.7: *Real space voltage drop along the device averaged over the two transverse directions. The dashed vertical lines indicate the interface between graphene leads and the ribbon.*

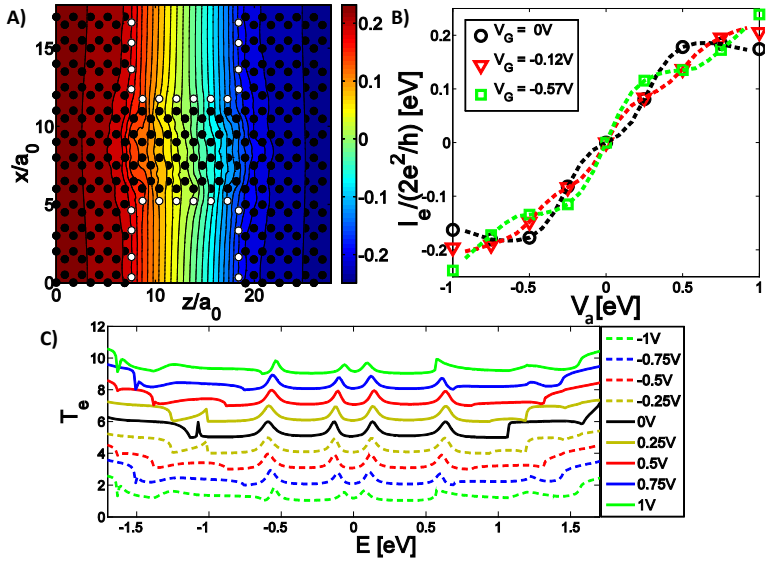

Figure 6.8: *Finite bias transport across the GNC. A) Real space potential drop ($V_a = 0.5\,eV$) integrated along the out of plane direction. B) IV-characteristics for the GNC gated to different chemical potential. Gating to a peak lowers the resistance at low V_a. C) Transmission curves (shifted vertically) for different applied bias ($E_F = 0$). From Paper VI.*

the GNC is shown in Fig. 6.8A,B. By employing a gate voltage(V_g) we may tune E_F to a highly conducting peak and consider the phonon excitation close to the resonance. We will focus on the constriction gated to the 2nd peak which is mostly unaffected by the boundary conditions in the electrodes(k-point sampling)[27], and which energy position exhibits little dependence on the applied bias (V_a), cf. Fig. 6.8C.

6.5.2 Modelling the phonon bath

The calculation of phonon modes and electron-phonon coupling inside the constriction was performed at zero bias. When the voltage drop is localized over a few atomic bonds or a tunnel barrier, the voltage dependence of the electron-phonon coupling could play an important role[182]. In our case the voltage drop is locally small since it is spread over the entire constriction region. Therefore, we neglect the additional correction in phonon frequencies due to the potential drop when performing the initial finite difference evaluation of the force constants. This would be a minor, computational expensive, addition to the model as compared to the additional forces due to the electronic current.

We elaborate on the definition of the phonon self-energy of the open system. The k-averaged phonon transmission is defined as

$$\mathcal{T}_{ph}(\omega) \;=\; \frac{1}{N_k}\sum_{i=1}^{N_k} \mathrm{Tr}\left[\mathbf{D}^r(\omega,k_i)\mathbf{\Gamma}_R(\omega,k_i)\mathbf{D}^a(\omega,k_i)\mathbf{\Gamma}_L(\omega,k_i)\right]. \tag{6.53}$$

where $\mathbf{\Gamma}_{L,R} = i[\mathbf{\Pi}^r_{L,R} - \mathbf{\Pi}^a_{L,R}]$ gives the coupling to the electrodes and N_k is the number of sampled k-points. This corresponds to a sequence of constrictions repeated in the transverse direction, resembling a line of holes akin to a single line of antidots[69]. We want to address the damping of a single constriction connected to graphene leads. Therefore, we propagate the self-energy to the device region. In this region we construct

a k-averaged/real-space self-energy describing the damping of a single constriction connected to infinite graphene leads[207]. In Fig. 6.9 we compare the transmission between

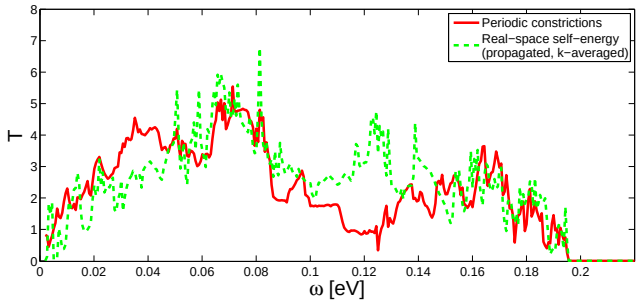

Figure 6.9: *Phonon transmission across the graphene nanoconstriction. We compare two different phonon baths: The one from periodic boundary conditions in the transverse direction and that from a real-space self-energy resembling the graphene nanoconstriction. The real-space phonon self-energy was obtained by propagating to the constriction part and performing the k-averaging. In both transmission calculations 43 transverse k-points were used.*

these two different setups. It is clear from the figure that the transmission and phonon damping to some extend is different for the two different configurations.

6.5.3 Harmonic stability analysis

From the SCLE we can obtain the nonequilibrium retarded phonon Green's function,

$$D^r(\omega) = (D^a(\omega))^\dagger = \left[(\omega + i\eta)^2 - K - \Pi^r(\omega)\right]^{-1} . \tag{6.54}$$

The phonon DOS is given by $-2/\pi\omega \mathrm{Im}\left(D^r(\omega)\right)$ and is illustrated in Fig. 6.10A. The DOS is affected both by the coupling to electrons, in particular giving rise to nonequilibrium forces, as well as coupling to the electrode phonons. We show the phonon DOS at an applied bias of $V_a = 0$ and $V_a = 0.5$V. Most importantly, the DOS becomes negative at a particular phonon frequency ($\omega \approx 170$meV), corresponding to a negatively damped mode. This runaway mode will have a negative life-time.

From the Langevin equation the position correlation function is directly related to the noise correlation kernel through the phonon Green's function. We can use this to calculate the excitation in terms of the average kinetic energy of the phonons,

$$\langle \dot{u}\dot{u}^* \rangle (\omega) = \int_{-\infty}^{\infty} \frac{d\omega}{2\pi} \omega^2 \mathrm{Tr}\left[D^r(\omega) S_f(\omega) D^a(\omega)\right] . \tag{6.55}$$

We define the local heating as the change in this energy compared to the zero bias result. Fig. 6.10B shows how the runaway gives rise to a divergence in the current-induced heating of the GNC at $V_a \approx 0.4$V. This again signifies an instability and the high excitation is likely to lead to dramatic effects such as contact disruption. We highlight several things with respect to the heating. First of all comparing the dashed line (Joule heating only) and the full line shows that the deterministic forces significantly increases the heating even before the very nonlinear instability kicks in. Additionally, we find that the main reason of the instability lies in the bias dependent electronic friction. However, by comparing the full line with the dotted, we see that the nonconservative (NC) and

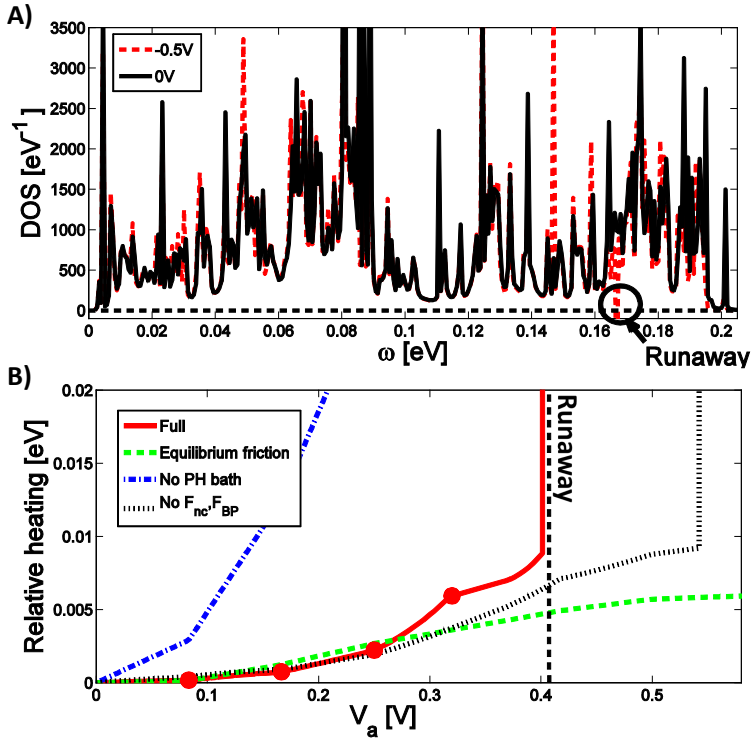

Figure 6.10: *Harmonic stability analysis of the GNC. A) Dashed(full) lines show the phonon density of states (DOS) of the GNC with(without) electronic current. A unstable "runaway" mode appears for an applied bias of $V_a \approx \pm 0.4\,V$ as a negative DOS peak. B) Heating (change in average kinetic energy per atom due to current) of the GNC at $300\,K$. Full line: Result incl. all current-induced forces. Dashed line: only fluctuating force (Joule heating) and zero-bias electronic friction. Dot-dashed line: The wide-band approximation(WBA) without coupling to the electrode phonon bath. Dotted line: Full calculation neglecting the wind and Berry-phase forces. From Paper VI.*

Berry-phase (PB) forces reduce the threshold voltage for the runaway mechanism. The heating resulting from the diagonal WBA calculation without phonon baths (dot-dashed line) vastly exaggerates the local heating of the nanoconstriction in the high bias limit. The main reason is that (1) the phonon damping is important and (2) the system is gated to a resonance, where the WBA assumes a constant electronic structure within the bias window. If one neglects the damping due to the phonon baths in the full calculation we find that the threshold for the runaway instability is reduced to 0.15 V.

In the general case of frequency dependent self-energies one obtains a nonlinear eigenvalue problem for the phonon modes. We can analyze the origin of the runaway in detail by linearizing the EVP near the runaway frequency. We define a set of nonequilibrium modes as the eigenvectors of $K + \Pi^r(\omega_0)$. From the complex eigenvalues of this matrix we can again define $1/Q = -2\frac{\mathrm{Im}(\omega)}{\mathrm{Re}(\omega)} = 1/Q_{\mathrm{ph}} + 1/Q_{\mathrm{el}}(V_a)$.

We start by showing that it is important to include the voltage drop in the electronic structure. Fig.6.11 shows a test calculation where the zero-bias electronic structure was

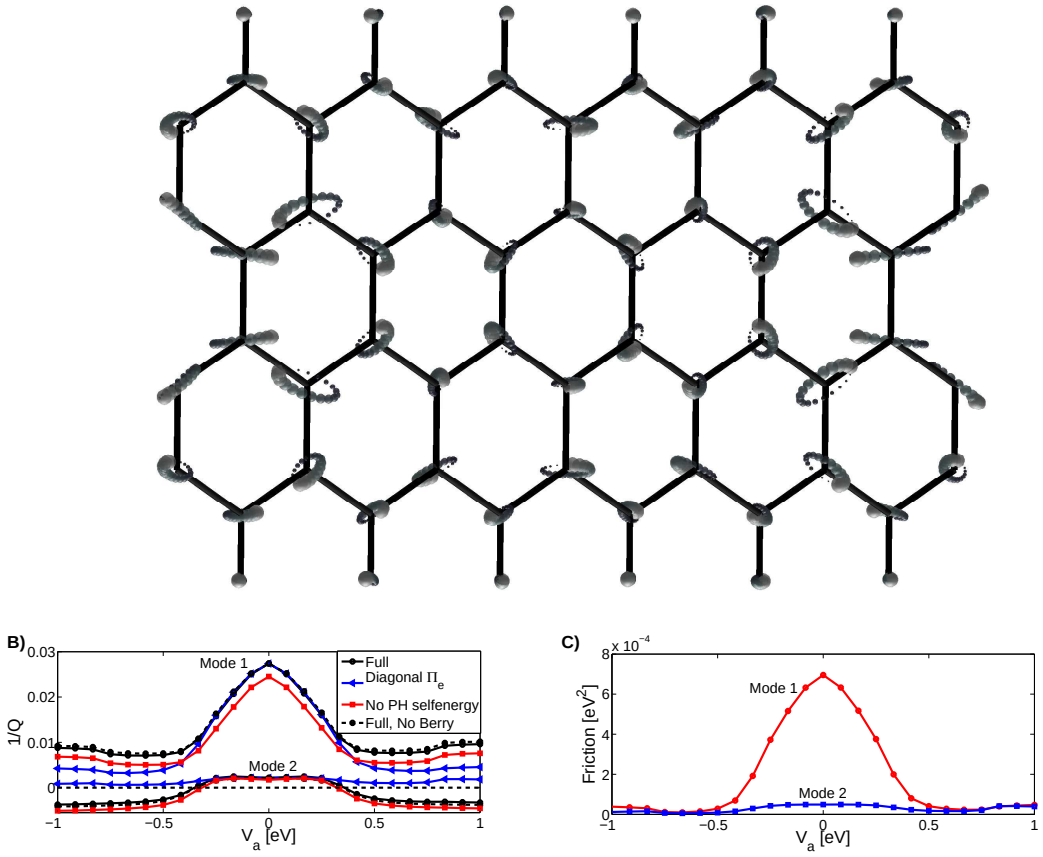

Figure 6.11: *Harmonic stability analysis of the GNC from the zero bias electronic structure. (A) Motion of the runaway mode at $V_a = 0.5$ V. We depict the motion using a number of discrete time steps roughly corresponding to a full oscillation period. The position of each atom is depicted as a sphere for a sequence of time steps indicated by an increasing radius with time. (B) $1/Q$ as a function of bias voltage, V_a, at fixed gate voltage $V_g = -0.58$ V. (C) Electronic friction as a function of bias voltage, V_a, at fixed gate voltage $V_g = -0.58$ V.*

used in the stability analysis. In contrast to the finite bias case, the runaway kicks in

due to the coupling between the IETS mode and the finite bias runaway mode. The zero bias calculation therefore predicts a waterwheel mode, Fig.6.11A. We do not find the negative friction from the zero bias calculation (Fig.6.11C) and the $1/Q$ remains positive if one use the diagonal approximation, that neglects the NC and BP forces, Fig.6.11B. We conclude that one cannot neglect the finite bias electronic structure. This simplified calculation does not include the dominating negative damping mechanism, even though other instabilities can still be found. Fig. 6.12 illustrates that the NC and BP forces

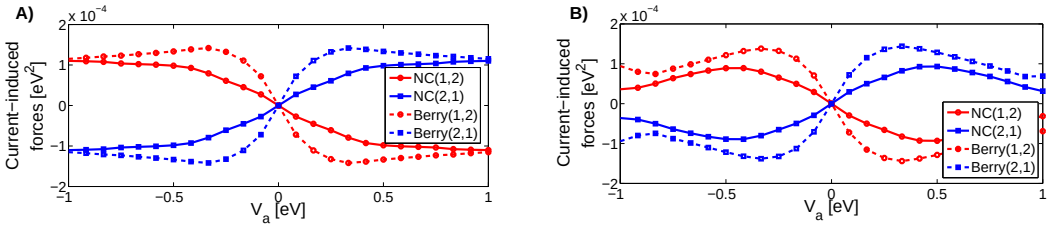

Figure 6.12: *NC and BP forces between the IETS and runaway mode in the case of zero bias electronic structure (A) and the finite bias electronic structure (B).*

are still large if the finite bias electronic structure is taken into account. However, the friction mechanism is simply dominating and the main effect of the NC and BP forces is to support the phenomena and reduce the threshold voltage.

The two main modes are displayed in Fig. 6.13. The "IETS-mode" exhibits the largest inelastic tunnel spectroscopy signal(IETS) in the electronic current and largest noise $S_{f,ii}(\omega_i)$, while the "runaway mode" is the first mode that turns unstable with increasing V_a. The $1/Q$-factor can become negative (amplifying) for a single mode due

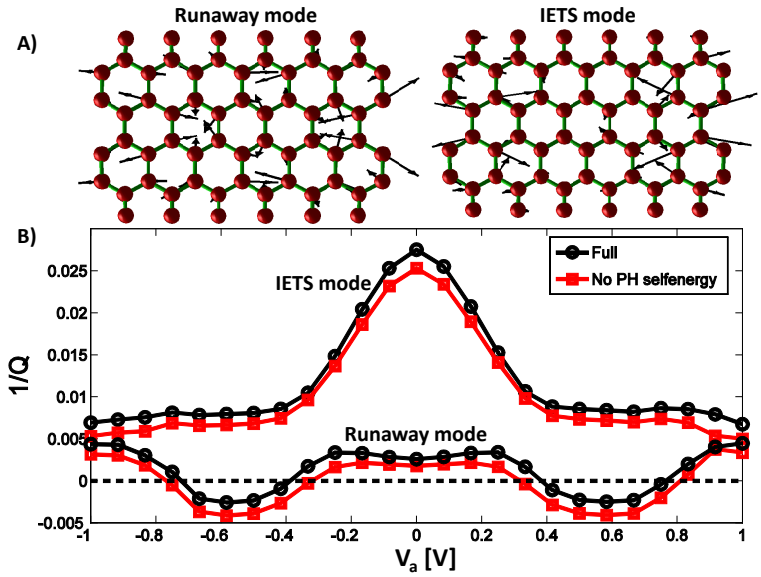

Figure 6.13: *A) Two degenerate modes ("runaway"/"IETS") at $V_a = 0.4V$ with $\omega_0 \approx 170meV$. The "runaway" mode break the left-right symmetry due to the coupling to the non-equilibrium electrons and becomes unstable at finite bias. The "IETS" mode yields the largest inelastic signal in the current. B) Inverse Q-factor (loss) as a function of bias for the modes. From Paper VI.*

to a current-induced negative friction. This shows that the potential drop is essential in the description of the current-induced forces. The friction mechanism only involves a single mode with increasing amplitude instead of the waterwheel motion due to the NC force. We will now analyze the origin of the negative friction mechanism in detail.

6.5.4 A and B coefficients

The negative friction can be expressed in terms of phonon absorption(emission) processes. We will now derive the Einstein rates for these processes. The occupation N of a single vibrational state coupled to an electron gas satisfy the semi-classical master equation

$$\dot{N} = \mathcal{B}(N+1) - \mathcal{A}N, \tag{6.56}$$

where the Einstein $\mathcal{A}$ and $\mathcal{B}$ coefficients describe the rates of absorption and emission of a vibration, respectively. In steady state $\dot{N}$ is zero, and the steady state occupation is

$$N_{ss} = \frac{1}{\mathcal{A}/\mathcal{B} - 1}. \tag{6.57}$$

From Fermi's golden rule (FGR) we can express the $\mathcal{A}$ and $\mathcal{B}$ coefficients as:

$$\mathcal{A} = \frac{2\pi}{\hbar} \sum_{if,\alpha\beta} |\langle f\beta|\hat{M}|i\alpha\rangle|^2 n_F^\alpha(\epsilon_i) \left(1 - n_F^\beta(\epsilon_f)\right) \delta(\epsilon_i - \epsilon_f + \hbar\omega), \tag{6.58}$$

and

$$\mathcal{B} = \frac{2\pi}{\hbar} \sum_{if,\alpha\beta} |\langle f\beta|\hat{M}|i\alpha\rangle|^2 n_F^\alpha(\epsilon_i) \left(1 - n_F^\beta(\epsilon_f)\right) \delta(\epsilon_i - \epsilon_f - \hbar\omega). \tag{6.59}$$

The α and β indices denotes leads, so e.g. a state $|i\alpha\rangle$ is a scattering state originating from lead α. Expressed in an orthonormal (tight binding) basis $\sum_n |n\rangle\langle n| = 1$ we rewrite the $\mathcal{A}$ as

$$\begin{aligned}\mathcal{A} = \frac{2\pi}{\hbar} \sum_{nmkl,\alpha\beta} \langle f\beta|n\rangle M_{nm} \langle m| \left(\int d\epsilon \sum_i |i\alpha\rangle\langle i\alpha|\delta(\epsilon - \epsilon_i) \right) |k\rangle \\ \times M_{kl} \langle l|f\beta\rangle n_F^\alpha(\epsilon) \left(1 - n_F^\beta(\epsilon + \hbar\omega)\right) \delta(\epsilon - \epsilon_f + \hbar\omega),\end{aligned} \tag{6.60}$$

here we used the properties of the Dirac-delta function to isolate the spectral function expanded in the scattering states $A_\alpha(\epsilon) = \sum_i |i\alpha\rangle\langle i\alpha|\delta(\epsilon - \epsilon_i)$. Hereby we have

$$\mathcal{A} = \frac{2\pi}{\hbar} \int d\epsilon \sum_{\alpha\beta} \mathrm{Tr}\left[\mathrm{MA}_\alpha(\epsilon)\mathrm{MA}_\beta(\epsilon + \hbar\omega)\right] \mathrm{n}_\mathrm{F}^\alpha(\epsilon) \left(1 - \mathrm{n}_\mathrm{F}^\beta(\epsilon + \hbar\omega)\right). \tag{6.61}$$

Using the standard formulas

$$n_F(\epsilon)(1 - n_F(\epsilon')) = n_B(\epsilon - \epsilon') \left(n_F(\epsilon') - n_F(\epsilon)\right), \qquad n_B(-\hbar\omega) = -(1 + n_B(\hbar\omega)), \tag{6.62}$$

we find that

$$\begin{aligned}\mathcal{A} &= \frac{2\pi}{\hbar} \int d\epsilon \sum_{\alpha\beta} \mathrm{Tr}\left[\mathrm{MA}_\alpha(\epsilon)\mathrm{MA}_\beta(\epsilon + \hbar\omega)\right] \left(1 + \mathrm{n}_\mathrm{B}(\hbar\omega + \mu_\alpha - \mu_\beta)\right) \left(\mathrm{n}_\mathrm{F}^\alpha(\epsilon) - \mathrm{n}_\mathrm{F}^\beta(\epsilon + \hbar\omega)\right) \\ &= 2\pi \sum_{\alpha\beta} \left(1 + n_B(\hbar\omega + \mu_\alpha - \mu_\beta)\right) \Lambda^{\alpha\beta}(-\omega).\end{aligned} \tag{6.63}$$

Since the diagonal elements of $\Lambda^{\alpha\beta}(-\omega) = -\Lambda^{*\beta\alpha}(\omega)$ are real we can rewrite this as

$$\mathcal{A} = -2\pi \sum_{\alpha\beta} \left(1 + n_B(\hbar\omega + \mu_\alpha - \mu_\beta)\right) \Lambda^{\beta\alpha}(\omega)\,. \tag{6.64}$$

A similar calculation for the $\mathcal{B}$ coefficient (a change of $\omega \to -\omega$) gives:

$$\begin{aligned}\mathcal{B} &= \frac{2\pi}{\hbar} \int d\epsilon \sum_{\alpha\beta} \mathrm{Tr}\left[\mathrm{MA}_\alpha(\epsilon)\mathrm{MA}_\beta(\epsilon - \hbar\omega)\right] \mathrm{n_B}(\hbar\omega - \mu_\alpha + \mu_\beta) \left(\mathrm{n_F^\beta}(\epsilon - \hbar\omega) - \mathrm{n_F^\alpha}(\epsilon)\right) \\ &= -2\pi \sum_{\alpha\beta} n_B(\hbar\omega + \mu_\alpha - \mu_\beta)\Lambda^{\beta\alpha}(\omega)\,. \end{aligned} \tag{6.65}$$

In the last expression we exchanged the α and β labeling in the summation for convenience when comparing the coefficients. We obtain the relation $\frac{\mathcal{A}_{eq}}{\mathcal{B}_{eq}} = \frac{1+n_B(\hbar\omega)}{n_B(\hbar\omega)} = e^{\hbar\omega/k_BT}$ in the equilibrium limit where all chemical potentials are equal. This ensures that the equilibrium distribution is given by the Bose-Einstein distribution. In general we find that the friction (or electron-hole pair damping rate) is given by

$$\mathcal{A} - \mathcal{B} = -2\pi \sum_{\alpha\beta} \Lambda^{\alpha\beta}(\omega)\,, \tag{6.66}$$

consistent with the previously derived expression. In the nonequilibrium low temperature limit, $eV_a \equiv \mu_L - \mu_R, \hbar\omega > k_BT$, we can use that $n_B(\hbar\omega + eV_a)$ is zero if $|eV_a| < \hbar\omega$ and -1 if $|eV_a| > \hbar\omega$. The $\mathcal{B}$ coefficient is only nonzero if the bias is sufficient to excite a phonon mode:

$$\mathcal{B} = 2\pi \left(\theta(-eV_a - \hbar\omega)\Lambda^{LR}(\omega) + \theta(eV_a - \hbar\omega)\Lambda^{RL}(\omega)\right) = \begin{cases} 2\pi\Lambda^{LR}(\omega)\,, \text{if } eV_a < -\hbar\omega \\ 0\,, \text{if } |eV_a| < \hbar\omega \\ 2\pi\Lambda^{RL}(\omega)\,, \text{if } eV_a > \hbar\omega \end{cases} \tag{6.67}$$

The $\mathcal{A}$ coefficient always have contributions from quantum fluctuations and contains remaining parts securing relation 6.66:

$$\begin{aligned}\mathcal{A} &= -2\pi \left(\Lambda^{LL}(\omega) + \Lambda^{RR}(\omega) + \theta(-eV_a - \hbar\omega)\Lambda^{RL}(\omega) + \theta(eV_a - \hbar\omega)\Lambda^{LR}(\omega)\right) \\ &= \begin{cases} -2\pi(\Lambda^{RL}(\omega) + \Lambda^{LL}(\omega) + \Lambda^{RR}(\omega))\,, \text{if } eV_a < -\hbar\omega \\ -2\pi(\Lambda^{LR}(\omega) + \Lambda^{RL}(\omega) + \Lambda^{LL}(\omega) + \Lambda^{RR}(\omega))\,, \text{if } |eV_a| < \hbar\omega \\ -2\pi(\Lambda^{LR}(\omega) + \Lambda^{LL}(\omega) + \Lambda^{RR}(\omega))\,, \text{if } eV_a > \hbar\omega \end{cases} \end{aligned} \tag{6.68}$$

6.5.5 Negative friction mechanism

We will now argue that the negative friction originates from an effective population inversion, and this is due to the difference in wavefunction symmetry and interaction matrix elements when absorbing or emitting a phonon. This is in contrast to a population inversion originating from a difference in the DOS at the changed electron energies, cf. Fig. 1.4.

We find that the phonon absorption rate decreases while the emission rate increases as the bias exceeds the mode frequency for the runaway mode, see Fig. 6.14A. The emission is zero ($\mathcal{B} = 0$) for $V_a < \omega_0$. When $|V_a| > 0.4$V emission exceeds absorption, $\mathcal{B} > \mathcal{A}$. The electronic friction, $\mathcal{A} - \mathcal{B}$, becomes negative at this threshold voltage which manifests itself in the $1/Q$-factor variation with bias for the runaway mode.

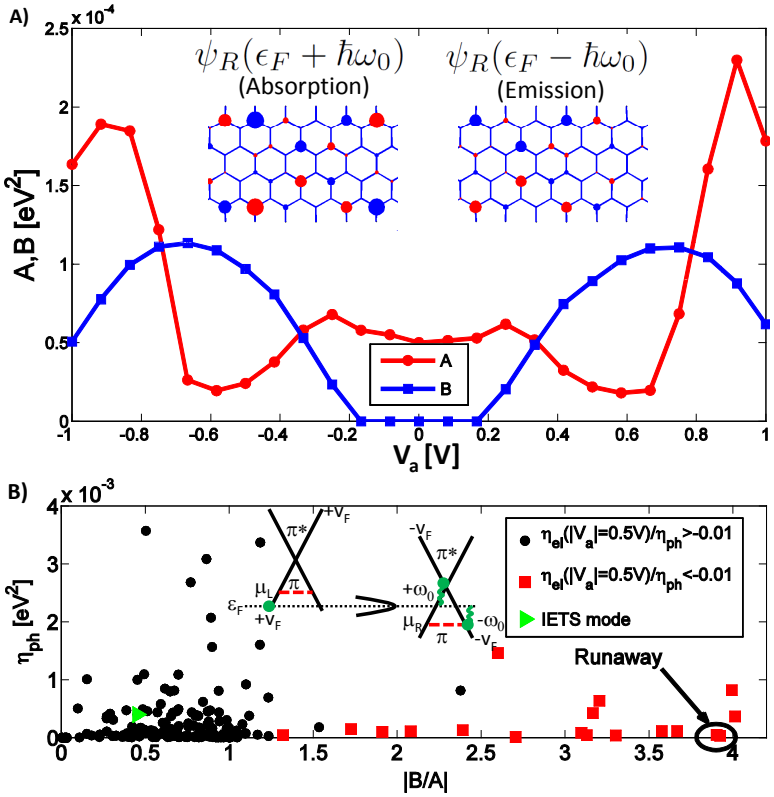

Figure 6.14: *Nonequilibrium friction mechanism. A) Phonon absorption/emission ($\mathcal{A}/\mathcal{B}$) rates for the runaway mode. Insert: At resonance scattering states giving the main contribution to the interaction integrals. The radius shows the absolute value $|\psi(x,y)|$ of the eigenstate, while the color indicates the sign of the real-part. B) Runaway occurs for the mode with the largest emission and lowest phonon friction. Squares indicate modes with a significant electron friction. These modes all have $\mathcal{A}$,$\mathcal{B}$ coefficients with same behavior as the first runaway mode. Insert: Resonance between two graphene leads at a certain filling (red dashed line) and bias voltage. An incoming scattering state (left green dot) at resonance (dashed line) can either absorb ($+\omega_0$) to a state with lower DOS close to the π-π^* crossing or change to a state with higher DOS by emission ($-\omega_0$). From Paper VI.*

It is illustrative to examine how each mode appears in a parameter space of the phonon friction and $\mathcal{B}/\mathcal{A}$, to evaluate if this is a generic behavior, Fig. 6.14B. As expected, the runaway modes show up at high $\mathcal{B}/\mathcal{A}$ and low phonon friction. The negative friction is a generic nonequilibrium effect that is rooted in the high phonon energies that lead to markedly different symmetry of the electronic states involved in emission and absorption. This is illustrated by the red squares all indicating modes with a significant negative electronic friction. These modes all have $\mathcal{A}$ and $\mathcal{B}$ coefficients with the same generic behavior as the first runaway mode.

We will make some additional remarks to elaborate on this conclusion. In the examined bias window one only find one contributing eigenchannel. Therefore, we can make an expansion in this single eigenvector, $\left|v_{L/R}\right\rangle$, and eigenvalue, $a_{L/R}$, of $A_{L/R}$:

$$\begin{aligned}
\mathcal{B} &= -2\pi \sum_{\alpha\beta} n_B(\hbar\omega_0 + \mu_\alpha - \mu_\beta)\Lambda^{\beta\alpha}(\omega_0) \\
&\approx \int_{\mu_R+\hbar\omega_0}^{\mu_L} |\langle v_L(\epsilon)|\mathbf{M}|v_R(\epsilon-\hbar\omega_0)\rangle|^2 a_L(\epsilon)a_R(\epsilon-\hbar\omega_0)\frac{d\epsilon}{4\pi^2} \qquad (6.69) \\
\mathcal{A} &\approx \int_{\mu_R-\hbar\omega_0}^{\mu_L} |\langle v_L(\epsilon)|\mathbf{M}|v_R(\epsilon+\hbar\omega_0)\rangle|^2 a_L(\epsilon)a_R(\epsilon+\hbar\omega_0)\frac{d\epsilon}{4\pi^2} \qquad (6.70)
\end{aligned}$$

Expressed in the single flux-normalized eigenchannel ($|\psi_{L/R}(\epsilon)\rangle \equiv \sqrt{a_{L/R}(\epsilon)/2\pi}|v_{L/R}(\epsilon)\rangle$) , and assuming $k_BT \ll \hbar\omega_0 < eV_a$, we have,

$$\begin{aligned}
\mathcal{B} &\approx \int_{\mu_R+\hbar\omega_0}^{\mu_L} |\langle \psi_L(\epsilon)|\mathbf{M}|\psi_R(\epsilon-\hbar\omega_0)\rangle|^2 \frac{d\epsilon}{2\pi} \\
\mathcal{A} &\approx \int_{\mu_R-\hbar\omega_0}^{\mu_L} |\langle \psi_L(\epsilon)|\mathbf{M}|\psi_R(\epsilon+\hbar\omega_0)\rangle|^2 \frac{d\epsilon}{2\pi}\,, \qquad (6.71)
\end{aligned}$$

where we did not include the intra-electrode terms($\Lambda^{LL/RR}$) in $\mathcal{A}$ since these vary only slightly with V_a for the runaway mode.

For the GNC, the eigenvalues ($a_{L/R}$) are found to be of secondary importance compared to how the wavelength of the eigenstates/scattering states changes with energy at a given bias potential. In the insert of Fig. 6.14A we illustrate how the right eigenchannel changes with energy. One contributes to the absorption and one to the emission. For this system we find that the variation of the eigenchannel with energy is quite large. It is this change in the eigenchannels with energy and bias that determines the overall trend in the emission and absorption. In Fig. 6.15 we plot the integrands of eqn. 6.69 and 6.70. The emission (red) and absorption (blue) integrands are each products of two overlapping peaks. The one closest to the Fermi level originates from the eigenvalues of the spectral function, $a_{L/R}$. These eigenvalues are found to behave similar with bias (contact regime), i.e. they cannot be tuned by the bias voltage independently. The next peak originates from the first factor in the integrand, eqn. 6.69 and 6.70. This factor describes what part of the current that interacts with the phonon. It is this part that determines the total decrease in absorption and increase in emission. Fig. 6.16 gives a supplementary calculation of the $\mathcal{B}/\mathcal{A}$ from the single scattering state. The calculation in the first figure row supports the spectral expansion result. The same result is obtained as for the spectral expansion calculation with the scattering state but now without assuming a constant self-energy or a limited number of eigenvalues. Having reduced the problem to a single scattering state and a single mode allows for a fast evaluation of the integrals were we can easily change the model of the e-ph coupling. The figure illustrates

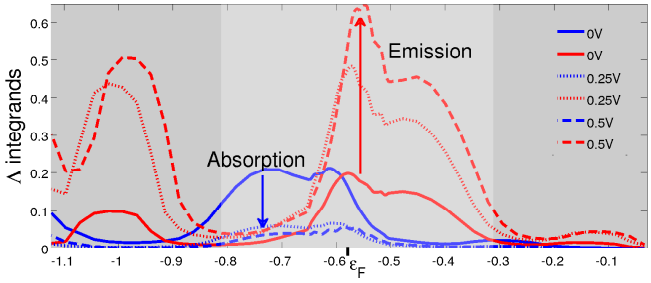

Figure 6.15: *The integrands that integrated over the relevant bias window will give the different contributions to the electron-hole pair interaction. The Fermi energy and a bias window of 0.5V are illustrated.*

that the full interaction matrix elements are needed to account for the phenomena. The eigenvalues cannot alone describe the observed variation. Also if the coupling matrix M is set to unity we do not observe the same limitation of the interlead part of $\mathcal{A}$.

In Fig. 6.17 we consider how the symmetry of the scattering states combines with a selective symmetry of the phonon mode to yield the very low absorption and high emission. Importantly, we note that the symmetry of the scattering state $\psi_L^*(E_F)$ is almost unchanged from going *up* in energy (absorption), see $\psi_R(E_F + \omega_0)$ shown in Fig. 6.17A. On the other hand the symmetry of $\psi_R(E_F - \omega_0)$ differs significantly from this (emission). Thus, in general we can expect that a given phonon will yield very different emission and absorption matrix elements due to the symmetry. The large phonon frequencies and linear DOS of graphene strengthens this symmetry breaking. Acting with the interaction matrix of the runaway mode, $M\psi_R$, is found to invert all signs. Therefore, we find a very large cancellation in the absorption elements for the runaway mode, Fig. 6.17B. This cancellation does not occur for the emission integral. The electronic (mode independent) DOS is not enough to describe the phenomena, but the mechanism is driven by the phase matching between the electron state and phonon modes involved. Selection rules, relating the scattering state symmetry to that of the vibration, dictate which modes that obtain a negative electronic friction.

In the general case where one has a resonance between graphene leads, insert of Fig. 6.14B, the wave incoming at resonance will absorb to an eigenstate close to the Dirac crossing. Hence the state contributing to absorption will have low DOS and a dissimilar phase. On the contrary, emission leads to an eigenstate with larger DOS and similar phase. This holds true for states dominated by the inter-lead contributions. The "IETS" mode on the other hand has a low emission-absorption ratio due to high intra-electrode terms, $\Lambda^{LL/RR}$ and a higher phonon damping.

Our main finding is that a significant fraction of the phonon modes in the GNC obtains a current-induced negative damping (amplification) due to the coupling to the nonequilibrium electrons at finite bias. This signifies an instability of the harmonic approximation, and thus is an important mechanism to include in the description of current-induced atomic-scale structural instabilities observed in graphene nanostructures. We can explain the mechanism by a significant asymmetry between phonon emission and absorption matrix elements around transmission resonances. We believe this is a mechanism applicable to general graphene nanostructures and should spur further investigations.

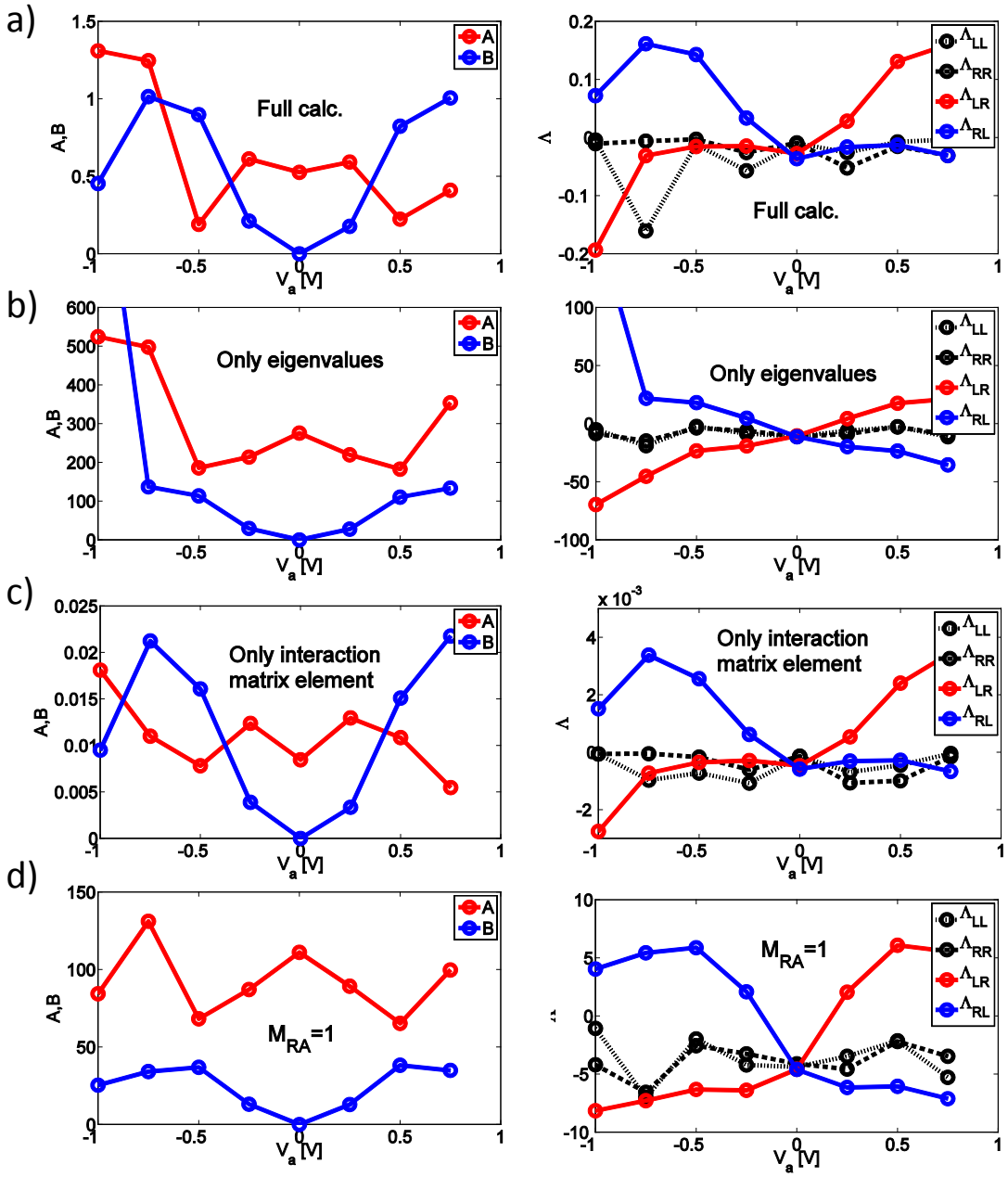

Figure 6.16: *Eigenchannel calculation of the $\mathcal{A}$,$\mathcal{B}$ coefficients for the runaway mode. The negative(positive) Λ elements contribute to $\mathcal{A}(\mathcal{B})$. a) Full calculation to be compared with the spectral expansion result. b) Only the eigenvalues were included - neglecting the interaction matrix element. c) Only the interaction matrix element was included - neglecting the eigenvalues. d) The coupling matrix was set to unity - including both eigenvalues and eigenvectors. In Fig. 6.14 the $\mathcal{A}$,$\mathcal{B}$ coefficients were calculated for the runaway mode. This is a good comparison for a single mode with the full calculation. We obtain the same result in (a) as with the spectral expansion. Besides being a good verification of the different numerical implementations, this method enables further examination of the origin of the variation with bias.*

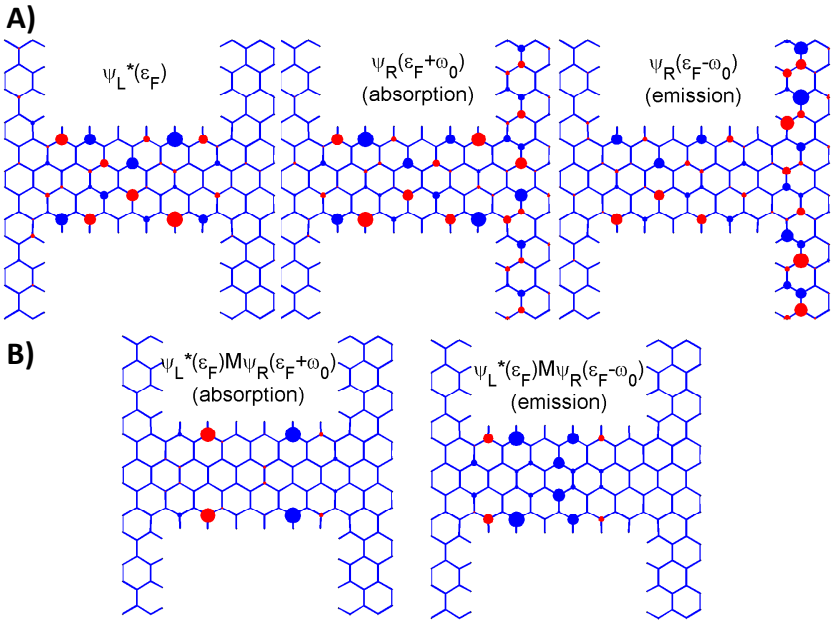

Figure 6.17: *Selection of the symmetry of the scattering state by mode vibration. A) Symmetry of the scattering states contributing to absorption and emission. The resonant scattering state from the left lead couple to the right scattering states shifted by a phonon frequency. We show the absolute magnitude of the scattering states, $|\psi(x,y)|$, (summed over orbitals) as a circle radius at each site and the color indicates the sign of the real-part. B) Real-space interaction elements that gives the total absorption and emission coefficients when summed together. In the absorption coefficient a cancellation takes place that reduces its overall magnitude. This cancellation is not present in case of emission.*

6.6 Summary and discussion

The previous sections illustrated two different current-induced mechanisms that can ignite a runaway phenomena in graphene based nanosystems. The nonconservative wind instabilities and laser-like phonon damping effects contribute significantly to the local heating of the considered examples even at low bias. Furthermore, they constitute a risk for device stability with a large applied bias.

In nonequilibrium there is no constraint on or relation between the absorption and emission. Therefore, we find regions in energy space that allows for a situation where the probability of emitting a phonon exceeds that of absorbing one. This holds true even for a system where the density of states for the left and right scattering states are not independently tunable by the bias. As a result the friction and $1/Q$-factor can turn negative. Two-dimensional systems like graphene make an exciting test-bed for probing such phenomena by gating of the device.

The phenomenon of contact disruption is formally a speculation within the harmonic stability analysis. Beyond the runaway threshold the harmonic approximation breaks down and anharmonic forces kicks in to accommodate the drastic increase in the heating. Whether this will result in contact disruption or another drastic change of geometry will remain unanswered within our harmonic phonon treatment. However, one main conclusion of the analysis of the GNC is that the harmonic instability/runaway is a common phenomenon for nanostructures under high (yet experimentally realistic) bias. Several runaway modes appear in our calculation and as the bias voltage is increased it seems likely that anharmonic effects may not be able to funnel all the heating to the bulk phonon modes and the contact will eventually disrupt. But in order to answer this definitively, it would require additional simulations, i.e. by molecular dynamics (MD). How one can perform such MD simulations in the presence of current is the subject of the next chapter.

Chapter 7

Molecular dynamics in the presence of current

This chapter presents a quantitative MD framework that enables quantum MD simulations in the presence of an electron current. We target dynamics at temperatures where the quantum distribution of the electrode phonons is necessary for graphene nanostructures. A quantum molecular dynamics (QMD) method, that includes the colored (non-Markovian) noise from the phonon baths, was developed by Wang *et al.*[188, 190], who demonstrated its usefulness in applications to graphene nanoribbons.

The idea of MD simulations is to split the ensemble averaging into two parts. One has to perform an initial (analytic) statistical averaging with respect to the bath variables before the MD simulation. This was performed in chapter 6, where the resulting noise spectral density and bath damping kernel was derived. The averaging with respect to the system degrees of freedom is performed from the trajectories from a MD simulation. In this way the device part can be subject to a general nonlinear force-field.

In this chapter, we discuss the QMD methodology and describe how one generates and use a colored noise sequence and the corresponding damping memory kernel. We apply the methodology to obtain the ballistic thermal conductance of a short GAL device. Furthermore, we extend the QMD framework to nonequilibrium simulations. Nonequilibrium QMD simulations could become an invaluable tool for predicting the behavior of current-driven molecular motors[7, 95] and to assess the stability of nanocontacts[108], before testing these designs in real experiments[26]. The strength of MD simulations to include a general nonlinear force-field is important when addressing the behavior of a system near the breakdown of the harmonic approximation. Additionally, we will demonstrate a significant difference in the current-induced heat dissipation between the harmonic and anharmonic simulations. Finally, we will present QMD results for the local heating and current-induced thermal expansion of a GNC.

7.1 QMD methodology

This section describes the methodology of non-Markovian quantum molecular dynamics. The quantum fluctuations cannot be neglected in graphene due to the large phonon frequencies of the optical modes. Classical MD simulations only predict properties correct above the Debye temperature (T_{DB} ≈2100 K[153]) making most transport and dynamical phenomena intrinsically quantum mechanical at standard conditions. Performing a

partial integration of the zero bias damping in the SCLE we obtain

$$\ddot{u}(t) \quad = \quad F_{con} - \int_{t_0}^{t} \mathbf{\Phi}(t-t')\dot{u}(t')dt' + f^{ph}(t)\,. \tag{7.1}$$

The first term gives the conservative force-field (broken into harmonic and nonlinear parts):

$$F_{con} = -\mathbf{K}u(t) + F_{nl}(t) + \sum_{\alpha} \mathbf{V}_{\alpha}^{ph}\mathbf{K}_{\alpha}^{-1}\mathbf{V}_{\alpha}^{ph,\dagger}u(t)\,. \tag{7.2}$$

The last part in eqn. 7.2 gives a renormalization of the local springs by the connection to the phonon baths and is neglected from hereon. The second term in eqn. 7.1 describes the damping force with a memory kernel defined as

$$\mathbf{\Phi}(t-t') = \sum_{\alpha} \int_{-\infty}^{\infty} \frac{d\omega}{2\pi} \frac{\Gamma_{\alpha}(\omega)}{\omega} e^{-i\omega t}\,. \tag{7.3}$$

Finally, the last term in eqn. 7.1 gives the random phonon noise discussed next.

7.1.1 Generating colored noise

We now outline the algorithm for generating colored noise:

1. ***Choose memory cutoff*:**
   The damping kernel, eqn. 7.3, in principle includes the full history of the MD simulation. The algorithm implemented deviates from the formulation by Wang in that we employ a large memory cutoff through a large artificial damping. We include this in a way that does not violate the fluctuation-dissipation theorem. We show below that the ballistic thermal conductance can be obtained correctly by a quite short memory kernel length, n_{cut}.

2. ***Calculate the memory kernel*:**
   We consider N_k positive frequencies and time steps (2 N_k, taking positive and negative time into account). The memory kernel is a matrix for each timestep up to n_{cut}. The damping kernel, including an artificial damping ϵ_a, is

   $$\mathbf{\Phi}(\tau) = \frac{\Delta\omega}{2\pi} \sum_{k=1}^{N_k} \sum_{\alpha=L,R} \left[\frac{\mathbf{\Gamma}_{\alpha}(\omega_k)}{\omega_k - i\epsilon_{ad}} e^{-i\omega_k\tau - \epsilon_{ad}\tau} + c.c. \right], \tag{7.4}$$

   where $\tau = t - t'$ is the relative time so that the frictional damping force includes the memory at time t of a displacement at time t'. We choose a discrete time step Δt for a N_k step long MD simulation (with corresponding $\Delta\omega$ and discrete ω_k in frequency space). To improve convergence and computation-time we include an artificial damping, ϵ_{ad}, to reduce the memory kernel length, n_{cut}.

3. ***Calculating frequency components of the memory kernel*:**
   We calculate a new effective Γ from the memory kernel including the artificial damping (to secure that the fluctuation-dissipation theorem is fulfilled).

   $$\mathbf{\Gamma}_b^{eff}(\omega) = \sum_{i=1}^{n_{cut}} \omega\Delta t \mathbf{\Phi}(\tau_i) e^{i\omega\tau_i} \tag{7.5}$$

4. ***Calculate spectral function*:**
Evaluate the spectral function but from the new effective Γ including the artificial damping.

$$\mathbf{S}_f^{ph}(\omega) \quad = \quad \hbar\left(n_B(\omega)+\frac{1}{2}\right)\mathbf{\Gamma}_b^{eff}(\omega) \tag{7.6}$$

This is the expression used for generating the full colored phonon noise spectrum.

5. ***Generate noise in frequency space and transform to time*:**
A factor of $2N_k dt$ enters in the expression for the covariance matrix from the $\delta(\omega+\omega')$ factor, $\tilde{\mathbf{S}}_f = \mathbf{S}_f 2N_k dt$. From this covariance matrix we can generate the noise for the statistical independent "noise-modes" in several ways.
a) Diagonalization:
Construct the transformation matrix to statistical independent variables $\mathbf{V}_f$ consisting of the eigenvectors of $\tilde{\mathbf{S}}_f$. This has to be done for each frequency component. That is, for each ω solve $\mathbf{V}_f\mathbf{D}_f = \tilde{\mathbf{S}}_f\mathbf{V}_f$ and generate noise and rotate back; $f_k(\omega) = \mathbf{V}_f\sqrt{D_f}\vec{\chi}$, where $\vec{\chi}$ is a vector of random numbers. Calculate the noise vector in each timestep:

$$f(t) = \frac{1}{dt2N_k}\sum_{k=1}^{N_k}\left[f_k(\omega)e^{-i\omega t} + f_k^*(\omega)e^{i\omega t}\right] \tag{7.7}$$

b) Cholesky factorization:
Calculate the real lower triangular factorization matrix $\mathbf{C}$ so that $\mathbf{C}\mathbf{C}^T = \tilde{\mathbf{S}}_f$. We then generate a real time noise sequence as:

$$f(t) = \frac{1}{\sqrt{2dt2N_k}}\sum_{k=1}^{N_k}\left[\mathbf{C}(\omega)\vec{\chi}e^{-i\omega t} + \mathbf{C}(\omega)\vec{\chi}^*e^{i\omega t}\right] \tag{7.8}$$

where $\vec{\chi}$ is a complex vector of random numbers.

We mention that the length of the MD simulations, n_{step}, should be long enough for the system to equilibrate (so that time-averages are definable). Furthermore, it should be long enough to define good Fourier transforms.

7.2 QMD applied to GALs

In this section we apply the QMD method to a $\{10, 3\text{arm}\}$ GAL device between graphene leads and illustrate that it is indeed possible to describe quantum thermal transport from MD simulations. We integrate the SCLE, in eqn. 7.1, by the velocity-Verlet MD algorithm[184] generalized to a non-Markovian matrix memory kernel. The simulations are based on the Brenner potential.

It is important that the artificial damping and memory cutoff fit together so that all main features of the damping kernel are taken into account. A given set of parameters influence how well the original self-energy is represented, Fig. 7.1. The self-energy of graphene was generated in 350 energy points and reveals several sharp features. Decreasing the memory cutoff plays the role of an effective damping, however abruptly applied in time. The sharp features in the frequency spectra are hard to reproduce by a short memory cutoff in time, see (a). With a very long memory, having more points than in the original energy-grid, one superimpose oscillations of high frequency.

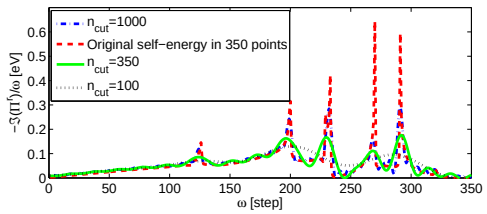

(a) Frequency dependence of graphene retarded self-energy generated from the memory kernel with varying memory length. The artificial damping is $\eta_{ad} = 0.001eV$.

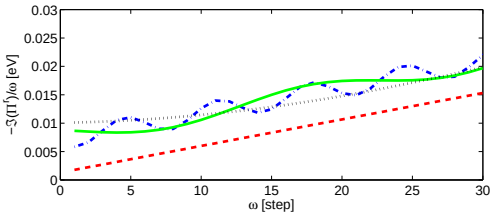

(b) Zoom around zero frequency.

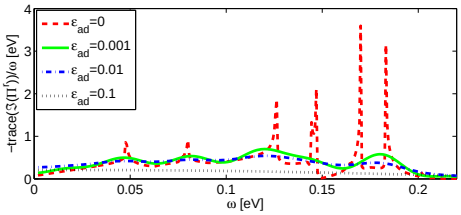

(c) Frequency dependence of graphene retarded self-energy generated from the memory kernel with varying artificial damping. The memory length is $n_{cut} = 150$.

Figure 7.1: *Effect of varying phonon memory cutoff and artificial damping in graphene. The calculations were performed with $T = 300K$, $dt = 0.5fs$ and $n_{step} = 10^5$.*

The phonon friction (constant value around zero frequency, see (a,b)) increases as the artificial damping is increased and the memory length shortened. One can argue that the system gradually becomes more classical as the phonon friction increases and becomes more well defined. However, one can still approximate many main features of the phonon self-energy with a relatively high artificial damping and short memory length.

We perform a sequence of thermal nonequilibrium QMD simulations with a 10% temperature deviation in each lead relative to the equilibrium temperature. In steady state we can evaluate the thermal current from each lead as

$$J_{L/R} = -\left\langle \frac{dH_{L/R}}{dt} \right\rangle = \left\langle \dot{u}(t) \left(-\int_{t_0}^{t} \mathbf{\Phi}_{L/R}(t-t')\dot{u}(t')dt' + f^{ph}_{L/R}(t) \right) \right\rangle . \tag{7.9}$$

The thermal conductance is then defined by

$$\kappa^{ph}_{L/R} = J_{L/R}/(T_{L/R} - T_{R/L}) . \tag{7.10}$$

One can test that the simulation has indeed reached steady state by comparing the left and right thermal currents and finally evaluate the average device conductance, $\kappa^{ph} = (\kappa^{ph}_L + \kappa^{ph}_R)/2$. In Fig. 7.2 we compare to the Green's function results for the GAL systems in the ballistic limit. The thermal conductance averaged over four QMD simulations agrees well with the ballistic NEGF calculation taking full account of the low-temperature quantum freeze-out of phonons. For this rather short device the harmonic and nonlinear simulations also agree. The insert of Fig. 7.2 illustrates the noise correlation function at varying temperatures compared to the damping kernel. As the

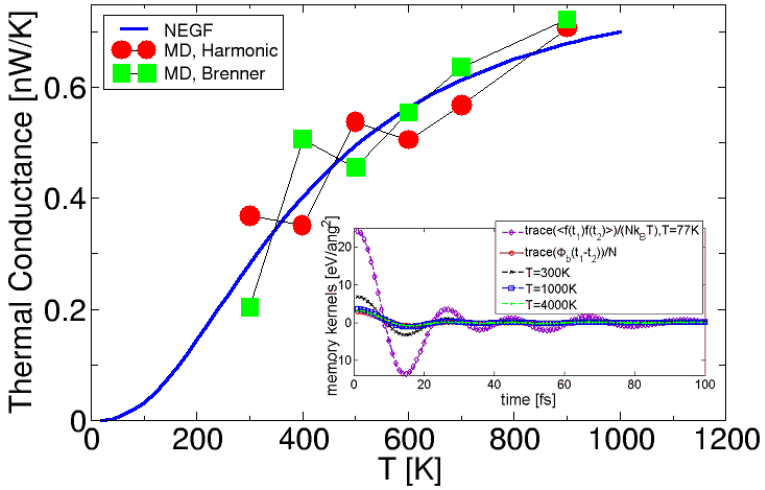

Figure 7.2: *Thermal conductance obtained from QMD and NEGF for a {10,3arm} GAL with $M = 1$. Parameters used in the simulations are: unequal lead temperatures $T_{L/R} = (1 \pm 0.1)T$, $\epsilon_{ad} = 0.05eV$, $\delta t = 0.5fs$ and $n_{cut} = 350$. Insert: Temperature dependence of the noise correlation function compared to the damping kernel. From Paper III.*

temperature is increased the quantum correlation functions eventually satisfy the classical fluctuation-dissipation theorem, i.e. the noise correlation function and damping kernel only differ by a factor k_BT. In this limit the obtained thermal conductance is equivalent to that obtained by conventional classical MD simulations. We conclude that quantum thermal transport properties can be obtained from generalized Langevin-MD simulations with quantum heat baths. This approach yields results similar to those obtained with the NEGF-Landauer approach. The MD approach is, in principle, able to address the effects of anharmonicity beyond perturbation theory in thermal transport.

7.3 Molecular dynamics including Joule heating

To illustrate how Langevin-type MD simulations can be performed including the Joule heating effect, we apply the TB+Brenner model in a simple test system consisting of a 5-atom linear carbon chain bridging two graphene leads, Fig. 7.3. As a starting point

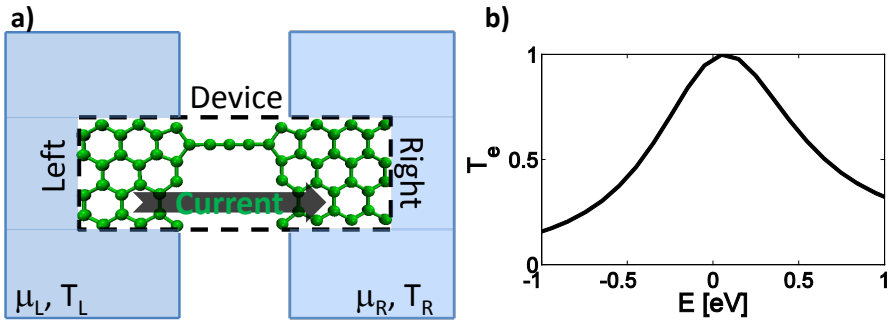

Figure 7.3: *Linear chain system (a) and electron transmission (b).*

we will neglect the quantum fluctuations and apply a time-local phonon damping. By Taylor expanding the Bose distribution function $n_B(\omega) \approx \frac{k_BT}{\hbar\omega}$ for $\omega \to 0$, we find the

physical appealing classical white noise spectrum

$$\mathbf{S}_f^{ph}(\omega) \approx 2\eta_{ph}k_BT\,, \tag{7.11}$$

where the friction matrix is given as

$$\eta_{ph} = -\frac{\partial}{\partial\omega}\left(\mathrm{Im}\left[\mathbf{\Pi}_{\mathrm{ph}}^{\mathrm{r}}\right]\right)|_{\omega=0}\,. \tag{7.12}$$

The time-local version is only correct in the high temperature limit. However, it is instructive to take the friction as a single tunable parameter to illustrate what effect the coupling to the environment and anharmonic coupling will have on the local Joule heating. Correspondingly, we approximate the electron spectral power by a white noise distribution by assuming a large bias voltage:

$$S_f^e(\omega) = 2(\eta_e)_{nn}k_BT + \mathrm{Re}\left(\mathrm{Tr}\left[\mathbf{A}_L(\mu_L)\mathbf{M}^n\mathbf{A}_R(\mu_R)\mathbf{M}^n\right]\right)\frac{|eV_a|}{2\pi}\,. \tag{7.13}$$

Here we have neglected the off-diagonal elements within the WBA expression to include the Joule heating effect in the simplest possible manner. Despite the crudeness of the model used in this section, it is a prove of concept that both illustrates the power of SCLE MD simulations and the importance of anharmonic interactions in the description of the local heating. The MD set up is shown in Fig. 7.4a. We include electrode regions without interaction with the current (DL, DR), and a device region (D) where the current density is highest and where the local heating is included. We vary the value of the phonon friction around typical values found for graphene. This enables one to quantify the dependence of the local electronic heating in the device region on this parameter (Fig. 7.4b). The bottleneck for heat transfer away from the device is at the chain-graphene interface for a high friction. This is an appealing result since the heat flow away from the contacts is sufficient to maintain the temperature of the heat baths in that case. As long as the chain-graphene interface acts as a bottleneck for the heat conduction the local heating is independent of the coupling to the environment and contacting further away from the device.

We now compare the local heating with(Fig. 7.4c,d) and without(Fig. 7.4e,f) the anharmonic interactions. In the absence of zero-point motion we define atomic temperatures for atom "a" from the equipartition theorem, $T_a(t) \equiv \frac{m_a}{3k_B}\langle\vec{v}_a^2(t)\rangle$. Anharmonic couplings between the vibrational modes have a significant influence on the local Joule heating of the system. Within the harmonic approximation we find isolated modes with very high temperatures. The heating is found to be less localized in the chain due to anharmonicity. This originates from the coupling of different modes and an increased coupling to the surroundings for configurations where the atoms are displaced from their equilibrium positions. When anharmonic interactions are included the energy is redistributed and the modes are collectively heated up. We conclude that MD simulations including current-induced forces enables an energy redistribution mechanism among the modes, mediated by anharmonic interactions, which is found to be vital in the description of the electronic heating.

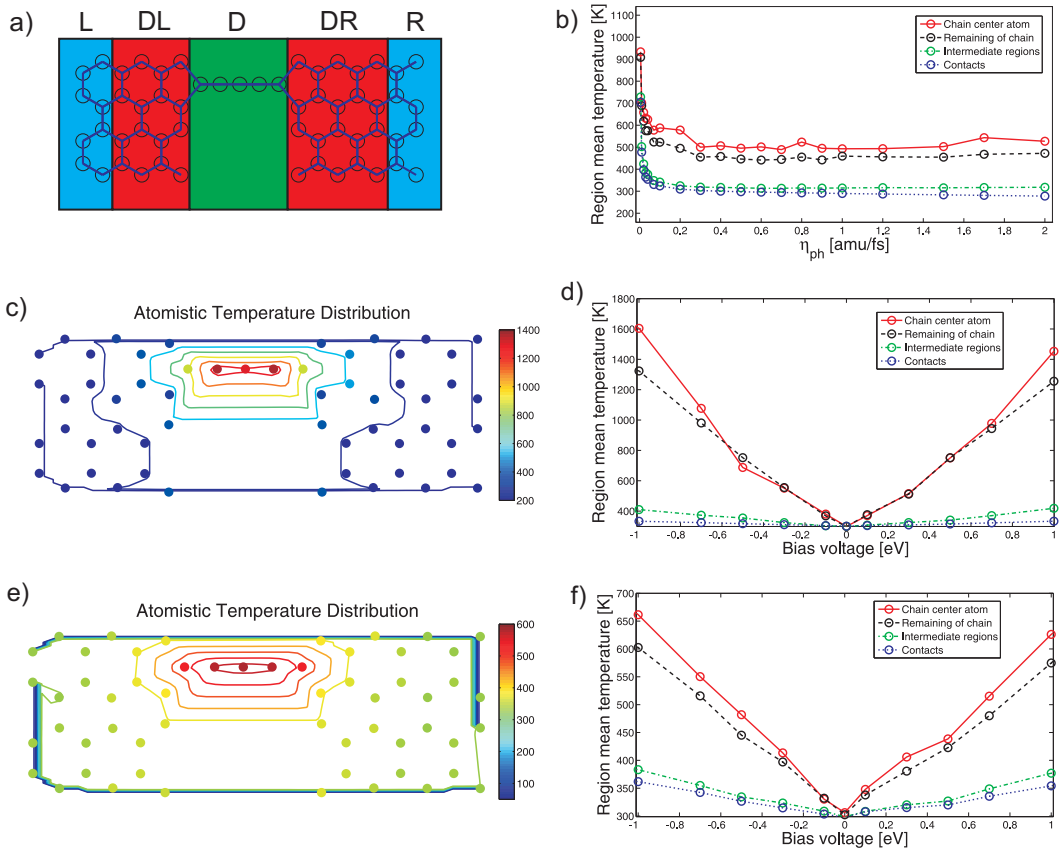

Figure 7.4: *Local heating of the linear 5-atom carbon chain. (a) Definition of system regions with different types of noise contributions. Leads (L, R) have a well-defined temperature specified from the phonon noise, the device (D) temperature will be defined from the electronic heating, and the intermediate regions (DL, DR) are free and will obtain a temperature from propagating noise. (b) Temperature of the regions as a function of phonon friction. (c,d) Obtained temperatures at different atoms within the harmonic approximation. (c) The simulations are run at T=300K and at $eV_a = 1eV$, and (d) varying bias voltages. (e,f) Corresponding atomistic temperature distributions including the anharmonic interactions. The lead temperature can exceed the equilibrium bath temperature due to propagating noise. Especially the anharmonic interactions redistribute part of the energy from the modes in the chain to the bulk modes in the lead. From Paper II.*

7.4 The origin of thermal expansion in current-carrying graphene nanoconstrictions

In a recent experiment, Börrnert *et al.* were able to electrically characterize a bilayer GNC while at the same time observing the structural response of the device[23]. Their configuration is illustrated in Fig. 1.2b. They find a highly localized "anomalously" large lattice expansion inside a less than 10 nm wide constriction, observed trough *in situ* atomic resolution TEM.

This section presents preliminary and unpublished results that might contribute to the explanation of the observed expansion of current-carrying GNCs. The phonons and anharmonicity is treated with the Brenner empirical potential as described in the QMD method in section 7.1. The electron bath is described by the DFT calculations within WBA, as discussed in chapter 6. In principle the novel deterministic forces could be important. However, to be able to compare with experiments on larger constrictions we only include the Joule heating mechanism here. The main idea is that a current can excite the local vibrations of a nanosystem, and that this could have consequences on the atomic bonds by a different relative occupation of the phonon modes. Within Grünesen theory one examine how a change in lattice parameters will change the phonon frequencies and the corresponding DOS. Here we ask the reversed question; how will a change in phonon populations influence the lattice parameters?

7.4.1 Thermal contraction in graphene and GNCs

Graphene is known to have a negative thermal expansion coefficient, $\alpha(T)$, for temperatures up to more than 400 K, recently measured by scanning electron microscope[12] and Raman scattering[200]. Marzari *et al.* estimated $\alpha(T)$ by first-principles calculations in a quasiharmonic model of the vibrational free energy. They found it was negative up to 2500 K and explain it as a result of the ZA (out-of-plane acoustic) vibration[21, 129]. Bao *et al.* used this effect to thermally generate a graphene ripple suspended over a trench[12].

We now apply the quasiharmonic approximation, which includes anharmonicity by the dependence of the phonon frequencies on the lattice parameter. However, it neglects stronger anharmonic effects such as phonon-phonon interactions. The total oscillator energy, $E_{\{n_{q,j}\}}$, is given by the cohesive energy, U, and the quantized phonon energies of a collection of quantum harmonic oscillators with occupation numbers, $n_{q,j}$:

$$E_{\{n_{q,j}\}} = U + \sum_{q,j} \hbar\omega(q,j)\left(n_{q,j} + \frac{1}{2}\right), \tag{7.14}$$

where j and q labels the modes and reciprocal lattice vectors, respectively. We then obtain the partition function as

$$Z = \sum_{\{n_{q,j}\}} e^{-\frac{E_{\{n_{q,j}\}}}{k_B T}} = e^{-\frac{U}{k_B T}} \prod_{q,j} \frac{e^{-\frac{\hbar\omega(q,j)}{2k_B T}}}{1 - e^{-\frac{\hbar\omega(q,j)}{k_B T}}}. \tag{7.15}$$

At zero pressure, the equilibrium lattice parameters minimize the Helmholtz free energy:

$$\begin{aligned} F(\{a_i\},T) &= -k_B T \ln(\mathrm{Z}) \\ &= U(\{a_i\}) + \sum_{q,j} \frac{\hbar\omega(q,j,\{a_i\})}{2} + k_B T \sum_{q,j} \ln\left[1 - \exp\left(-\frac{\hbar\omega(q,j,\{a_i\})}{k_B T}\right)\right]. \end{aligned} \tag{7.16}$$

Here we included the parametric dependence on the lattice parameters, $\{a_i\}$. Besides the cohesive energy, the free energy includes contributions from the temperature independent zero-point-motion, F_{ZPM}, and a third term, F_T, from the thermal occupation of phonon modes. One define the linear thermal expansion coefficients $\alpha_i(T) = \frac{1}{a_i}\frac{\partial a_i}{\partial T}$. It is possible to evaluate the free energy, eqn. 7.16, as a function of lattice parameters to find the minimum and directly evaluate the temperature dependence. Alternatively, within the Grünesen formalism one assumes a linear dependence of the phonon frequencies on the lattice parameters. In graphene, Marzari *et al.* expressed the thermal expansion coefficient of the single lattice parameter as[129].

$$\alpha = \frac{1}{a_0^2 \frac{\partial^2 E}{\partial a^2}} \sum_{q,j} c_v(q,j) 2\gamma(q,j) \tag{7.17}$$

from the condition that $(\partial F/\partial a)_T = 0$. Here we have defined the Grünesen parameter

$$\gamma(q,j) = -\frac{a_0}{2\omega(q,j)} \frac{\partial \omega(q,j)}{\partial a} \tag{7.18}$$

The mode specific heat contributions, $c_v(q,i)$, are always positive and the total thermal expansion coefficient is obtained from the competition between modes with Grünesen parameters of possible alternating sign. The dispersion of the six phonon branches of graphene are illustrated in Fig. 7.5, together with the Grünesen parameters and mode displacements. The Grünesen parameter is evaluated by finite differences for a slightly strained system to avoid imaginary frequencies close to the Γ-point. Clearly, the source of negative thermal expansion is the ZA out-of-plane mode. At the Γ-point the ZA mode has a Grünesen parameter as low as -165. Since this mode has a very low frequency it will dominate the thermal expansion at low effective temperature, where other modes are still not excited.

We conclude that we, consistent with the results by Marzari *et al.*, find that the origin of the contraction is the ZA mode due to its quadratic dispersion. The origin of this is called the membrane effect, originally predicted by I.M. Lifshitz in 1952. In terms of a simple vibrating string the vibrational frequency increases if one pull harder at the ends. Interestingly, the in-plane motion is always coupled anharmonically to the out-of-plane motion. If one displaces an atom z in the out-of-plane the in-plane force goes as z^2. So even for a harmonic membrane the projected force is always anharmonic. We conclude that with increasing lattice parameter, the tension of the graphene sheet grows, making out-of-plane motion more difficult. Therefore, the out-of-plane force constants increase (becomes harder) and the phonon frequencies effectively increase.

We now consider the velocity-velocity correlation function, $C_v(\omega) \equiv \langle v(\omega) v^*(\omega) \rangle = \delta(\omega - \omega') w^2 \langle u(\omega) u^*(\omega') \rangle$. This is also called the power spectrum, since it gives the kinetic energy distribution among the modes. It is obtained from the Fourier transformed displacements along a QMD trajectory, $u(\omega)$. In Fig. 7.6, we show the power spectrum obtained from QMD simulations for the GNC at different temperatures. The total power increases with temperature. Additionally, the highest frequency modes around 0.2 eV are shifting down in frequency. We find that the GNC contracts with temperature from evaluating the average bond-lengths consistent with the quasiharmonic calculation.

Interestingly, the measurements by Börrnert *et al.* suggest the opposite effect due to a current for a bilayer constriction. They observe a large expansion in contrast to the contraction one should expect from a general temperature increase as above. Several things could go into the current-induced expansion. For example there is no guarantee that there is no intrinsic strain in the experiments due to a fixed lead-lead distance.

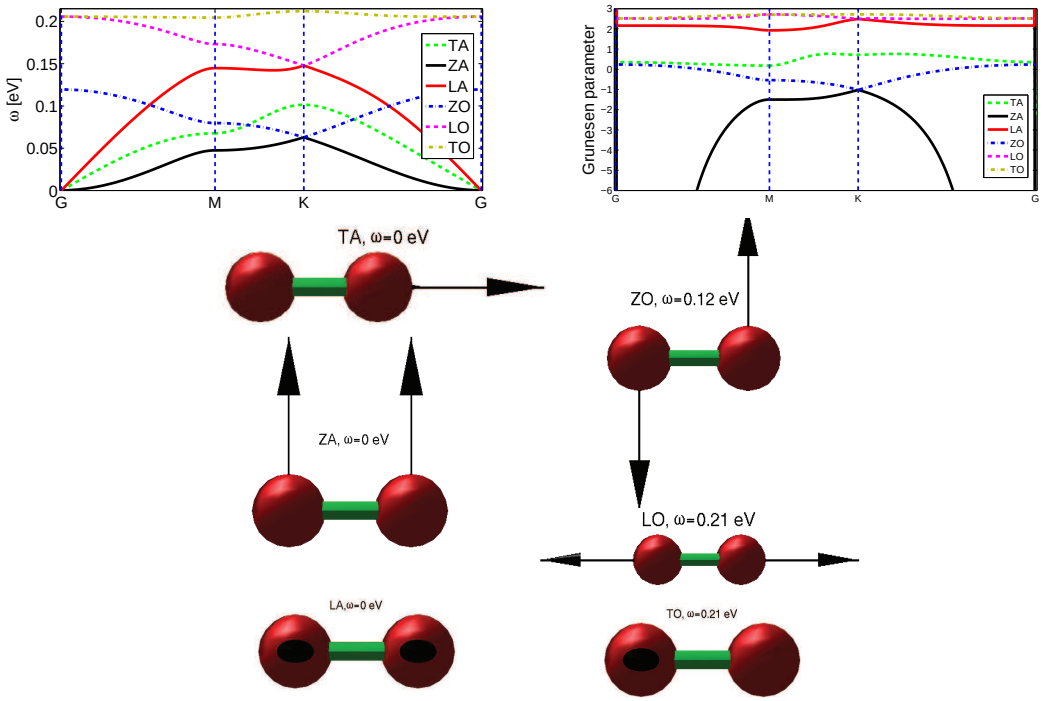

Figure 7.5: *Phonon dispersion and Grünesen parameters of graphene. (Top leftmost) Phonon dispersion of graphene between the three high symmetry points, $\vec{G} = (0, 0, 0)$, $\vec{M} = \frac{1}{a_0}(\pi/3, \pi/\sqrt{3}, 0)$ and $\vec{K} = \frac{1}{a_0}(2\pi/3, 2\pi/(3\sqrt{3}), 0)$, from the empirical Brenner potential. (Top rightmost) Corresponding Grünesen parameters of the six phonon branches. The modes are sorted according to the symmetry (overlap) of the displacements. (Bottom) Displacements for the six phonon modes of graphene.*

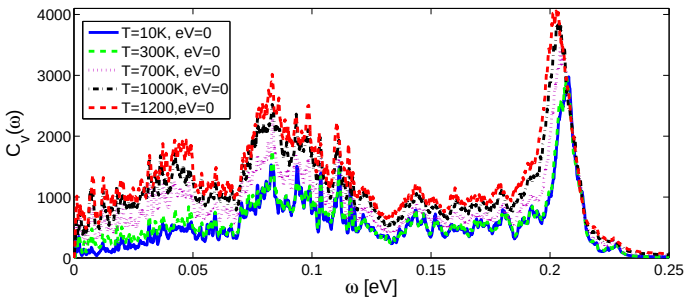

Figure 7.6: *Power spectrum at different temperatures. It is obtained as an average over four independent QMD simulations.*

However, the phonon excitation due to the current is the main actor in the explanation. The optical modes localized in the constriction are softening as the lattice parameter is increased. At a high bias, it is mainly the optical modes that will be excited as compared to the ZA-mode. The power spectrum illustrates that the high frequency modes around 0.2 eV gets remarkedly softer. This down shift in the optical frequencies was correspondingly observed by Raman spectroscopy on graphene[200]. A hypothesis is that the different effective temperatures among the modes due to the heating at finite bias could invert the picture. One could expect to find thermal expansion at low temperature, where the system was contracting at zero bias voltage.

7.4.2 A two-temperature quasiharmonic model

The Grünesen formalism is convenient and very illustrative for small systems, where each mode can be clearly distinguished. However, for larger systems such as the GNC with many modes at nearly equal frequencies it becomes exceedingly hard to sort the modes by symmetry. To illustrate the above idea we have instead calculated the free energy, eqn. 7.16, as a function of nearest-neighbor distances to find the optimal lattice parameter. To include the effect of the current we assume that two different temperatures exist. We take an equilibrium temperature, $T = T_0$, for modes with $\omega_j < 0.15\,\text{eV}$ and an elevated temperature, $T = T_0 + \Delta T$, for modes with $\omega_j \geq 0.15\,\text{eV}$. The optimal nearest

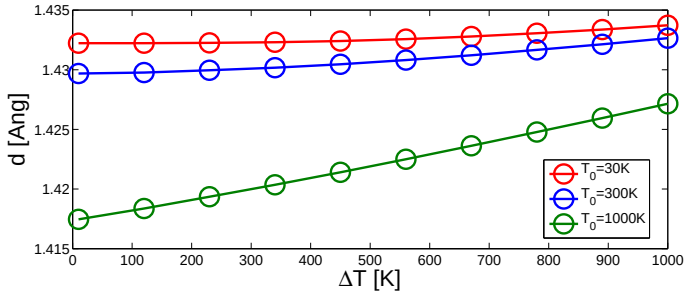

Figure 7.7: *Nearest neighbor distance, d, minimizing the Helmholtz free energy.*

neighbor distance, d, is given as a function of ΔT in Fig. 7.7. Notice the large increase in the equilibrium lattice constant ($\Delta T = 0$) with decreasing temperature. The origin of this is found to be the zero-point-motion, F_{ZPM}. This term exceeds the thermal contribution, F_T, up to above 1000 K. We find that the GNC would expand within this model as the local heating is increasing with bias. This clearly illustrates that the phenomena of current-induced expansion is within the physical available parameter space. However, there may be more important ingredients in the explanation of the experiment than taken account of in this simple two-temperature model. First of all, the main assumption (that no modes below the threshold are excited) used in this model will not hold perfectly true. Anharmonic coupling will transfer heat to the lower lying modes. Furthermore, the experiment observed a highly localized lattice expansion in the direction of the current along the constriction. E.g. an anisotropic lattice expansion only in the constriction part and not in the leads. Furthermore, the experiment was on bilayer graphene, and it is therefore interesting to consider the importance of a substrate in the explanation of the effect. We will now consider the heating and lattice parameters from MD of the constriction on a substrate.

7.4.3 Nonsuspended graphene

We now include a second graphene layer. As a model we only include the current in the top layer and treat the second layer as a substrate with varying mass and interaction potential. The layer interaction is taken to be of the Lennard-Jones form, $\phi^{ij}_{LJ}(|\vec{r}_{ij}|) = -4\epsilon_0\left(\left(\frac{\sigma_0}{|\vec{r}_{ij}|}\right)^6 - \left(\frac{\sigma_0}{|\vec{r}_{ij}|}\right)^{12}\right)$, and is scaled between that of bilayer graphene and SiO_2. We take $\sigma_0 = 3.326\,\text{Å}$ and $\epsilon_0 = \chi\, 8.909\,\text{meV}$. For $\chi = 1$ these parameters are equal to the Si-C interaction of graphene on SiO_2[131, 139]. For $\chi = 0.31$ the potential is similar to that of the graphite and bilayer graphene interaction[98]. For graphene with a strong interaction with a substrate ($\chi = 10$) an optical surface mode develops as a hybridization between the ZA mode and Rayleigh surface waves in the substrate[140]. In Fig. 7.8 we

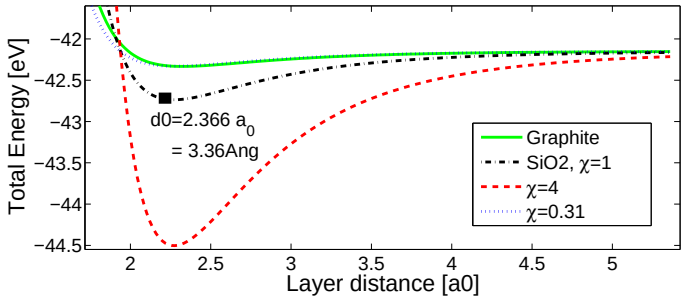

Figure 7.8: *Total energy of a bilayer graphene slap from the Lennard-Jones potential with a cut-off radius of $r_{cut} = 25\,\text{Å}$*

illustrate the total energy, as the interaction strength is tuned between that of bilayer graphene and graphene on top a SiO_2 substrate. In Fig. 7.9 we show the resulting

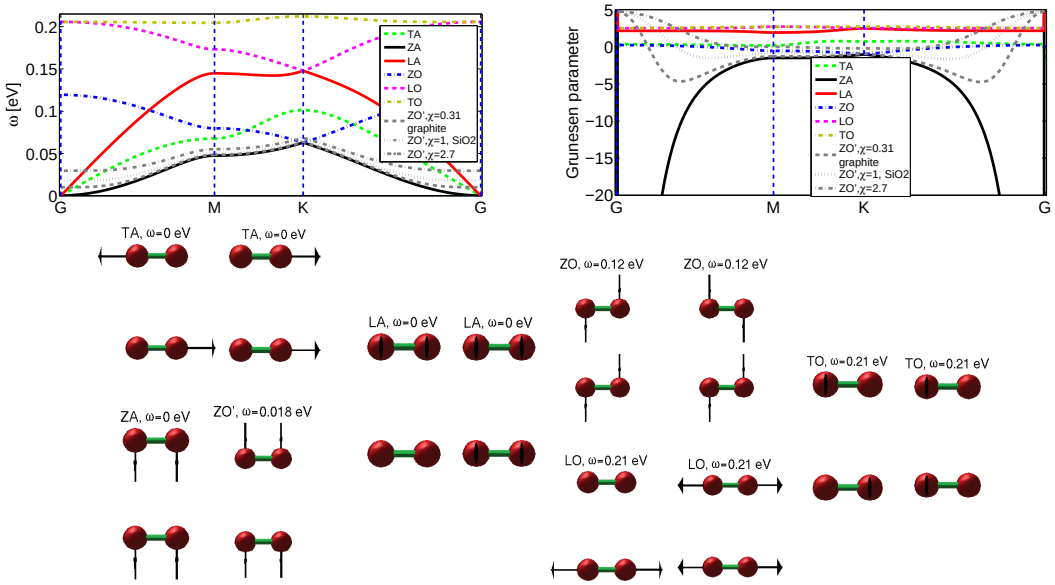

Figure 7.9: *(Top) Phonon dispersion (top left) and Grünesen parameters (top right) of graphene on a substrate. (Bottom) Corresponding mode displacements of the bilayer system.*

phonon dispersions and Grünesen parameters. As we increase the substrate interaction

the two ZA modes of the uncoupled graphene layers split into a conventional ZA mode and an additional optical ZO' out-of-plane mode. In the figure we used the carbon mass of the atoms in the substrate layer. We have also tested what happens if the mass of the substrate layer is increased beyond that of graphene. In the infinite mass limit the ZA mode dispersion vanishes ($\omega_{ZA} = 0$), the ZO' mode is shifted slightly downwards (the effective interaction, χ_{eff}, is scaled slightly down) and the remaining modes are unaffected. We conclude that substrate interaction increases the ZO' mode frequency and stabilizes the system (less tendency to rippling). Furthermore, the Grünesen parameter of the ZO' mode becomes less negative. Substrate interaction will therefore decrease the barrier for crossing from an contracting to an expanding regime by relative phonon occupations.

7.4.4 Thermal expansion and local heating of the GNC from QMD

We now consider the effect of Joule heating and substrate interaction in QMD simulations for the GNC. Fig.7.10a illustrates the power spectrum obtained from the simulations

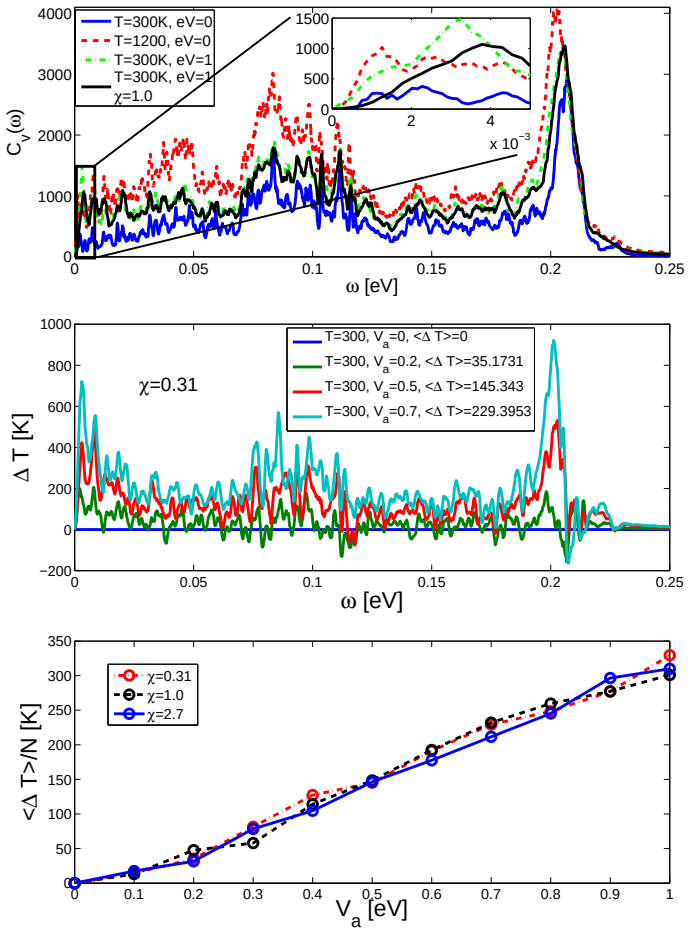

Figure 7.10: *Power and heating spectrum from QMD. (Top) Average power spectrum from QMD simulations with varying temperature, bias and substrate interaction. (Middle) Relative change in power at different bias voltages. (Bottom) The total additional kinetic energy per atom, stored in the system, as a function of bias voltage.*

with varying bias voltage and substrate interaction. The substrate interaction is mainly observed as a decrease of the occupation of the lowest acoustic modes, Fig.7.10top. We define a heating spectrum as a relative change in kinetic energy, $\Delta T(\omega_i, V_a) = \frac{2}{k_B}\left(C_v(\omega_i, V_a) - C_v(\omega_i, 0)\right)\frac{d\omega}{2\pi}$. Here we included both positive and negative frequency contributions and choose units so that the total heating is just a sum over discrete frequencies, $\Delta T(V_a) = \sum_i \Delta T(\omega_i, V_a)$. Despite the substrate interaction, there is still a significant heating of the low frequency vibrations due to the anharmonic coupling, Fig.7.10middle. The average heating for the full system is unaffected by the substrate, Fig.7.10bottom.

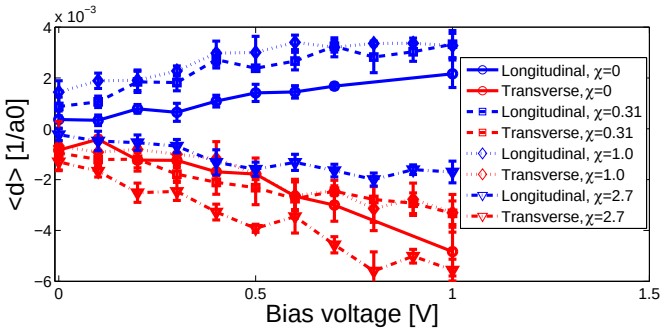

Figure 7.11: *Change in the in-plane components of the nearest-neighbor distance, inside the constriction, with bias voltage. The average lattice parameter is found from an average over 4 QMD simulations.*

In Fig. 7.11 we consider the change in the in-plane components of the nearest-neighbor distance with bias voltage. In agreement with the experiment we find a clear anisotropy between the two in-plane directions. However, we do not find that both directions are expanding. Only the longitudinal direction is expanding while the GNC contracts in the transverse direction. At a low degree of substrate interaction the constriction is expanding more than without substrate. As we increase the substrate interaction above that of SiO_2, all graphene modes will eventually expand and the constriction will be squeezed between the two leads. This is a somewhat artificial effect since the total unit cell parameter is kept fixed in the QMD simulations. One can expect that the trend of thermal expansion in the longitudinal direction will be more evident if the unit cell was not fixed.

The real-space heating can be obtained from the total relative change in kinetic energy with bias. The result is illustrated in Fig. 7.12. Nonequilibrium QMD simulations enables one to include a general nonlinear force-field and obtain the local heating with an accurate description of the quantum occupations and heat dissipation. In a classical MD simulation all vibrational modes are equally excited, while in QMD simulations phonon modes are occupied according to the Bose distribution and the bias voltage. One can therefore not expect to obtain a correct description of the different effective temperatures obtained from classical MD. We conclude that nonequilibrium QMD simulations may be a promising tool for describing to local heating and how relative phonon populations influence the lattice parameters.

7.5 Summary and discussion

This chapter described the QMD methodology and applied it to obtain the ballistic thermal conductance of a short GAL device. In the presence of bias we demonstrated a

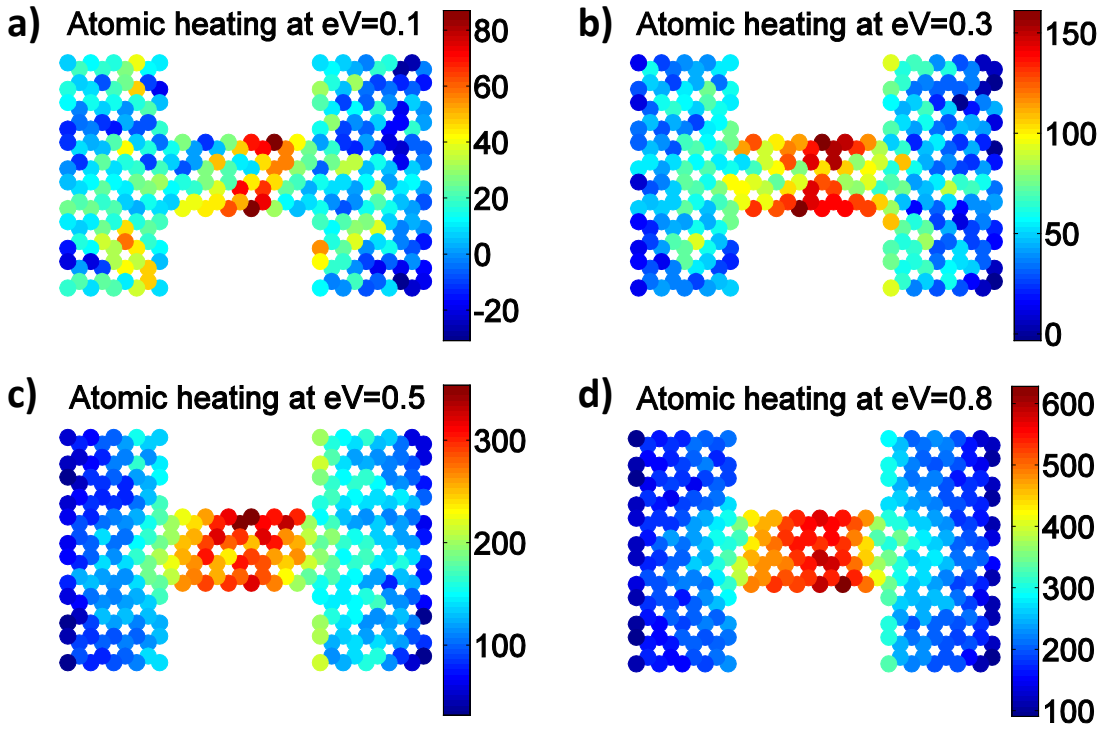

Figure 7.12: *Local Joule heating from QMD simulations at different bias voltages.*

significant difference in the current-induced heat dissipation between the harmonic and anharmonic simulations. Furthermore, QMD was used to obtain the local heating of a GNC. We have argued that the origin of the experimental observation, that a bilayer GNC expands in the longitudinal direction with increasing bias voltage, is related to the relative quantum occupation of phonon modes. In contrast to a conventional temperature the current may excite optical modes with a positive Grünesen parameter relatively more than the ZA mode with a negative Grünesen parameter. Substrate interaction will further decrease the barrier for crossing from a contracting to an expanding regime by relative phonon occupations.

Chapter 8

Summary and outlook

The interplay between electronic current and phonon dynamics is an important and intriguing problem in nanoelectronics. This thesis contributes to the understanding of phonon dynamics in graphene based nanostructures in the presence of an electrical current. Graphene is particularly interesting since it is capable of sustaining high current densities and enables fine tuning of the electronic structure by a gate voltage.

The two-dimensional nature of graphene allows us to create nanoscale "circuits" or paths for the current, for instance by confining charge carriers in GNRs, GAL waveguides or between functionalized kinks considered in this work. We found that GAL waveguides support modes which are highly confined to the waveguide region and are robust against structural disorder and kinks in the waveguide. We also suggested that the reduction in the absorption barrier when bending graphene could be used in a curvature-directed process for templated chemical functionalization of graphene.

Another main result was on the prospect of using "holey graphene" as thermoelectric devices, perhaps as an integrated element in future graphene nanoelectronics. Graphene cannot be used for thermoelectric applications by itself. Its efficiency in transforming heat into charge current is limited by its very high ability to conduct heat, exceeding that of copper. However, our transport calculations indicate that drilling a periodic lattice of nanosized holes in graphene could modify the thermal conductance substantially such that thermoelectric applications in principle could be possible. It is indeed surprising that an almost ideal thermal conductor can be used as a basis of thermoelectric components. Several recent experiments have shown how such nano-perforations indeed are possible. Our simulations predict that not only does the nanoperforated graphene provide a flexible platform for creating a tunable electronic band gab, it is also a platform for thermal management and thereby reveals several routes to increased thermoelectric efficiency. Topology optimization may be used for prototyping of interesting configurations, that may assist in developing new devices with increased thermoelectric performance.

Due to the high current densities one inevitably has to consider the effects of having localized vibrations in nanostructured graphene. The IV-characteristics can provide a spectroscopic fingerprint of local vibrations in molecular junctions. However, we found that the electronic spectrum of nanostructured graphene features electronic resonances, with a broadening on the scale of the phonon frequencies. To accommodate this regime we presented an extended lowest order expansion that incorporates the effect from the electronic energy variation on the phonon energy scale in the electronic conductance.

We also developed a spectral expansion technique for quantitative analysis of local heating effects, that is computational efficient and more predictive for systems with Lorentzian-like resonances in the spectral function. Our simulations indicate that

a "laser-like" mechanism is behind current-induced vibrational instabilities in narrow graphene constrictions (GNRs). Recent developments in graphene research enable the study of the structural response by *in situ* transmission electron microscopy, while the current density can be very high locally at narrow GNRs. There may be an unique possibility in understanding the fundamental mechanisms behind current-induced instabilities observed as contact disruption in experiments and used for current-annealing of nanostructured graphene. To this end, we have presented state-of-the-art calculations on a generic GNR formed in graphene, conducting an electronic current. Our main finding was that a significant fraction of the phonon/vibrational modes in the system obtain a current-induced negative damping (amplification) due to the coupling to the nonequilibrium electrons at finite bias. This signifies a vibrational instability and breakdown in the harmonic approximation. We explained the mechanism by a large variation of symmetry of the electronic states with energy, with the consequence that the rate of emission of phonons can exceed that of absorption.

MD simulations in the presence of current demonstrated a significant difference in the current-induced heat dissipation between the harmonic and anharmonic simulations. Furthermore, QMD was used to obtain the local heating of a GNC. We argued that GNCs expand in the longitudinal direction with increasing bias voltage, due to the relative quantum occupation of phonon modes. The current may excite optical modes with a positive Grünesen parameter relatively more than the ZA mode with a negative Grünesen parameter, in contrast to a conventional temperature. Substrate interaction will further decrease the barrier for crossing from a contracting to an expanding regime by relative phonon occupations.

In this thesis, we mainly examined ideal structures, and we just briefly considered disorder effects in GAL devices. However, a more detailed study of the influence of disorder could be conducted by utilizing scaling theory from effective single scatterer cross sections[119, 120]. Recently, effects of disorder on diffusive electron transport in GALs was examined by a time-dependent Kubo method[118, 204]. However, the relative scattering by disorder of electrons and phonons has not yet been addressed.

Our calculations provide a first step towards evaluating the change in thermoelectric performance due to e-ph coupling. How large such corrections will be for realizable systems is still an open question. A possible next step could also be to consider the nonlinear regime, where a finite temperature and bias voltage is applied simultaneously, in close resemblance to actual experiments. To this end, QMD in the presence of current seems a very promising tool. Several new methods are emerging that enables one to generate colored noise 'on the fly'[14, 41]. Hereby, one reduces the memory requirement in the inverse Fourier transform of the noise spectral density over the entire time duration of the MD simulation. Such methods could be useful in making QMD, in and out of equilibrium, more accessible to the MD community. In addition to graphene a range of other 2D materials are emerging, such as hexagonal Boron-nitride (hBN) and transition metal dichalcogenides like MoS_2[193]. hBN was suggested as a promising, defect free, tunnel barrier, which can be used as a support layer, gate dielectric and to encapsulate devices[61, 133]. In that sense, graphene can be viewed as a key in developing a range of new layered materials[134], that combines in an unique toolbox to realize patchwork 2D circuits[156].

In summary, the developed methods was described and applied to a number of experimentally relevant devices based on nanostructured graphene. The obtained results contributes to the evolving understanding of thermal transport and the interplay between electronic current and phonon dynamics at the atomic scale.

List of Figures

1.1 Nanostructuring and applications of graphene. 2
(a) GNCs fabricated by *in situ* transmission electron microscopy. 2
(b) GAL device fabricated by block copolymer lithography. 2
(c) Areas in which many device applications of graphene are developing. 2
1.2 Transport measurements in nanostructured graphene. 3
(a) Electrical transport measured in atomic carbon chains. 3
(b) Electrical transport and thermal expansion measured in bilayer GNCs. 3
1.3 Thermal rectification in axial asymmetric carbon nanotube. 4
1.4 Two types of current-induced instabilities, or 'runaway'-effects, different from local Joule heating. 6
(a) Design of a single-atom "waterwheel" driven by the nonconservative force. 6
(b) "Laser-like" population inversion in a two-level model for the donor-acceptor(DA) system 6
1.5 Measured local Joule heating in molecular junctions and graphene constrictions. 7
(a) Measurement setup for Raman spectroscopic studies of electrically biased graphene constrictions. 7
(b) Effective temperature distribution along a graphene constriction of width 0.6μm and length 1.5μm. 7

2.1 Schematic of the general NEGF system setup. 11
2.2 Lowest order diagrams in the electron-phonon coupling self-energies of the perturbation expansion of the electron and phonon Green's function. . . . 14
2.3 Different nearest neighbor distances obtained from SIESTA. 18
2.4 Phonon transmission as a function of frequency across ideal graphene and the GNC. 19
2.5 Thermoelectric figure of merit for the GNC. 19

3.1 GAL system setup and the computational rectangular unit cell (green rectangle). 20
3.2 Antidot shapes and resulting strain fields. 21
3.3 GAL device transmission convergence and transport gap definition. 22
3.4 Band structures, transmission curves and eigenstates of two GALs. 23
3.5 Comparison of GAL band structures with and without passivation. 24

3.6 Thermal transmission and conductance from phonons as a function of hole dimension and device length. . . . 25
3.7 ZT for {10,6arm} and {10,5zz} lattices at the four temperatures. . . . 27
3.8 ZT dependence on the ratio of removed atoms in the nanoperforation at $T = 300\,\mathrm{K}$. . . . 27
3.9 ZT variation with a decrease of the phonon thermal conductance at $T = 300\,\mathrm{K}$. . . . 28
3.10 The effect of isotopes for a long GAL-system. . . . 29
3.11 Transmission across a minimal GNR as a function of the design variable. . 32
3.12 Hamiltonian block partitioning and needed Green's function blocks in recursive transport. . . . 33
3.13 Topology optimization of a GNR. . . . 35

4.1 Conceptual illustration of a GAL waveguide. . . . 38
4.2 Dispersion relation and DOS of a GAL waveguide. . . . 41
4.3 Energy and effective mass as a function of waveguide width of the lowest localized waveguide state. . . . 42
4.4 Conductances of GAL waveguides and GNRs. . . . 44
4.5 Bond current and conductance across a 'kinked' GAL waveguide. . . . 45
4.6 Rippling and kink formation by hydrogen absorption. . . . 46
4.7 Calculated reaction barriers for hydrogenation of bend graphene as a function of the local radius of curvature. . . . 47
4.8 Electronic transmission through a single kink. . . . 48
4.9 Comparison of band structures for H-passivated armchair ribbons with the electronic transmission across pseudo-ribbons. . . . 49

5.1 Model transmissions with variations on different energy scales. . . . 52
5.2 Generic functions in the LOE expression. . . . 53
5.3 Transport across a GNC passivated by hydrogen between two pristine graphene leads. . . . 54
5.4 Inelastic current and conductance for the GNC. . . . 55
5.5 Inelastic signal for the GNC. . . . 56
5.6 Inelastic signal for the GNC gated or with adatoms. . . . 57

6.1 Transport setup for the carbon chain system. . . . 66
6.2 Modes in and out of equilibrium. . . . 66
6.3 Harmonic stability analysis of the carbon chain system. . . . 68
6.4 Constant self-energy approximation. . . . 72
6.5 Convergence with the number of included eigenvalues in the eigen expansion. 72
6.6 Transport setup illustrating the hydrogen passivated GNC, transmission and bond currents. . . . 74
6.7 Real space voltage drop along the device averaged over the two transverse directions. . . . 74
6.8 Finite bias transport across the GNC. . . . 75
6.9 Phonon transmission across the graphene nanoconstriction. . . . 76
6.10 Harmonic stability analysis of the GNC. . . . 77
6.11 Harmonic stability analysis of the GNC from the zero bias electronic structure. . . . 78
6.12 NC and BP forces between the IETS and runaway mode. . . . 79
6.13 Modes and inverse Q-factor (loss) of the GNC. . . . 79

6.14 Nonequilibrium friction mechanism. 82
6.15 Emission and absorption integrands from electron-hole pair interaction. . 84
6.16 Eigenchannel calculation of the $\mathcal{A}$,$\mathcal{B}$ coefficients for the runaway mode. . . 85
6.17 Selection of the symmetry of the scattering state by mode vibration. . . . 86

7.1 Effect of varying phonon memory cutoff and artificial damping in graphene. 91
(a) Frequency dependence of graphene retarded self-energy generated from the memory kernel with varying memory length. 91
(b) Zoom around zero frequency. 91
(c) Frequency dependence of graphene retarded self-energy generated from the memory kernel with varying artificial damping. 91
7.2 Thermal conductance obtained from QMD and NEGF for a {10,3arm} GAL. 92
7.3 Linear chain system and electron transmission. 92
7.4 Local heating of the linear 5-atom carbon chain. 94
7.5 Phonon dispersion and Grünesen parameters of graphene. 97
7.6 Power spectrum at different temperatures. 97
7.7 Nearest neighbor distance, d, minimizing the Helmholtz free energy. . . . 98
7.8 Total energy of a bilayer graphene slap from the Lennard-Jones potential 99
7.9 Phonon dispersion and Grünesen parameters of graphene on a substrate. . 99
7.10 Power and heating spectrum from QMD. 100
7.11 Change in the in-plane components of the nearest-neighbor distance, inside the constriction, with bias voltage. 101
7.12 Local Joule heating from QMD simulations at different bias voltages. . . . 102

9.1 Numerical noise in finite difference (FD) sensitivity calculation. This illustrates the correctness of the sensitivity analysis and the numerical stability. 131

Bibliography

[1] Adelman, S. A. and J. D. Doll (1976, March). Generalized langevin equation approach for atom/solid-surface scattering: General formulation for classical scattering off harmonic solids. *The Journal of Chemical Physics 64*(6), 2375–2388.

[2] Adelman, S. A. and J. D. Doll (1977, October). Brownian motion and chemical dynamics on solid surfaces. *Accounts of Chemical Research 10*(10), 378–384.

[3] Andreassen, E., A. Clausen, M. Schevenels, B. S. Lazarov, and O. Sigmund (2011, January). Efficient topology optimization in MATLAB using 88 lines of code. *Structural and Multidisciplinary Optimization 43*(1), 1–16.

[4] Areshkin, D. A. and C. T. White (2007, November). Building blocks for integrated graphene circuits. *Nano Letters 7*(11), 3253–3259.

[5] Bae, S., H. Kim, Y. Lee, X. Xu, J.-S. Park, Y. Zheng, J. Balakrishnan, T. Lei, H. Ri Kim, Y. I. Song, Y.-J. Kim, K. S. Kim, B. Özyilmaz, J.-H. Ahn, B. H. Hong, and S. Iijima (2010, August). Roll-to-roll production of 30-inch graphene films for transparent electrodes. *Nature Nanotechnology 5*(8), 574–578.

[6] Bai, J., X. Zhong, S. Jiang, Y. Huang, and X. Duan (2010, March). Graphene nanomesh. *Nat. Nanotech. 5*(3), 190–194.

[7] Bailey, S. W. D., I. Amanatidis, and C. J. Lambert (2008, June). Carbon nanotube electron windmills: A novel design for nanomotors. *Physical Review Letters 100*(25), 256802.

[8] Balandin, A. A. (2005, July). Nanophononics: Phonon engineering in nanostructures and nanodevices. *Journal of Nanoscience and Nanotechnology 5*(7), 1015–1022.

[9] Balandin, A. A. (2011). Thermal properties of graphene and nanostructured carbon materials. *Nat Mater 10*(8), 569–581.

[10] Balandin, A. A., S. Ghosh, W. Bao, I. Calizo, D. Teweldebrhan, F. Miao, and C. N. Lau (2008, March). Superior thermal conductivity of Single-Layer graphene. *Nano Lett. 8*(3), 902–907.

[11] Ballentine, L. E. (2006). *Quantum Mechanics* (1st ed.). World Scientific.

[12] Bao, W., F. Miao, Z. Chen, H. Zhang, W. Jang, C. Dames, and C. N. Lau (2009, September). Controlled ripple texturing of suspended graphene and ultrathin graphite membranes. *Nature Nanotechnology 4*(9), 562–566.

[13] Bao, W. S., S. Y. Liu, and X. L. Lei (2010, August). Thermoelectric power in graphene. *J. Phys.: Condens. Matter 22*(31), 315502.

[14] Barrat, J.-L. and D. Rodney (2011, August). Portable implementation of a quantum thermal bath for molecular dynamics simulations. *Journal of Statistical Physics 144*(3), 679–689.

[15] Barreiro, A., F. Börrnert, M. H. Rümmeli, B. Büchner, and L. M. K. Vandersypen (2012, April). Graphene at high bias: Cracking, layer by layer sublimation, and fusing. *Nano Lett. 12*(4), 1873–1878.

[16] Bendsøe, M. P. and O. Sigmund (2003). *Topology Optimization: Theory, Methods and Applications* (2nd ed.). Springer.

[17] Bennett, S. D., J. Maassen, and A. A. Clerk (2010, November). Scattering approach to backaction in coherent nanoelectromechanical systems. *Physical Review Letters 105*(21), 217206.

[18] Berciaud, S., M. Y. Han, K. F. Mak, L. E. Brus, P. Kim, and T. F. Heinz (2010, June). Electron and optical phonon temperatures in electrically biased graphene. *Phys. Rev. Lett. 104*(22), 227401.

[19] Berry, M. V. and R. J. Mondragon (1987, August). Neutrino billiards: Time-reversal symmetry-breaking without magnetic fields. *Proceedings of the Royal Society of London. A. Mathematical and Physical Sciences 412*(1842), 53–74.

[20] Bode, N., S. V. Kusminskiy, R. Egger, and F. von Oppen (2011, July). Scattering theory of current-induced forces in mesoscopic systems. *Physical Review Letters 107*(3), 036804.

[21] Bonini, N., M. Lazzeri, N. Marzari, and F. Mauri (2007, October). Phonon anharmonicities in graphite and graphene. *Physical Review Letters 99*(17), 176802.

[22] Born, M. and R. Oppenheimer (1927). Zur quantentheorie der molekeln. *Annalen der Physik 389*(20), 457–484.

[23] Börrnert, F., A. Barreiro, D. Wolf, M. I. Katsnelson, B. Büchner, L. M. K. Vandersypen, and M. H. Rümmeli (2012, August). Lattice expansion in seamless bilayer graphene constrictions at high bias. *Nano Lett.*.

[24] Botello-Mendez, A. R., E. Cruz-Silva, J. M. Romo-Herrera, F. Lopez-Urias, M. Terrones, B. G. Sumpter, H. Terrones, J.-C. Charlier, and V. Meunier (2011, August). Quantum transport in graphene nanonetworks. *Nano Letters 11*(8), 3058–3064.

[25] Boykin, T. B., M. Luisier, G. Klimeck, X. Jiang, N. Kharche, Y. Zhou, and S. K. Nayak (2011, February). Accurate six-band nearest-neighbor tight-binding model for the pi-bands of bulk graphene and graphene nanoribbons. *eprint arXiv:1102.1718*.

[26] Brandbyge, M. (2009, February). Computational nanoscience: Atomic waterwheels go to work. *Nature Nanotechnology 4*(2), 81–82.

[27] Brandbyge, M., J.-L. Mozos, P. Ordejon, J. Taylor, and K. Stokbro (2002, March). Density-functional method for nonequilibrium electron transport. *Phys. Rev. B 65*(16), 165401.

[28] Brandbyge, M., J. Schiøtz, M. R. Sørensen, P. Stoltze, K. W. Jacobsen, J. K. Nørskov, L. Olesen, E. Laegsgaard, I. Stensgaard, and F. Besenbacher (1995, September). Quantized conductance in atom-sized wires between two metals. *Physical Review B 52*(11), 8499–8514.

[29] Brenner, D. W. (1990, November). Empirical potential for hydrocarbons for use in simulating the chemical vapor deposition of diamond films. *Phys. Rev. B 42*(15), 9458.

[30] Brey, L. and H. A. Fertig (2006). Electronic states of graphene nanoribbons studied with the Dirac equation. *Phys. Rev. B 73*, 235411.

[31] Carruthers, P. (1961, January). Theory of thermal conductivity of solids at low temperatures. *Reviews of Modern Physics 33*(1), 92–138.

[32] Castellanos-Gomez, A., G. Rubio-Bollinger, S. Barja, M. Garnica, A. L. Vázquez de Parga, R. Miranda, and N. Agraït (2013, February). Periodic spatial variation of the electron-phonon interaction in epitaxial graphene on ru(0001). *Applied Physics Letters 102*(6), 063114–063114–4.

[33] Castro Neto, A. H., F. Guinea, N. M. R. Peres, K. S. Novoselov, and A. K. Geim (2009, January). The electronic properties of graphene. *Reviews of Modern Physics 81*(1), 109–162.

[34] Chae, D.-H., B. Krauss, K. von Klitzing, and J. H. Smet (2009). Hot phonons in an electrically biased graphene constriction. *Nano Lett. 10*(2), 466–471.

[35] Chang, C. W., D. Okawa, A. Majumdar, and A. Zettl (2006, November). Solid-State thermal rectifier. *Science 314*(5802), 1121–1124.

[36] Chang, P.-H. and B. K. Nikolic (2012, July). Edge currents and nanopore arrays in zigzag and chiral graphene nanoribbons as a route toward high-ZT thermoelectrics. *Physical Review B 86*(4), 041406.

[37] Chen, S., Q. Wu, C. Mishra, J. Kang, H. Zhang, K. Cho, W. Cai, A. A. Balandin, and R. S. Ruoff (2012). Thermal conductivity of isotopically modified graphene. *Nat. Mat. 11*(3), 203–207.

[38] Chen, Y., T. Jayasekera, A. Calzolari, K. W. Kim, and M. Buongiorno Nardelli (2010, September). Thermoelectric properties of graphene nanoribbons, junctions and superlattices. *J. Phys.: Condens. Matter 22*(37), 372202.

[39] Chutinan, A. and S. Noda (2000, August). Waveguides and waveguide bends in two-dimensional photonic crystal slabs. *Physical Review B 62*(7), 4488–4492.

[40] Cretu, O., A. R. Botello-Mendez, I. Janowska, C. Pham-Huu, J.-C. Charlier, and F. Banhart (2013, August). Electrical transport measured in atomic carbon chains. *Nano Letters 13*(8), 3487–3493.

[41] Dammak, H., Y. Chalopin, M. Laroche, M. Hayoun, and J.-J. Greffet (2009, November). Quantum thermal bath for molecular dynamics simulation. *Physical Review Letters 103*(19), 190601.

[42] Darancet, P., A. Ferretti, D. Mayou, and V. Olevano (2007, February). Ab initio GW electron-electron interaction effects in quantum transport. *Physical Review B 75*(7), 075102.

[43] Darancet, P., V. Olevano, and D. Mayou (2009, March). Coherent electronic transport through graphene constrictions: Subwavelength regime and optical analogy. *Phys. Rev. Lett. 102*(13), 136803.

[44] Datta, S. (1997). *Electronic Transport in Mesoscopic Systems* (1st ed.). Cambridge, UK: Cambridge University Press.

[45] Delaney, P. and J. C. Greer (2004, July). Correlated electron transport in molecular electronics. *Physical Review Letters 93*(3), 036805.

[46] Dragoman, D. and M. Dragoman (2007). Giant thermoelectric effect in graphene. *Appl. Phys. Lett. 91*(20), 203116.

[47] Dresselhaus, M., G. Chen, M. Tang, R. Yang, H. Lee, D. Wang, Z. Ren, J. Fleurial, and P. Gogna (2007, April). New directions for Low-Dimensional thermoelectric materials. *Adv. Mater. 19*(8), 1043–1053.

[48] Dubi, Y. and M. Di Ventra (2011, March). Colloquium: Heat flow and thermoelectricity in atomic and molecular junctions. *Reviews of Modern Physics 83*(1), 131.

[49] Dundas, D., B. Cunningham, C. Buchanan, A. Terasawa, A. T. Paxton, and T. N. Todorov (2012, October). An ignition key for atomic-scale engines. *Journal of Physics: Condensed Matter 24*(40), 402203.

[50] Dundas, D., E. J. McEniry, and T. N. Todorov (2009). Current-driven atomic waterwheels. *Nature Nanotechnology 4*(2), 99–102.

[51] Elias, D. C., R. R. Nair, T. M. G. Mohiuddin, S. V. Morozov, P. Blake, M. P. Halsall, A. C. Ferrari, D. W. Boukhvalov, M. I. Katsnelson, A. K. Geim, and K. S. Novoselov (2009, January). Control of graphene's properties by reversible hydrogenation: Evidence for graphane. *Science 323*(5914), 610–613. PMID: 19179524.

[52] Engelund, M., J. A. Fürst, A. P. Jauho, and M. Brandbyge (2010, January). Localized edge vibrations and edge reconstruction by joule heating in graphene nanostructures. *Phys. Rev. Lett. 104*(3), 036807.

[53] Eroms, J. and D. Weiss (2009). Weak localization and transport gap in graphene antidot lattices. *New J. Phys. 11*(9), 095021.

[54] Esfarjani, K., M. Zebarjadi, and Y. Kawazoe (2006, February). Thermoelectric properties of a nanocontact made of two-capped single-wall carbon nanotubes calculated within the tight-binding approximation. *Phys. Rev. B 73*(8), 085406.

[55] Evgrafov, A., K. Maute, R. G. Yang, and M. L. Dunn (2009). Topology optimization for nano-scale heat transfer. *International Journal for Numerical Methods in Engineering 77*(2), 285–300.

[56] Frederiksen, T. (2007). *Inelastic transport theory for nanoscale systems*. DTU, DK: DTU Nanotech (MIC).

[57] Frederiksen, T., M. Brandbyge, N. Lorente, and A.-P. Jauho (2004, December). Inelastic scattering and local heating in atomic gold wires. *Physical Review Letters 93*(25), 256601.

[58] Frederiksen, T., M. Paulsson, M. Brandbyge, and A.-P. Jauho (2007, May). Inelastic transport theory from first principles: Methodology and application to nanoscale devices. *Phys. Rev. B 75*(20), 205413.

[59] Fürst, J. A., J. G. Pedersen, C. Flindt, N. A. Mortensen, M. Brandbyge, T. G. Pedersen, and A. Jauho (2009). Electronic properties of graphene antidot lattices. *New J. Phys. 11*(9), 095020.

[60] Gale, J. D. and A. L. Rohl (2003). The general utility lattice program (GULP). *Mol. Simulat. 29*(5), 291.

[61] Gao, G., W. Gao, E. Cannuccia, J. Taha-Tijerina, L. Balicas, A. Mathkar, T. N. Narayanan, Z. Liu, B. K. Gupta, J. Peng, Y. Yin, A. Rubio, and P. M. Ajayan (2012, July). Artificially stacked atomic layers: Toward new van der waals solids. *Nano Letters 12*(7), 3518–3525.

[62] Geim, A. K. (2009, June). Graphene: Status and prospects. *Science 324*(5934), 1530 –1534.

[63] Geim, A. K. and K. S. Novoselov (2007, March). The rise of graphene. *Nature Materials 6*(3), 183–191.

[64] Giesbers, A. J. M., E. C. Peters, M. Burghard, and K. Kern (2012, July). Charge transport gap in graphene antidot lattices. *Physical Review B 86*(4), 045445.

[65] Goldhaber-Gordon, D. (2011). Nanoelectronics: Making light of electrons. *Nature Nanotechnology 6*(4), 196–197.

[66] Goler, S., C. Coletti, V. Tozzini, V. Piazza, T. Mashoff, F. Beltram, V. Pellegrini, and S. Heun (2013, June). Influence of graphene curvature on hydrogen adsorption: Toward hydrogen storage devices. *The Journal of Physical Chemistry C 117*(22), 11506–11513.

[67] Guedon, C. M., H. Valkenier, T. Markussen, K. S. Thygesen, J. C. Hummelen, and S. J. van der Molen (2012, May). Observation of quantum interference in molecular charge transport. *Nature Nanotechnology 7*(5), 305–309.

[68] Guinea, F., M. I. Katsnelson, and A. K. Geim (2010, January). Energy gaps and a zero-field quantum hall effect in graphene by strain engineering. *Nat. Phys. 6*(1), 30–33.

[69] Gunst, T., T. Markussen, A.-P. Jauho, and M. Brandbyge (2011, October). Thermoelectric properties of finite graphene antidot lattices. *Physical Review B 84*(15), 155449.

[70] Hamann, D. R., M. Schlüter, and C. Chiang (1979, November). Norm-conserving pseudopotentials. *Physical Review Letters 43*(20), 1494–1497.

[71] Harrison, W. A. (1989). Electronic structure and the properties of solids - the physics of the chemical bond. *Dover Publications Inc.*.

[72] Haug, H. J. W. and A. P. Jauho (2008). *Quantum Kinetics in Transport and Optics of Semiconductors* (2nd ed.). Springer.

[73] Head-Gordon, M. and J. C. Tully (1995, December). Molecular dynamics with electronic frictions. *The Journal of Chemical Physics 103*(23), 10137–10145.

[74] Heremans, J. P., M. S. Dresselhaus, L. E. Bell, and D. T. Morelli (2013, July). When thermoelectrics reached the nanoscale. *Nature Nanotechnology 8*(7), 471–473.

[75] Hohenberg, P. and W. Kohn (1964, November). Inhomogeneous electron gas. *Physical Review 136*(3B), B864–B871.

[76] Holldobler, B. and E. O. Wilson (2008). *The Superorganism: The Beauty, Elegance, and Strangeness of Insect Societies* (1st ed.). W. W. Norton and Company.

[77] Hornekær, L., E. Rauls, W. Xu, Ž. Šljivančanin, R. Otero, I. Stensgaard, E. Lægsgaard, B. Hammer, and F. Besenbacher (2006, October). Clustering of chemisorbed h(d) atoms on the graphite (0001) surface due to preferential sticking. *Physical Review Letters 97*(18), 186102.

[78] Hu, J., X. Ruan, and Y. P. Chen (2009, July). Thermal conductivity and thermal rectification in graphene nanoribbons: A molecular dynamics study. *Nano Lett. 9*(7), 2730–2735.

[79] Hu, J., S. Schiffli, A. Vallabhaneni, X. Ruan, and Y. P. Chen (2010). Tuning the thermal conductivity of graphene nanoribbons by edge passivation and isotope engineering: A molecular dynamics study. *Appl. Phys. Lett. 97*(13), 133107.

[80] Huang, Z., T. S. Fisher, and J. Y. Murthy (2009). Simulation of phonon transmission through graphene and graphene nanoribbons with a green's function method. *J. Appl. Phys. 2010 108*(9), 094319.

[81] Huang, Z., T. S. Fisher, and J. Y. Murthy (2010). Simulation of thermal conductance across dimensionally mismatched graphene interfaces. *J. Appl. Phys. 108*(11), 114310.

[82] Ihnatsenka, S. and G. Kirczenow (2012, March). Conductance quantization in graphene nanoconstrictions with mesoscopically smooth but atomically stepped boundaries. *Phys. Rev. B 85*(12), 121407.

[83] Jia, X., M. Hofmann, V. Meunier, B. G. Sumpter, J. Campos-Delgado, J. M. Romo-Herrera, H. Son, Y.-P. Hsieh, A. Reina, J. Kong, M. Terrones, and M. S. Dresselhaus (2009, March). Controlled formation of sharp zigzag and armchair edges in graphitic nanoribbons. *Science 323*(5922), 1701–1705.

[84] Jiang, J., J. Wang, and B. Li (2009, May). Thermal conductance of graphene and dimerite. *Phys. Rev. B 79*(20), 205418.

[85] Jin, C., H. Lan, L. Peng, K. Suenaga, and S. Iijima (2009, May). Deriving carbon atomic chains from graphene. *Physical Review Letters 102*(20), 205501.

[86] Jo, I., I.-K. Hsu, Y. J. Lee, M. M. Sadeghi, S. Kim, S. Cronin, E. Tutuc, S. K. Banerjee, Z. Yao, and L. Shi (2010). Low-frequency acoustic phonon temperature distribution in electrically biased graphene. *Nano Lett. 11*(1), 85–90.

[87] Jones, R. O. and O. Gunnarsson (1989, July). The density functional formalism, its applications and prospects. *Reviews of Modern Physics 61*(3), 689–746.

[88] Kantorovich, L. (2008, September). Generalized langevin equation for solids. i. rigorous derivation and main properties. *Physical Review B 78*(9), 094304.

[89] Kantorovich, L. and N. Rompotis (2008, September). Generalized langevin equation for solids. II. stochastic boundary conditions for nonequilibrium molecular dynamics simulations. *Physical Review B 78*(9), 094305.

[90] Katsnelson, M. I., K. S. Novoselov, and A. K. Geim (2006, September). Chiral tunnelling and the klein paradox in graphene. *Nature Physics 2*(9), 620–625.

[91] Kim, M., N. S. Safron, E. Han, M. S. Arnold, and P. Gopalan (2010, April). Fabrication and characterization of Large-Area, semiconducting nanoperforated graphene materials. *Nano Lett. 10*(4), 1125–1131.

[92] Kim, R., S. Datta, and M. S. Lundstrom (2009). Influence of dimensionality on thermoelectric device performance. *J. Appl. Phys. 105*(3), 034506.

[93] Kögl, M. and E. C. N. Silva (2005, April). Topology optimization of smart structures: design of piezoelectric plate and shell actuators. *Smart Materials and Structures 14*(2), 387.

[94] Kohn, W. and L. J. Sham (1965, November). Self-consistent equations including exchange and correlation effects. *Physical Review 140*(4A), A1133–A1138.

[95] Král, P. and T. Seideman (2005, November). Current-induced rotation of helical molecular wires. *The Journal of Chemical Physics 123*(18), 184702–184702–5.

[96] Krauss, B., P. Nemes-Incze, V. Skakalova, L. P. Biro, K. von Klitzing, and J. H. Smet (2010, November). Raman scattering at pure graphene zigzag edges. *Nano Lett. 10*(11), 4544–4548.

[97] Kurth, S., G. Stefanucci, C.-O. Almbladh, A. Rubio, and E. K. U. Gross (2005, July). Time-dependent quantum transport: A practical scheme using density functional theory. *Physical Review B 72*(3), 035308.

[98] Lebedeva, I. V., A. A. Knizhnik, A. M. Popov, Y. E. Lozovik, and B. V. Potapkin (2011, March). Interlayer interaction and relative vibrations of bilayer graphene. *Physical Chemistry Chemical Physics 13*(13), 5687–5695.

[99] Lee, J.-K., S. Yamazaki, H. Yun, J. Park, G. P. Kennedy, G.-T. Kim, O. Pietzsch, R. Wiesendanger, S. Lee, S. Hong, U. Dettlaff-Weglikowska, and S. Roth (2013, August). Modification of electrical properties of graphene by substrate-induced nanomodulation. *Nano Letters 13*(8), 3494–3500.

[100] Li, N., J. Ren, L. Wang, G. Zhang, P. Hänggi, and B. Li (2012, July). Colloquium: Phononics: Manipulating heat flow with electronic analogs and beyond. *Reviews of Modern Physics 84*(3), 1045–1066.

[101] Li, W., H. Sevinçli, G. Cuniberti, and S. Roche (2010, July). Phonon transport in large scale carbon-based disordered materials: Implementation of an efficient order- n and real-space kubo methodology. *Phys. Rev. B 82*(4), 041410.

[102] Li, W., H. Sevinçli, S. Roche, and G. Cuniberti (2011, April). Efficient linear scaling method for computing the thermal conductivity of disordered materials. *Physical Review B 83*(15), 155416.

[103] Li, X., W. Cai, L. Colombo, and R. S. Ruoff (2009, December). Evolution of graphene growth on ni and cu by carbon isotope labeling. *Nano Lett. 9*(12), 4268–4272.

[104] Lin, Y.-M., C. Dimitrakopoulos, K. A. Jenkins, D. B. Farmer, H.-Y. Chiu, A. Grill, and P. Avouris (2010, May). 100-GHz transistors from wafer-scale epitaxial graphene. *Science 327*(5966), 662–662. PMID: 20133565.

[105] Liu, H., B. Kang, and J. Y. Lee (2013, August). Hidden role of a hydroxyl group in mediating the oxygen line defect on a graphene surface. *The Journal of Physical Chemistry C*.

[106] Liu, M., X. Yin, E. Ulin-Avila, B. Geng, T. Zentgraf, L. Ju, F. Wang, and X. Zhang (2011, June). A graphene-based broadband optical modulator. *Nature 474*(7349), 64–67.

[107] Löwdin, P.-O. (1951, November). A note on the Quantum-Mechanical perturbation theory. *The Journal of Chemical Physics 19*(11), 1396–1401.

[108] Lü, J.-T., M. Brandbyge, and P. Hedegård (2010, May). Blowing the fuse: Berry's phase and runaway vibrations in molecular conductors. *Nano Letters 10*(5), 1657–1663.

[109] Lü, J.-T., M. Brandbyge, P. Hedegård, T. N. Todorov, and D. Dundas (2012, June). Current-induced atomic dynamics, instabilities, and raman signals: Quasiclassical langevin equation approach. *Physical Review B 85*(24), 245444.

[110] Lü, J.-T., T. Gunst, P. Hedegård, and M. Brandbyge (2011, December). Current-induced dynamics in carbon atomic contacts. *Beilstein Journal of Nanotechnology 2*, 814–823.

[111] Lü, J.-T., P. Hedegård, and M. Brandbyge (2011, July). Laserlike vibrational instability in rectifying molecular conductors. *Physical Review Letters 107*(4), 046801.

[112] Lü, J. T. and J.-S. Wang (2007, Oct). Coupled electron and phonon transport in one-dimensional atomic junctions. *Phys. Rev. B 76*(16), 165418.

[113] Lü, J.-T., J.-S. Wang, P. Hedegård, and M. Brandbyge (2013). Thermoelectric transport in molecular conductors with electron-vibration interactions. *In preparation*.

[114] Mahen, G. D. (1990). *Many-Particle Physics* (2nd ed.). Plenum Press.

[115] Majumdar, A. (2004, February). Thermoelectricity in semiconductor nanostructures. *Science 303*(5659), 777 –778.

[116] Markussen, T. (2013, August). Phonon interference effects in molecular junctions. *arXiv e-print* (1308.2543).

[117] Markussen, T., A. Jauho, and M. Brandbyge (2009, July). Surface-Decorated silicon nanowires: A route to High-ZT thermoelectrics. *Phys. Rev. Lett. 103*(5), 055502.

[118] Markussen, T., R. Rurali, M. Brandbyge, and A. Jauho (2006, December). Electronic transport through si nanowires: Role of bulk and surface disorder. *Phys. Rev. B 74*(24), 245313.

[119] Markussen, T., R. Rurali, X. Cartoixà, A.-P. Jauho, and M. Brandbyge (2010, March). Scattering cross section of metal catalyst atoms in silicon nanowires. *Physical Review B 81*(12), 125307.

[120] Markussen, T., R. Rurali, A.-P. Jauho, and M. Brandbyge (2007, August). Scaling theory put into practice: First-principles modeling of transport in doped silicon nanowires. *Physical Review Letters 99*(7), 076803.

[121] Markussen, T., R. Stadler, and K. S. Thygesen (2010, October). The relation between structure and quantum interference in single molecule junctions. *Nano Letters 10*(10), 4260–4265.

[122] Martin, R. M. (2008). *Electronic structure - Basic theory and practical methods* (Corrected ed.). Cambridge University Press.

[123] Meir, Y. and N. S. Wingreen (1992, Apr). Landauer formula for the current through an interacting electron region. *Phys. Rev. Lett. 68*, 2512–2515.

[124] Mingo, N. (2009). Green's function methods for phonon transport through nanocontacts. In S. Volz (Ed.), *Thermal Nanosystems and Nanomaterials*, Volume 118, pp. 63–94. Berlin, Heidelberg: Springer Berlin Heidelberg.

[125] Mingo, N., K. Esfarjani, D. A. Broido, and D. A. Stewart (2010, January). Cluster scattering effects on phonon conduction in graphene. *Phys. Rev. B 81*(4), 045408.

[126] Mingo, N., D. A. Stewart, D. A. Broido, and D. Srivastava (2008, January). Phonon transmission through defects in carbon nanotubes from first principles. *Physical Review B 77*(3), 033418.

[127] Moore, G. (1998). Cramming more components onto integrated circuits. *Proceedings of the IEEE 86*(1), 82–85.

[128] Morozov, S. V., K. S. Novoselov, M. I. Katsnelson, F. Schedin, D. C. Elias, J. A. Jaszczak, and A. K. Geim (2008, January). Giant intrinsic carrier mobilities in graphene and its bilayer. *Physical Review Letters 100*(1), 016602.

[129] Mounet, N. and N. Marzari (2005, May). First-principles determination of the structural, vibrational and thermodynamic properties of diamond, graphite, and derivatives. *Physical Review B 71*(20), 205214.

[130] Nakada, K., M. Fujita, G. Dresselhaus, and M. S. Dresselhaus (1996). Edge state in graphene ribbons: Nanometer size effect and edge shape dependence. *Phys. Rev. B 54*, 17954.

[131] Neek-Amal, M. and F. M. Peeters (2012, May). Strain-engineered graphene through a nanostructured substrate. i. deformations. *Physical Review B 85*(19), 195445.

[132] Neel, N., J. Kröger, L. Limot, T. Frederiksen, M. Brandbyge, and R. Berndt (2007, February). Controlled contact to a c$_{60}$ molecule. *Physical Review Letters 98*(6), 065502.

[133] Neto, A. H. C. and K. Novoselov (2011a, August). New directions in science and technology: two-dimensional crystals. *Reports on Progress in Physics 74*(8), 082501.

[134] Neto, A. H. C. and K. Novoselov (2011b, March). Two-dimensional crystals: Beyond graphene. *Materials Express 1*(1), 10–17.

[135] Nikolic, B. K., K. K. Saha, T. Markussen, and K. S. Thygesen (2012, March). First-principles quantum transport modeling of thermoelectricity in single-molecule nanojunctions with graphene nanoribbon electrodes. *Journal of Computational Electronics 11*(1), 78–92.

[136] Nitzan, A. and M. A. Ratner (2003, May). Electron transport in molecular wire junctions. *Science 300*(5624), 1384–1389. PMID: 12775831.

[137] Novoselov, K. S., A. K. Geim, S. V. Morozov, D. Jiang, Y. Zhang, S. V. Dubonos, I. V. Grigorieva, and A. A. Firsov (2004, October). Electric field effect in atomically thin carbon films. *Science 306*(5696), 666–669. PMID: 15499015.

[138] Olesen, L. H., F. Okkels, and H. Bruus (2006). A high-level programming-language implementation of topology optimization applied to steady-state Navier–Stokes flow. *International Journal for Numerical Methods in Engineering 65*(7), 975–1001.

[139] Ong, Z.-Y. and E. Pop (2010, April). Molecular dynamics simulation of thermal boundary conductance between carbon nanotubes and SiO_{2}. *Physical Review B 81*(15), 155408.

[140] Ong, Z.-Y. and E. Pop (2011). Effect of substrate modes on thermal transport in supported graphene. *Physical Review B 84*(7), 075471.

[141] Ouyang, F., S. Peng, Z. Liu, and Z. Liu (2011, May). Bandgap opening in graphene antidot lattices: The missing half. *ACS Nano 5*(5), 4023–4030.

[142] Ouyang, Y. and J. Guo (2009). A theoretical study on thermoelectric properties of graphene nanoribbons. *Appl. Phys. Lett. 94*(26), 263107.

[143] Pan, Z., N. Liu, L. Fu, and Z. Liu (2011, November). Wrinkle engineering: A new approach to massive graphene nanoribbon arrays. *Journal of the American Chemical Society 133*(44), 17578–17581.

[144] Paulsson, M. and S. Datta (2003, June). Thermoelectric effect in molecular electronics. *Phys. Rev. B 67*(24), 241403.

[145] Paulsson, M., T. Frederiksen, and M. Brandbyge (2005). Modeling inelastic phonon scattering in atomic- and molecular-wire junctions. *Phys. Rev. B 72*(20), 201101.

[146] Paulsson, M., T. Frederiksen, and M. Brandbyge (2006, February). Inelastic transport through molecules: Comparing first-principles calculations to experiments. *Nano Letters 6*(2), 258–262.

[147] Pecchia, A. and A. D. Carlo (2004, August). Atomistic theory of transport in organic and inorganic nanostructures. *Reports on Progress in Physics 67*(8), 1497.

[148] Pedersen, T. G., C. Flindt, J. Pedersen, N. A. Mortensen, A. Jauho, and K. Pedersen (2008, April). Graphene antidot lattices: Designed defects and spin qubits. *Phys. Rev. Lett. 100*(13), 136804.

[149] Pedersen, T. G., A.-P. Jauho, and K. Pedersen (2009, March). Optical response and excitons in gapped graphene. *Physical Review B 79*(11), 113406.

[150] Perdew, J. P., K. Burke, and Y. Wang (1996, December). Generalized gradient approximation for the exchange-correlation hole of a many-electron system. *Physical Review B 54*(23), 16533–16539.

[151] Petersen, R., T. G. Pedersen, and A. Jauho (2011, January). Clar sextet analysis of triangular, rectangular, and honeycomb graphene antidot lattices. *ACS Nano 5*(1), 523–529.

[152] Pichanusakorn, P. and P. Bandaru (2010, January). Nanostructured thermoelectrics. *Mater. Sci. Eng.: R: Reports 67*(2-4), 19–63.

[153] Pop, E., V. Varshney, and A. K. Roy (2012). Thermal properties of graphene: Fundamentals and applications. *MRS Bulletin 37*(12), 1273–1281.

[154] Reddy, P., S. Jang, R. A. Segalman, and A. Majumdar (2007, March). Thermoelectricity in molecular junctions. *Science 315*(5818), 1568 –1571.

[155] Rocha, A. R., V. M. Garcia-Suarez, S. W. Bailey, C. J. Lambert, J. Ferrer, and S. Sanvito (2005, April). Towards molecular spintronics. *Nature materials 4*(4), 335–339. PMID: 15750597.

[156] Rubio, A. (2010, May). Hybridized graphene: Nanoscale patchworks. *Nature Materials 9*(5), 379–380.

[157] Ruffieux, P., O. Gröning, M. Bielmann, P. Mauron, L. Schlapbach, and P. Gröning (2002, December). Hydrogen adsorption on sp^{2}-bonded carbon: Influence of the local curvature. *Physical Review B 66*(24), 245416.

[158] Ryndyk, D. A., M. Hartung, and G. Cuniberti (2006, January). Nonequilibrium molecular vibrons: An approach based on the nonequilibrium green function technique and the self-consistent born approximation. *Physical Review B 73*(4), 045420.

[159] Saha, K. K., T. Markussen, K. S. Thygesen, and B. K. Nikolic (2011, March). Multiterminal single-molecule–graphene-nanoribbon thermoelectric devices with gate-voltage tunable figure of merit ZT. *arXiv:1103.0573v1*.

[160] Sancho, M. P. L., J. M. L. Sancho, and J. Rubio (1984, May). Quick iterative scheme for the calculation of transfer matrices: application to mo (100). *Journal of Physics F: Metal Physics 14*(5), 1205.

[161] Savin, A. V., Y. S. Kivshar, and B. Hu (2010, November). Suppression of thermal conductivity in graphene nanoribbons with rough edges. *Phys. Rev. B 82*(19), 195422.

[162] Schrödinger, E. (1926, December). An undulatory theory of the mechanics of atoms and molecules. *Physical Review 28*(6), 1049–1070.

[163] Seol, J. H., I. Jo, A. L. Moore, L. Lindsay, Z. H. Aitken, M. T. Pettes, X. Li, Z. Yao, R. Huang, D. Broido, N. Mingo, R. S. Ruoff, and L. Shi (2010, April). Two-Dimensional phonon transport in supported graphene. *Science 328*(5975), 213 –216.

[164] SevinÃ§li, H. and G. Cuniberti (2010, March). Enhanced thermoelectric figure of merit in edge-disordered zigzag graphene nanoribbons. *Phys. Rev. B 81*(11), 113401.

[165] Sivan, U. and Y. Imry (1986, January). Multichannel landauer formula for thermoelectric transport with application to thermopower near the mobility edge. *Phys. Rev. B 33*(1), 551.

[166] Slater, J. C. and G. F. Koster (1954, June). Simplified LCAO method for the periodic potential problem. *Physical Review 94*(6), 1498–1524.

[167] Soler, J. M., E. Artacho, J. D. Gale, A. Garcia, J. Junquera, P. Ordejon, and D. Sanchez-Portal (2002, March). The SIESTA method for ab initio order- n materials simulation. *J. Phys.: Condens. Matter 14*(11), 2745–2779.

[168] Sorbello, R. S. (1997). Theory of electromigration. In H. EHRENREICH and F. SPAEPEN (Eds.), *Solid State Physics*, Volume Volume 51, pp. 159–231. Academic Press.

[169] Srivastava, D., D. W. Brenner, J. D. Schall, K. D. Ausman, M. Yu, and R. S. Ruoff (1999, May). Predictions of enhanced chemical reactivity at regions of local conformational strain on carbon nanotubes: Kinky chemistry. *The Journal of Physical Chemistry B 103*(21), 4330–4337.

[170] Strange, M., I. S. Kristensen, K. S. Thygesen, and K. W. Jacobsen (2008, March). Benchmark density functional theory calculations for nanoscale conductance. *The Journal of Chemical Physics 128*(11), 114714–114714–8.

[171] Sutton, A. P. (2004). *Electronic Structure of materials* (1st ed.). Oxford University Press.

[172] Takezawa, A. and M. Kitamura (2012). Geometrical design of thermoelectric generators based on topology optimization. *International Journal for Numerical Methods in Engineering 90*(11), 1363–1392.

[173] Tan, X. and P. Zapol (2013, August). Regioselective oxidation of strained graphene for controllable synthesis of nanoribbons. *The Journal of Physical Chemistry C*.

[174] Tang, J., H. Wang, D. H. Lee, M. Fardy, Z. Huo, T. P. Russell, and P. Yang (2010, October). Holey silicon as an efficient thermoelectric material. *Nano Lett. 10*(10), 4279–4283.

[175] Taylor, J., M. Brandbyge, and K. Stokbro (2002, September). Theory of rectification in tour wires: The role of electrode coupling. *Physical Review Letters 89*(13), 138301.

[176] Taylor, J., H. Guo, and J. Wang (2001, June). Ab initio modeling of quantum transport properties of molecular electronic devices. *Physical Review B 63*(24), 245407.

[177] Tekman, E. and S. Ciraci (1991, March). Theoretical study of transport through a quantum point contact. *Physical Review B 43*(9), 7145–7169.

[178] Thygesen, K. S. (2008, April). Impact of exchange-correlation effects on the IV characteristics of a molecular junction. *Physical Review Letters 100*(16), 166804.

[179] Thygesen, K. S. and A. Rubio (2008, March). Conserving GW scheme for nonequilibrium quantum transport in molecular contacts. *Physical Review B 77*(11), 115333.

[180] Todorov, T. N. (2002). Tight-binding simulation of current-carrying nanostructures. *J. Phys.: Condens. Matter 14*(11), 3049.

[181] Troullier, N. and J. Martins (1990, May). A straightforward method for generating soft transferable pseudopotentials. *Solid State Communications 74*(7), 613–616.

[182] Ulstrup, S., T. Frederiksen, and M. Brandbyge (2012, December). Nonequilibrium electron-vibration coupling and conductance fluctuations in a c_{60} junction. *Physical Review B 86*(24), 245417.

[183] Vanevic, M., V. M. Stojanovic, and M. Kindermann (2009, July). Character of electronic states in graphene antidot lattices: Flat bands and spatial localization. *Phys. Rev. B 80*(4), 045410.

[184] Verlet, L. (1967, July). Computer "Experiments" on classical fluids. i. thermodynamical properties of lennard-jones molecules. *Physical Review 159*(1), 98–103.

[185] Vining, C. B. (2009, February). An inconvenient truth about thermoelectrics. *Nat. Mater.er 8*(2), 83–85.

[186] Wang, F., J. S. Jensen, and O. Sigmund (2011, March). Robust topology optimization of photonic crystal waveguides with tailored dispersion properties. *Journal of the Optical Society of America B 28*(3), 387–397.

[187] Wang, F., B. S. Lazarov, and O. Sigmund (2011, June). On projection methods, convergence and robust formulations in topology optimization. *Structural and Multidisciplinary Optimization 43*(6), 767–784.

[188] Wang, J.-S. (2007, October). Quantum thermal transport from classical molecular dynamics. *Physical Review Letters 99*(16), 160601.

[189] Wang, J.-S., B. K. Agarwalla, H. Li, and J. Thingna (2013). Nonequilibrium green's function method for quantum thermal transport. *Frontiers of Physics*, 1–24.

[190] Wang, J.-S., X. Ni, and J.-W. Jiang (2009, December). Molecular dynamics with quantum heat baths: Application to nanoribbons and nanotubes. *Physical Review B 80*(22), 224302.

[191] Wang, J.-S., N. Zeng, J. Wang, and C. K. Gan (2007, June). Nonequilibrium green's function method for thermal transport in junctions. *Physical Review E 75*(6), 061128.

[192] Wang, L. and B. Li (2008). Phononics gets hot. *IOP physics world 21*(3), 27–29. From electronics to "phononics".

[193] Wang, Q. H., K. Kalantar-Zadeh, A. Kis, J. N. Coleman, and M. S. Strano (2012, November). Electronics and optoelectronics of two-dimensional transition metal dichalcogenides. *Nature Nanotechnology 7*(11), 699–712.

[194] Williams, J. R., T. Low, M. S. Lundstrom, and C. M. Marcus (2011). Gate-controlled guiding of electrons in graphene. *Nature Nanotechnology 6*(4), 222–225.

[195] Xia, Y., Z. Li, and H. Kreuzer (2011, November). Adsorption, diffusion and desorption of hydrogen on graphene. *Surface Science 605*(21–22), L70–L73.

[196] Xu, Q., M.-Y. Wu, G. F. Schneider, L. Houben, S. K. Malladi, C. Dekker, E. Yucelen, R. E. Dunin-Borkowski, and H. W. Zandbergen (2013, January). Controllable atomic scale patterning of freestanding monolayer graphene at elevated temperature. *ACS Nano*.

[197] Xue, Y., S. Datta, and M. A. Ratner (2002, August). First-principles based matrix green's function approach to molecular electronic devices: general formalism. *Chemical Physics 281*(2–3), 151–170.

[198] Yan, Y. and H. Zhao (2012, June). Phonon interference and its effect on thermal conductance in ring-type structures. *Journal of Applied Physics 111*(11), 113531–113531–4.

[199] Yin, H., W. Li, X. Hu, and R. Tao (2010, May). Coherent transport of armchair graphene constrictions. *J. Appl. Phys. 107*(10), 103706–103706–6.

[200] Yoon, D., Y.-W. Son, and H. Cheong (2011, August). Negative thermal expansion coefficient of graphene measured by raman spectroscopy. *Nano Letters 11*(8), 3227–3231.

[201] Yoon, G. H. and O. Sigmund (2008, August). A monolithic approach for topology optimization of electrostatically actuated devices. *Computer Methods in Applied Mechanics and Engineering 197*(45–48), 4062–4075.

[202] Yu, J., S. Mitrovic, D. Tham, J. Varghese, and J. R. Heath (2010, October). Reduction of thermal conductivity in phononic nanomesh structures. *Nat. Nanotech. 5*(10), 718–721.

[203] Yuan, J.-H., Z. Cheng, Q.-J. Zeng, J.-P. Zhang, and J.-J. Zhang (2011, November). Velocity-controlled guiding of electron in graphene: Analogy of optical waveguides. *Journal of Applied Physics 110*(10), 103706–103706–6.

[204] Yuan, S., R. Roldán, A.-P. Jauho, and M. I. Katsnelson (2013, February). Electronic properties of disordered graphene antidot lattices. *Physical Review B 87*(8), 085430.

[205] Zhang, F.-M., Y. He, and X. Chen (2009, May). Guided modes in graphene waveguides. *Applied Physics Letters 94*(21), 212105–212105–3.

[206] Zhang, H., G. Lee, A. F. Fonseca, T. L. Borders, and K. Cho (2010). Isotope effect on the thermal conductivity of graphene. *J. Nanomater. 2010*, 1–6.

[207] Zhang, W., N. Mingo, and T. S. Fisher (2007, November). Simulation of phonon transport across a non-polar nanowire junction using an atomistic greenâ€™s function method. *Physical Review B 76*(19), 195429.

Chapter 9

Appendix A: Derivations and technical information

9.1 DFT settings

We use single-zeta-polarized (SZP) localized pseudoatomic orbitals in the basis set for both hydrogen and carbon. Exchange-correlation effects are handled within GGA-PBE and a grid cutoff of 210 Ry is applied. The Brillouin zone was sampled with a [5 1 2] Monkhorst-Pack grid, with the x-axis as the transverse direction and the z-axis as the transport direction. With these parameters the optimal nearest neighbor distance of graphene is approximately 1.46 Å. The system was relaxed until all forces were smaller than 0.005eV/Ang. The potential drop was applied between the semi-infinite leads as implemented in the TranSIESTA method[27]. We used 150 points along the bias contour with a broadening of 0.01 eV.

9.2 Transport cheat sheet: Symmetries and technical relations

This section collects the most important matrix properties of Greens functions, self-energies and variables for both electrons and phonons.

The Fourier transform between time and frequency is defined as

$$\mathcal{F}\{f(t)\} = \int dt f(t) e^{i\omega t}, \tag{9.1}$$

$$\mathcal{F}^{-1}\{f(\omega)\} = \int \frac{d\omega}{2\pi} f(\omega) e^{-i\omega t}, \tag{9.2}$$

throughout this project. We frequently apply the Sokhatsky–Weierstrass theorem:

$$\lim_{\eta\to 0^+} \int dx \frac{f(x)}{x \pm i\eta} = \mathcal{P}\int dx \frac{f(x)}{x} \mp i\pi f(0) \tag{9.3}$$

The principal value, denoted $\mathcal{P}$, integral is related to the Hilbert transform defined as:

$$\mathcal{H}\{f(x')\}(x) = \frac{1}{\pi}\mathcal{P}\int \frac{f(x')}{x'-x} dx' \,. \tag{9.4}$$

9.2.1 Mathematical relations - distribution functions

The Bose-Einstein distribution is related to $coth(x)$. They can be expanded to first order in $\hbar\omega$ by using that $e^x \approx 1 + x$:

$$\coth(\beta\frac{\hbar\omega}{2}) = 2n_B(\hbar\omega) + 1 = \frac{2}{e^{\beta\hbar\omega} - 1} + 1 \approx 2\frac{k_B T}{\hbar\omega} + 1 \tag{9.5}$$

The Fermi distribution satisfy

$$\begin{aligned} \frac{\partial n_F}{\partial \mu} &= -\frac{\partial n_F}{\partial \varepsilon} \\ \frac{\partial n_F}{\partial T} &= -\frac{\varepsilon - \mu}{T}\frac{\partial n_F}{\partial \varepsilon} \end{aligned} \tag{9.6}$$

The Bose distribution satisfy

$$\begin{aligned} n_B(-\hbar\omega) &= -(1 + n_B(\hbar\omega)) \\ \frac{\partial n_B}{\partial \hbar\omega}(-\omega, T) &= \frac{\partial n_B}{\partial \hbar\omega}(\omega, T) \\ \frac{\partial n_B}{\partial T}(-\omega, T) &= -\frac{\partial n_B}{\partial T}(\omega, T) \\ \frac{\partial n_B}{\partial T}(\omega, T) &= -\frac{\hbar\omega}{T}\frac{\partial n_B}{\partial \hbar\omega}(\omega, T) \end{aligned} \tag{9.7}$$

In case the electronic temperature in two Fermi distributions is the same we have

$$\begin{aligned} n_F^\alpha(\varepsilon_1)\left[1 - n_F^\beta(\varepsilon_2)\right] &= -n_B(\varepsilon_1 - \varepsilon_2 + \mu_\beta - \mu_\alpha)\left[n_F^\alpha(\varepsilon_1) - n_F^\beta(\varepsilon_2)\right] \\ &= -\left(n_B(\varepsilon_2 - \varepsilon_1 + \mu_\alpha - \mu_\beta) + 1\right)\left[n_F^\beta(\varepsilon_2) - n_F^\alpha(\varepsilon_1)\right] \end{aligned} \tag{9.8}$$

9.2.2 Relations for the noninteracting system

The free electron and phonon greater and lesser Green's functions are directly related to the spectral functions as:

$$\begin{aligned} G_0^>(\varepsilon) &= -i\sum_\alpha \left(1 - n_F^\alpha(\varepsilon)\right) A_\alpha(\varepsilon) \\ G_0^<(\varepsilon) &= i\sum_\alpha n_F^\alpha(\varepsilon) A_\alpha(\varepsilon) \\ D_0^>(\omega) &= -i\sum_\alpha \left(1 + n_B^\alpha(\omega)\right) \mathcal{A}_\alpha(\omega) \\ D_0^<(\omega) &= -i\sum_\alpha n_B^\alpha(\omega) \mathcal{A}_\alpha(\omega) \end{aligned} \tag{9.9}$$

The electron self-energies of the noninteraction leads are expressed in terms of the lead coupling matrices, Γ^α:

$$\begin{aligned} \Sigma_\alpha^<(\varepsilon) &= i n_F(\varepsilon)\Gamma^\alpha(\varepsilon) \\ \Sigma_\alpha^>(\varepsilon) &= i(n_F(\varepsilon) - 1)\Gamma^\alpha(\varepsilon) \end{aligned} \tag{9.10}$$

The corresponding equations for the free phonon baths are:

$$\begin{aligned} \Pi_\alpha^<(\omega) &= -i n_B(\omega)\Gamma_{ph}^\alpha(\omega) \\ \Pi_\alpha^>(\omega) &= -i(n_B(\omega) + 1)\Gamma_{ph}^\alpha(\omega) \end{aligned} \tag{9.11}$$

9.2.3 Symmetry relations

The free phonon variables satisfy

$$\begin{aligned} A_\alpha(-\omega) &= -A^*_\alpha(\omega) \\ \tilde{A}_\alpha(-\omega) &= -\tilde{A}^*_\alpha(\omega) \\ \Gamma^\alpha_{ph}(-\omega) &= -2\mathrm{Im}(\Pi^{*\mathrm{r}}_\alpha(\omega)) = -\Gamma^\alpha_{\mathrm{ph}}(\omega) \\ D_0^{r/a}(-\omega) &= D_0^{*r/a}(\omega) \end{aligned} \tag{9.12}$$

The interaction weighted electron-hole density of states satisfy

$$\Lambda^{\alpha\beta}_{kl}(\omega) = \Lambda^{\alpha\beta *}_{lk}(\omega), \tag{9.13}$$
$$\Lambda^{\alpha\beta}_{kl}(\omega) = -\Lambda^{\beta\alpha}_{lk}(-\omega), \tag{9.14}$$
$$\Lambda(-\omega) = -\Lambda^*(\omega), \tag{9.15}$$

where we have defined $\Lambda = \sum_{\alpha,\beta} \Lambda^{\alpha\beta}$.

The spectral density describing the stochastic electronic forces satisfy:

$$S^{e\dagger}_f(\omega) = S^e_f(\omega) \tag{9.16}$$
$$S^e_f(-\omega) = S^{e*}_f(\omega) \tag{9.17}$$

Consequently $S^e_f(t)$ is real, but $S^e_f(-t) \neq S^e_f(t)$ at finite bias.

The full self-energy describing the deterministic forces satisfy:

$$\tilde{\Pi}^\dagger(\omega) = -\tilde{\Pi}(\omega) \tag{9.18}$$
$$\tilde{\Pi}(-\omega) = \tilde{\Pi}^*(\omega) \tag{9.19}$$

9.3 Ballistic thermoelectric properties

The thermoelectric performance of a device with electrons that do not interact with phonons is related to the difference in electron distribution if a temperature difference is imposed between the leads. Starting from the Landauer formula, eqn. 2.4, and assuming a small bias and temperature difference, we can do a linear expansion of the Fermi distribution function over $\delta T^e/T^e$ and $\delta\mu$:

$$\begin{aligned} n_F(\mu, T) &\approx n_F(\mu_0, T_0) + \frac{\partial n_F}{\partial T}\delta T + \frac{\partial n_F}{\partial \mu}\delta\mu \\ &= n_F(\mu_0, T_0) - \frac{\varepsilon - \mu}{T}\frac{\partial n_F}{\partial \varepsilon}\delta T - \frac{\partial n_F}{\partial \varepsilon}\delta\mu\,. \end{aligned} \tag{9.20}$$

Inserting in the Landauer formula, eqn. 2.4, we obtain the linear response to a infinitesimal difference in temperature or chemical potential between the leads:

$$\delta I = \frac{2e}{\hbar}\int \frac{d\varepsilon}{2\pi}\mathcal{T}_e(\varepsilon)\left((\varepsilon-\mu)\frac{\delta T^e}{T^e} + \delta\mu\right)\left(-\frac{\partial n_F}{\partial\varepsilon}\right). \tag{9.21}$$

In the same way, the heat current is:

$$\delta J^e = \frac{2}{\hbar}\int \frac{d\varepsilon}{2\pi}(\varepsilon-\mu)\mathcal{T}_e(\varepsilon)\left((\varepsilon-\mu)\frac{\delta T^e}{T^e} + \delta\mu\right)\left(-\frac{\partial n_F}{\partial\varepsilon}\right). \tag{9.22}$$

Collecting the equations in matrix form, we get:

$$\begin{pmatrix} \frac{\delta I}{e} \\ \delta J^e \end{pmatrix} = \begin{pmatrix} L_0 & L_1 \\ L_1 & L_2 \end{pmatrix} \begin{pmatrix} \delta\mu \\ \frac{\delta T^e}{T^e} \end{pmatrix} \tag{9.23}$$

with

$$\delta\mu = \mu_L - \mu_R, \tag{9.24}$$
$$\delta T_L^e = T^e + \delta T^e, \tag{9.25}$$
$$\delta T_R^e = T^e, \tag{9.26}$$

and

$$L_n(\mu) = \frac{2}{\hbar}\int \frac{d\varepsilon}{2\pi}(\varepsilon-\mu)^n \mathcal{T}_e(\varepsilon)\left(-\frac{\partial n_F}{\partial\varepsilon}\right) \tag{9.27}$$

The Onsager reciprocal relation is obviously satisfied. We readily obtain the thermoelectric transport coefficients as given in section 2.1 from eqn. 9.23. The Seebeck coefficient is negative(positive) if electrons(holes) are dominating the transport.

9.4 Thermoelectric properties of an electron-phonon interacting nanojunction

We consider a system consisting of an interacting central region connected to two noninteracting electron baths and two phonon baths, see Fig. 2.1. We label the chemical potentials μ_L and μ_R, electronic temperatures T_L^e and T_R^e and the phonon bath temperatures T_L^{ph} and T_R^{ph}. The setup in mind is further described in section 2.2. The derivation was originally carried out by my colleague Jing-Tao Lü, who I thank for the sharing of knowledge. The problem is well-suited for the NEGF approach due to the free nature of the separate baths and the strong interactions in a central region driven by nonequilibrium conditions. The influence of the electronic current on the phonon distribution and opposite is evaluated as a perturbation to the equilibrium distribution (to second order in the electron-phonon coupling). The treatment is equivalent to the first Born approximation applied in the lowest order expansion. This is a current-conserving approximation that reduce computational demands, and at the same time agrees with the results of self-consistent approximations, for a range of realistic devices[58].

9.4.1 Electron current

Inserting the lowest order expansion, i.e. the closed Dyson and Keldysh equations in eqn. 9.35, in eqn. 2.13 we obtain:

$$\begin{aligned} I_\alpha = & \sum_\sigma \frac{e}{\hbar}\int_{-\infty}^{\infty}\frac{d\varepsilon}{2\pi}\mathrm{Tr}\left[\left(\Sigma_\alpha^< G_0^r \Sigma_{LR}^> G_0^a - G_0^r\Sigma_{LR}^< G_0^a\Sigma_\alpha^>\right)\right. \\ & + \left(G_0^r\Sigma_{eph}^r G_0^r\Sigma_{LR}^> G_0^a\Sigma_\alpha^< - G_0^r\Sigma_{eph}^r G_0^r\Sigma_{LR}^< G_0^a\Sigma_\alpha^>\right) \\ & + \left(G_0^r\Sigma_{LR}^> G_0^a\Sigma_{eph}^a G_0^a\Sigma_\alpha^< - G_0^r\Sigma_{LR}^< G_0^a\Sigma_{eph}^a G_0^a\Sigma_\alpha^>\right) \\ & + \left.\left(\Sigma_\alpha^< G_0^r\Sigma_{eph}^> G_0^a - G_0^r\Sigma_{eph}^< G_0^a\Sigma_\alpha^>\right)\right] \end{aligned} \tag{9.28}$$

Here $\Sigma_{LR}^{</>} = \Sigma_L^{</>} + \Sigma_R^{</>}$. In the following we label the four terms in separate parentheses by $I_\alpha^{(i)}$ with $i = 1,..,4$. We apply the self-energies of the noninteraction leads as

expressed in terms of the lead coupling matrices, Γ^α, see eqn. 9.10. After some algebra, we obtain the following relation:

$$\Sigma^>_{LR} g \Sigma^<_\alpha - \Sigma^<_{LR} g \Sigma^>_\alpha = \Gamma^{\bar{\alpha}} g \Gamma^\alpha \left(n_F^\alpha - n_F^{\bar{\alpha}} \right) \tag{9.29}$$

where $\bar{\alpha}$ is the lead opposite to α and g is any sequence of matrices, i.e. $g = G_0^r$ for $I_\alpha^{(2)}$ and $g = G_0^a \Sigma^<_{eph} G_0^a$ for $I_\alpha^{(3)}$. Inserting this in eqn. 9.28 we obtain:

$$\begin{aligned}
I_\alpha &= \sum_{i=1}^{4} I_\alpha^{(i)}, \\
I_\alpha^{(1)} &= \sum_\sigma \frac{e}{\hbar} \int_{-\infty}^{\infty} \frac{d\varepsilon}{2\pi} \mathrm{Tr} \left[\Gamma^\alpha(\varepsilon) G_0^r(\varepsilon) \Gamma^{\bar{\alpha}}(\varepsilon) G_0^a(\varepsilon) \right] \\
I_\alpha^{(2)} &= \sum_\sigma \frac{e}{\hbar} \int_{-\infty}^{\infty} \frac{d\varepsilon}{2\pi} \mathrm{Tr} \left[\Gamma_\alpha(\varepsilon) G_0^r(\varepsilon) \Sigma^r_{eph}(\varepsilon) A_{\bar{\alpha}}(\varepsilon) \right] \\
I_\alpha^{(3)} &= \sum_\sigma \frac{e}{\hbar} \int_{-\infty}^{\infty} \frac{d\varepsilon}{2\pi} \mathrm{Tr} \left[\Gamma_\alpha(\varepsilon) A_{\bar{\alpha}}(\varepsilon) \Sigma^a_{eph}(\varepsilon) G_0^a(\varepsilon) \right]
\end{aligned} \tag{9.30}$$

The first term is the noninteracting Landauer part, while the next two terms originate from a correction in the electron DOS due to e-ph coupling. The fourth, $I_\alpha^{(4)}$, term is more complicatedly related to the phonon emission and absorption:

$$\begin{aligned}
I_\alpha^{(4)} &= \sum_\sigma \frac{e}{\hbar} \int_{-\infty}^{\infty} \frac{d\varepsilon}{2\pi} \mathrm{Tr} \left[G_0^r \Sigma^>_{eph} G_0^a \Sigma^<_\alpha - G_0^r \Sigma^<_{eph} G_0^a \Sigma^>_\alpha \right] \\
&= \sum_\sigma \frac{e}{\hbar} \int_{-\infty}^{\infty} \frac{d\varepsilon}{2\pi} i \mathrm{Tr} \left[G_0^r \Sigma^>_{eph} G_0^a \Gamma^\alpha n_F^\alpha - G_0^r \Sigma^<_{eph} G_0^a \Gamma^\alpha \left(n_F^\alpha - 1 \right) \right]
\end{aligned} \tag{9.31}$$

For small bias, $\delta\mu$, and temperature difference, $\delta T^e / T^e$, we can do a linear expansion of the Fermi distribution function, eqn. 9.20. $I_\alpha^{(1)}$ gives the usual free electron thermoelectric coefficients, $L_n(\mu)$ in eqn. 2.6, while $I_\alpha^{(2,3,4)}$ each gives corrections due to e-ph coupling.

To obtain a closed relation for $I_\alpha^{(4)}$ we need to assume a specific form of interaction self-energy, Σ_{eph}. Here we apply the two lowest order 'Hartree' and 'Fock' diagrams in eqn. 2.27. Inserting the free electron Green's functions, in eqn. 9.9, together with the definition of the direct and time-reversed spectral functions, in eqn. 2.25, in the expression for the fourth current term, in eqn. 9.31, we obtain:

$$\begin{aligned}
I_\alpha^{(4)} &= \sum_\sigma \frac{e}{\hbar} \int_{-\infty}^{\infty} \frac{d\varepsilon}{2\pi} \hbar \sum_{i,j,\gamma,\beta} \int_{-\infty}^{\infty} \frac{d\omega}{2\pi} X_{ji}^{\tilde{\alpha}\beta}(\varepsilon, \varepsilon - \omega) \mathcal{A}_{ij}^\gamma(\omega) \\
&\times \left[(1 - n_F^\beta(\varepsilon - \omega)) n_F^\alpha(\varepsilon) (1 + n_B^\gamma(\omega)) - n_F^\beta(\varepsilon - \omega)(1 - n_F^\alpha(\varepsilon)) n_B^\gamma(\omega) \right],
\end{aligned} \tag{9.32}$$

where we defined

$$X_{ji}^{\tilde{\alpha}\beta}(\varepsilon, \varepsilon - \omega) \equiv \mathrm{Tr} \left[M_{\lambda_n} \tilde{A}_\alpha(\varepsilon) M_{\lambda_n} A_{\bar{\alpha}}(\varepsilon - \omega) \right] \tag{9.33}$$

Here α, β are indices labeling the electronic baths and γ label the phonon baths.

In case of equal electronic temperatures we can apply eqn. 9.8 to obtain

$$\begin{aligned}
I_\alpha^{(4)} &= \sum_\sigma e \sum_{\gamma\beta} \int_{-\infty}^{\infty} \frac{d\varepsilon}{2\pi} \int_{-\infty}^{\infty} \frac{d\omega}{2\pi} \mathrm{Tr} \left[X^{\tilde{\alpha}\bar{\alpha}}(\varepsilon, \varepsilon - \omega) \mathcal{A}^\gamma(\omega) \right] \\
&\times \left(n_B^\gamma(\omega) - n_B(\omega + \mu_\beta - \mu_\alpha) \right) \left(n_F^\alpha(\varepsilon) - n_F^\beta(\varepsilon - \omega) \right)
\end{aligned} \tag{9.34}$$

9.4.2 Thermal current

Once again we apply the LOE of the Green's functions:

$$\begin{aligned} D^{r/a}(\omega) &= D_0^{r/a}(\omega) + D_0^{r/a}(\omega)\Pi_{eph}^{r/a}(\omega)D^{r/a}(\omega) \approx D_0^{r/a}(\omega) + D_0^{r/a}(\omega)\Pi_{eph}^{r/a}(\omega)D_0^{r/a}(\omega) \\ D^{</>}(\omega) &= D^{</>}(\omega)\Pi^{</>}(\omega)D^{a}(\omega) \\ &\approx D_0^{</>}(\omega) + D_0^{r}(\omega)\Pi_{eph}^{</>}(\omega)D_0^{a}(\omega) \\ &+ D_0^{r}(\omega)\Pi_{eph}^{r}(\omega)D_0^{r}(\omega)\Pi_{LR}^{</>}(\omega)D_0^{a}(\omega) + D_0^{r}(\omega)\Pi_{LR}^{</>}(\omega)D_0^{a}(\omega)\Pi_{eph}^{a}(\omega)D_0^{a}(\omega) \end{aligned} \tag{9.35}$$

where $D_0^{</>} = D_0^r \Pi_{LR}^{</>} D_0^a$. Inserting these expression in the Meir-Wingreen expression for the phonon thermal current, eqn. 2.15, we once again obtain four different contributions, J_α^{ph}. Using the relations for the free phonon self-energies, eqn. 9.11, we obtain the general relation:

$$\Pi_{LR}^{>} g \Pi_\alpha^{<} - \Pi_{LR}^{<} g \Pi_\alpha^{>} = \Gamma^{\bar{\alpha}} g \Gamma^{\alpha} \left(n_B^{\bar{\alpha}} - n_B^{\alpha} \right) , \tag{9.36}$$

where g is any sequence of matrices, i.e. $g = D_0^a$ for $J_\alpha^{(1,2)}$ and $g = D_0^a \Pi_{eph}^a D_0^a$ for $J_\alpha^{(3)}$. We hereby obtain four contributions to the thermal conductance:

$$\mathcal{K}_{ph} = \sum_{i=1}^{4} \mathcal{K}_{ph}^{(i)} , \tag{9.37}$$

with

$$\mathcal{K}_{ph}^{(1)} = \int \frac{d\omega}{4\pi} \hbar\omega \mathrm{Tr} \left[\mathcal{A}_{\bar{\alpha}}(\omega) \Gamma_\alpha^{ph}(\omega) \right] \frac{\partial n}{\partial T^{ph}} T^{ph}, \tag{9.38}$$

$$\mathcal{K}_{ph}^{(2)} = \int \frac{d\omega}{4\pi} \hbar\omega \mathrm{Tr} \left[D_0^r(\omega) \Pi_{eph}^r(\omega) \mathcal{A}_{\bar{\alpha}}(\omega) \Gamma_\alpha^{ph}(\omega) \right] \frac{\partial n}{\partial T^{ph}} T^{ph}, \tag{9.39}$$

$$\mathcal{K}_{ph}^{(3)} = \int \frac{d\omega}{4\pi} \hbar\omega \mathrm{Tr} \left[\mathcal{A}_{\bar{\alpha}}(\omega) \Pi_{eph}^a(\omega) D_0^a(\omega) \Gamma_\alpha^{ph}(\omega) \right] \frac{\partial n}{\partial T^{ph}} T^{ph}, \tag{9.40}$$

$$\mathcal{K}_{ph}^{(4)} = i \int \frac{d\omega}{4\pi} \hbar\omega \mathrm{Tr} \left[D_0^r(\omega) (\Pi_{eph}^{>}(\omega) - \Pi_{eph}^{<}(\omega)) D_0^a(\omega) \Gamma_\alpha^{ph}(\omega) \right] \frac{\partial n}{\partial T^{ph}} T^{ph}. \tag{9.41}$$

Similarly to the electron case, $\mathcal{K}_n^{(2)}$ and $\mathcal{K}_n^{(3)}$ are due to corrections to the phonon DOS

$$\Delta \mathcal{A}_{\bar{\alpha}} = D_0^r(\varepsilon) \Pi_{eph}^r(\varepsilon) \mathcal{A}_{\bar{\alpha}}(\varepsilon) + \mathcal{A}_{\bar{\alpha}}(\varepsilon) \Pi_n^a(\varepsilon) D_0^a(\varepsilon). \tag{9.42}$$

Therefore, we have three corrections to the ballistic transmission function, $\mathcal{T}_{ph}^{(1)}$, due to electron-phonon interaction:

$$\mathcal{T}_{ph}^{(1)} = \mathrm{Tr} \left[\mathcal{A}_{\bar{\alpha}}(\omega) \Gamma_\alpha^{ph}(\omega) \right], \tag{9.43}$$

$$\mathcal{T}_{ph}^{(2)} = \mathrm{Tr} \left[D_0^r(\omega) \Pi_{eph}^r(\omega) \mathcal{A}_{\bar{\alpha}}(\omega) \Gamma_\alpha^{ph}(\omega) \right], \tag{9.44}$$

$$\mathcal{T}_{ph}^{(3)} = \mathrm{Tr} \left[\mathcal{A}_{\bar{\alpha}}(\omega) \Pi_{eph}^a(\omega) D_0^a(\omega) \Gamma_\alpha^{ph}(\omega) \right], \tag{9.45}$$

$$\mathcal{T}_{ph}^{(4)} = i \mathrm{Tr} \left[D_0^r(\omega) \Pi_{eph}(\omega) D_0^a(\omega) \Gamma_\alpha^{ph}(\omega) \right]. \tag{9.46}$$

where in the last term $\Pi_{eph}(\omega) = \Pi_{eph}^{>}(\omega) - \Pi_{eph}^{<}(\omega) = \Pi_{eph}^r(\omega) - \Pi_{eph}^a(\omega)$, while the $J_\alpha^{(4)}$ includes an additional term from the drag coefficient, not derived here.

9.5 Derivation of the exLOE

The derivation was originally carried out by my colleague Jing-Tao Lü, and is only roughly sketched here for the purpose of illustrating the underlying main assumptions.

9.5.1 Fock selfenergy

For the Fock part we have

$$\begin{aligned}\Sigma^{r,a}_{eph}(\varepsilon) &= \pm\frac{1}{2}\left(\Sigma^{>}_{eph}(\varepsilon)-\Sigma^{<}_{eph}(\varepsilon)\right)-\frac{i}{2}\mathcal{H}\left(\Sigma^{>}_{eph}(\varepsilon')-\Sigma^{<}_{eph}(\varepsilon')\right)(\varepsilon)\\ &\equiv \pm\mathcal{X}(\varepsilon)-i\mathcal{H}\left(\mathcal{X}\right)(\varepsilon)\end{aligned} \tag{9.47}$$

Here

$$\begin{aligned}\mathcal{X}(\varepsilon) &= \frac{1}{2}\left(\Sigma^{>}_{eph}(\varepsilon)-\Sigma^{<}_{eph}(\varepsilon)\right)=\mathcal{X}_1(\varepsilon)+\mathcal{X}_2(\varepsilon) \qquad (9.48)\\ \mathcal{X}_1(\varepsilon) &= \frac{1}{2}\sum_{kl}\int_{-\infty}^{+\infty}\frac{d\omega}{2\pi}M^kA(\varepsilon-\omega)M^lD^{>}_{kl}(\omega)\\ \mathcal{X}_2(\varepsilon) &= \frac{i}{2}\sum_{kl}\sum_{\beta}\int_{0}^{+\infty}\frac{d\omega}{2\pi}\left(MA_\beta(\varepsilon-\omega)M\mathcal{A}(\omega)n^\beta_F(\varepsilon-\omega)+MA_\beta(\varepsilon+\omega)M\mathcal{A}(-\omega)n^\beta_F(\varepsilon+\omega)\right)\end{aligned}$$

We can use the symmetry $\mathcal{A}(-\omega)=-\mathcal{A}^*(\omega)$ and by shifting $x'\to x'-x_0$ that $\mathcal{H}\left(f(x')\right)(x-x_0)=\int dx'\frac{f(x')}{x'-(x-x0)}=\int dx'\frac{f(x'-x0)}{x'-x}=\mathcal{H}\left(f(x'-x_0)\right)(x)$.

9.5.2 Transmission correction by Fock diagram

The different transmission corrections will then have four contributions labeled $\mathcal{T}_e^{(n),\mathcal{X}_1}$, $\mathcal{T}_e^{(n),\mathcal{X}_2}$, $\mathcal{T}_e^{(n),\mathcal{H}(\mathcal{X}_1)}$, $\mathcal{T}_e^{(n),\mathcal{H}(\mathcal{X}_2)}$ from $\mathcal{X}_1,\mathcal{X}_1$ and their Hilbert transforms respectively.

The first transmission correction has the following contributions:

$$\begin{aligned}\mathcal{T}_e^{(2),\mathcal{X}_1} &= \frac{1}{2}\sum_{kl}\int_{-\infty}^{+\infty}\frac{d\omega}{2\pi}\mathrm{Tr}\left[M^kA(\varepsilon-\omega)M^lA_{\bar\alpha}(\varepsilon)\Gamma_\alpha(\varepsilon)G^r_0(\varepsilon)\right]D^{>}_{kl}(\omega)\\ \mathcal{T}_e^{(2),\mathcal{H}(\mathcal{X}_1)} &= -\frac{i}{2}\sum_{kl}\int_{-\infty}^{+\infty}\frac{d\omega}{2\pi}\mathrm{Tr}\left[M^k\mathcal{H}\left(A(\varepsilon')\right)(\varepsilon-\omega)M^lA_{\bar\alpha}(\varepsilon)\Gamma_\alpha(\varepsilon)G^r_0(\varepsilon)\right]D^{>}_{kl}(\omega)\\ \mathcal{T}_e^{(2),\mathcal{X}_2} &= \frac{i}{2}\sum_{kl}\sum_{\beta}\int_{0}^{+\infty}\frac{d\omega}{2\pi}\Big(\mathrm{Tr}\left[M^k\left(A_\beta(\varepsilon-\omega)n^\beta_F(\varepsilon-\omega)\right)M^lA_{\bar\alpha}(\varepsilon)\Gamma_\alpha(\varepsilon)G^r_0(\varepsilon)\right]\mathcal{A}_{kl}(\omega)\\ &+ \mathrm{Tr}\left[M^k\left(A_\beta(\varepsilon+\omega)n^\beta_F(\varepsilon+\omega)\right)M^lA_{\bar\alpha}(\varepsilon)\Gamma_\alpha(\varepsilon)G^r_0(\varepsilon)\right]\mathcal{A}_{kl}(-\omega)\Big)\\ \mathcal{T}_e^{(2),\mathcal{H}(\mathcal{X}_2)} &= \frac{1}{2}\sum_{kl}\sum_{\beta}\int_{0}^{+\infty}\frac{d\omega}{2\pi}\Big(\mathrm{Tr}\left[M^k\mathcal{H}\left(A_\beta(\varepsilon')n^\beta_F(\varepsilon')\right)(\varepsilon-\omega)M^lA_{\bar\alpha}(\varepsilon)\Gamma_\alpha(\varepsilon)G^r_0(\varepsilon)\right]\mathcal{A}_{kl}(\omega)\\ &+ \mathrm{Tr}\left[M^k\mathcal{H}\left(A_\beta(\varepsilon')n^\beta_F(\varepsilon')\right)(\varepsilon+\omega)M^lA_{\bar\alpha}(\varepsilon)\Gamma_\alpha(\varepsilon)G^r_0(\varepsilon)\right]\mathcal{A}_{kl}(-\omega)\Big)\end{aligned} \tag{9.49}$$

The second transmission correction has the following contributions:

$$\begin{aligned}
\mathcal{T}_e^{(3),\mathcal{X}_1} &= -\frac{1}{2}\sum_{kl}\int_{-\infty}^{+\infty}\frac{d\omega}{2\pi}\mathrm{Tr}\left[M^k A(\varepsilon-\omega)M^l G_0^a(\varepsilon\Gamma_\alpha(\varepsilon)A_{\bar{\alpha}}(\varepsilon))\right]D_{kl}^{>}(\omega)\\
\mathcal{T}_e^{(3),\mathcal{H}(\mathcal{X}_1)} &= -\frac{i}{2}\sum_{kl}\int_{-\infty}^{+\infty}\frac{d\omega}{2\pi}\mathrm{Tr}\left[M^k\mathcal{H}\left(A(\varepsilon')\right)(\varepsilon-\omega)M^l G_0^a(\varepsilon\Gamma_\alpha(\varepsilon)A_{\bar{\alpha}}(\varepsilon))\right]D_{kl}^{>}(\omega)\\
\mathcal{T}_e^{(3),\mathcal{X}_2} &= -\frac{i}{2}\sum_{kl}\sum_{\beta}\int_{0}^{+\infty}\frac{d\omega}{2\pi}\Big(\mathrm{Tr}\left[M^k\left(A_\beta(\varepsilon-\omega)n_F^\beta(\varepsilon-\omega)\right)M^l G_0^a(\varepsilon)\Gamma_\alpha(\varepsilon)A_{\bar{\alpha}}(\varepsilon)\right]\mathcal{A}_{kl}(\omega)\\
&+ \mathrm{Tr}\left[M^k\left(A_\beta(\varepsilon+\omega)n_F^\beta(\varepsilon+\omega)\right)M^l G_0^a(\varepsilon)\Gamma_\alpha(\varepsilon)A_{\bar{\alpha}}(\varepsilon)\right]\mathcal{A}_{kl}(-\omega)\Big)\\
\mathcal{T}_e^{(3),\mathcal{H}(\mathcal{X}_2)} &= \frac{1}{2}\sum_{kl}\sum_{\beta}\int_{0}^{+\infty}\frac{d\omega}{2\pi}\Big(\mathrm{Tr}\left[M^k\mathcal{H}\left(A_\beta(\varepsilon')n_F^\beta(\varepsilon')\right)(\varepsilon-\omega)M^l G_0^a(\varepsilon)\Gamma_\alpha(\varepsilon)A_{\bar{\alpha}}(\varepsilon)\right]\mathcal{A}_{kl}(\omega)\\
&+ \mathrm{Tr}\left[M^k\mathcal{H}\left(A_\beta(\varepsilon')n_F^\beta(\varepsilon')\right)(\varepsilon+\omega)M^l G_0^a(\varepsilon)\Gamma_\alpha(\varepsilon)A_{\bar{\alpha}}(\varepsilon)\right]\mathcal{A}_{kl}(-\omega)\Big) \qquad (9.50)
\end{aligned}$$

9.5.3 Symmetric part

Adding the terms that does not contain Hilbert transforms together, the resulting current has the same structure as in eqn. 5.1. We therefore obtain a contribution to $C_{sym}(\omega_n, V_a)$ equal to:

$$\begin{aligned}
&\mathrm{Im}\left\{\mathrm{Tr}\left[\mathbf{M}_{\lambda_\mathrm{n}}\mathbf{A}_{\bar{\alpha}}(\mu_\alpha)\mathbf{\Gamma}^\alpha(\mu_\alpha)\mathbf{G}^\mathrm{r}(\mu_\alpha)\mathbf{M}_{\lambda_\mathrm{n}}\mathbf{A}_{\bar{\alpha}}(\mu_{\bar{\alpha}})\right]\right.\\
&\left.+\ \mathrm{Tr}\left[\mathbf{M}_{\lambda_n}\mathbf{A}_{\bar{\alpha}}(\mu_{\bar{\alpha}})\mathbf{\Gamma}^\alpha(\mu_{\bar{\alpha}})\mathbf{G}^r(\mu_{\bar{\alpha}})\mathbf{M}_{\lambda_n}\mathbf{A}_{\alpha}(\mu_\alpha)\right]\right\} \qquad (9.51)
\end{aligned}$$

9.5.4 Asymmetric part

We will assume that there is no bandgap or similar sudden change in the spectral function. This enables one to ignore terms that was not part of the original LOE. The remaining part is related to the explicit Hilbert transform of the spectral function and Fermi functions:

$$\mathcal{H}\{A_\beta(\varepsilon')f_\beta(\varepsilon')\}(\varepsilon) = \frac{1}{\pi}\lim_{\delta\to 0}\int_{-\infty}^{\mu_\beta}\frac{(\varepsilon'-\varepsilon)A_\beta(\varepsilon')}{(\varepsilon'-\varepsilon)^2+\delta^2}d\varepsilon' \qquad (9.52)$$

In the wide-band approximation one could move the spectral functions outside this transform. However, here we will keep track of the energy shift due to the phonon frequencies by performing a Taylor expansion of the spectral function around ε:

$$A_\beta(\varepsilon') = A_\beta(\varepsilon) + a(\varepsilon'-\varepsilon)+\cdots \qquad (9.53)$$

Then, if A_β is smooth function, only Hilbert transform of the first term will give a sharp divergence. So we only keep this term. The Hilbert transform now becomes

$$\mathcal{H}\{A_\beta(\varepsilon')f_\beta(\varepsilon')\}(\varepsilon) \approx A_\beta(\varepsilon)\mathcal{H}\{f_\beta(\varepsilon')\}(\varepsilon). \qquad (9.54)$$

Inserting this in the correction to the current we obtain the asymmetric coefficient near the phonon threshold:

$$\mathcal{I}^{asym} = \int_{-\infty}^{+\infty}\frac{d\varepsilon}{2\pi}\mathcal{H}\{n_F(\varepsilon'-\omega_n)-n_F(\varepsilon'+\omega_n)\}(\varepsilon)\left(n_F(\varepsilon-eV_a)-n_F(\varepsilon)\right), \qquad (9.55)$$

and the corresponding system specific rate coefficient:

$$\begin{aligned}
C_{asym}(\omega_n, V_a) &= 2\Re\left\{\mathrm{Tr}\left[\mathbf{M}_{\lambda_n}\mathbf{A}_{\bar{\alpha}}(\mu_\alpha)\mathbf{\Gamma}^\alpha(\mu_\alpha)\mathbf{G}^r(\mu_\alpha)\mathbf{M}_{\lambda_n}\mathbf{A}_{\bar{\alpha}}(\mu_{\bar{\alpha}})\right]\right.\\
&- \left.\mathrm{Tr}\left[\mathbf{M}_{\lambda_n}\mathbf{A}_{\bar{\alpha}}(\mu_{\bar{\alpha}})\mathbf{\Gamma}^\alpha(\mu_{\bar{\alpha}})\mathbf{G}^r(\mu_{\bar{\alpha}})\mathbf{M}_{\lambda_n}\mathbf{A}_{\alpha}(\mu_\alpha)\right]\right\}. \qquad (9.56)
\end{aligned}$$

9.6 Sensitivity analysis

We apply the adjoint method to get rid of derivatives of the Green's functions but instead solving an adjoint problem. We subtract two **fixed** complex adjoint operators λ and $\mathbf{\Omega}$ and subtract two zeros in a clever way in the form of the equilibrium equations:

$$\begin{aligned}\mathcal{T}_e(E) &= \mathrm{Tr}\left[\mathbf{G}^r\mathbf{\Gamma}_R\mathbf{G}^a\mathbf{\Gamma}_L\right. \\ &- \left(\mathbf{G}^r\left[E-\mathbf{H}-\mathbf{\Sigma}^r\right]-\mathbf{I}\right)\lambda\mathbf{\Gamma}_R\mathbf{G}^a\mathbf{\Gamma}_L \\ &- \left.\mathbf{G}^r\mathbf{\Gamma}_R\left(\mathbf{G}^a\left[E-\mathbf{H}-\mathbf{\Sigma}^a\right]-\mathbf{I}\right)\mathbf{\Omega}\mathbf{\Gamma}_L\right]\end{aligned} \tag{9.57}$$

(9.58)

Evaluating the derivative one obtains

$$\begin{aligned}\frac{\partial\mathcal{T}_e(E)}{\partial\rho_i} &= \mathrm{Tr}\left[\frac{\partial\mathbf{G}^r}{\partial\rho_i}\mathbf{\Gamma}_R\mathbf{G}^a\mathbf{\Gamma}_L+\mathbf{G}^r\mathbf{\Gamma}_R\frac{\partial\mathbf{G}^a}{\partial\rho_i}\mathbf{\Gamma}_L\right. \\ &- \left(\frac{\partial\mathbf{G}^r}{\partial\rho_i}\left[E-\mathbf{H}-\mathbf{\Sigma}^r\right]+\mathbf{G}^r\left[-\frac{\partial\mathbf{H}}{\partial\rho_i}\right]\right)\lambda\mathbf{\Gamma}_R\mathbf{G}^a\mathbf{\Gamma}_L \\ &- \left.\mathbf{G}^r\mathbf{\Gamma}_R\left(\frac{\partial\mathbf{G}^a}{\partial\rho_i}\left[E-\mathbf{H}-\mathbf{\Sigma}^a\right]+\mathbf{G}^a\left[-\frac{\partial\mathbf{H}}{\partial\rho_i}\right]\right)\mathbf{\Omega}\mathbf{\Gamma}_L\right]\end{aligned} \tag{9.59}$$

(9.60)

The additional terms where the derivative does not go into the zero factor was removed since these terms are still zero. Using the cyclic property of the trace we can rewrite this as

$$\begin{aligned}\frac{\partial\mathcal{T}_e(E)}{\partial\rho_i} &= \mathrm{Tr}\left[\frac{\partial\mathbf{G}^r}{\partial\rho_i}\left\{\mathbf{I}-\left[E-\mathbf{H}-\mathbf{\Sigma}^r\right]\lambda\right\}\mathbf{\Gamma}_R\mathbf{G}^a\mathbf{\Gamma}_L\right. \\ &+ \mathbf{G}^r\mathbf{\Gamma}_R\frac{\partial\mathbf{G}^a}{\partial\rho_i}\left\{\mathbf{I}-\left[E-\mathbf{H}-\mathbf{\Sigma}^a\right]\mathbf{\Omega}\right\}\mathbf{\Gamma}_L \\ &+ \mathbf{G}^r\frac{\partial\mathbf{H}}{\partial\rho_i}\lambda\mathbf{\Gamma}_R\mathbf{G}^a\mathbf{\Gamma}_L \\ &+ \left.\mathbf{G}^r\mathbf{\Gamma}_R\mathbf{G}^a\frac{\partial\mathbf{H}}{\partial\rho_i}\mathbf{\Omega}\mathbf{\Gamma}_L\right]\end{aligned} \tag{9.61}$$

Choosing the adjoint operators as $\lambda=\mathbf{G}^r$ and $\mathbf{\Omega}=\mathbf{G}^a$ we can evaluate the sensitivity without requiring the calculation of the direct derivative of the Green's function with density. Using that the Hamiltonian is Hermitian and that $\mathbf{G}^{r,\dagger}=\mathbf{G}^a$ we obtain the final result:

$$\frac{\partial\mathcal{T}_e(E)}{\partial\rho_i} = 2\mathrm{ReTr}\left[\mathbf{G}^{\mathrm{r}}\frac{\partial\mathbf{H}}{\partial\rho_{\mathrm{i}}}\mathbf{G}^{\mathrm{r}}\mathbf{\Gamma}_{\mathrm{R}}\mathbf{G}^{\mathrm{a}}\mathbf{\Gamma}_{\mathrm{L}}\right] \tag{9.62}$$

The remaining $\frac{\partial\mathbf{H}}{\partial\rho_i}$ factor is evaluated according to the chosen density models in the topology optimization. In Fig. 9.1 we illustrate the numerical error compared to a numerical expensive brute force finite difference calculation.

9.7 Recursive relations

The block size of each Green's function is determined by the coupling length of the problem at hand. Since the coupling matrices between the (n+1)'th cell and the previous

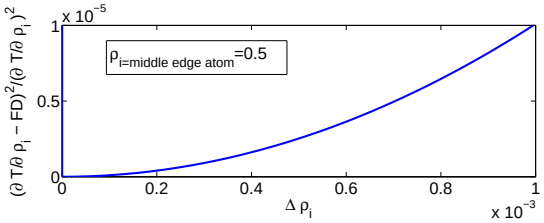

Figure 9.1: *Numerical noise in finite difference (FD) sensitivity calculation. This illustrates the correctness of the sensitivity analysis and the numerical stability.*

subsystem is only nonzero at the sites coupled to the n'th cell we obtain following recursive procedure. At the (n+1)'th step the matrices of the (n+1)'th Green's function will be:

$$\mathbf{G}^{(n+1)}_{n+1,n+1} = \left[E\mathbf{I} - \mathbf{H}^{n+1}_D - \mathbf{\Sigma}_n\right]^{-1} \tag{9.63}$$

$$\mathbf{G}^{(n+1)}_{i,n+1} = \mathbf{G}^{(n)}_{i,n}\mathbf{V}_n\mathbf{G}^{(n+1)}_{n+1,n+1},\ i \le n \tag{9.64}$$

$$\mathbf{G}^{(n+1)}_{n+1,j} = \mathbf{G}^{(n+1)}_{n+1,n+1}\mathbf{V}^\dagger_n\mathbf{G}^{(n)}_{n,j},\ j \le n \tag{9.65}$$

$$\mathbf{G}^{(n+1)}_{i,j} = \mathbf{G}^{(n)}_{i,j} + \mathbf{G}^{(n)}_{i,n}\mathbf{V}_n\mathbf{G}^{(n+1)}_{n+1,n+1}\mathbf{V}^\dagger_n\mathbf{G}^{(n)}_{n,j},\ i,j \le n \tag{9.66}$$

where the self-energy is defined as

$$\mathbf{\Sigma}_n(E) = \mathbf{V}^\dagger_n\mathbf{G}^{(n)}_{n,n}(E)\mathbf{V}_n,\ n+1 < N \tag{9.67}$$

$$\mathbf{\Sigma}_n(E) = \mathbf{V}^\dagger_n\mathbf{G}^{(n)}_{n,n}(E)\mathbf{V}_n + \mathbf{\Sigma}_R(E),\ n+1 = N \tag{9.68}$$

These equation can be used to obtain recursive relations for the transmission and density of states.

Recursive approach for the density of states:
The density of states is related to the trace of the Greens function, $\rho_e(E) = -\frac{1}{\pi}\mathrm{Im}\left(\mathrm{Tr}\left[\mathbf{G}^{\mathrm{r}}(\mathrm{E})\right]\right)$. At a given system length we define a temporary trace over the diagonal of all diagonal blocks:

$$\mathrm{Tr}\left[\mathbf{G}^{(n)}\right] = \sum_{j'}\sum_{i}^{n}\left(\mathbf{G}^{(n)}_{i,i}\right)_{j',j'}. \tag{9.69}$$

We now use three set of indices: the upper iteration step (length of system), the lower block, and the lower inside block with $'$ to sum the final trace. At the (n+1)'th step we get

$$\begin{aligned}
\mathrm{Tr}\left[\mathbf{G}^{(n+1)}\right] &= \sum_{j'}\left(\sum_{i=1}^{n}\mathbf{G}^{(n+1)}_{i,i} + \mathbf{G}^{(n+1)}_{n+1,n+1}\right)_{j',j'} \\
&= \sum_{j'}\sum_{i=1}^{n}\left(\mathbf{G}^{(n)}_{i,i} + \mathbf{G}^{(n)}_{i,n}\mathbf{V}_n\mathbf{G}^{(n+1)}_{n+1,n+1}\mathbf{V}^\dagger_n\mathbf{G}^{(n)}_{n,i}\right)_{j',j'} + \sum_{j'}\left(\mathbf{G}^{(n+1)}_{n+1,n+1}\right)_{j',j'} \\
&= \mathrm{Tr}\left[\mathbf{G}^{(n)}\right] + \mathrm{Tr}\left[\mathbf{G}^{(n+1)}_{n+1,n+1}\left\{\mathbf{V}^\dagger_n\sum_i^n\mathbf{G}^{(n)}_{n,i}\mathbf{G}^{(n)}_{i,n}\mathbf{V}_n + \mathbf{I}\right\}\right].
\end{aligned}$$

We insert the remaining recursive relations for the Green's function to derive a recursive

relation for the nontrivial factor in the curly bracket:

$$\begin{aligned} E_\rho^{(n)} &\equiv \mathbf{V}_n^\dagger \sum_i^n \mathbf{G}_{n,i}^{(n)} \mathbf{G}_{i,n}^{(n)} \mathbf{V}_n \\ E_\rho^{(n+1)} &= \mathbf{V}_{n+1}^\dagger \sum_i^{n+1} \mathbf{G}_{n+1,i}^{(n+1)} \mathbf{G}_{i,n+1}^{(n+1)} \mathbf{V}_{n+1} \\ &= \mathbf{V}_{n+1}^\dagger \sum_i^{n+1} \{\mathbf{G}_{n+1,n+1}^{(n+1)} \mathbf{V}_n^\dagger \mathbf{G}_{n,i}^{(n)}\} \{\mathbf{G}_{i,n}^{(n)} \mathbf{V}_n \mathbf{G}_{n+1,n+1}^{(n+1)}\} \mathbf{V}_{n+1} \\ &= \mathbf{V}_{n+1}^\dagger \mathbf{G}_{n+1,n+1}^{(n+1)} \left(E_\rho^{(n)} + \mathbf{I}\right) \mathbf{G}_{n+1,n+1}^{(n+1)} \end{aligned} \tag{9.70}$$

Recursive approach for the transmission:
A very intuitive, and simple in terms of bookkeeping, approach is to include each subsystem cell by cell, e.g. in the left lead, to obtain both left and right self-energies in the last subsystem at the right side. In this way we only need eqn. 9.63 and do a transmission calculation with the Green's function obtained at the last cell. This approach is what we have used so far to obtain transmissions for GAL systems. It can be extended to obtain the tridiagonal blocks of Green's functions (and hence the density of states and other relevant parameters) by storing the left Green's function for each cell. Propagating back we can obtain the diagonal blocks by a Dyson equation and the coupling parts. However, as shown previously the tridiagonal part of the Green's function is not what is needed for the sensitivity. An alternative method is to use the original equations 9.63-9.66 to obtain the relevant part of the Green's function for the transmission.

9.8 Löwdin transformation

We can orthonormalize a basis set by using the Löwdin orthogonalization procedure[107, 147]. In case of a localized-orbital basis set, such as in SIESTA, the overlap between the basis functions is nonzero. For basis state 'i' and 'j' one defines the overlap matrix element $S_{ij} =< i|j >$. Even if the orbitals from each atom are orthogonal the overlap between orbitals originated at different atoms will be nonzero. The Löwdin procedure has the important feature of preserving the symmetry of the basis functions and the hermiticity of the Hamiltonian. The idea is to diagonalize the real and symmetric overlap matrix by a transformation V:

$$S = V\lambda V^\dagger = V\sqrt{\lambda}V^\dagger V\sqrt{\lambda}V^\dagger = S^{1/2}S^{1/2}\,, \tag{9.71}$$

where we have used $V^\dagger V = I$ and defined a real and symmetric matrix $S^{1/2} = S^{1/2,\dagger} = V\sqrt{\lambda}V^\dagger$, $\sqrt{\lambda} = diag\left(\sqrt{\{\lambda_n\}}\right)$.

Since the Löwdin transformation is nonunitary we should always test if the quantities of interest are transformation invariant. We define the transformed Hamiltonian as $\tilde{H} = S^{-1/2}HS^{-1/2}$. The Green's function transforms like H^{-1}; $\tilde{G}^r = S^{1/2}G^rS^{1/2}$. The self-energy transforms like H and therefore $\tilde{\Gamma}_\alpha = i(\tilde{\Sigma}_\alpha - \tilde{\Sigma}_{\alpha,\dagger}) = S^{-1/2}\mathrm{Im}\left(\Sigma_\alpha\right)\mathrm{S}^{-1/2}$ also transforms like H. The spectral function transforms like H^{-1}: $\tilde{A}_\alpha = \tilde{G}^r\tilde{\Gamma}_\alpha\tilde{G}^a = S^{1/2}A_\alpha S^{1/2}$. From this we see that the transmission is transformation invariant, $\mathrm{Tr}[\tilde{\Gamma}_{\overline{\alpha}}\tilde{\mathrm{A}}_\alpha] = \mathrm{Tr}[\Gamma_{\overline{\alpha}}\mathrm{A}_\alpha]$. However, the density of states is not; $\mathrm{Tr}[\tilde{\mathrm{A}}_\alpha] = \mathrm{Tr}[\mathrm{S}^{1/2}\mathrm{A}_\alpha\mathrm{S}^{1/2}] \neq \mathrm{Tr}[\mathrm{A}_\alpha]$.

The physical density of states is obtained from $\mathrm{Tr}[\tilde{\mathrm{A}}_\alpha]$ since bond charge will be partially double counted if a nonorthogonal basis is used[147]. One should also notice that

the new orthogonal basis functions are far less spatially localized[147]. As a consequence it is sometimes difficult to define a bond current or bond charge between two atoms in the sense that the basis functions in some cases goes beyond the bonding region.

In general the Löwdin transformation will be trace conserving as long as the Tr kernel consists of an alternating sequence of factors transforming like H (e.g. $\Gamma_\alpha, \Sigma_\alpha$) and H^{-1} (e.g. G^r, A_α).

Chapter 10

Appendix B: List of conference contributions

1. International Workshop on Computational Electronics (IWCE), 2012, Madison, USA (oral, Received a best student paper award).
2. Kick-off meeting at the center of nanostructured graphene (CNG), 2011, DTU (oral).
3. Belfast symposium on current induced dynamical phenomena, 2011, Queens University (oral).
4. Carbonhagen conference on applications of graphene, DTU/KU, 2010, 2011 (Sigma poster award for strong scientific results) and 2013 (poster).
5. Ab Initio Molecular Simulations: Toward a First-Principles Understanding of Materials Properties and Functions, Workshop, Berlin, 2011 (poster).
6. CECAM conference on thermal transport, Lugano, 2010 (poster).

I have further contributed to the research community as a referee of > 5 papers in 'Physical Review journals and Reviews of Modern Physics'.

Chapter 11

Appendix C: Publications

Paper I

Tue Gunst, Troels Markussen, Antti-Pekka Jauho and Mads Brandbyge

Thermoelectric properties of finite graphene antidot lattices

Phys. Rev. B **84**, 155449 (2011)

Thermoelectric properties of finite graphene antidot lattices

Tue Gunst,[1,*] Troels Markussen,[2] Antti-Pekka Jauho,[1] and Mads Brandbyge[1]

[1]*Department of Micro- and Nanotechnology (DTU Nanotech), Technical University of Denmark, DK-2800 Kgs. Lyngby, Denmark*

[2]*Center for Atomic-scale Materials Design (CAMD), Department of Physics, Technical University of Denmark, DK-2800 Kgs. Lyngby, Denmark*

(Received 27 July 2011; revised manuscript received 7 October 2011; published 31 October 2011)

We present calculations of the electronic and thermal transport properties of graphene antidot lattices with a finite length along the transport direction. The calculations are based on the π-tight-binding model and the Brenner potential. We show that both electronic and thermal transport properties converge fast toward the bulk limit with increasing length of the lattice: only a few repetitions ($\simeq$6) of the fundamental unit cell are required to recover the electronic band gap of the infinite lattice as a transport gap for the finite lattice. We investigate how different antidot shapes and sizes affect the thermoelectric properties. The resulting thermoelectric figure of merit, ZT, can exceed 0.25, and it is highly sensitive to the atomic arrangement of the antidot edges. Specifically, hexagonal holes with pure armchair edges lead to an order-of-magnitude larger ZT as compared to pure zigzag edges. We explain this behavior as a consequence of the localization of states, which predominantly occurs for zigzag edges, and of an increased splitting of the electronic minibands, which reduces the power factor S^2G_e (S is the Seebeck coefficient and G_e is the electric conductance).

DOI: 10.1103/PhysRevB.84.155449 PACS number(s): 85.80.Fi, 73.23.Ad, 63.22.Rc, 68.65.Cd

I. INTRODUCTION

Ideal thermoelectric materials conduct electricity very well while the heat conduction is poor. Their applications include power generation and refrigeration.[1,2] The optimization of thermoelectric properties has been a topic of wide interest,[3,4] and in particular, nanostructured materials for thermoelectrics is a rapidly expanding field of research. One proposal has been to increase the Seebeck coefficient S by reducing the dimensionality of the system.[5–7] Another idea is to utilize the low thermal conductance, together with a sharp resonance in the electronic conductance G_e, of molecular junctions.[8–11] Reduction of the thermal conductivity in nanostructured materials may be achieved using nanomesh structures, surface-disorder and -decoration, passivation, or by other means. However, the electronic conductance ideally should not be affected. Examples of nanostructured thermoelectric materials include passivated Si nanowires,[12] Si antidot lattices,[13,14] chevron-type graphene nanoribbons,[15] and connected capped carbon nanotubes.[16] Here we turn our attention toward graphene antidot lattices (GALs), a nanomesh of holes in graphene with promising electronic properties such as a tunable band gap.[17]

The efficiency in converting temperature gradients into an electric voltage, at an average temperature T, is quantified by the dimensionless figure of merit $ZT = S^2G_eT/\kappa$, where high ZT implies a good thermoelectric. We thus seek a high electronic power factor S^2G_e and minimal thermal conductance $\kappa = \kappa_{ph} + \kappa_e$, which includes contributions both from phonons and electrons. Thermoelectric materials with $ZT \approx 1$ have an efficiency in the range of available thermoelectric components based on nanostructured bulk materials, whereas $ZT > 3$ is needed to compete with conventional refrigerators and generators.[18,19]

Graphene can sustain current densities six orders of magnitude larger than copper, has a measured record high stiffness, and is foreseen to have numerous applications ranging from nanoelectronics, spintronics, and nanoelectromechanical devices.[20] Graphene is furthermore one of the best thermal conductors known.[21,22] It has been predicted to posses a giant Seebeck coefficient when gated by a sequence of metal electrodes.[23] However, ways to reduce the superior thermal conductivity of graphene are needed if one looks for thermoelectric applications.[24] Several ways to reduce the thermal conductivity have already been examined, such as interface mismatching between graphene and nanoribbons,[25,26] the presence of isotopes,[27–30] cross-plane phonon coupling in a few layers of graphene,[31] strain,[32] random hydrogen vacancies in graphene,[33] and point defects.[34–36] Edge disorder has been predicted theoretically to suppress heat conductance of graphene nanoribbons,[37–39] and ZT exceeding 3 has been theoretically predicted for such systems in the diffusive limit.[40]

GALs have been proposed as a flexible platform for creating a semiconducting material with a band gap which can be tuned by varying the antidot size, shape, or lattice symmetry.[17,41–43] GALs can be fabricated by electron beam lithography,[44,45] by block copolymer lithography[46,47] with hole distances down to 5 nm, and at a larger scale through nanorod photocatalysis[48] and anisotropic etching.[49] To the best of our knowledge, no studies have been reported on the thermal properties of finite GALs. Apart from their intrinsic scientific interest, these studies are necessary to assess whether the thermal properties can be engineered in a manner similar to the electronic case. Of course, all realistic devices are of finite length, and the study of size effects is important for practical purposes.[50] For completeness, we mention here other related studies that have recently been reported. A number of studies of electron and/or phonon transport properties of regular defects in ribbons are available (see, e.g., Refs. 51–53). Recently, Lopata *et al.* studied electron transport of infinite GALs.[54] Finally, during the preparation of this manuscript Karamitaheri *et al.* reported a combined study of electron and phonon transport properties based on the band structures of infinite GALs,[55,56] and Tretiakov *et al.* reported results for topological insulators,[57] which share certain key properties (e.g., flatbands) with GALs.

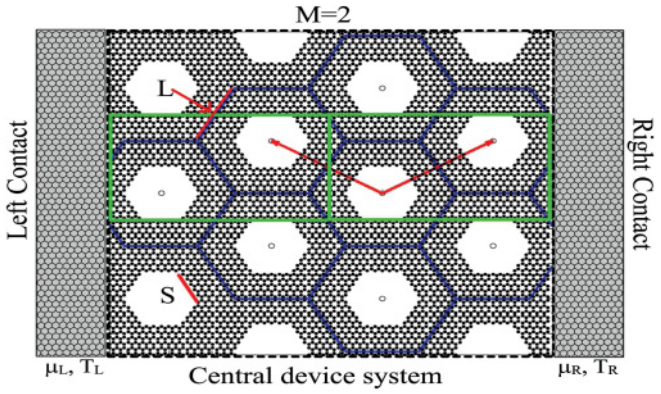

FIG. 1. (Color online) System setup and the computational rectangular unit cell (green rectangle). Two graphene leads are connected by the finite GAL. The depicted system is a {10,5zz} GAL with a length of 2 ($M = 2$) corresponding to four holes in the direction of transport.

The topic of this paper is thus the electronic and thermal transport properties of finite graphene antidot lattices. The finite GALs are viewed as a part of an integrated graphene-based system, e.g., used as an electrode for molecular conductors[8,58] (see Fig. 1). In order to shed light on the question of to what extent it may be possible to engineer the thermoelectric properties, we investigate how different antidot shapes and sizes affect the thermoelectric properties. Interestingly, even though the base material—graphene—is an outstanding thermal conductor, we find that the resulting thermoelectric figure of merit, ZT, can exceed 0.25. However, ZT is highly sensitive to the atomic arrangement at the edge of the etched holes, partly due to electronic quasilocalized edge states. As we shall show below, this favors antidots with armchair-type edges for thermoelectrics.

The paper is organized as follows. In Sec. II we introduce the systems and outline the theoretical and numerical methods used. In Sec. III we present our results for the electronic transport properties of GALs. Specifically, we discuss the convergence with number of repetitions of the basic unit cell and also consider the localization of electronic states at zigzag edges. In Sec. IV we examine the influence of the perforation and geometrical effects on the thermal transport properties. This leads to the analysis of thermoelectric properties in Sec. V. The results are summarized and discussed in Sec. VI.

II. SYSTEMS AND METHODS

Throughout in this paper we focus on triangular graphene antidot lattices: these systems are known to lead to a gap in the electronic spectrum,[42,43] which is essential for the present purposes. Due to the high lattice symmetry the number of independent lattice parameters is small, and furthermore, these systems are the most thoroughly studied, both theoretically and experimentally. Recent experiments have illustrated that hexagonal antidots may stabilize with pure zigzag and armchair edge chirality.[49] The antidot diameter, shape, position and the ratio of removed atoms to unit cell size are all important parameters which we examine to get a full picture of the electronic, thermal, and thermoelectric properties of GALs. Another important variable is the length of the region exposed to the nanoperforation. The systems studied here consist of an antidot lattice of finite length connected to two pristine graphene leads (Fig. 1), and the infinite direction perpendicular to the transport direction is treated using periodic boundary conditions and corresponding k-point sampling.

We use the nomenclature introduced in Ref. 17 and specify the GAL by $\{Ls_1,Ss_2\}$, where the L is the length of the side of a hexagonal Wigner-Seitz cell, and S is the side length of the antidot (see Fig. 1), both in units of the lattice constant $\sqrt{3}a_0$, with $a_0 = 1.42$ Å being the carbon-carbon distance. The label $s_2 = \{\text{zz,arm,cir}\}$ indicates whether the hole has zigzag or armchair edges, or if the hole is circular, resulting in mixed armchair and zigzag edges. In principle, one could also consider different sheet orientations compared to the transport direction; we do not present a systematic study here and fix the underlying graphene sheet as armchair ($s_1 = \text{arm}$, as in Fig. 1). We have tested a selection of "zigzag sheets" and did not find any qualitative difference with respect to thermoelectric properties. As an example, {10,5zz} is a $L = 10$ antidot lattice with transport direction perpendicular to the armchair direction[59] and with a hexagonal hole with the same orientation as the lattice hexagons, resulting in zigzag edges and a side length of $S = 5$ (see Fig. 1). Armchair edges are obtained if the hexagonal holes are rotated opposite to the lattice hexagons (see also Fig. 2 below).

A. Method

Both electronic and phonon transport properties are calculated from atomistically determined energy-dependent transmission functions $\mathcal{T}_e$ and $\mathcal{T}_{ph}$, as described below, and using these in a Landauer-type formula. For a spin degenerate electronic system the Landauer formula reads

$$I_e = \frac{2e}{\hbar}\int \frac{dE}{2\pi}\mathcal{T}_e(E)[n_F(E,\mu_L) - n_F(E,\mu_R)]\,, \qquad (1)$$

where $n_F(E,\mu_{L/R})$ is the Fermi-Dirac distribution at the chemical potential of the left or right lead. We employ this in the linear-response limit and consider variations with changes in the chemical potential, e.g., by doping or gating of the graphene system. The following integrals can be evaluated from the electronic transmission,

$$L_n(\mu) = \frac{2}{\hbar}\int \frac{dE}{2\pi}(E-\mu)^n\mathcal{T}_e(E)\left(-\frac{\partial n_F}{\partial E}\right). \qquad (2)$$

They relate the electronic current and the electron heat current I_Q in the linear response regime:

$$\begin{pmatrix} \frac{\Delta I_e}{e} \\ \Delta I_Q \end{pmatrix} = \begin{pmatrix} L_0 & L_1 \\ L_1 & L_2 \end{pmatrix}\begin{pmatrix} \Delta\mu \\ \frac{\Delta T}{T} \end{pmatrix}, \qquad (3)$$

where $\Delta\mu = \mu_L - \mu_R$ and $\Delta T = T_L - T_R$. From these integrals several physical properties follow;[60] the electrical conductance $G_e(\mu) = \frac{\partial I}{\partial V} = e^2L_0$, the electron thermal conductance $\kappa_e(\mu) = [L_2 - \frac{L_1^2}{L_0}]/T$, and the Seebeck coefficient $S(\mu) = \frac{\Delta V}{\Delta T}|_{I_e=0} = \frac{L_1}{eL_0T}$.

For phonons the Landauer formula takes an analogous form,

$$I_{ph} = \int_0^\infty d\omega\frac{\hbar\omega}{2\pi}\mathcal{T}_{ph}(\omega)\,[n_B(\omega,T_L) - n_B(\omega,T_R)]\,, \qquad (4)$$

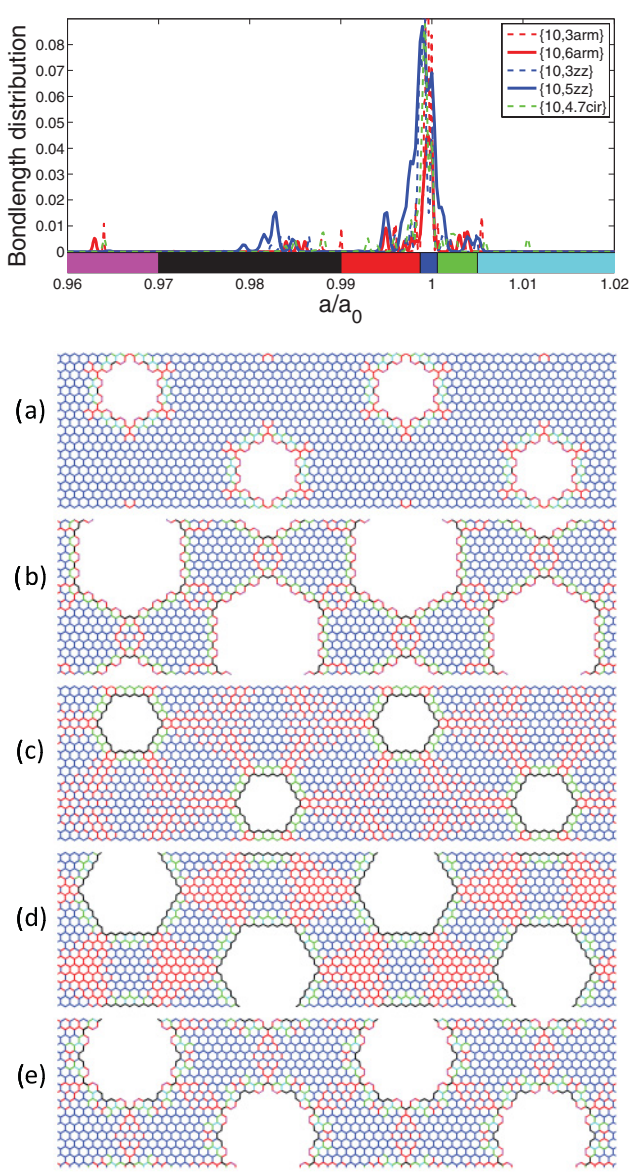

FIG. 2. (Color online) Change of bond lengths due to the relaxation of the graphene antidots. Top: Coloring scheme for the bond lengths. The distribution of bond lengths after relaxation is given for five different lattices. From top to bottom the considered lattices have (a) small armchair holes {10,3arm}, (b) large armchair holes {10,6arm}, (c) small zigzag holes {10,3zz}, (d) large zigzag holes {10,5zz}, and (e) mixed edges {10,4.7cir}. When the hole size is increased the spectrum broadens and peaks occur at different bond lengths. The peaks occur at different positions characteristic of different hole types. The highly compressed "pink" bond for armchair edges is positioned between the two atoms pointing into the hole.

where $n_B(\omega)$ is the Bose distribution function. Again we use it in linear response and consider the thermal conductance from phonons given by

$$\kappa_{ph} = \int_0^\infty d\omega \frac{(\hbar\omega)^2}{2\pi k_B T^2} \mathcal{T}_{ph}(\omega) \frac{e^{\frac{\hbar\omega}{k_B T}}}{\left(e^{\frac{\hbar\omega}{k_B T}} - 1\right)^2}. \quad (5)$$

Both transmission functions $\mathcal{T}_e$ and $\mathcal{T}_{ph}$ are obtained using a recursive Green's function method (see Ref. 61 and the references cited therein), with self-energies representing the semi-infinite perfect graphene electrodes. The self-energies $\Sigma_{L,R}$ are iteratively constructed from the semi-infinite graphene left (L) and right (R) leads. The calculation of both electron and phonon k-averaged Landauer transmissions together with the thermoelectric properties are performed by an atomistic Green's function method,[16,62]

$$\mathcal{T}_e(E) = \frac{1}{N_k} \sum_{i=1}^{N_k} \mathrm{Tr}\big[\mathbf{G}_D^r(E,k_i)\mathbf{\Gamma}_R(E,k_i) \times \mathbf{G}_D^a(E,k_i)\mathbf{\Gamma}_L(E,k_i)\big]. \quad (6)$$

Here the retarded Green's function $\mathbf{G}_D^r(E,k)$ is obtained from the Hamiltonian $\mathbf{H}$, $\mathbf{G}_D^r = [E\mathbf{I} - \mathbf{H} - \mathbf{\Sigma}_L^r - \mathbf{\Sigma}_R^r]^{-1}$, and the broadening matrices due to the electrode coupling are defined as $\Gamma_{L,R} = i[\mathbf{\Sigma}_{L,R}^r - \mathbf{\Sigma}_{L,R}^a]$. The parameter N_k gives the number of sampled k points.[63] Similar equations hold for the phonon transmission: the Hamiltonian is replaced with the dynamical matrix $\mathbf{H} \to \mathbf{K}$, and the energy is replaced with $E\mathbf{I} \to \omega^2\mathbf{M}$, ω being the frequency and $\mathbf{M}$ is the diagonal mass matrix. We first perform a structural relaxation and then calculate the Hamiltonian/dynamical matrix for three unit cells ($M = 3$, 6 holes) between the pristine graphene leads. The elements corresponding to the center cell (two holes) are then subsequently repeated to increase the length of the GAL.

The electronic system is modeled by a nearest-neighbor π model ($V_{pp\pi} = 2.7\,\mathrm{eV}$) together with the Harrison scaling law to take into account the changes in the hopping matrix element due to the edge relaxation.[64] Based on the same method, Guinea and co-workers[65] have shown how strain in graphene can lead to a pseudomagnetic field affecting the electronic properties. We find that the modulation of the hopping elements is of minor importance for the present applications. In order to examine the effect of passivation we have performed calculations of the band structures with a model including two d orbitals for each C atom and an explicit model for the carbon-hydrogen interaction.[66] The qualitative features of the band diagram, and the edge states discussed below, depend surprisingly little on the presence of hydrogen passivation. However, the effect of passivation might be more important in antidot lattices with localized zero energy states such as in the triangular antidots considered in Ref. 67.

The dynamical matrix is computed using the empirical Brenner interatomic potential.[68] This is done for the system cell by the finite difference approach after a structure relaxation performed by the General Utility Lattice Program (GULP).[69] Momentum conservation is important for low-frequency modes, and it is imposed after the finite difference calculation by adjusting the diagonal elements of the dynamical matrix. A few representative results of the relaxation are shown in Fig. 2.

We see that the changes in the bond lengths compared to a_0 are below 4%. Compression of bonds at the edge is followed by a region with elongation of bonds, and the relaxation is confined in small regions in space. Matching of edge relaxations can result in longer-ranged relaxations (small compressions) emanating from the corners. This occurs mainly for zigzag edges (Fig. 2).

The results presented below are based on a set of electron and phonon transport simulations of 20 configurations with varying hole size and lattice parameters. In addition to this set, the electronic structure of another 27 systems was studied to examine the formation of edge states. Finally, a number of systems has been studied with either the zigzag transport direction or a rectangular lattice of holes. No qualitative differences in thermoelectric properties were found for these systems, and we shall not present these results here.

III. ELECTRON TRANSPORT

In this section we consider the electronic properties of finite GALs. The result for a series of unit cell repetitions (M) is shown in Fig. 3. As can be seen the electronic transmission $\mathcal{T}_e$ converges fast toward a length-independent result. The behavior of the transmission function can directly be traced back to the band structure of the infinite GAL if one defines a transport gap as the energy range where the transmission is below a certain small value. The transport gap is in general found to converge to the band gap of the infinite antidot lattice found from the band structure, and the system behaves "bulklike" after only six to seven unit cell repetitions. Thus the transport gap can be determined from a calculation of the dispersion on an infinite GAL using a primitive unit cell due to the fast convergence property illustrated in this section. The converged values of the transport gap are given in Fig. 4.[70]

To access the effect of relaxation on the electronic structure, we have plotted the obtained transport gaps neglecting the

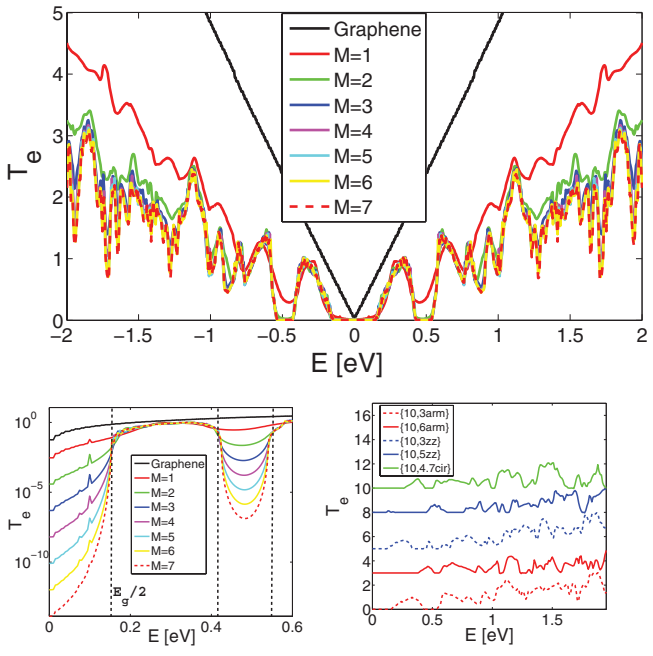

FIG. 3. (Color online) Top: Convergence with length (M, the number of unit cells with two holes along the device) of transmission for a {10,3arm} antidot lattice. Bottom left: Zoom at the transport gap for the {10,3arm} GAL. The leftmost vertical dashed line marks the value of the band gap obtained from the band structure of an infinite GAL. Bottom right: Transmissions close to the Fermi level for the selected GALs shown in Fig. 2. The transmission curves have been shifted by an integer to ease the comparison.

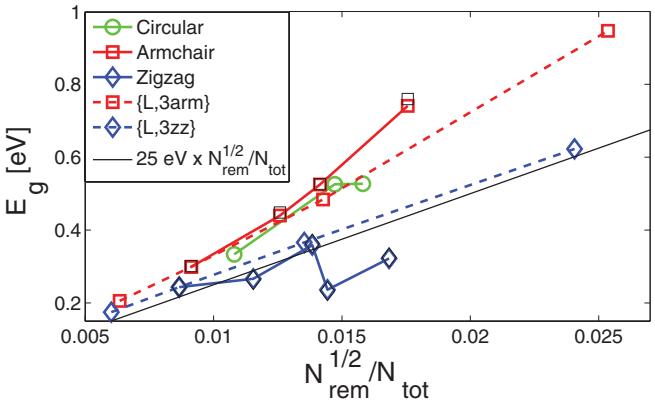

FIG. 4. (Color online) Scaling of the electronic transport gap E_g with increasing ratio of removed atoms compared to the simple scaling law estimated for circular holes.[17] The systems considered are {10,Szz} with $S = 3$, 4, 4.5, 5, 5.5; {10,Sarm} with $S = 3$, 4.5, 5, 6; and {10,Scir} with $S = 3.5$, 4.7, 5. Furthermore, we include two sets, {L,3arm} and {L,3zz} for $L = 6$, 8, 10, 12, with fixed hole geometry.

modulation of the hopping elements for the results with varying hole size for the armchair holes (black squares) and zigzag holes (black diamonds). The relaxation is found not to play a qualitative role in the equilibrium electronic properties of GALs within this model. The convergence is independent of the lattice parameters, and in all simulations presented hereafter between eight and ten unit cells are used.

Besides the transport gap, we observe that it is possible to approximate the transmission versus energy as linear curves corresponding to a simple reduction of the pristine transmission, $\mathcal{T}_0 \propto |E|$ (see example in the transmission plots in Fig. 5). We have calculated envelope lines obtained from a scaling of the pristine transmission with the width of the constriction $\mathcal{T}_{\text{eff}} = R_{\text{eff}}\,\mathcal{T}_0$, where $\mathcal{T}_0$ is the transmission of pristine graphene. The reduction factor R_{eff} describes the amount of pristine transmission that survives the lattice perturbation in terms of a regular perforation. The actual reduction factor is estimated as the average reduction found at each energy point. We find that the electronic transmission is reduced more than what would be expected from the effective width reduction $R_{\text{eff}} = W/W_0$. Here W is the minimal width along the device and W_0 is the width of the pristine graphene sheet. For the systems considered in Fig. 2, the hole dimension is varying between 1.2 and 2.6 nm, giving an effective width reduction between 71% and 26%. The actual reduction factor is decreasing linearly with hole dimensions from 24% to 5%. Therefore only a minor part of the average transmission reduction can be ascribed to the narrowing of the conducting plane. The present model does not take special account of the band gap opening. One could instead ask if the peak transmission is limited by the effective width. The peak transmission reduction factor is found to be decreasing from 65% to 21% and fits the effective width reduction very well for small holes. As the hole size increases the effective width is overestimated due to the triangular lattice structure of the perforation, and the reduction factor approaches the averaged value.

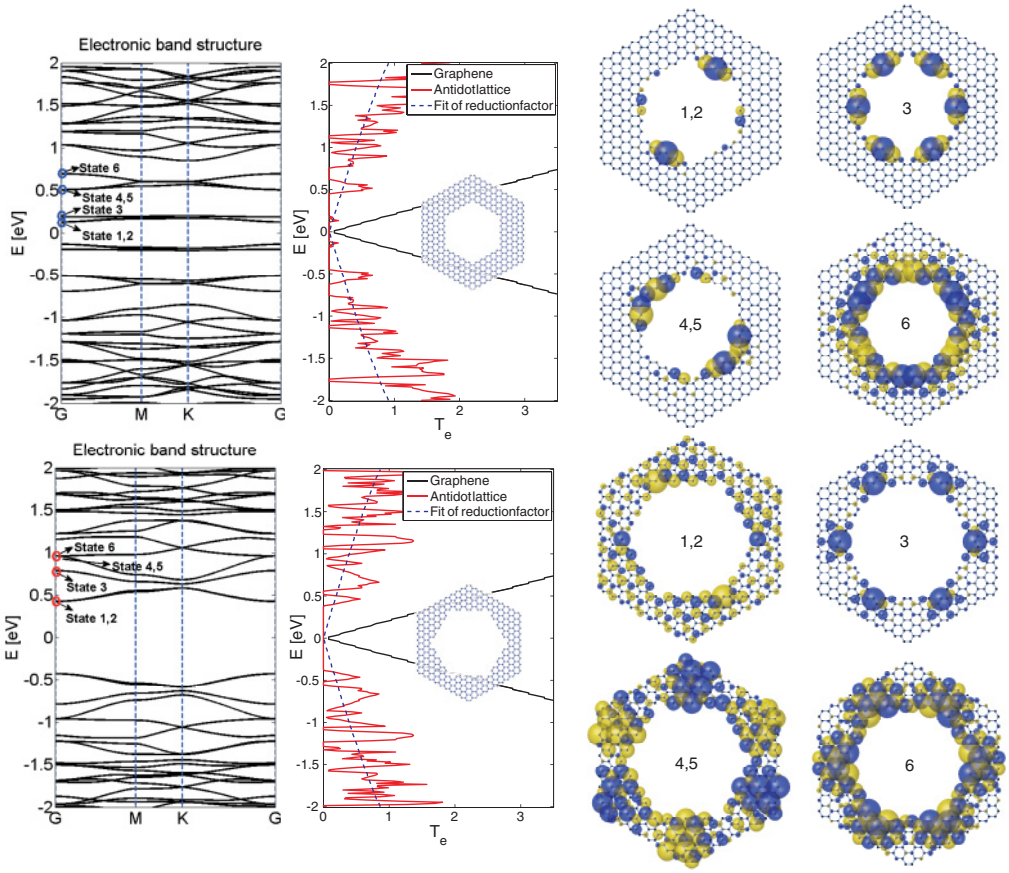

FIG. 5. (Color online) Left: Band structure for {10arm,5zz} (top) and {10arm,6arm} (bottom) antidot lattices, respectively. Middle: Corresponding electronic transmission around the Fermi level. The energies of the states illustrated and compared further have been marked with circles. Right: Eigenstates 1, 3, 4, and 6 at the Γ point with energies as marked in the corresponding band structures. The eigenstates of the {10,5zz} antidot lattice (top) are very localized at the edges. The eigenstates of the {10,6arm} antidot lattice (bottom) are less localized at the edges but resemble corner states. A phase of zero and π is colored blue and yellow, respectively.

A. Localization at zigzag edges

There is an important difference between holes of different atomic arrangements at the edges. In Fig. 5 we compare the electronic transmission and the band structures for two large holes with zigzag and armchair edges, respectively. The figure illustrates how the transmission can be directly traced back to the band structure of the GAL. It is furthermore seen how the structure with zigzag edges leads to an additional splitting into flat minibands around the Fermi level. This feature can be understood in terms of localized states due to a local excess of atoms of one of the two sublattices in the graphene bipartite lattice.[67] The local imbalance of A- and B-type atoms at the edges leads to the corresponding number of defect states. In hexagonal holes with zigzag edges, each side consists of a segment of either type A or B atoms. The hybridization will be small between these defect states, which are partially separated in space. As illustrated at the rightmost of Fig. 5, the flat minibands are highly localized at the edges. In the case of hexagonal holes with armchair edges, each side consists of an alternating sequence of A and B atoms. Therefore these defect states hybridize more, resulting in a larger shift from the Fermi level and a reduced flatness of the bands. As can be seen from Fig. 5, the first bands with minimal dispersion are mainly localized in the small zigzag corner region between two AB sequences. We expect the localized states to be sensitive to disorder, destroying the pristine edge chirality of the antidots. However, as is indicated by the {10,6arm} corner states, one can always expect to have some degree of localization at zigzag edge segments, which we have also found to be true in the mixed edges.

It is possible to quantify the degree of localization from the weight of the eigenstate at each atom. The localization factor for a given eigenstate in the site basis $\psi_n = [u_1, u_2, \ldots, u_N]$ is here defined as[71,72]

$$L_f(\psi_n) = \frac{\sum_{i=1}^{N} |u_i|^4}{\left(\sum_{i=1}^{N} |u_i|^2\right)^2}. \tag{7}$$

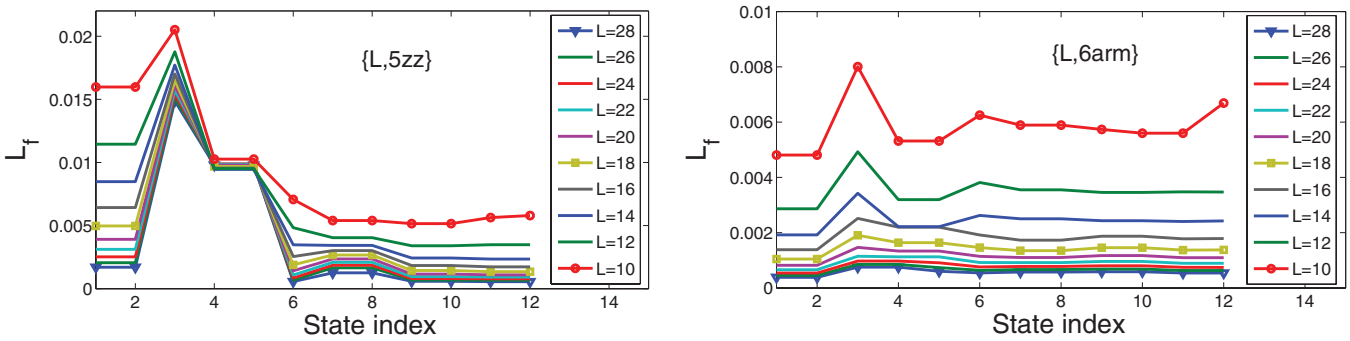

FIG. 6. (Color online) Localization factor as a function of conduction state index for a selection of distances between neighboring holes. We compare two fixed hole geometries, namely, the {L,5zz} (top) and {L,6arm} (bottom) GALs. These figures illustrate the physical difference between localization of states in GALs with pure zigzag and armchair edges through the variation of L and thereby the distance between the holes. Localization of states in GALs with zigzag edges is due to edge state localization as opposed to GALs with armchair edges, where localization is a result of the confinement of the electrons.

This factor equals $1/N$ when the state is fully delocalized, and all weights u_i have the same value. In the case of a state localized at a single site it gives 1. The inverse localization factor gives a measure of the number of sites that contribute to a given state.

A numerical example is given in Fig. 6. For the system with $L = 10$ and zigzag edges, we see that the first conduction states corresponding to the flat minibands are more localized than the following bands. For the armchair edge the localization parameter shows a weaker dependence on the state index. We conclude that the flat minibands of the zigzag edge are more localized than the corresponding states of an antidot lattice with armchair edges. Figure 6 further illustrates that this conclusion is independent of the values considered here for the unit cell dimension L. The localization factor for the armchair edge depends more strongly on the dimension of the unit cell, that is, the hole-hole distance, and is in general an order of magnitude lower compared to the zigzag edge. Therefore the band gaps of GALs with armchair edges are determined by the confinement, as opposed to the case of zigzag edges where it is governed by edge state formation. This is the reason the band gap scales differently depending on the edge type of the hole (Fig. 4). For very small holes with zigzag edges we find that the almost dispersionless GAL minibands are positioned further into the band structure (see the {L,3zz} curve in Fig. 4). However, as the length of the edge is increased the zigzag edge-state energies are located directly at the band gap. It is therefore not to be expected that a larger hole with certainty results in a larger band gap or transport gap. Even though this happens for holes with armchair edges, introduction of zigzag regions may suppress the band gap, which is important for electronic and optical applications of antidot lattices.

We conclude that GALs with armchair edge geometry have a larger band gap as compared to both zigzag edge geometries and the predicted scaling.[17] Furthermore, the hexagonal antidots with armchair edges show a systematic scaling of the transport gap with hole size, making this system preferable for electronic applications.

IV. HEAT TRANSPORT

We now turn to the thermal transport properties of finite GALs. In Fig. 7 we show the phonon transmission as a function of M, the number of repeated unit cells. To quantify the convergence with length we have calculated the thermal conductance at 300 K for the antidot lattices of Fig. 2 at different lengths. This shows that the thermal properties converge at a length scale similar to that of the electrons, so the phonons also behave "bulklike" after six to seven unit cell repetitions. In all simulations presented hereafter we use $8 - 10$ unit cells.

The thermal conductance due to phonons in pristine graphene at 300 K should be compared to a measured thermal

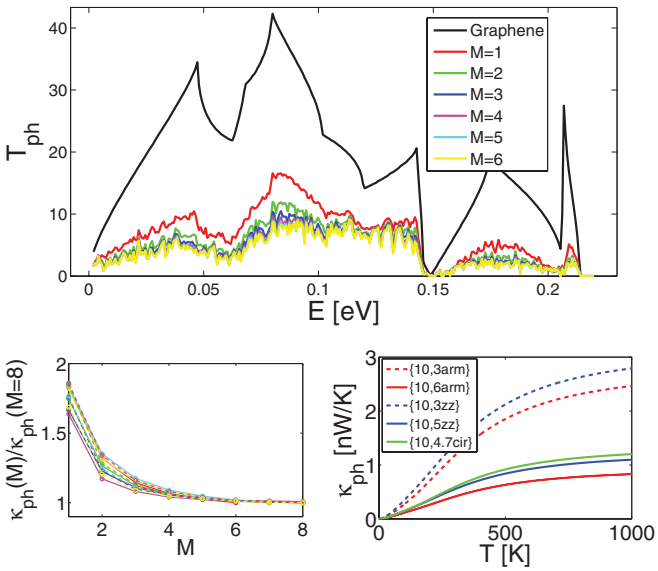

FIG. 7. (Color online) Top: Convergence with length of phonon transmission for a {10,3arm} antidot lattice. Bottom left: Convergence of the thermal conductance at 300 K from phonons with length, normalized by its value at $M = 8$. Bottom right: Comparison of the thermal conductance as a function of temperature for the selected GALs shown in Fig. 2.

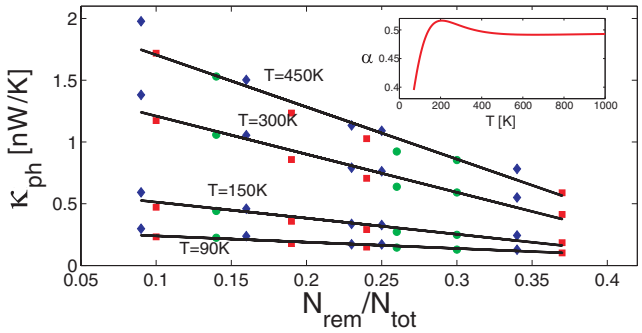

FIG. 8. (Color online) Thermal conductance from phonons as a function of hole dimension. The red squares, blue diamonds, and green circles label holes with armchair, zigzag, and circular or mixed edges, respectively. Four different temperatures are plotted for each system. From top to bottom the thermal conductance is found at temperatures of [450, 300, 150, 90] K. The thermal conductance at these four temperatures is for pristine graphene found to be [8.5, 6.1, 2.6, 1.2] $\frac{\mathrm{nW}}{\mathrm{K}}$. Inset: fitted dimensionless parameter α describing the scaling with hole size of the thermal conductance.

conductivity[21,73] of $\sigma_{ph}^{\mathrm{exp}} \approx 4.5 - 5.5 \times 10^3$ W/(m K). Our result compares well to other theoretical calculations, where it similarly was reported[74] that the reduced ballistic thermal conductance, which we find to be $\kappa_{ph}^{\mathrm{pri}}/(W_0 h) \approx 4.27 \times 10^9$ W/(m^2 K), is much larger than the experimentally extracted partially diffusive result $\sigma_{ph}^{\mathrm{exp}}/(L^{\mathrm{exp}}) \approx 0.39 - 0.48 \times 10^9$ W/(m^2 K). Here $h = 3.35$ Å and $L^{\mathrm{exp}} \approx 11.5\,\mu$m are the graphite interlayer distance and traveled distance, respectively, by the phonons in the experiment by Balandin *et al.*[21] and W_0 is the computational unit cell width. The main difference here can probably be attributed to isotopes, electron-phonon scattering, and especially anharmonicity, being important for long devices.

In analogy with the electronic transmission we have calculated an average reduction factor for the phonon transmission. The transmission of the lowest acoustic and especially the highest optical modes is generally reduced more than the remaining of the phonon spectrum. Similarly to the electron case, the average reduction factor decreases linearly with the hole width for the considered systems. The average phonon transmission reduction factor is found to be of the same order of magnitude as compared to the electron transmission. Once again only a minor part of the transmission reduction can be ascribed to the reduction in effective width of the conducting plane due to the perforation. There is a tendency that the phonons are scattered more than the electrons by the nanoperforation for small antidot concentrations. Furthermore, the electronic reduction factor can be much larger at a specific chemical potential for small holes. For large hole dimensions both the electrons and phonons are scattered to an extent where the transmission is reduced by more than 80% on average for the systems considered. For the largest holes up to 36% of the atoms have been removed from the pristine graphene plane.

In Fig. 8 the temperature and hole size dependence of the phonon thermal conductance is given for our selection of systems with varying hole size and shape. Figure 8 illustrates how the thermal conductance decreases almost linearly with the hole size for typical perforation removal ratios (larger than 5% perforation). Furthermore, the graph shows that the thermal conductance has a tendency to be slightly larger for holes with zigzag edges (shown as diamonds in Fig. 8). A similar behavior has been found for graphene nanoribbons with zigzag edges.[52] However, compared to the electronic case the thermal transport features are less sensitive to the exact shape and edge of the holes.

For the purpose of making it easy to compare our result with other calculations and experiments, we give an empirical expression for the thermal conductance. In the regime where the thermal conductance is linear in the hole dimension, one can parametrize the thermal conductance as

$$\kappa_{ph} \approx \left(-\alpha(T)\frac{N_{\mathrm{rem}}}{N_{\mathrm{tot}}} + \beta\right)\kappa_{ph}^{\mathrm{pri}}(T)\,. \tag{8}$$

From this approximation we fit the "linear regime offset" $\beta \approx 0.25$ and the dimensionless parameter $\alpha(T)$, given in the inset of Fig. 8. The lines in Fig. 8 are illustrating this parametrization. Only the variation of absolute hole size is plotted in Fig. 8, for a fixed unit cell dimension L. No qualitative difference is found regarding antidot concentration dependence of the thermal conductance, keeping the hole geometry fixed and varying the unit cell parameter L. Again, this illustrates that the phonon properties are less sensitive to the exact nature of the holes as compared to the corresponding electronic properties.

In Fig. 9 we have illustrated the electronic contribution to the thermal conductance at four different temperatures. Due to the vanishing electronic density of states around zero chemical potential, the thermal conductance of GALs is

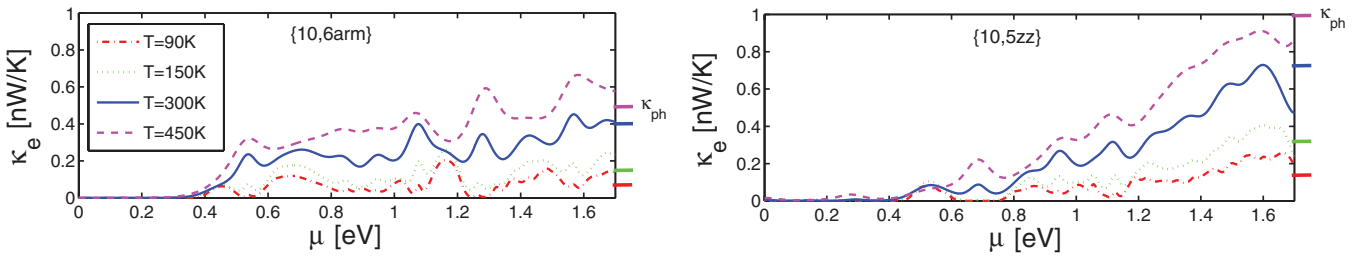

FIG. 9. (Color online) Electronic contribution to the thermal conduction. Top: {10,6arm} antidot lattice. Bottom: {10,5zz} antidot lattice. From top to bottom the curves are found at a temperature of [450, 300, 150, 90] K. The corresponding phonon thermal conductance has been marked to the right of the plot for comparison.

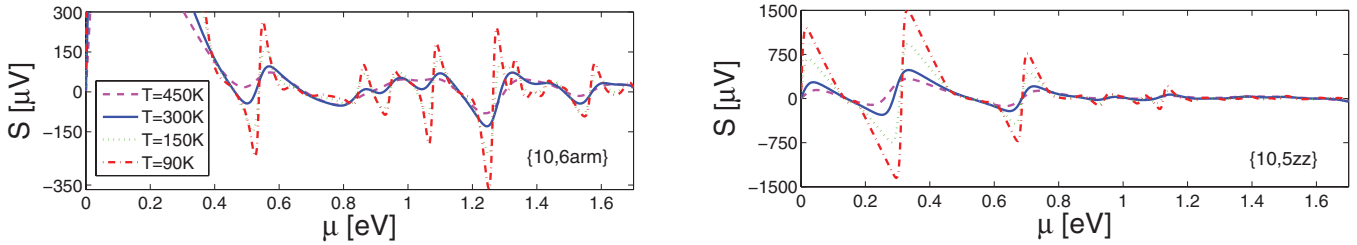

FIG. 10. (Color online) Seebeck coefficient at the four different temperatures [450, 300, 150, 90] K for the {10,6arm} (top) and {10,5zz} (bottom) GAL. Notice the different scale on the Seebeck coefficient. The main Seebeck peaks of the GAL with zigzag edges occur at the energies of the low transmitting localized states, whereas the main contribution to the thermoelectric power of the GAL with armchair edges is positioned at energies further into the band structure.

dominated by phonons, as is also the case of pristine graphene. However, the electronic contribution can dominate, even at room temperature, when a large gate bias is applied.

V. THERMOELECTRIC FIGURE OF MERIT

Next we report the thermoelectric properties of the considered GALs. In Fig. 10 we compare the Seebeck coefficient for a GAL with armchair edges (top) and zigzag edges (bottom). The Seebeck coefficient displays peak values[75] of the order of $0.1 - 1.5\,\mathrm{mV/K}$, which is similar to what has been obtained for other carbon-based nanosystems and molecular contacts.[8,34,76]

For bulk materials the thermoelectric figure of merit is defined in terms of the electrical and thermal conductivities, σ_e, σ_t, as $ZT = T\sigma_e S^2/\sigma_t$. For the ballistic graphene systems we can write it in terms of their respective conductances by introducing a width, effective length, and thickness, $ZT = TG_e S^2/(\kappa_e + \kappa_{ph})$. The maximal thermoelectric figure of merit ZT is obtained after length convergence due to the increased band gap and decreased thermal conductance. Within the ballistic limit the thermoelectric figure of merit eventually becomes independent of M at the same scale as the electron and phonon transmissions ($M \geqslant 7$). Since our system consists of two graphene leads connected by a perfect superlattice of holes, it never reaches a diffusive transport limit. In the following we consider the thermoelectric properties after length convergence has been achieved. We expect that a further gain in thermoelectric efficiency could be obtained in the diffusive limit (in the presence of disorder), as was seen for edge-disordered nanoribbons.[40] This topic should be investigated in the future. The obtained ZT shown in Fig. 11 as a function of chemical potential has a number of peaks corresponding to a large variation of the transmission with energy. The Seebeck coefficient is a measure of these changes and their robustness to temperature smoothening. One important feature is that the high peaks in the Seebeck coefficient for the {10,5zz} lattice mainly occur at very low energy, where the transmission is low, whereas for the {10,6arm} lattice the dominating peaks occur at higher chemical potential. Therefore the peak ZT is higher for the {10,6arm} as a result of the higher electronic conductance at peak position, as illustrated in Fig. 11. The Seebeck coefficient is highly sensitive to the variations in the electronic transmission resulting from different hole edges, sizes, and so forth. In Fig. 12 we collect the maximum ZT values we have found for a selection of GALs. It seems possible to obtain larger ZT from GALs based on hexagonal holes with armchair edges. This is a result of the additional splitting into minibands for zigzag edges. The reason for this additional splitting is, as mentioned in Sec. III A, the formation of edge states at zigzag edges. As a consequence the Seebeck coefficient can be larger for zigzag edges. However, the power factor is significantly lower due to the lower transmission from the isolated energy levels with low dispersion. There is also a weak trend that the hole dimension compared to the system size should be maximized. By increasing the hole dimension we actually reduce the electronic figure of merit, defined as

$$ZT_{el} = \frac{S^2 G_e T}{\kappa_e} = \frac{\kappa_{ph} + \kappa_e}{\kappa_e} ZT, \tag{9}$$

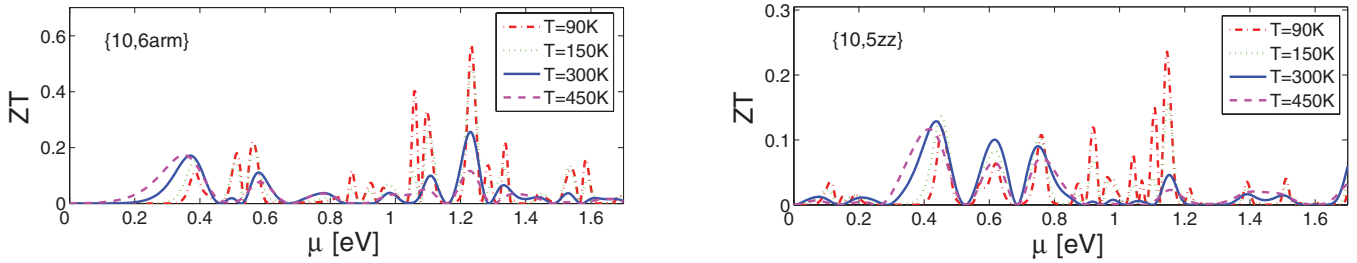

FIG. 11. (Color online) ZT for {10,6arm} and {10,5zz} lattices at the four temperatures [450, 300, 150, 90] K. At low temperature the pure electronic figure of merit ZT_{el} can be very large due to a vanishing thermal conductance from electrons and sharp features in the transmission spectrum. At low temperature many sharp transmission features also becomes visible in the actual ZT.

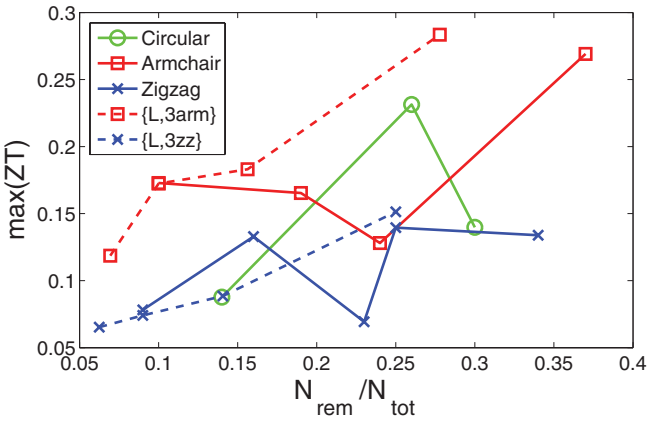

FIG. 12. (Color online) ZT dependence on the ratio of removed atoms in the nanoperforation at $T = 300$ K. Systems included in the figure are $\{10,S\text{zz}\}$ with $S = 3$, 4, 4.5, 5, 5.5, $\{10,S\text{arm}\}$ with $S = 3$, 4.5, 5, 6 and $\{10,S\text{cir}\}$ with $S = 3.5$, 4.7, 5 (full lines) and furthermore, two set of systems with a fixed hole $\{L,3\text{arm}\}$ and $\{L,3\text{zz}\}$ with $L = 6$, 8, 10, 12 (dotted lines).

but obtain a larger fraction of it due to a reduced phonon conductance. Higher ZT could possibly be obtained by increasing the hole dimension even further, but these systems will be very challenging to fabricate.

We have presented calculations in which the antidot concentration is varied either by changing the hole size (and shapes), while keeping the lattice parameter L fixed, or keeping the hole size and shape fixed under L variation. However, the latter examination is computationally possible only for small antidot dimensions. Therefore it is possible to see if the thermoelectric properties depend on the absolute hole size or only on the antidot concentration. For the examined systems we find that antidots with smaller absolute sizes seem to result in better thermoelectric performance for holes with armchair edges. For holes with zigzag edges the exact nature of the localized states comes into play and seems to keep the thermoelectric performance less sensitive to the absolute hole size.

The electrons-only result, ZT_{el} ($\kappa_{ph} = 0$), describes an upper bound of the figure of merit. However, we find it to be somewhat artificial, due to the fact that the phonon contribution to the thermal conductance shifts the position of the peaks and ZT_{el} possess a (in principle unbound) peak every time the electronic thermal conductance is zero [Eq. (9)]. Especially in the presence of gaps in the electronic band structure, the computation of ZT_{el} can be numerically challenging. However, evaluating the ZT_{el} expression at the true peak position can give an estimate of the gain by a further reduction of the phonon conductance. For the $\{10,6\text{arm}\}$ GAL the first peak ($\mu = 0.37$ eV) and the highest peak ($\mu = 1.23$ eV) have a $ZT = 0.17$ and 0.26 with corresponding $ZT_{el} = 4.78$ and 0.77, a factor of 28 and 3 larger than the true ZT, respectively. For the $\{10,5\text{zz}\}$ lattice we have the first peak value $ZT = 0.13$ with corresponding $ZT_{el} = 5.77$, a factor of 44 larger at the same energy. At high chemical potential the main limitation is the electronic structure and not a further reduction of the phonon heat conductance. On the contrary, one could obtain a significant ZT enhancement at low chemical potential by further reducing the thermal conductance. Isotope scattering, anharmonic interactions, electron-phonon interactions, and graphene-substrate interactions could all contribute to a reduction of the phonon thermal conductance. In Fig. 13 we illustrate the effect of a reduction of the phonon thermal conductance. The parameter Δ gives the fraction of the original phonon thermal conductance kept in the calculation. For the $\{10,6\text{arm}\}$ GAL the first peak ($\mu \approx 0.37$ eV) increases more rapidly than the high-energy peaks. The peak position crossover happens at around $\Delta \approx 0.35$. When the phonon thermal conductance dominates, the figure of merit variation goes as ZT/Δ, clearly present in the low-energy ZT variation (see Fig. 13, bottom), even when the phonon thermal conductance is reduced below 5% of its original value.

We propose one of two routes to obtaining higher ZT. Either one could find a way to reduce the thermal conductance without affecting the electrons. Surface decoration might be a promising way to obtain this. Another route could be to improve the electronic properties of GALs, e.g., by combining this system with other nanostructured devices. This could

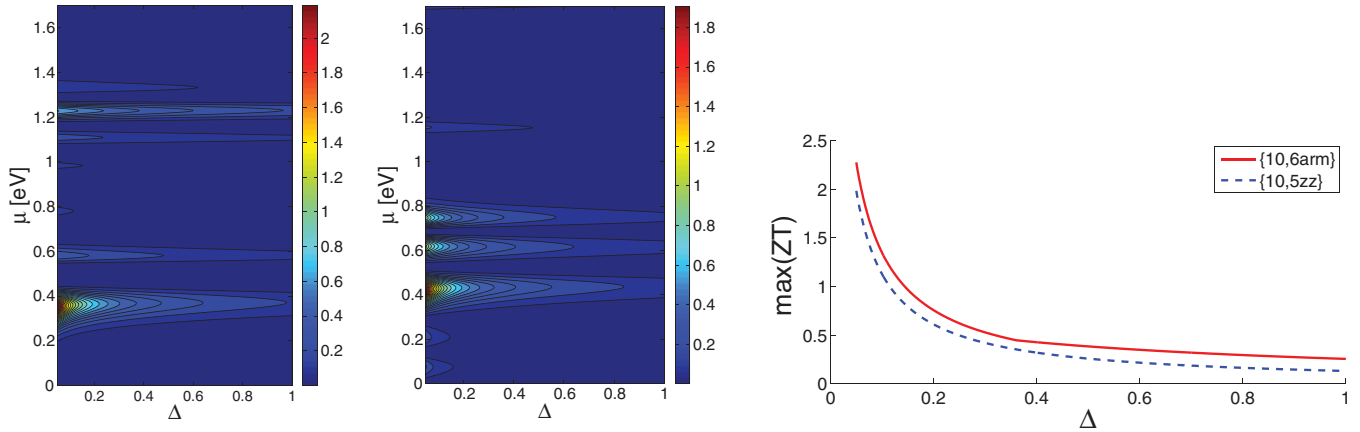

FIG. 13. (Color online) ZT variation with a decrease of the phonon thermal conductance at $T = 300$ K. Δ describes the fraction of the original thermal conductance used in the calculation. Top: ZT as a function of the chemical potential and the phonon thermal conductance for the $\{10,6\text{arm}\}$ (left) and $\{10,5\text{zz}\}$ (right) GAL. Bottom: Peak ZT as a function of the variation of the phonon thermal conductance.

increase the peak ZT obtained at high chemical potential. We note that one-dimensional nanosystems may display a large Seebeck coefficient leading to larger ZT. However, on the other hand, the two-dimensional (2D) GAL structure may have an important advantage. In a 2D GAL the system geometry does not pose inherent limits for the converted power, as it does for a system of parallel quasi-one-dimensional systems, such as quantum wires or graphene nanoribbons: the power can be increased by simply making the GAL system broader. This provides a strong motivation for further investigations of GALs as thermoelectric devices, perhaps as an integrated element in future graphene nanoelectronics. Despite the high intrinsic thermal conductance of graphene, it is noticeable that one can utilize the nanoperforation to obtain ZT exceeding 0.25, a factor of 35 enhancement compared to what is found for bulk graphene.

VI. DISCUSSION AND CONCLUSION

We have theoretically shown that GALs allow the simultaneous manipulation of both electronic and thermal transport properties of graphene sheets. Our calculations have been carried out in the ballistic limit, which gives a reasonable first estimate for short devices whose dimensions are smaller than the various scattering lengths (important scattering mechanisms include the anharmonic phonon-phonon interactions, electron-phonon scattering, and electron-electron scattering). Also, spin polarization may turn important: recent studies have shown that one can have spin-splitting and a magnetic moment in triangular[77–79] antidots with pure zigzag edges. Above all, the most important future task is a systematic study of disorder effects. Our preliminary results suggest that a low degree of disorder can increase ZT due to a decrease of the thermal conductance, whereas a high degree of disorder affects both electrons and phonons so that the decrease in power factor outweighs the decrease in thermal conductance.

A key result of our analysis is the convergence of transport properties with length for GALs. The ballistic transport properties converge fast toward that of the infinite antidot lattice. We have also found that the quantization is an important feature of both electron and phonon transport properties of GALs. This is seen from the fact that the transmissions are reduced far more than what would be expected from an effective width estimation and therefore the exact scattering rate for the different edge types is important. The average transmission reduction factor is found to be on the same order of magnitude for electrons and phonons. In general, the formation of edge states determine the band gap of GALs with pure zigzag edges as opposed to pure armchair edges, where the band gap is determined by the confinement of electrons. Furthermore, the different edge characteristics play an important role in the observed difference in thermoelectric properties. ZT is found to be lower for GALs with zigzag edges due to the additional splitting into minibands for large structures and a corresponding lower power factor. The maximal thermoelectric efficiency $ZT \approx 0.3$ has been obtained for GALs with pure armchair edges. Therefore, it is possible to obtain fair thermoelectric properties of graphene-based nanosystems, even despite lattice distortions which highly affect both the π-electron-determined electronic properties and the sp_2-bonding-determined thermal conductance, such as the nanoperforations. The main limitation in thermoelectric applications of GALs at high chemical potential is set by the electronic structure because the electronic heat conductance is large at the high-energy peak position of S and ZT. At low chemical potential we expect that one could benefit from a further reduction of the phononic thermal conductance due to isotope scattering and anharmonic interactions.

ACKNOWLEDGMENTS

We thank the Danish Center for Scientific Computing (DCSC) and Direktør Henriksens Fond for providing computer resources. T.M. acknowledges support from FTP Grant No. 274-08-0408. A.P.J. is grateful to the FiDiPro program of the Academy of Finland.

*Tue.Gunst@nanotech.dtu.dk

[1] K. Saqr and M. Musa, J. Therm. Sci. **13**, 165 (2009).
[2] L. E. Bell, Science **321**, 1457 (2008).
[3] G. D. Mahan and J. O. Sofo, Proc. Natl. Acad. Sci. USA **93**, 7436 (1996).
[4] C. Jeong, R. Kim, and M. S. Lundstrom, e-print arXiv:1103.1274 (2011).
[5] R. Kim, S. Datta, and M. S. Lundstrom, J. Appl. Phys. **105**, 034506 (2009).
[6] P. Pichanusakorn and P. Bandaru, Mater. Sci. Eng. R **67**, 19 (2010).
[7] M. Dresselhaus, G. Chen, M. Tang, R. Yang, H. Lee, D. Wang, Z. Ren, J. Fleurial, and P. Gogna, Adv. Mater. **19**, 1043 (2007).
[8] K. K. Saha, T. Markussen, K. S. Thygesen, and B. K. Nikolic, Phys. Rev. B **84**, 041412(R) (2011).
[9] Y. Dubi and M. Di Ventra, Rev. Mod. Phys. **83**, 131 (2011).
[10] P. Reddy, S. Jang, R. A. Segalman, and A. Majumdar, Science **315**, 1568 (2007).
[11] M. Paulsson and S. Datta, Phys. Rev. B **67**, 241403 (2003).
[12] T. Markussen, A. P. Jauho, and M. Brandbyge, Phys. Rev. Lett. **103**, 055502 (2009).
[13] J. Tang, H. Wang, D. H. Lee, M. Fardy, Z. Huo, T. P. Russell, and P. Yang, Nano Lett. **10**, 4279 (2010).
[14] J. Yu, S. Mitrovic, D. Tham, J. Varghese, and J. R. Heath, Nat. Nanotechnol. **5**, 718 (2010).
[15] Y. Chen, T. Jayasekera, A. Calzolari, K. W. Kim, and M. Buongiorno Nardelli, J. Phys. Condens. Matter **22**, 372202 (2010).
[16] K. Esfarjani, M. Zebarjadi, and Y. Kawazoe, Phys. Rev. B **73**, 085406 (2006).
[17] T. G. Pedersen, C. Flindt, J. Pedersen, N. A. Mortensen, A. P. Jauho, and K. Pedersen, Phys. Rev. Lett. **100**, 136804 (2008).
[18] C. B. Vining, Nature Mater. **8**, 83 (2009).
[19] A. Majumdar, Science **303**, 777 (2004).
[20] A. K. Geim, Science **324**, 1530 (2009).
[21] A. A. Balandin, S. Ghosh, W. Bao, I. Calizo, D. Teweldebrhan, F. Miao, and C. N. Lau, Nano Lett. **8**, 902 (2008).

[22] J. H. Seol, I. Jo, A. L. Moore, L. Lindsay, Z. H. Aitken, M. T. Pettes, X. Li, Z. Yao, R. Huang, D. Broido, N. Mingo, R. S. Ruoff, and L. Shi, Science **328**, 213 (2010).
[23] D. Dragoman and M. Dragoman, Appl. Phys. Lett. **91**, 203116 (2007).
[24] A. A. Balandin, Nature Mater. **10**, 569 (2011).
[25] Z. Huang, T. S. Fisher, and J. Y. Murthy, J. Appl. Phys. **108**, 094319 (2010).
[26] Z. Huang, T. S. Fisher, and J. Y. Murthy, J. Appl. Phys. **108**, 114310 (2010).
[27] J. Hu, S. Schiffli, A. Vallabhaneni, X. Ruan, and Y. P. Chen, Appl. Phys. Lett. **97**, 133107 (2010).
[28] N. Mingo, K. Esfarjani, D. A. Broido, and D. A. Stewart, Phys. Rev. B **81**, 045408 (2010).
[29] H. Zhang, G. Lee, A. F. Fonseca, T. L. Borders, and K. Cho, J. Nanomater. **2010**, 537657 (2010).
[30] J. Jiang, J. Lan, J. Wang, and B. Li, J. Appl. Phys. **107**, 054314 (2010).
[31] S. Ghosh, W. Bao, D. L. Nika, S. Subrina, E. P. Pokatilov, C. N. Lau, and A. A. Balandin, Nature Mater. **9**, 555 (2010).
[32] N. Wei, L. Xu, H. Wang, and J. C. Zheng, Nanotechnology **22**, 105705 (2011).
[33] X. Ni, G. Liang, J. S. Wang, and B. Li, Appl. Phys. Lett. **95**, 192114 (2009).
[34] Y. Ouyang and J. Guo, Appl. Phys. Lett. **94**, 263107 (2009).
[35] V. Adamyan and V. Zavalniuk, J. Phys. Condens. Matter **23**, 015402 (2011).
[36] J. B. Haskins, A. Kinaci, C. Sevik, H. Sevincli, G. Cuniberti, and T. Cagin, ACS Nano **5**, 3779 (2011).
[37] W. Li, H. Sevinçli, G. Cuniberti, and S. Roche, Phys. Rev. B **82**, 041410 (2010).
[38] A. V. Savin, Y. S. Kivshar, and B. Hu, Phys. Rev. B **82**, 195422 (2010).
[39] W. Li, H. Sevincli, S. Roche, and G. Cuniberti, Phys. Rev. B **83**, 155416 (2011).
[40] H. Sevincli and G. Cuniberti, Phys. Rev. B **81**, 113401 (2010).
[41] J. A. Fürst, J. G. Pedersen, C. Flindt, N. A. Mortensen, M. Brandbyge, T. G. Pedersen, and A. P. Jauho, New J. Phys. **11**, 095020 (2009).
[42] R. Petersen, T. G. Pedersen, and A. P. Jauho, ACS Nano **5**, 523 (2011).
[43] F. Ouyang, S. Peng, Z. Liu, and Z. Liu, ACS Nano **5**, 4023 (2011).
[44] J. Eroms and D. Weiss, New J. Phys. **11**, 095021 (2009).
[45] M. Begliarbekov, O. Sul, J. Santanello, N. Ai, X. Zhang, E. H. Yang, and S. Strauf, Nano Lett. **11**, 1254 (2011).
[46] M. Kim, N. S. Safron, E. Han, M. S. Arnold, and P. Gopalan, Nano Lett. **10**, 1125 (2010).
[47] J. Bai, X. Zhong, S. Jiang, Y. Huang, and X. Duan, Nat. Nanotechnol. **5**, 190 (2010).
[48] O. Akhavan, ACS Nano **4**, 4174 (2010).
[49] B. Krauss, P. Nemes-Incze, V. Skakalova, L. P. Biro, K. von Klitzing, and J. H. Smet, Nano Lett. **10**, 4544 (2010).
[50] Y. Xu, X. Chen, J. S. Wang, B. L. Gu, and W. Duan, Phys. Rev. B **81**, 195425 (2010).
[51] Y. Zhang, Q. Li, Y. Li, Y. Zhang, and F. Zhai, J. Phys. Condens. Matter **22**, 315304 (2010).
[52] J. Hu, X. Ruan, and Y. P. Chen, Nano Lett. **9**, 2730 (2009).
[53] Y. Hancock, A. Uppstu, K. Saloriutta, A. Harju, and M. J. Puska, Phys. Rev. B **81**, 245402 (2010).
[54] K. Lopata, R. Thorpe, S. Pistinner, X. Duan, and D. Neuhauser, Chem. Phys. Lett. **498**, 334 (2010).
[55] H. Karamitaheri, M. Pourfath, R. Faez, and H. Kosina, *Proceedings of The Electrochemical Society* (Montreal, Quebec, Canada, 2011), pp. 185–192.
[56] H. Karamitaheri, M. Pourfath, R. Faez, and H. Kosina, *12th International Conference on Thermal, Mechanical and Multi-Physics Simulation and Experiments in Microelectronics and Microsystems (EuroSimE)*, (IEEE, 2011), pp. 1–4.
[57] O. A. Tretiakov, A. Abanov, and J. Sinova, Appl. Phys. Lett. **99**, 113110 (2011).
[58] J. T. Lü and J. S. Wang, Phys. Rev. B **78**, 235436 (2008).
[59] Similar notation is used for carbon nanotubes. The Γ-point calculation of the electronic transmission corresponds to that of the corresponding carbon nanotube.
[60] U. Sivan and Y. Imry, Phys. Rev. B **33**, 551 (1986).
[61] T. Markussen, R. Rurali, M. Brandbyge, and A. P. Jauho, Phys. Rev. B **74**, 245313 (2006).
[62] T. Markussen, A. P. Jauho, and M. Brandbyge, Phys. Rev. B **79**, 035415 (2009).
[63] The number of k points per unit cell width is kept fixed. For the $L = 10$ systems a number of $N_k = 25k$ points are used.
[64] W. A. Harrison, *Electronic Structure and the Properties of Solids* (Dover Publications, Inc., New York, 1989).
[65] F. Guinea, M. I. Katsnelson, and A. K. Geim, Nat. Phys. **6**, 30 (2010).
[66] T. B. Boykin, M. Luisier, G. Klimeck, X. Jiang, N. Kharche, Y. Zhou, and S. K. Nayak, J. Appl. Phys. **109**, 104304 (2011).
[67] M. Vanevic, V. M. Stojanovic, and M. Kindermann, Phys. Rev. B **80**, 045410 (2009).
[68] D. W. Brenner, Phys. Rev. B **42**, 9458 (1990).
[69] J. D. Gale and A. L. Rohl, Mol. Simul. **29**, 291 (2003).
[70] Here we use a transmission cutoff value of 5 10^{-5} to define the transport gap and find the same values as obtained from a band structure calculation of the band gap.
[71] W. Visscher, J. Non-Cryst. Solids **8-10**, 477 (1972).
[72] L. Kaplan, Physica E **9**, 502 (2001).
[73] D. L. Nika, E. P. Pokatilov, A. S. Askerov, and A. A. Balandin, Phys. Rev. B **79**, 155413 (2009).
[74] J. W. Jiang, J. S. Wang, and B. Li, Phys. Rev. B **79**, 205418 (2009).
[75] It is worth mentioning that the larger Seebeck coefficient obtained within the band gap has a numerical origin. This can be seen from the low-temperature Mott formula, $S(T,\mu) \approx \frac{\pi^2 k_B^2 T}{3e} \frac{\partial ln T_e}{\partial E}|\mu$, since the logarithmic derivative of the electronic transmission should be zero within the band gap, except from contributions from numerical fluctuations. The power factor SG_e is correctly found to be zero within the band gap.
[76] W. S. Bao, S. Y. Liu, and X. L. Lei, J. Phys. Condens. Matter **22**, 315502 (2010).
[77] H. Yang, M. Chshiev, X. Waintal, and S. Roche, e-print arXiv:1103.4188 (2011).
[78] W. Liu, Z. F. Wang, Q. W. Shi, J. Yang, and F. Liu, Phys. Rev. B **80**, 233405 (2009).
[79] X. H. Zheng, G. R. Zhang, Z. Zeng, V. M. García-Suárez, and C. J. Lambert, Phys. Rev. B **80**, 075413 (2009).

Paper II

Jing-Tao Lü, Tue Gunst, Antti-Pekka Jauho and Mads Brandbyge

Current-induced dynamics in carbon atomic contacts

Beilstein Journal of Nanotechnology **2**, 814-823 (2011)

Beilstein Journal of Nanotechnology

Current-induced dynamics in carbon atomic contacts

Jing-Tao Lü[*1], Tue Gunst[1], Per Hedegård[*2] and Mads Brandbyge[*1]

Full Research Paper

Open Access

Address:
[1]DTU-Nanotech, Dept. of Micro- and Nanotechnology, Technical University of Denmark (DTU), Ørsteds Plads, Bldg. 345E, DK-2800 Lyngby, Denmark and [2]Niels Bohr Institute, Nano-Science Center, University of Copenhagen, Denmark

Email:
Jing-Tao Lü[*] - jtlu@nanotech.dtu.dk;
Per Hedegård[*] - hedegard@fysik.ku.dk;
Mads Brandbyge[*] - mads.brandbyge@nanotech.dtu.dk

* Corresponding author

Keywords:
carbon-nanoelectronics; current-induced forces; molecular contacts; nanoscale Joule heating; semiclassical Langevin equation

Beilstein J. Nanotechnol. **2011,** *2,* 814–823.
doi:10.3762/bjnano.2.90

Received: 14 July 2011
Accepted: 25 November 2011
Published: 16 December 2011

This article is part of the Thematic Series "Transport through molecular junctions".

Guest Editor: J. M. van Ruitenbeek

Abstract

Background: The effect of electric current on the motion of atoms still poses many questions, and several mechanisms are at play. Recently there has been focus on the importance of the current-induced nonconservative forces (NC) and Berry-phase derived forces (BP) with respect to the stability of molecular-scale contacts. Systems based on molecules bridging electrically gated graphene electrodes may offer an interesting test-bed for these effects.

Results: We employ a semi-classical Langevin approach in combination with DFT calculations to study the current-induced vibrational dynamics of an atomic carbon chain connecting electrically gated graphene electrodes. This illustrates how the device stability can be predicted solely from the modes obtained from the Langevin equation, including the current-induced forces. We point out that the gate offers control of the current, independent of the bias voltage, which can be used to explore current-induced vibrational instabilities due the NC/BP forces. Furthermore, using tight-binding and the Brenner potential we illustrate how Langevin-type molecular-dynamics calculations including the Joule heating effect for the carbon-chain systems can be performed. Molecular dynamics including current-induced forces enables an energy redistribution mechanism among the modes, mediated by anharmonic interactions, which is found to be vital in the description of the electrical heating.

Conclusion: We have developed a semiclassical Langevin equation approach that can be used to explore current-induced dynamics and instabilities. We find instabilities at experimentally relevant bias and gate voltages for the carbon-chain system.

Introduction

The effects of electric current on the motion of atoms have become particular important in the on-going quest for molecular-scale electronics [1-4]. Atomic motion due to electric current is behind the long-term breakdown of interconnects leading to failure in integrated circuits. This effect is of even greater importance for systems where the bottle-neck for the current

flow is a few chemical bonds. The inelastic scattering of electrons by atomic vibrations leads to the well-known effect of Joule heating, which can have an impact on the electrical behavior and stability. However, recently it was pointed out [5-8] that other current-induced forces can play a role. For instance, in the case of molecular contacts with conductance on the order of $G_0 = 2e^2/h = 1/12.9$ kΩ (e being the electron charge and h Planck's constant), and under "high" bias voltage (~1 V), the current-induced forces that do not conserve the energy of the atomic motion may lead to run-away behavior. However, experiments in this regime are very challenging. For example, for the typical experiments involving molecular-scale contacts between bulk electrodes it is not possible to image the atomic structure while the contacts are in place and current is flowing. Furthermore, it is far from being trivial to add additional gate potentials in order to modify the electronic structure and gain independent control of the bias voltage and current [3,9].

On the theoretical side, it is desirable to develop computer simulation techniques, such as molecular dynamics (MD), preferably without adjustable parameters, to study in detail the complex current-driven atomic processes. To this end, we recently developed an approach based on the semiclassical Langevin equation, which may form the basis of MD. In this description the nonequilibrium electronic environment is described as an effective "bath" influencing the atomic dynamics. In particular, we identified the forces acting on the atoms due to the electric current. These include "extra" fluctuating forces yielding the Joule heating, a nonconservative "electron-wind" force (denoted NC), recently discussed by Todorov and co-workers [5], and a Lorentz-like force originating from the quantum-mechanical "Berry phase" of the electronic subsystem [6] (denoted BP). The purpose of this article is twofold. We will illustrate this semiclassical Langevin approach and show how the current-induced effects could be investigated in molecular contacts connecting gated graphene or nanotube electrodes.

Graphene is now being explored very extensively due to its outstanding electrical and thermal transport properties [10-12]. Besides being highly important in their own right, carbon nanotube- or graphene-based nanostructures may offer an interesting test bed for studies of current-induced effects at the atomic scale. For such systems, experiments with atomic resolution, employing for instance state-of-the-art electron microscopes, can be performed in the presence of current, allowing the dynamics to be followed down to single adatoms [13]. Electric current has been used to induce changes in graphene-edges, which were monitored while a current was simultaneously passed through the structure [14]. This was explained as carbon edge-dimers desorbing due to Joule-heating [15]. Taking this a step further, one can imagine that nanostructured nanotubes or graphene can be used as an electrode interface to molecular devices based on organic chemistry [16]. Especially promising aspects include the inherent 2-D geometry of graphene, which enables both straightforward electrical gating, and atomic-scale imaging in the presence of current. There have been a number of microscopy studies of single-atom carbon chains bridging graphene [13,17] or nanotubes [18]. On the theoretical side, various aspects of these systems have been studied, such as the formation of chains [19,20], their stability [21], and electron-transport properties [22-24]. Here we explore the current-induced forces and nanoscale Joule heating of the carbon chain system between electrically gated graphene electrodes.

The paper is organized as follows. After a brief outline of the semiclassical Langevin method, we will use it to study the dynamics of the carbon chain as a function of bias and gate voltages. We point out that the gate, which offers independent control of bias voltage and current in the system, can be used to explore current-induced vibrational instabilities in the current-carrying chain. Finally, we illustrate how the Langevin molecular dynamics can be performed for a carbon-chain system with the Joule heating effect included, by using tight-binding and the Brenner potential.

Results and Discussion

Semiclassical Langevin dynamics

We outline the Langevin approach here. For a classical oscillator system (mass-scaled coordinate x) in a general nonlinear force-field, F, coupled linearly to a *bath* of harmonic oscillators, it is possible to eliminate the bath variables and describe the system using the generalized Langevin equation, [25-27],

$$\ddot{x} = F(x) - \int_{t_0}^{t} \Pi^r(t,t')x(t')\mathrm{d}t' + \xi(t). \qquad (1)$$

Here the bath influences the motion through two distinct force contributions, (i) a retarded time-kernel, Π^r, describing the back-action at time t after propagation in the bath due to the motion of x at an earlier time, and (ii) a force ξ of statistical nature originating from the thermal fluctuations of the bath. In the case of thermodynamic equilibrium, ξ is characterized by a temperature and is related to Π^r by the fluctuation-dissipation theorem. Note that in general x, F, and ξ are vectors and Π^r is a matrix. This method was used by Wang and co-workers [28,29] to describe thermal transport in the quantum limit, with phonons in the two connecting reservoirs with different temperature acting as baths and with their quantum fluctuations included in ξ. This reproduced the Landauer result of thermal transport in the harmonic case [28].

It is possible to reach a semiclassical Langevin equation description of the motion of the ions coupled to the electron gas if we assume a linear coupling to the electronic environment: Either in the displacement from an equilibrium or in the velocity (adiabatic expansion) of the ions. This Langevin/Brownian motion approach to atomic scattering at metal surfaces has a rather long history in the case of metal electrons in thermal equilibrium [30,31].

We have extended this to describe the dynamics of the ions in a nanoconductor between metal electrodes in the nonequilibrium case, where an electric current is present [6,32]. In order to sketch the derivation, we consider a displacement-dependent tight-binding model with electron states in the scattering region of interest *k,l*, and with H_{el} being the static electronic Hamiltonian (scattering region and its coupling to the left and right electrodes [33]),

$$H = H_{ph}(x) + H_{el} + \sum_{k,l,n} \mathbf{M}_{n,kl} c_k^\dagger c_l \, x_n . \qquad (2)$$

Here x is a column vector comprising the mass-normalized displacement operators for each degree of freedom, e.g., $x_n = \sqrt{m_n} u_n$, u_n and m_n being the displacement operator and mass, and $H_{ph} = 1/2\, \dot{x}^{\mathrm{T}} \dot{x} + 1/2 x^{\mathrm{T}} K x$ corresponds to a set of harmonic oscillators that couple with the electrons, K being the dynamical matrix. We construct a localized basis-set describing the electrons in the scattering region, where $c_k^\dagger (c_k)$ is the electron creation (annihilation) operator at site k in this region [34]. Here we only consider the coupling to the electron bath, but the linear coupling to an external phonon bath can be taken into account along the same lines and adds a contribution to Π^r. The derivation and result for a linearly coupled harmonic phonon bath is similar, and was given in [28]. Alternatively, the dynamics of some external phonons, not coupling to the electrons directly, may be treated explicitly in actual MD calculations, as we illustrate below (regions *DL, DR* in Figure 6a). The electron–phonon coupling corresponds to matrix elements of the force operator $\mathbf{M}_{n,kl} = \langle k \,|\, \nabla_{x_n} H_{el} \,|\, l \rangle$. We assumed that **M** is small by keeping only the term that is linear in x.

We may obtain an equation of motion for x using Heisenberg's equation of motion, $\ddot{x} = i[\dot{x}, H]$, based on atomic units ($\hbar$ = 1) and implicit mode index (n),

$$\ddot{x} = -Kx - \sum_{kl} \mathbf{M}_{kl} c_k^\dagger c_l \equiv -Kx + f_e . \qquad (3)$$

The term f_e describes the "forces" due to the interaction with the electron gas. Importantly, these forces are random in nature [35]. We can calculate the mean value of f_e by averaging it over the nonequilibrium electronic state,

$$\langle f_e \rangle = i\mathrm{Tr}[\mathbf{M}\mathbf{G}^<(t,t)] = \mathrm{Tr}[(-\nabla_x H_{el})\rho(t)]. \qquad (4)$$

Here we introduce the electrical lesser-Green's function, $\mathbf{G}_{ij}^<(t,t) \equiv i\langle c_i^\dagger(t) c_j(t) \rangle$, which is equivalent to the density matrix, ρ (multiplied by $-i$), and depends on $x(t)$, since the electrons are coupled to x in the Hamiltonian. This is similar to the expression for the average force in Ehrenfest dynamics [5].

We can evaluate this perturbatively by using the unperturbed-electron lesser Green's function, $\mathbf{G}_0^<$, corresponding to the case of steady-state electron transport without electron–phonon interaction [33],

$$\mathbf{G}_0^<(\omega) = i\mathbf{A}_L(\omega) n_F(\omega - \mu_L) + i\mathbf{A}_R(\omega) n_F(\omega - \mu_R), \qquad (5)$$

where $\mathbf{A}_{L/R}$ are the density of state matrices for electronic states originating in the left/right electrodes, each with chemical potential $\mu_{L/R}$ [33], which differ for finite bias voltage, V, as $\mu_L - \mu_R = eV$, and $n_F(\omega) = 1/(e^{\omega/k_B T} + 1)$ is the Fermi-Dirac distribution function. We thus treat the nonequilibrium electron system as a reservoir unperturbed by the phonons. Using the nonequilibrium Greens function (NEGF) technique [36], we may write the 2nd lowest orders in **M** of $\langle f_e \rangle$ as,

$$\langle f_e(t) \rangle \approx \int \mathrm{d}\omega \mathrm{Tr}[(-\nabla_x H_{el})\rho_0] - \int_{t_0}^{t} \Pi^r(t,t') x(t') \mathrm{d}t'. \qquad (6)$$

The first term yields a constant force due to the change in electron bonding with bias and a "direct force" due to interaction of charges with the field [37]. Here $\rho_0 = \rho_{\mathrm{eq}} + \delta\rho$ is the nonequilibrium electron-density matrix *without* electron–phonon interaction. We split it into an equilibrium contribution ρ_{eq} and a nonequilibrium correction δρ. In linear response, we obtain a term $\mathcal{E} \cdot x$ from the field in H_{el}, $\mathcal{E}$ being the external field, which yields a "direct" force involving the equilibrium ρ_{eq}. We also obtain a term involving $H_{el}(\mathcal{E} = 0)$, together with the change in density to first order in the field $\Delta\rho \propto \mathcal{E}$, in the first term of Equation 6, resulting from the change of density in the chemical bonds due to the current [38,39].

The second contribution is the retarded back-action of the electron gas due to the motion and is equivalent to the retarded phonon self-energy. In the steady state, Π^r only depends on the time difference, and it is convenient to work in the frequency (energy) domain. This can be expressed by using the coupling-weighted electron–hole-pair density of states, $\Lambda^{\alpha\beta}$, inside or between electrodes $\alpha,\beta \in L,R$,

$$\Pi^r(t-t') = \int \Pi^r(\omega) e^{-i\omega t} \frac{\mathrm{d}\omega}{2\pi}, \tag{7}$$

$$\Pi^r(\omega) = \int \frac{\Lambda(\omega')}{\omega' - \omega - i\delta} \mathrm{d}\omega', \tag{8}$$

where Λ can be expressed in terms of the electrode DOS,

$$\Lambda \equiv \sum_{\alpha\beta} \Lambda^{\alpha\beta}, \tag{9}$$

$$\begin{aligned}\Lambda^{\alpha\beta}_{mn}(\omega) = \frac{1}{\pi}\int_{-\infty}^{\infty} \frac{\mathrm{d}\omega'}{2\pi} \mathrm{Tr}[\mathbf{M}_m \mathbf{A}_\alpha(\omega') \mathbf{M}_n \mathbf{A}_\beta(\omega'-\omega)] \\ \times\Big(n_F(\omega'-\mu_\alpha) - n_F(\omega'-\omega-\mu_\beta)\Big).\end{aligned} \tag{10}$$

We have included a factor of 2 from the spin degeneracy and have explicitly included the mode index, *m,n* on the coupling matrices, **M**, and on Λ in Equation 10.

The forces described by $\Pi^r_{mn}(\omega)$ in Equation 6 contain a number of interesting current-induced effects. It is instructive to split the kernel into parts,

$$\begin{aligned}\Pi^r_{mn}(\omega) = i\pi\mathrm{Re}(\Lambda_{mn}(\omega)) - \pi\mathrm{Im}(\Lambda_{mn}(\omega)) \\ +\pi\mathcal{H}\{\mathrm{Re}(\Lambda_{mn})\}(\omega) + i\pi\mathcal{H}\{\mathrm{Im}(\Lambda_{mn})\}(\omega),\end{aligned} \tag{11}$$

where

$$\mathcal{H}\{f(x')\}(x) = \frac{1}{\pi}\mathcal{P}\int \frac{g(x')}{x'-x}\mathrm{d}x'$$

is the Hilbert transform. The Λ matrix has the following symmetry properties when exchanging modes($n \leftrightarrow m$) and electrodes($\alpha \leftrightarrow \beta$),

$$\Lambda^{\alpha\beta}_{mn}(\omega) = \Lambda^{\alpha\beta *}_{nm}(\omega), \tag{12}$$

and

$$\Lambda^{\alpha\beta}_{mn}(\omega) = -\Lambda^{\beta\alpha}_{nm}(-\omega), \tag{13}$$

which are helpful when examining the terms in Equation 11, which are summarized in the following:

- **Friction** – The first term in Equation 11 is imaginary and symmetric in mode index *m,n*. It describes the friction force due to the generation of electron–hole pairs in the electronic environment by the ionic motion. This process exists even in equilibrium [31]. For slowly varying $\mathbf{A}_{L/R}$ with energy as compared to the vibrational energies (wide-band limit) we obtain the simple time-local electron friction force, $-\eta_{el}\dot{x}$, with

$$\begin{aligned}\eta_{el} &= -\frac{\pi\mathrm{Re}(\Lambda)}{\omega}|_{\omega\to 0} \\ &\approx \frac{1}{2\pi}\sum_{\alpha,\beta}\mathrm{Tr}[\mathbf{M}\mathbf{A}_\alpha(\mu_\alpha)\mathbf{M}\mathbf{A}_\beta(\mu_\beta)]\end{aligned} \tag{14}$$

- **NC (wind) force** – The second term in Equation 11 is real and antisymmetric, which means that the general curl of this force is not zero. It describes the NC force, discussed very recently by Dundas and co-workers [5]. This force is finite, even in the limit of zero frequency, where the friction and Joule heating effect is not important anymore.
- **Renormalization** – The third term is real and symmetric and can be interpreted as a renormalization of the dynamical matrix. It contains an equilibrium part and a nonequilibrium correction. The equilibrium part is already included in the dynamical matrix when we calculate it within the Born–Oppenheimer approximation. The nonequilibrium part gives a bias-induced modification of the harmonic potential.
- **BP force** – Finally, the last term is imaginary, antisymmetric, and proportional to ω for small frequencies. It can be identified as the "Berry phase" (BP) force in [6]. Since the direction of this force is always normal to the velocity in the abstract phase space, it does no work, resembling a Lorentz force with effective magnetic field

$$\mathcal{B} = -\pi\frac{\mathcal{H}\{\mathrm{Im}(\Lambda(\omega'))\}(\omega)}{\omega}|_{\omega\to 0}. \tag{15}$$

- **Random forces** – The randomness of the force f_e is characterized by its correlation function in the frequency domain, which can again be calculated with NEGF. However, we note that since f_e is a quantum operator, $\langle f_e(t) f_e(0)\rangle$ does not result in a real number. Instead we use the symmetrized and real $\langle f_e(t) f_e^T(0) + (f_e(0) f_e^T(t))^T\rangle$. This expression equals the semiclassical result obtained from the path-integral derivation of the Langevin equation [6,35] and reads, in Fourier space,

$$\begin{aligned}\langle \xi_e \xi_e^T\rangle(\omega) &\equiv \langle f_e f_e^T\rangle(\omega) - \langle f_e\rangle\langle f_e\rangle^T(\omega) \\ &= -\pi\sum_{\alpha\beta}\coth\left(\frac{\omega-(\mu_\alpha-\mu_\beta)}{2k_BT}\right)\Lambda^{\alpha\beta}(\omega).\end{aligned} \tag{16}$$

- This spectral power density can be used to generate an instance of the Gaussian random noise as a function of time that is needed in MD simulations. Most importantly this random force contains not only the thermal excitations but also the excess excitations leading to Joule heating [32], through the dependence of the chemical potentials $\mu_L - \mu_R = eV$. Thus with this formalism it is possible to disentangle the various contributions to the forces, being either deterministic or random in nature.

Current-induced vibrational instability

We now turn to illustrations of the use of the semiclassical Langevin equation to describe current-induced effects. In this section we employ it to study the effect of the current-induced forces and Joule heating on the stability of the system, within the harmonic approximation. We will here ignore the coupling to electrode phonons. This makes an eigen-mode analysis possible, which eases the interpretation of the results. The model system we use is shown in Figure 1, in which a four-atom carbon chain is bridged between two graphene electrodes (L and R). We assume a field effect transistor setup, in which a gate potential, V_g, is applied to the system in addition to the bias applied between the two electrodes, V_b. We will show that this offers a convenient way to explore current-induced vibrational instabilities. We can already see the effect of the gate potential in the current–voltage ($I - V_b$) characteristics shown in Figure 2.

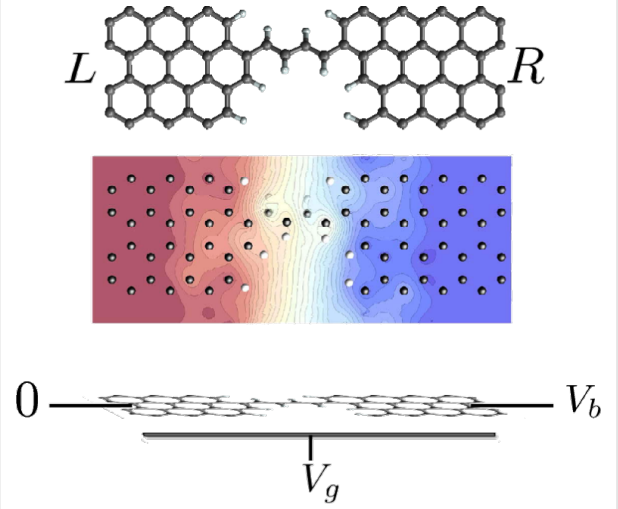

Figure 1: The system considered in the present study is a four-atom carbon chain bridging two graphene electrodes. The dangling bonds are passivated by hydrogen atoms. In addition to the bias applied between the left (L) and right (R) electrodes (V_b), a gate potential (V_g) can also be applied perpendicular to the graphene surface. The center panel shows the calculated contour plot of the electrostatic-potential drop across the junction at V_g = 0 V, and V_b = 1 V. The equal drop at the left and right electrodes reflects the electron–hole symmetry for V_g = 0 V [40].

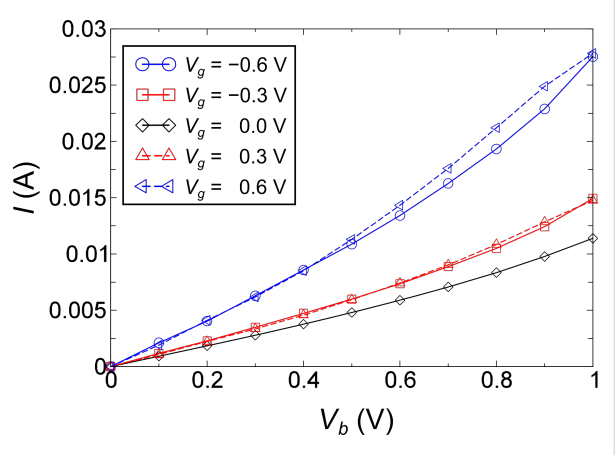

Figure 2: Current–Voltage (I–V_b) curves at different V_g.

The effect of the NC and BP forces is to couple different phonon modes with nearly similar frequencies. From now on, we will focus on the two phonon modes around 200 meV, shown in Figure 3, since the alternating-bond-length-type modes (200 meV) couple most strongly with the electric current. This type of mode also gives rise to the most intensive Raman signals in unpassivated chains between graphene-like pieces [41].

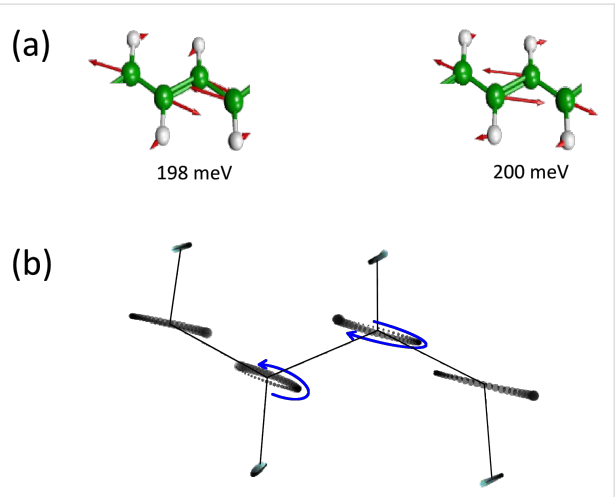

Figure 3: (a) Motion of the two phonon modes around 200 meV. (b) Motion of the runaway mode at V_g = 0.6 V, and V_b = 1 V. We depict the motion using a number of discrete time steps roughly corresponding to a full period. The position of each atom is depicted as a circle for a sequence of time steps indicated by an increasing radius with time. The motion is a phase-shifted linear combination of the two modes in (a). We can see the elliptical motion of the carbon atoms from the plot. The enclosed area indicates that work can be done by the current-induced NC force.

The calculation was performed by using the SIESTA density-functional theory (DFT) method [42], which has been extended to study elastic [33] and inelastic [34] transport in molecular

conductors. We used similar parameters as detailed in [34], and in order to keep the calculation simple and tractable, we modeled the electrodes by simply employing the Γ k-point in the transverse electrode direction. The electron–phonon coupling matrix (**M**) was calculated at zero bias, whereas we calculated the electronic structure at finite bias. We note that the voltage dependence of the coupling matrix could play a role, but this is beyond the scope of the present more illustrative purpose [43]. Based on these approximations, we can calculate the full ω-dependent Λ function, and the self-energies, Π^r. To perform the eigen-mode analysis, we further assumed linear ω-dependent friction, Berry force (BP), constant nonconservative force (NC), and ignore the renormalization of the dynamical matrix.

We model the effect of V_b as a shift of the equilibrium chemical potential, E_F. In this way we can tune the electronic structure within the bias window by changing the gate potential. In the following, we look at the bias and gate dependence of the inverse Q-factor ($1/Q$) and effective phonon number N. The inverse Q-factor for mode i (note we use index i for full modes including the current-induced forces) is defined as

$$1/Q_i \equiv -2\frac{\mathrm{Im}\{\omega_i\}}{\mathrm{Re}\{\omega_i\}}, \tag{17}$$

where ω_i are the eigenvalues of the full dynamical matrix, including the current-induced forces. These modes thus consist of linear combinations of the "unperturbed" normal modes of the system, n,m, as calculated by using the standard Born–Oppenheimer approximation. The phonon number can be calculated from the displacement correlation function,

$$N_i + \frac{1}{2} \approx \mathrm{Re}\{\omega_i\}\int \langle x_i x_i\rangle(\omega)\frac{\mathrm{d}\omega}{2\pi}. \tag{18}$$

We show the bias and gate potential dependence of the inverse Q-factor and phonon number in Figure 4 and Figure 5. The coupling of these two modes due to the bias (gate) dependent NC and BP force changes their lifetime. The two modes always have opposite dependence. The vibrational instability occurs at the critical point where $1/Q = 0$ around $V_g = \pm 0.4$ V. This corresponds to an infinite phonon number in Figure 5, and we there-

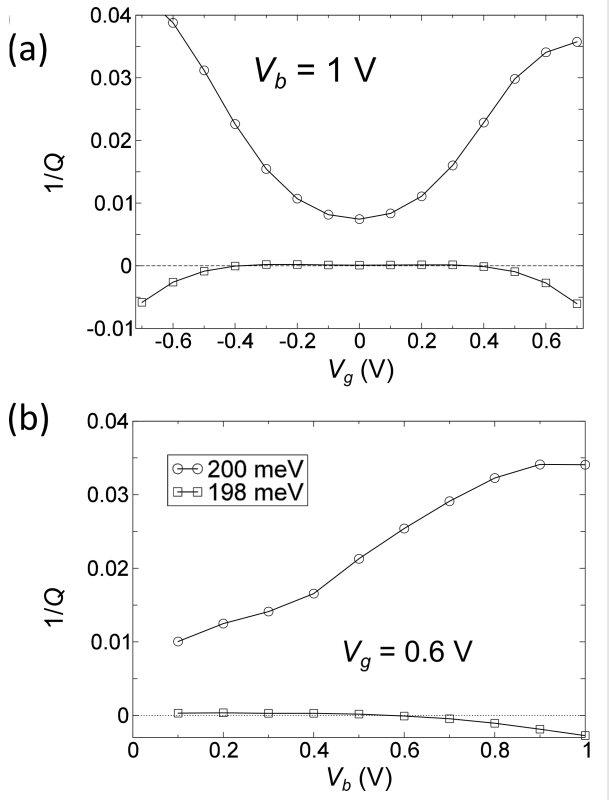

Figure 4: (a) Inverse Q-factor ($1/Q$) as a function of gate voltage, V_g, at V_b = 1 V for the two modes around 200 meV. (b) $1/Q$ as a function of bias voltage, V_b, at fixed gate voltage V_g = 0.6 V, for the same pair of phonon modes.

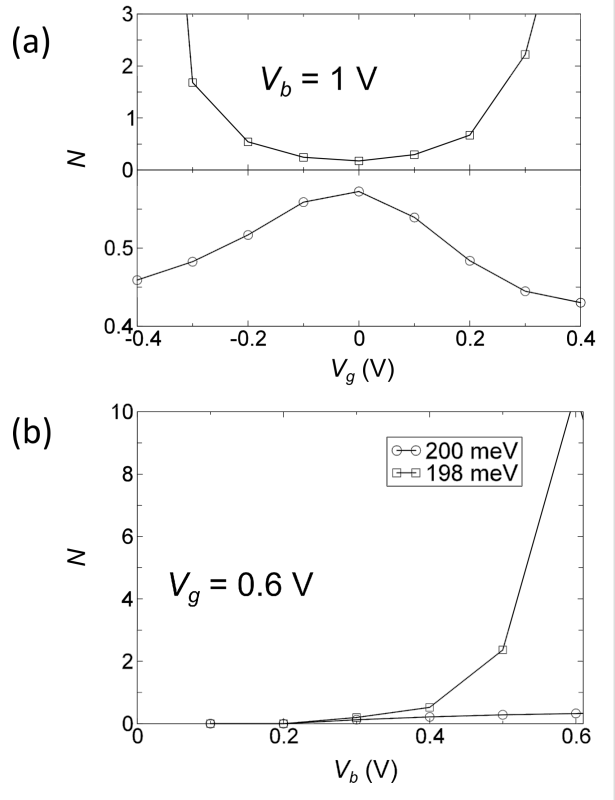

Figure 5: (a) Effective phonon number (N) for the two phonon modes around 200 meV as a function of gate voltage, V_g, at fixed bias voltage, V_b = 1 V. (b) N as a function of bias voltage, V_b, at fixed gate voltage V_g = 0.6 V. Note that it diverges at the critical point when the damping ($1/Q$) in Figure 4 goes to zero.

fore call it a "runaway" mode. The motion of this mode at $V_b = 1$ V, $V_g = 0.6$ V is plotted in Figure 3b. We can observe the elliptical motion of several atoms in real-space. This is critical because in order for the nonconservative force to do work on the atoms their motion has to enclose a finite area, either in real or in abstract phase space.

Finally, we should mention that when the current hits the instability threshold it will drive the system into a highly anharmonic regime, where the preceding eigenanalysis breaks down. One scenario is that the motion of the system will reach a limit-cycle determined by the detailed anharmonic potential and the interaction with the current [7]. In this regime the details of the damping due to the coupling with phonons in the electrodes could be important, and the electron–phonon coupling could also change from the value given around the harmonic equilibrium position. In order to address this regime we can perform molecular-dynamics simulations, taking into account both the coupling between different modes and their coupling with the electrode phonons, in order to study how the system actually reacts due to the instability.

Molecular dynamics with Joule heating

Next we illustrate the use of the Langevin equation to perform molecular-dynamics simulations of a carbon-chain system, in the presence of current flow, in the simplest possible setting, but now including coupling to the electrode phonons. Therefore we abandon the DFT approach, and instead employ the widely used π-tight-binding model with hopping parameter β = 2.7 eV, and the Brenner potential for calculations of the interatomic forces [44]. We consider the unpassivated structure in Figure 6. The electron–phonon coupling is modeled by the Harrison scaling law [45], $\beta = 2.7\text{eV}\ (a_0/d)^2$, determining how β is modified when the nearest neighbor distance, d, is changed from the equilibrium value, $a_0 = 1.4$ Å. The same model has recently been applied in the study of the effect of strain on the electronic structure of graphene [46]. In the simulation we model the coupling to the electrode phonons by a friction parameter, η_{ph}, and a corresponding white equilibrium phonon noise $\langle \xi_{ph} \xi_{ph}^T \rangle = 2\eta_{ph} k_B T$ on the L,R-electrode regions. This is similar to the stochastic boundary conditions [27] in which L,R-atoms act as a boundary. The setup for the MD is shown in (Figure 6a). We include electrode regions that have no interaction with the current (DL,DR), and a device region (D) where the current density is highest and where the nonconservative forces and Joule heating are included.

Furthermore, instead of using the full nonlocal time-kernel for the electrons in Equation 14, we use the wide-band approximation, and neglect the off-diagonal elements of the electron-noise spectral power density, $\langle \xi_e \xi_e^T \rangle(\omega)$. The diagonal of the electron spectral power can be approximated by white noise in the high-bias and wide-band limits, where variations in the electronic DOS are neglected [47]. The assumption of a white-noise spectrum implies neglect of the equilibrium zero-point motion of the atoms, but most importantly here, it includes the Joule heating effects,

$$\langle (\xi_e)_n (\xi_e)_n^T \rangle(\omega) = 2(\eta_{el})_{nn} k_B T + \mathrm{Re}\Big(\mathrm{Tr}\big[\mathbf{A}_L(\mu_L)\mathbf{M}_n \mathbf{A}_R(\mu_R)\mathbf{M}_n\big]\Big)\frac{|eV_b|}{2\pi}. \quad (19)$$

A factor of 2 should be included in the case of spin degeneracy. Based on the velocity Verlet algorithm [48] we carried out MD simulations at a varying bias voltage for zero gate bias ($V_g = 0$ V), and phonon friction, η_{ph}. The MD results are summarized in Figure 6b–f. We note that for the present system setup the nonconservative force is found not to play a dominant role compared to the effect of Joule heating. The main insight we gain from the MD example here is that the anharmonic couplings are important and effective in redistributing the energy supplied by the nonequilibrium electrons.

The approximate local phonon friction, η_{ph}, can in general be expressed from the slope of the corresponding phonon self-energy at zero frequency, as for electrons, see Equation 14. However, here we simply varied its value around this in order to quantify the dependence of the local electrical heating in the device region on this parameter (Figure 6b). The electrical heating of the chain was found not to depend much on the phonon friction when this was chosen to be sufficiently high. This is an appealing result, since it indicates that the electrical heating does not depend critically on the measurement setup, but mainly on the nature of the actual constriction. This seems to be true as long as the heat flow away from the contacts is sufficient to maintain the temperature of the heat baths, and the chain acts as a bottleneck for the heat conduction. However, we note that for heat conduction in the quantum limit it is important to go beyond the white band approximation and include realistic self-energies for the L,R-electrode phonons [49]. This will be explored in future work.

Inspired by the equipartition theorem, we define a local temperature variable for the atoms (indexed by a) with mass, m_a,

$$T_a(t) \equiv \frac{m_a}{3k_B}\langle \vec{v}_a^{\,2}(t) \rangle. \quad (20)$$

A comparison of the obtained temperature distributions with (Figure 6c, Figure 6d) and without (Figure 6e, Figure 6f) the anharmonic interactions shows that anharmonic couplings

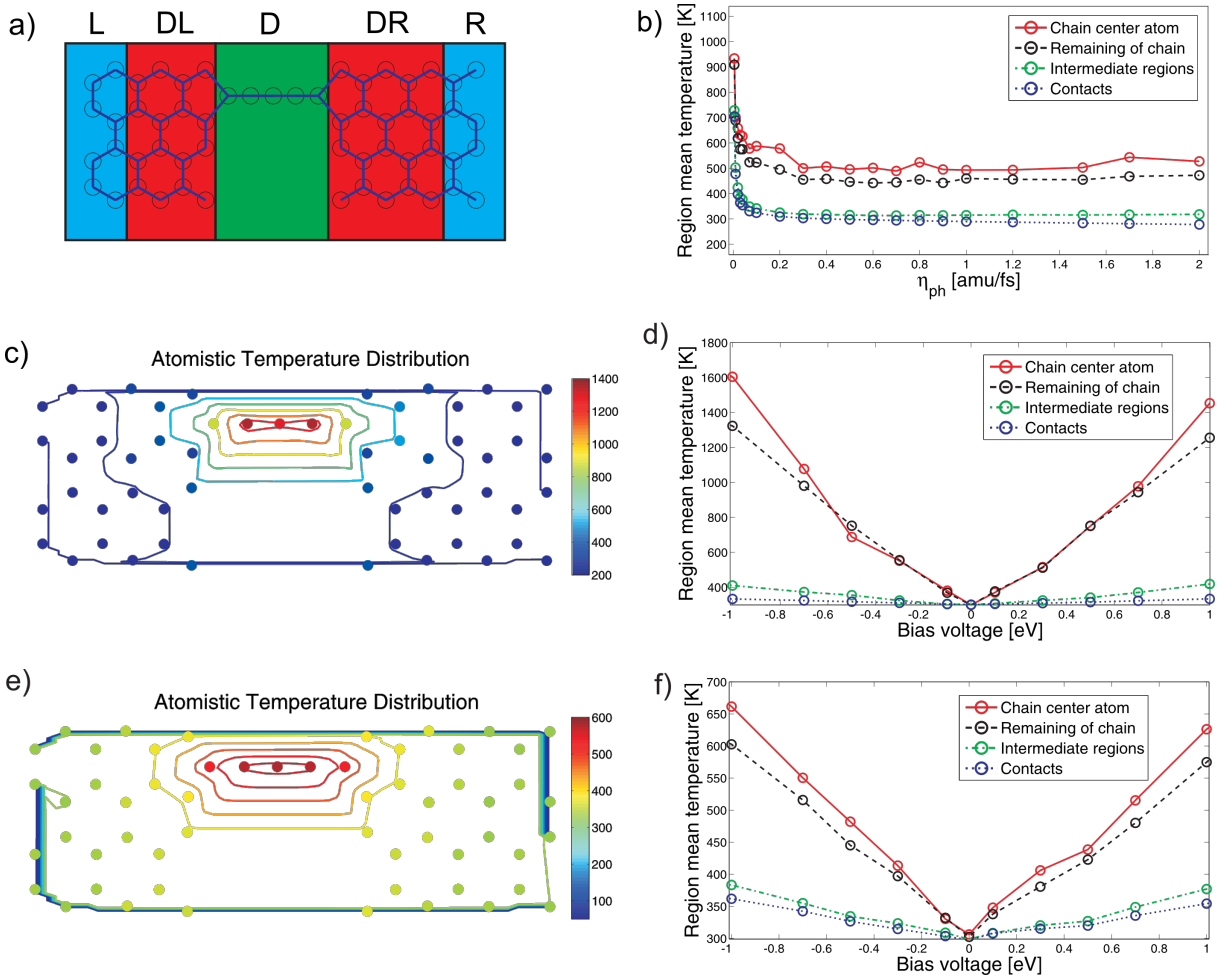

Figure 6: (a) Definition of the system regions with different types of noise contributions. Leads (*L*,*R*) have a well-defined temperature determined by the phonon noise, the device (*D*) temperature is defined from the electrical heating, and the intermediate regions (*DL*,*DR*) are free and are heated by propagation noise. In the MD setup no atoms are held fixed, but periodic boundary conditions are applied. The figure describes the setup in which the local temperatures plotted in (c) and (e) should be understood. (b) Temperature of the regions as a function of phonon friction. (c, d) Obtained temperatures at different atoms within the harmonic approximation. (c) The simulations were run at T = 300 K and at eV_b = 1 eV, and (d) varying bias voltages. (e, f) Corresponding atomistic temperature distributions including the anharmonic interactions. The lead temperature can exceed the equilibrium bath temperature due to propagation noise. In particular, the anharmonic interactions redistribute part of the energy from the modes in the chain to the bulk modes in the lead.

between the vibrational modes have a significant influence on the heat-transport properties and local Joule heating of the system. The heating is less localized in the chain due to anharmonicity. This originates from the coupling between different modes and an increased coupling to the surroundings for configurations in which the atoms are displaced from their equilibrium positions. Modes localized in the chain can be heated up to very high temperatures in the harmonic approximation. When anharmonic interactions are included the energy is redistributed and the modes are collectively heated up.

The electron–phonon interaction is typically included through a Taylor expansion of the electronic Hamiltonian around the equilibrium positions (Equation 2). Within the time-local white-noise approximation it is possible to address the effect of changes of electronic Hamiltonian and, especially, electron-phonon coupling on the motion, which was both included in the nonequilibrium force calculations here. This amounts to updating the nonconservative force, friction and noise on the fly along the path. This is possible for the simple parametrization used here. Our preliminary results based on this approximation show that the extra noise contribution from the higher-order couplings may significantly influence the results and increase the electronic heating compared to the static electronic structure approximation. A method which goes beyond white noise and includes the change in electron–phonon coupling when the system is far from the equilibrium positions, e.g., close to bond breaking, remains a challenge for the future.

Conclusion

We have developed a semiclassical Langevin equation approach, which can be used to explore current-induced atomic dynamics and instabilities in molecular conductors. The Langevin approach can be solved in the harmonic approximation to obtain eigenmodes and their excitation in the presence of current, as well as used for molecular-dynamics simulations based on the full anharmonic potential. Our simple, approximate MD simulation indicates that anharmonic couplings play an important role for the energy redistribution and effective heat dissipation to the electrode reservoirs. However, the MD is computationally very demanding beyond simplified model electronic structures and interatomic potentials, and further developments are necessary. We have used carbon-chain systems both to illustrate the Langevin approach, and in order to highlight how graphene might offer a unique test bed for research into current-induced dynamic effects. Especially, it is straightforward to employ a gate potential to the gate electrode, and thereby obtain independent control of current and bias voltage in the system. Furthermore, atomic-scale resolution can be obtained in electron microscopes in the presence of current, and Raman spectroscopy can give insights into the excitation and effective temperature originating from the electric current [50-52]. Our results for the simplified carbon-chain systems indicate that it may be possible to tune the current-induced instabilities in the atomic dynamics with gate and bias voltages in the experimentally relevant range.

Acknowledgements

We acknowledge the Lundbeck Foundation for financial support (R49-A5454), and the Danish Center for Scientific Computing (DCSC) for providing computer resources.

References

1. Tao, N. J. *Nat. Nanotechnol.* **2006,** *1,* 173–181. doi:10.1038/nnano.2006.130
2. Moth-Poulsen, K.; Bjørnholm, T. *Nat. Nanotechnol.* **2009,** *4,* 551–556. doi:10.1038/nnano.2009.176
3. Song, H.; Kim, Y.; Jang, Y. H.; Jeong, H.; Reed, M. A.; Lee, T. *Nature* **2009,** *462,* 1039–1043. doi:10.1038/nature08639
4. Seideman, T., Ed. *Curren-driven phenomena in nanoelectronics;* Pan Stanford Publishing: Singapore, 2011.
5. Dundas, D.; McEniry, E. J.; Todorov, T. N. *Nat. Nanotechnol.* **2009,** *4,* 99–102. doi:10.1038/nnano.2008.411
6. Lü, J. T.; Brandbyge, M.; Hedegård, P. *Nano Lett.* **2010,** *10,* 1657–1663. doi:10.1021/nl904233u
7. Bode, N.; Kusminskiy, S. V.; Egger, R.; von Oppen, F. *Phys. Rev. Lett.* **2011,** *107,* 036804. doi:10.1103/PhysRevLett.107.036804
8. Lü, J. T.; Hedegård, P.; Brandbyge, M. *Phys. Rev. Lett.* **2011,** *107,* 046801. doi:10.1103/PhysRevLett.107.046801
9. Kubatkin, S.; Danilov, A.; Hjort, M.; Cornil, J.; Brédas, J.; Stuhr-Hansen, N.; Hedegård, P.; Bjørnholm, T. *Nature* **2003,** *425,* 698–701. doi:10.1038/nature02010
10. Geim, A. K.; Novoselov, K. S. *Nat. Mater.* **2007,** *6,* 183–191. doi:10.1038/nmat1849
11. Castro Neto, A. H.; Guinea, F.; Peres, N. M. R.; Novoselov, K. S.; Geim, A. K. *Rev. Mod. Phys.* **2009,** *81,* 109–162. doi:10.1103/RevModPhys.81.109
12. Geim, A. K. *Science* **2009,** *324,* 1530–1534.
13. Meyer, J. C.; Girit, C. O.; Crommie, M. F.; Zettl, A. *Nature* **2008,** *454,* 319–322. doi:10.1038/nature07094
14. Jia, X.; Hofmann, M.; Meunier, V.; Sumpter, B. G.; Campos-Delgado, J.; Romo-Herrera, J. M.; Son, H.; Hsieh, Y.-P.; Reina, A.; Kong, J.; Terrones, M.; Dresselhaus, M. S. *Science* **2009,** *323,* 1701–1705. doi:10.1126/science.1166862
15. Engelund, M.; Fürst, J. A.; Jauho, A. P.; Brandbyge, M. *Phys. Rev. Lett.* **2010,** *104,* 036807. doi:10.1103/PhysRevLett.104.036807
16. Guo, X.; Gorodetsky, A. A.; Hone, J.; Barton, J. K.; Nuckolls, C. *Nat. Nanotechnol.* **2008,** *3,* 163–167. doi:10.1038/nnano.2008.4
17. Jin, C.; Lan, H.; Peng, L.; Suenaga, K.; Iijima, S. *Phys. Rev. Lett.* **2009,** *102,* 205501. doi:10.1103/PhysRevLett.102.205501
18. Börrnert, F.; Börrnert, C.; Gorantla, S.; Liu, X.; Bachmatiuk, A.; Joswig, J.-O.; Wagner, F. R.; Schäffel, F.; Warner, J. H.; Schönfelder, R.; Rellinghaus, B.; Gemming, T.; Thomas, J.; Knupfer, M.; Büchner, B.; Rümmeli, M. H. *Phys. Rev. B* **2010,** *81,* 085439. doi:10.1103/PhysRevB.81.085439
19. Hobi, E., Jr..; Pontes, R. B.; Fazzio, A.; da Silva, A. J. R. *Phys. Rev. B* **2010,** *81,* 201406. doi:10.1103/PhysRevB.81.201406
20. Erdogan, E.; Popov, I.; Rocha, C. G.; Cuniberti, G.; Roche, S.; Seifert, G. *Phys. Rev. B* **2011,** *83,* 041401. doi:10.1103/PhysRevB.83.041401
21. Lin, Z. Z.; Yu, W. F.; Wang, Y.; Ning, X. J. *EPL* **2011,** *94,* 40002. doi:10.1209/0295-5075/94/40002
22. Chen, W.; Andreev, A. V.; Bertsch, G. F. *Phys. Rev. B* **2009,** *80,* 085410. doi:10.1103/PhysRevB.80.085410
23. Fürst, J. A.; Brandbyge, M.; Jauho, A.-P. *EPL* **2010,** *91,* 37002. doi:10.1209/0295-5075/91/37002
24. Akdim, B.; Pachter, R. *ACS NANO* **2011,** *5,* 1769–1774. doi:10.1021/nn102403j
25. Adelman, S.; Doll, J. *J. Chem. Phys.* **1976,** *64,* 2375–2388. doi:10.1063/1.432526
26. Kantorovich, L. *Phys. Rev. B* **2008,** *78,* 094304. doi:10.1103/PhysRevB.78.094304
27. Kantorovich, L.; Rompotis, N. *Phys. Rev. B* **2008,** *78,* 094305. doi:10.1103/PhysRevB.78.094305
28. Wang, J.-S. *Phys. Rev. Lett.* **2007,** *99,* 160601. doi:10.1103/PhysRevLett.99.160601
29. Lü, J. T.; Wang, J.-S. *Phys. Rev. B* **2008,** *78,* 235436. doi:10.1103/PhysRevB.78.235436
30. Nourtier, A. *J. Phys. (Paris)* **1977,** *38,* 479–502. doi:10.1051/jphys:01977003805047900
31. Head-Gordon, M.; Tully, J. C. *J. Chem. Phys.* **1995,** *103,* 10137. doi:10.1063/1.469915
32. Brandbyge, M.; Hedegård, P. *Phys. Rev. Lett.* **1994,** *72,* 2919–2922. doi:10.1103/PhysRevLett.72.2919
33. Brandbyge, M.; Mozos, J. L.; Ordejón, P.; Taylor, J.; Stokbro, K. *Phys. Rev. B* **2002,** *65,* 165401. doi:10.1103/PhysRevB.65.165401
34. Frederiksen, T.; Paulsson, M.; Brandbyge, M.; Jauho, A.-P. *Phys. Rev. B* **2007,** *75,* 205413. doi:10.1103/PhysRevB.75.205413
35. Schmid, A. *J. Low Temp. Phys.* **1982,** *49,* 609–626. doi:10.1007/BF00681904

36. Haug, H.; Jauho, A.-P. *Quantum Kinetics in Transport and Optics of Semiconductors,* 2nd ed.; Springer Series in Solid State Sciences, Vol. 123; Springer: Berlin, Heidelberg, 2008.
37. Bevan, K. H.; Guo, H.; Williams, E. D.; Zhang, Z. *Phys. Rev. B* **2010,** *81,* 235416. doi:10.1103/PhysRevB.81.235416
38. Brandbyge, M.; Stokbro, K.; Taylor, J.; Mozos, J. L.; Ordejón, P. *Phys. Rev. B* **2003,** *67,* 193104. doi:10.1103/PhysRevB.67.193104
39. Brandbyge, M. *Nat. Nanotechnol.* **2009,** *4,* 81–82. doi:10.1038/nnano.2008.413
40. Brandbyge, M.; Kobayashi, N.; Tsukada, M. *Phys. Rev. B* **1999,** *60,* 17064–17070. doi:10.1103/PhysRevB.60.17064
41. Rivelino, R.; dos Santos, R. B.; de Brito Mota, F.; Gueorguiev, G. K. *J. Phys. Chem. C* **2010,** *114,* 16367–16372. doi:10.1021/jp1066154
42. Soler, J. M.; Artacho, E.; Gale, J. D.; Garcia, A.; Junquera, J.; Ordejón, P.; Sánchez-Portal, D. *J. Phys.: Condens. Matter* **2002,** *14,* 2745–2779. doi:10.1088/0953-8984/14/11/302
43. Sergueev, N.; Roubtsov, D.; Guo, H. *Phys. Rev. Lett.* **2005,** *95,* 146803. doi:10.1103/PhysRevLett.95.146803
44. Brenner, D. W. *Phys. Rev. B* **1990,** *42,* 9458–9471. doi:10.1103/PhysRevB.42.9458
45. Harrison, W. A. *Electronic Structure, the Properties of Solids: The Physics of the Chemical Bond;* Dover Publications: New York, 1989.
46. Guinea, F.; Katsnelson, M. I.; Geim, A. K. *Nat. Phys.* **2010,** *6,* 30–33. doi:10.1038/nphys1420
47. Gunst, T. Molecular Dynamics of nano-conductors in the presence of electronic current. M.Sc. Thesis, Technical University of Denmark, DTU Nanotech, Denmark, 2010.
48. Allen, M. P. Introduction to Molecular Dynamics Simulation. In *Computational Soft Matter: From Synthetic Polymers to Proteins;* Attig, N.; Binder, K.; Grubmüller, H.; Kremer, K., Eds.; NIC Series, Vol. 23; Gustav-Stresemann-Institut: Bonn, Germany, 2004; pp 1–28.
49. Wang, J.-S.; Ni, X.; Jiang, J.-W. *Phys. Rev. B* **2009,** *80,* 224302. doi:10.1103/PhysRevB.80.224302
50. Ioffe, Z.; Shamai, T.; Ophir, A.; Noy, G.; Yutsis, I.; Kfir, K.; Cheshnovsky, O.; Selzer, Y. *Nat. Nanotechnol.* **2008,** *3,* 727–732. doi:10.1038/nnano.2008.304
51. Ward, D. R.; Halas, N. J.; Ciszek, J. W.; Tour, J. M.; Wu, Y.; Nordlander, P.; Natelson, D. *Nano Lett.* **2008,** *8,* 919–924. doi:10.1021/nl073346h
52. Chae, D.-H.; Krauss, B.; von Klitzing, K.; Smev, J. H. *Nano Lett.* **2010,** *10,* 466–471. doi:10.1021/nl903167f

License and Terms

Paper III

Tue Gunst, Jing-Tao Lü, Troels Markussen, Antti-Pekka Jauho and Mads Brandbyge

Thermoelectric properties of disordered graphene antidot devices

IEEE Xplore Conf. Proc. 10.1109/IWCE.2012.6242835 (2012)

Thermoelectric properties of disordered graphene antidot devices

Tue Gunst*§, Jing-Tao Lü*§, Troels Markussen†§, Antti-Pekka Jauho*‡§ and Mads Brandbyge*‡§
‡Center for Nanostructured Graphene (CNG)
§Technical University of Denmark DK-2800 Kgs. Lyngby, Denmark
*Department of Micro- and Nanotechnology (DTU Nanotech), Email: Tue.Gunst@nanotech.dtu.dk
†Center for Atomic-scale Materials Design (CAMD), Department of Physics

***Abstract*—We calculate the electronic and thermal transport properties of devices based on finite graphene antidot lattices (GALs) connected to perfect graphene leads. We use an atomistic approach based on the π-tight-binding model, the Brenner potential, and employing recursive Green's functions. We consider the effect of random disorder on the electronic and thermal transport properties, and examine the potential gain of thermoelectric merit by tailoring of the disorder. We propose several routes to optimize the transport properties of the GAL systems. Finally, we illustrate how quantum thermal transport can be addressed by molecular dynamics simulations, and compare to the Green's function results for the GAL systems in the ballistic limit.**

I. Introduction

Thermal management in nanoelectronics is a topic of great importance[1], and it is relevant to consider materials for thermo-electric cooling at the nanoscale. Although graphene is an excellent heat conductor, its thermoelectric properties seem to be highly tunable in nanostructured graphene, such as graphene antidot lattices (GALs)[2]. GALs have been proposed as a flexible platform for creating a semiconducting material[3], [4], [5], [6] and the regular nanoperforation of a graphene layer may be a solution for making graphene a versatile material for electronics as well as thermal management.

Several groups have developed fabrication techniques for creating this nanostructured system, e.g. by electron beam lithography[7], [8] or block copolymer lithography[9], [10]. The latter method results in a highly regular hexagonal lattice of holes. In another experiment hexagonal holes were obtained with very pure edge chirality by anisotropic etching[11]. Various types of disorder play an important role for transport properties. Edge disorder in nanoribbons has previously been theoretically predicted to increase the thermoelectric efficiency[12] and widen the band gap distribution of GALs with periodic disorder[13]. Recent experiments have managed to control the concentration of the ^{13}C isotope in both amount and space[14] and it has also been possible to measure the thermal conductivity by Raman spectroscopy[15]. Several theoretical predictions have been made on the isotope effect in graphene[16], [17], nanoribbons[18], [19], [20] and carbon nanotubes[21].

Here we use atomistic modelling to address how structural and isotope disorder can reduce the thermal conductance of GAL devices.

II. The role of disorder in GALs

The electronic and phonon transport properties are calculated from the energy-dependent transmission functions, $\mathcal{T}_e$ and $\mathcal{T}_{ph}$, using a Landauer-type formula. The Landauer formula for the electrons reads

$$I_e = \frac{2e}{\hbar}\int \frac{dE}{2\pi}\mathcal{T}_e(E)[n_F(E,\mu_L) - n_F(E,\mu_R)]\,, \qquad (1)$$

where $n_F(E,\mu_{L/R})$ is the Fermi-Dirac distribution at the chemical potential of the left/right lead. Within the linear-response limit we can consider variations with changes in the chemical potential, μ, e.g. by doping or gating of the graphene system, by evaluated the following moments of the electronic transmission,

$$L_n(\mu) = \frac{2}{\hbar}\int \frac{dE}{2\pi}(E-\mu)^n\mathcal{T}_e(E)\left(-\frac{\partial n_F}{\partial E}\right). \qquad (2)$$

They relate the electronic current and the electron heat current, in the linear response regime. Thus, we have[22] the electrical conductance $G_e(\mu) = \frac{\partial I}{\partial V} = e^2 L_0$, the electron thermal conductance $\kappa_e(\mu) = \left[L_2 - \frac{L_1^2}{L_0}\right]/T$, and the Seebeck coefficient $S(\mu) = \frac{\Delta V}{\Delta T}|_{I_e=0} = \frac{L_1}{eL_0T}$. For phonons the Landauer formula takes an analogous form and within linear response the thermal conductance is given by

$$\kappa_{ph} = \int_0^\infty d\omega \frac{(\hbar\omega)^2}{2\pi k_B T^2}\mathcal{T}_{ph}(\omega)\frac{e^{\frac{\hbar\omega}{k_BT}}}{(e^{\frac{\hbar\omega}{k_BT}}-1)^2}\,. \qquad (3)$$

From these we can evaluate the thermoelectric figure of merit,

$$ZT = \frac{S^2 G_e T}{\kappa_{ph}+\kappa_e}\,. \qquad (4)$$

We consider only disorder in the transport direction in GAL structures with periodicity in the direction perpendicular to transport, see Fig. 1, and employ averaging of the transmission functions over a dense $k_\perp$-point sampling. Using the Brenner potential[23] we perform structural relaxation, obtain the dynamical matrix, and then calculate the electronic Hamiltonian using the π-tight-binding model for the device region of a given length between pristine graphene leads. Based on this we calculate the k-averaged $\mathcal{T}_e$ and $\mathcal{T}_{ph}$ by an atomistic Green's function method, which is efficient for long systems with different kinds of disorder[24], [25]. Note that we assume the

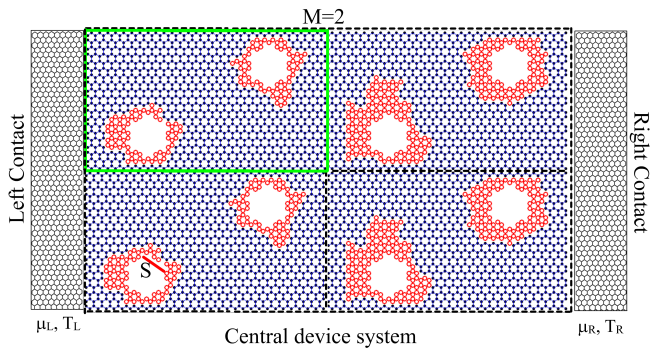

Fig. 1. System setup and the computational rectangular unit cell (green rectangle). Two graphene leads are connected by the finite GAL of length 2 ($M = 2$) corresponding to 4 holes in the direction of transport. The depicted system is based on a $\{L = 10, S = 3\text{arm}\}$ GAL, where we use the nomenclature from [2]. The red atoms are randomly removed during the generation of edge noise. The unit cell is 10 four-atom armchair units wide. We apply periodic boundary conditions in the transverse direction.

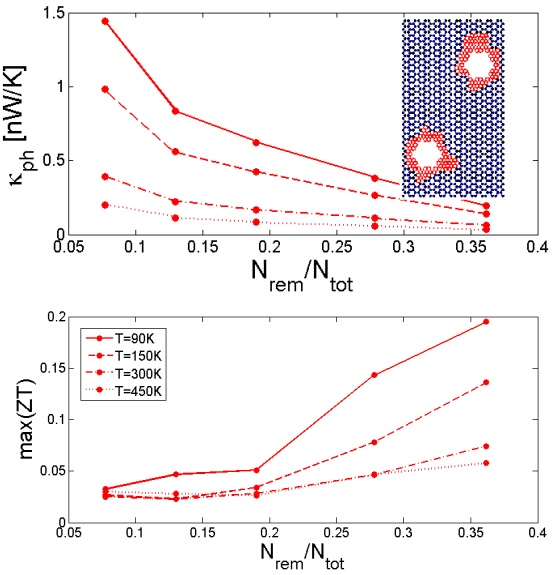

Fig. 2. Edge disorder in a GAL system with 5 unit cells along the device, corresponding to a length of 380Å. The system is based on a {10,2.3arm} GAL (with a width of 43Å) and we increase the number of atoms removed at random positions at the edge (the red atoms in the insert, showing one unit cell at $N_{rem}/N_{tot} = 0.19$). The ratio of removed atoms to unit cell size is changed through the interval previously considered for perfect antidots[2]. The resulting edges are highly disordered and can be taken as a worst case scenario (e.g. by vapor deposition of carbon atoms on a surface).

device to be free-standing, and neglect all effects of electron-phonon interaction such as phonon-drag. Later, we comment on how anharmonic effects may be included using molecular dynamics. In the remaining of this section we apply this method to three types of disorder; edge disorder, position disorder, and the isotope effects.

A. *Lattice disorder*

In Fig. 2, we show the outcome of transport simulations for various GALs with random edge disorder. The system is constructed from a sequence of GAL unit cells (with two holes) in which a chosen number of atoms are randomly removed at the edge one by one. We start from a very small {10,2.3arm}-GAL, and increase the hole size in this random fashion until it is comparable to the {10,6arm}, which have a $max(ZT) \approx 0.25$ at 300K[2]. Here, $max(ZT)$ refers to the maximal occurring ZT within a gate bias range of $[-1.5; 1.5]$eV. We do not allow for C-atoms with a single nearest neighbor, since these are energetically less favorable. Regarding edge disorder the decrease of thermal conductance outweighs the decrease in the power factor (S^2G_e), as can be seen in the increase in ZT with the number of removed atoms in Fig. 2. However, the effect for disordered antidots is much smaller as compared to the effect for hole-size for edges with pure chirality[2]. Therefore, one should preferable avoid the edge disorder during fabrication if one seeks to optimize thermoelectric applications. We note that the kinetics of the system or electronic current[26] may stabilize pure edges to some extent.

Next, we examine disorder in the hole lattice positions by randomly shifting a sequence of 2-hole unit-cells along the transverse direction by dN (armchair unit periodicity). The resulting figure of merit is given in Fig. 3. The full cell is $L = 10$ armchair units wide, and we examine $dN = 1, 2, ..5$ corresponding to increasing lateral disorder. The electronic conductance is almost unchanged at a low degree of position disorder ($dN = 1$), and the power factor can even initially increase at a low degree of position disorder, before it eventually decreases. Meanwhile, the thermal conductance decreases with increasing dN. Therefore, especially a weak degree of position disorder increases ZT to above 0.5. For perfect GALs with a high antidot density the electronic ZT (setting $\kappa_{ph} = 0$) is not much larger at the chemical potential of the largest peak. For low μ the κ_{ph} dominates, and therefore it is the first ZT peak which is increased by the disorder. On the other hand, the highest peak at higher μ mainly follows the change in power factor.

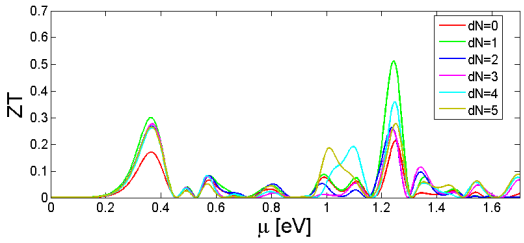

Fig. 3. Position disorder is here studied by increasing an interface mismatch between two GAL regions. Increasing the position disorder tends to reduce both the thermal conductance and also the power factor except at a very low degree of disorder. The system has a length of 380Å($M = 5$) and is based on a $\{10, 6arm\}$ GAL.

B. *Isotope disorder*

Now we address the effect of isotopes positioned at random sites or in a pattern changing with every 2nd 2-hole supercell (Fig. 4). The effect of isotopes on the thermal conductivity of

graphene has recently attracted much attention due to the advances in graphene synthesized by chemical vapour deposition (CVD). By using sequential input of $^{13}CH_4$ and $^{12}CH_4$ several groups have managed to fabricate graphene with regions of different isotopes[14]. The local thermal conductivity of the regions with different isotopes has been measured by Raman spectroscopy[15]. The isotope effect has been addressed theoretically for graphene[16], [17] and nanoribbons[18]. Inspired by this we here consider how the isotopes reduce the thermal conductance of GAL devices. In Fig. 4A we show $\mathcal{T}_{ph}$ (scaled

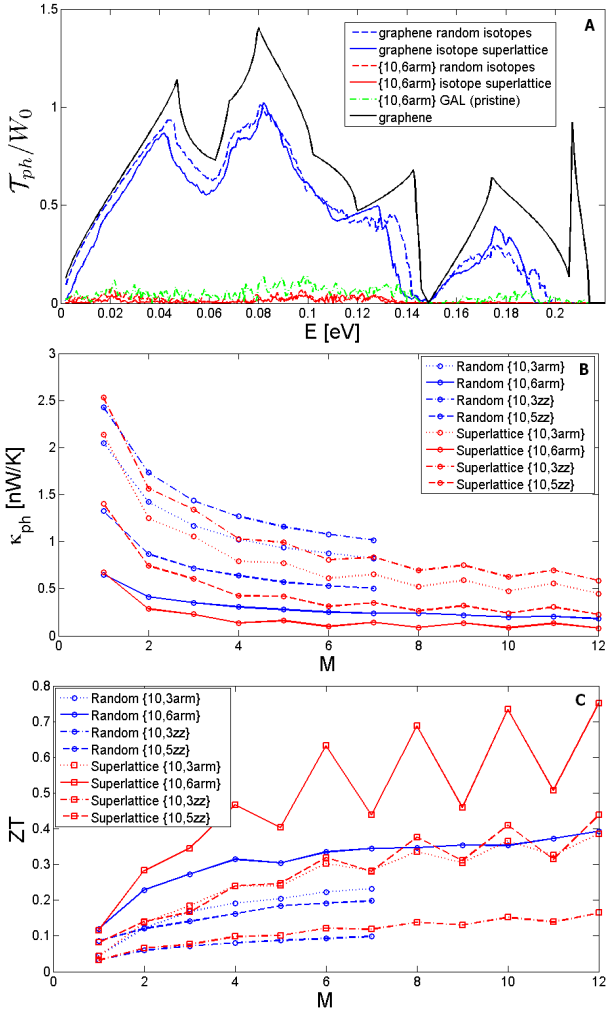

Fig. 4. The effect of isotopes is considered for a long system ($M = 12$). The random isotopes of ^{13}C atoms are distribution at random positions at each M with a concentration of 50%. For the supercell pattern every second unit cell consist of ^{13}C isotopes. The temperature is 300K.

by cell-width) for the longest system considered ($M = 12$ two-hole unit cells). We clearly see that isotope scattering give rise to a significant reduction in the thermal transmission. Comparing the reduction from the random isotope distribution to that of a pattern (alternating isotopes for every 2-hole supercell), it is clear that the "clustering" of isotopes leads to an extra reduction for especially the acoustic modes in the GAL region. Furthermore, we see that the difference will be less important at higher temperatures ($> 300K$ used here). In Fig. 4b we consider the thermal conductance for two GAL systems with different hole shape and size, as a function of length of GAL-device. For comparison, the thermal conductance is found to be 6.1nW/K for a pristine graphene device of the same width, and 0.41nW/K, 1.17nW/K, 0.76nW/K and 1.38nW/K for ideal $\{10,6arm\}$, $\{10,3arm\}$, $\{10,9zz\}$ and $\{10,3zz\}$ GALs, with length $M > 5$, respectively. With random isotopes the thermal conductance of the $M = 12$-$\{10,6arm\}$-device is reduced by 55%, compared to 88% with the ordered isotope pattern. For devices of longer lengths we enter the diffusive region and cannot neglect phonon-phonon scattering as considered here.

Since isotopes only affect the thermal properties we get a significant increase in ZT, especially at low gate bias where thermal transport is dominated by phonons. A peak $max(ZT) \approx 0.8$ is observed for the supercell pattern of isotopes at 300K, compared to $max(ZT) \approx 0.26$, 0.17, 0.07 and 0.13 for the ideal $\{10,6arm\}$, $\{10,3arm\}$, $\{10,9zz\}$ and $\{10,3zz\}$ GALs without isotopes. The oscillations in ZT with M stems from the choice of patterning where we only have $50 - 50\%$ isotopes for even M. With random isotopes we can exceed $max(ZT) \approx 0.4$ for the $\{10,6arm\}$ lattice. This illustrates that one can benefit from a further reduction of the heat conductance in GAL devices to increase the thermoelectric efficiency.

III. A MOLECULAR DYNAMICS APPROACH TO QUANTUM THERMAL TRANSPORT

Finally, we will briefly discuss how the elastic quantum phonon transport can be obtained from generalized Langevin molecular dynamics(MD), as an alternative to the Green's function method. The method was proposed by Wang *et al.*[27], and is a promising method for handling both low temperature quantum freeze-out of phonons, as well as the anharmonic interaction beyond perturbation theory. Both of these effects need to be included for graphene at 300K for devices longer than $\approx$ 600Å[28]. Anharmonic effects are clearly a very challenging problem for larger nanostructures such as GALs, where the role of the nanostructuring on the thermal properties needs clarification.

We solve the generalized Langevin equation for the mass-normalized displacements,

$$\ddot{\vec{u}}_s(t) = \vec{F}_{con} - \int_{t_0}^{t} \mathbf{\Phi}(t-t') \cdot \vec{u}_s(t')dt' + \tilde{\varepsilon}_{ph}(t)\,, \quad (5)$$

by using the velocity-Verlet algorithm. The forces on the right hand side are from the full Brenner potential, the frictional damping force and the quantum noise. The two latter are due to the connection of the device to the two thermal baths (each lead). The essential variable in quantum thermal transport is the coupling matrix obtained from the retarded phonon self energy, $\mathbf{\Gamma}_b(\omega) = i(\mathbf{\Pi}^r(\omega) - \mathbf{\Pi}^a(\omega))$. This object describes how much heat is absorbed(emitted) to(from) the surroundings. The non-Markovian damping kernel is obtained

from $\mathbf{\Gamma}_b$ as[27]:

$$\mathbf{\Phi}(\tau) = \frac{\Delta\omega}{\pi}\sum_{k=1}^{N_k}\left[\frac{\Gamma_b(\omega_k)}{\omega_k - i\epsilon_{ad}}e^{-i\omega_k\tau-\epsilon_{ad}\tau} + c.c.\right]. \quad (6)$$

Where $\tau = t - t'$ is the relative time so that the frictional damping force includes the memory at time t of a displacement at time t'. We choose a discrete time step Δt for a N_k step long MD simulation (with corresponding $\Delta\omega$ and discrete ω_k in frequency space). To improve convergence and computation-time we include an artificial damping, ϵ_{ad}, to reduce the memory kernel length, n_{cut}. We can from this calculate an effective imaginary part of the phonon self energy including this extra damping,

$$\mathbf{\Gamma}_b^{eff}(\omega) = \sum_{i=1}^{n_{cut}}\omega\Delta t\mathbf{\Phi}(\tau_i)e^{i\omega\tau_i} \quad (7)$$

From this we can calculate the noise spectral power density from the quantum fluctuation-dissipation theorem:

$$\mathbf{S}_f^{ph}(\omega) = \hbar\left(n_B(\omega)+\frac{1}{2}\right)\mathbf{\Gamma}_b^{eff}(\omega) \quad (8)$$

We have implemented this method of generating a colored noise sequence and show several tests of the outcome with a large artificial damping below. The aim is to find out how accurate one has to represent the self-energy in terms of memory length and artificial damping to get results consistent with NEGF calculations. In Fig. 5 we show the imaginary part of the frequency dependent phonon bath self energy, and the noise correlation function. The first two figures (A and B) show how, even if we shorten the memory length (which in principle is as long as the simulation itself) to 100 time steps and increase the artificial damping to 0.1eV, the selfenergy is still approximated quite well. In the insert in Fig. 5C we have calculated the noise correlation function (noise product at two different times averaged over 10^4 starting points), which classically should equal $k_BT\mathbf{\Phi}(t-t')$. This is not the case for graphene at 300K. As can be seen from the figure one has to go above 1000K for the classical fluctuation-dissipation theorem to be a good approximation. The reason for this is the quantum fluctuations, which give rise to a larger noise and kinetic energy below the Debye temperature, and the Bose-distribution of the phonons. Furthermore, we see from the last figure that MD with quantum heat baths gives results for the thermal conductance consistent with NEGF for short devices even at low temperatures.

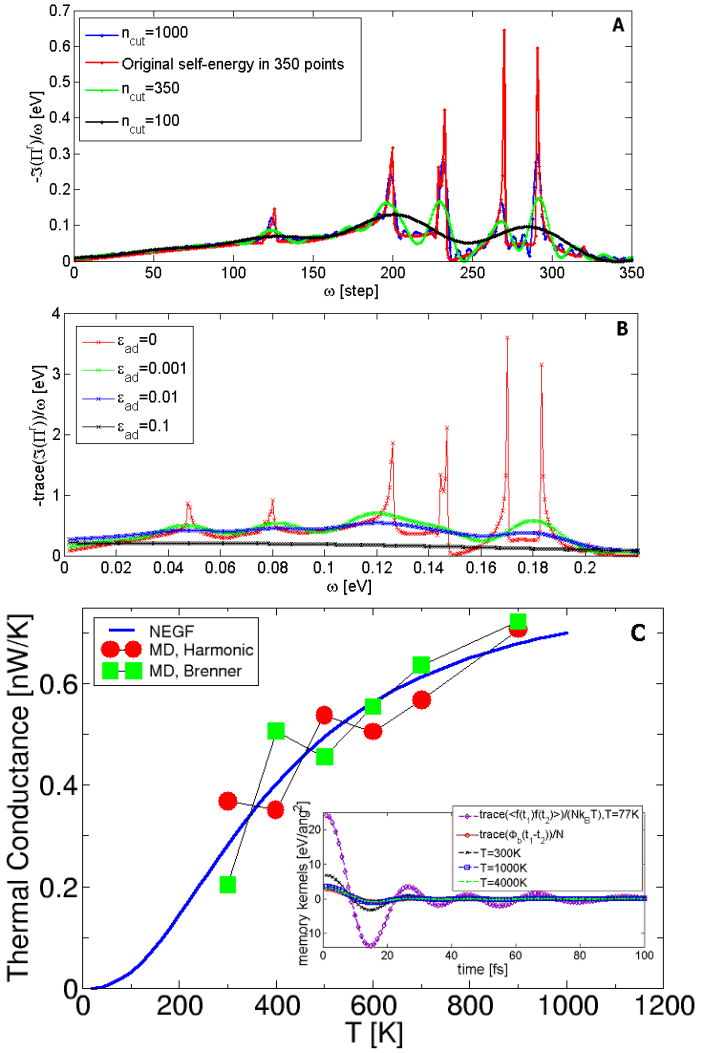

Fig. 5. A: Effect of memory length in the effective self energy used in MD. B: Effect of artificial damping in the effective self energy. C insert: Temperature dependence of the noise correlation function compared to the damping kernel. C: Thermal conductance from nonequalibrium MD with a temperature difference of 10% compared to the NEGF result for a {10,3arm} GAL with $M = 1$. $\epsilon_{ad} = 0.05$eV, $\delta t = 0.5$fs and $n_{cut} = 350$ is used.

IV. Conclusion

We have considered electronic and thermal transport properties of finite GAL structures with disorder. We conclude that disorder can be a limiting factor for thermoelectric applications of GALs. A high degree of disorder either due to lattice irregularity or the lack of pure edge chirality will degrade the overall thermoelectric performance. However, the trend that an increased antidot density enhances the thermoelectric efficiency still survives. The presence of isotopes is found to drastically reduce the thermal conductance for GALs. Both in the case of lattice disorder and isotope mass-variation we have shown that disorder can be used to greatly enhance thermoelectric performance. In particular, if lattice disorder is kept at a minimum, and isotopes are changed in patterns on a length scale that affect most phonon modes, one can benefit from a very large reduction of the thermal conductance in such devices to obtain a good thermoelectric efficiency. Finally, we have illustrated how the harmonic quantum thermal transport can be obtained from generalized Langevin-MD simulations with quantum heat baths, yielding results similar to those obtained with the Green's-function/Landauer approach. The MD approach is, in principle, able to address the effects of anharmonicity in thermal transport of nanostructured graphene.

ACKNOWLEDGMENT

The Center for Nanostructured Graphene is sponsored by the Danish National Research Foundation. We thank the DCSC for computational resources.

REFERENCES

[1] Alexander A. Balandin. Thermal properties of graphene and nanostructured carbon materials. *Nat. Mat.*, 10(8):569–581, 2011.

[2] Tue Gunst, Troels Markussen, A. P. Jauho, and Mads Brandbyge. Thermoelectric properties of finite graphene antidot lattices. *Phys. Rev. B*, 84(15):155449, October 2011.

[3] Thomas G. Pedersen, Christian Flindt, Jesper Pedersen, Niels Asger Mortensen, Antti-Pekka Jauho, and Kjeld Pedersen. Graphene antidot lattices: Designed defects and spin qubits. *Phys. Rev. Lett.*, 100(13):136804, April 2008.

[4] J. A. Fürst, J. G. Pedersen, C. Flindt, N. A. Mortensen, M. Brandbyge, T. G. Pedersen, and A. P. Jauho. Electronic properties of graphene antidot lattices. *New J. Phys.*, 11(9):095020, 2009.

[5] R. Petersen, T. G. Pedersen, and A. P. Jauho. Clar sextet analysis of triangular, rectangular, and honeycomb graphene antidot lattices. *ACS Nano*, 5(1):523–529, 2011.

[6] F. Ouyang, S. Peng, Z. Liu, and Z. Liu. Bandgap opening in graphene antidot lattices: The missing half. *ACS Nano*, 5(5):4023–4030, 2011.

[7] J. Eroms and D. Weiss. Weak localization and transport gap in graphene antidot lattices. *New J. Phys.*, 11(9):095021, 2009.

[8] M. Begliarbekov, O. Sul, J. Santanello, N. Ai, X. Zhang, E. H. Yang, and S. Strauf. Localized states and resultant band bending in graphene antidot superlattices. *Nano Lett.*, 11(2):1254–1258, Feb 2011.

[9] Myungwoong Kim, Nathaniel S. Safron, Eungnak Han, Michael S. Arnold, and Padma Gopalan. Fabrication and characterization of Large-Area, semiconducting nanoperforated graphene materials. *Nano Lett.*, 10(4):1125–1131, April 2010.

[10] Jingwei Bai, Xing Zhong, Shan Jiang, Yu Huang, and Xiangfeng Duan. Graphene nanomesh. *Nat. Nanotech.*, 5(3):190–194, March 2010.

[11] Benjamin Krauss, Peter Nemes-Incze, Viera Skakalova, Laszlo P. Biro, Klaus von Klitzing, and Jurgen H. Smet. Raman scattering at pure graphene zigzag edges. *Nano Lett.*, 10(11):4544–4548, November 2010.

[12] H. Sevinli and G. Cuniberti. Enhanced thermoelectric figure of merit in edge-disordered zigzag graphene nanoribbons. *Phys. Rev. B*, 81(11):113401, March 2010.

[13] Hideyuki Jippo, Mari Ohfuchi, and Chioko Kaneta. Theoretical study on electron transport properties of graphene sheets with two- and one-dimensional periodic nanoholes. *Phys. Rev. B*, 84(7):075467, 2011.

[14] Xuesong Li, Weiwei Cai, Luigi Colombo, and Rodney S. Ruoff. Evolution of graphene growth on ni and cu by carbon isotope labeling. *Nano Lett.*, 9(12):4268–4272, December 2009.

[15] Shanshan Chen, Qingzhi Wu, Columbia Mishra, Junyong Kang, Hengji Zhang, Kyeongjae Cho, Weiwei Cai, Alexander A. Balandin, and Rodney S. Ruoff. Thermal conductivity of isotopically modified graphene. *Nat. Mat.*, 11(3):203–207, 2012.

[16] Natalio Mingo, K. Esfarjani, D. A. Broido, and D. A. Stewart. Cluster scattering effects on phonon conduction in graphene. *Phys. Rev. B*, 81(4):045408, January 2010.

[17] Hengji Zhang, Geunsik Lee, Alexandre F. Fonseca, Tammie L. Borders, and Kyeongjae Cho. Isotope effect on the thermal conductivity of graphene. *Journal of Nanomaterials*, 2010:1–6, 2010.

[18] Jiuning Hu, Stephen Schiffli, Ajit Vallabhaneni, Xiulin Ruan, and Yong P. Chen. Tuning the thermal conductivity of graphene nanoribbons by edge passivation and isotope engineering: A molecular dynamics study. *Appl. Phys. Lett.*, 97(13):133107, 2010.

[19] Jin-Wu Jiang, Jinghua Lan, Jian-Sheng Wang, and Baowen Li. Isotopic effects on the thermal conductivity of graphene nanoribbons: Localization mechanism. *J. Appl. Phys.*, 107(5):054314, 2010.

[20] Zhen Huang, Timothy S. Fisher, and Jayathi Y. Murthy. Simulation of thermal conductance across dimensionally mismatched graphene interfaces. *J. Appl. Phys.*, 108(11):114310, 2010.

[21] Takahiro Yamamoto, Kenji Sasaoka, and Satoshi Watanabe. Universality and diversity in a Phonon-Transmission histogram of Isotope-Disordered carbon nanotubes. *Phys. Rev. Lett.*, 106(21):215503, May 2011.

[22] U. Sivan and Y. Imry. Multichannel landauer formula for thermoelectric transport with application to thermopower near the mobility edge. *Phys. Rev. B*, 33(1):551, January 1986.

[23] Donald W. Brenner. Empirical potential for hydrocarbons for use in simulating the chemical vapor deposition of diamond films. *Phys. Rev. B*, 42(15):9458, November 1990.

[24] Troels Markussen, Antti Pekka Jauho, and Mads Brandbyge. Electron and phonon transport in silicon nanowires: Atomistic approach to thermoelectric properties. *Phys. Rev. B*, 79(3):035415, January 2009.

[25] Keivan Esfarjani, Mona Zebarjadi, and Yoshiyuki Kawazoe. Thermoelectric properties of a nanocontact made of two-capped single-wall carbon nanotubes calculated within the tight-binding approximation. *Phys. Rev. B*, 73(8):085406, February 2006.

[26] Xiaoting Jia, Mario Hofmann, Vincent Meunier, Bobby G. Sumpter, Jessica Campos-Delgado, Jos Manuel Romo-Herrera, Hyungbin Son, Ya-Ping Hsieh, Alfonso Reina, Jing Kong, Mauricio Terrones, and Mildred S. Dresselhaus. Controlled formation of sharp zigzag and armchair edges in graphitic nanoribbons. *Science*, 323(5922):1701–1705, March 2009.

[27] Jian-Sheng Wang. Quantum thermal transport from classical molecular dynamics. *Phys. Rev. Lett.*, 99(16):160601, October 2007.

[28] Jian-Sheng Wang, Xiaoxi Ni, and Jin-Wu Jiang. Molecular dynamics with quantum heat baths: Application to nanoribbons and nanotubes. *Phys. Rev. B*, 80(22):224302, December 2009.

Paper IV

Jesper G. Pedersen, Tue Gunst, Troels Markussen and Thomas G. Pedersen

Graphene antidot lattice waveguides

Phys. Rev. B **86**, 245410 (2012)

Graphene antidot lattice waveguides

Jesper Goor Pedersen,[1] Tue Gunst,[2,3] Troels Markussen,[4] and Thomas Garm Pedersen[1,3]
[1]*Department of Physics and Nanotechnology, Aalborg University, Skjernvej 4A DK-9220 Aalborg East, Denmark*
[2]*Department of Micro- and Nanotechnology (DTU Nanotech), Technical University of Denmark, DK-2800 Kgs. Lyngby, Denmark*
[3]*Center for Nanostructured Graphene, Technical University of Denmark, DK-2800 Kgs. Lyngby, Denmark*
[4]*Center for Atomic-Scale Materials Design, Department of Physics, Technical University of Denmark, DK-2800 Kgs. Lyngby, Denmark*
(Received 8 October 2012; published 11 December 2012)

We introduce graphene antidot lattice waveguides: nanostructured graphene where a region of pristine graphene is sandwiched between regions of graphene antidot lattices. The band gaps in the surrounding antidot lattices enable localized states to emerge in the central waveguide region. We model the waveguides via a position-dependent mass term in the Dirac approximation of graphene and arrive at analytical results for the dispersion relation and spinor eigenstates of the localized waveguide modes. To include atomistic details we also use a tight-binding model, which is in excellent agreement with the analytical results. The waveguides resemble graphene nanoribbons, but without the particular properties of ribbons that emerge due to the details of the edge. We show that electrons can be guided through kinks without additional resistance and that transport through the waveguides is robust against structural disorder.

DOI: 10.1103/PhysRevB.86.245410 PACS number(s): 72.80.Vp, 73.22.−f, 73.21.Hb, 73.21.Cd

I. INTRODUCTION

Graphene, the two-dimensional allotrope of carbon first isolated in 2004,[1,2] has emerged as a highly attractive material for future electronic devices. Graphene has exceptional electronic properties, as demonstrated in its extremely high carrier mobility,[3] which even at room temperature is limited predominantly by impurity scattering.[4] Already, extremely fast graphene-based transistors have been realized,[5] and fabrication methods have emerged which allow for large-scale production of single-layered graphene.[6] One key element of future graphene-based electronics is the ability to localize carriers in graphene *wires*, in order to facilitate electronic graphene networks. The most immediate way of realizing such wire structures is by cutting graphene into so-called graphene nanoribbons (GNRs).[7] Quantum confinement will in general induce a band gap in such structures, the magnitude of which scales with the inverse of the width of the GNR. However, the exact atomistic configuration of the edge of the ribbon greatly influences the magnitude of this gap, with particular edge configurations resulting in vanishing gaps or localized edge states.[8,9] An alternative to this is to rely on controlled generation of extended defects in graphene to act as metallic wires.[10] Relying on results from two-dimensional electron gases (2DEGs) formed at the interface of semiconductor heterostructures, one could also imagine applying electrostatic gating to define wire geometries. Graphene presents an interesting challenge in this regard via the phenomenon of Klein tunneling,[11] which makes it difficult to achieve carrier localization in graphene via ordinary gating. Electrons impinging on a potential barrier at close to normal incidence are transmitted with vanishing reflection, regardless of the height of the potential barrier. In spite of this, guiding of electrons via electrostatic gating has been demonstrated experimentally,[12] albeit with the caveat that guiding is restricted to a specific range of wave vectors for which Klein tunneling is negligible. In contrast, a so-called mass term in graphene provides confinement that is a close analog of gate-defined localization in an ordinary 2DEG. This term originates from a Dirac description of graphene, which emerges as a low-energy approximation of a tight-binding (TB) model on the honeycomb lattice.[13] Adding a diagonal term $\pm\Delta$ to the resulting Hamiltonian, with the sign alternating between the two sublattices of graphene, the spectrum becomes that of gapped graphene, a semiconductor with an energy gap of twice the mass term. This staggered potential is commonly denoted a mass term due to the analogy of the low-energy carriers in graphene with massless Dirac fermions, which acquire a mass via such a term in the Hamiltonian.

In this paper, we propose realizing a waveguiding structure in graphene via graphene antidot lattices (GALs). GALs are nanostructured graphenes, which in their simplest description take the form of periodically perforated graphene structures.[14] GALs have recently been produced experimentally with both electron-beam lithography[15,16] and block copolymer lithography.[17,18] The periodic perforation induces a band gap in graphene, rendering it semiconducting, and the resulting band structure closely resembles that of gapped graphene in the low-energy limit. GALs thus allow for the realization of a position-dependent mass term, as illustrated in Fig. 1. The idea is to sandwich a region of pristine graphene between two GAL regions, the band gaps of which define an energy range for which localized guided modes are expected to emerge in the central region. This idea is closely analogous to how photonic waveguiding is realized in photonic crystal structures.[19] We note that other methods beside GALs have been proposed for achieving gaps in graphene via superlattices, such as, e.g., patterned hydrogenation[20] or superlattices of boron nitride islands embedded in graphene.[21] Another alternative is to sandwich graphene between hexagonal boron nitride, which is predicted to induce significant band gaps in graphene.[22]

We denote a waveguide geometry as $\{L,R\}_N^{\mathrm{zz/ac}}$, where L is the sidelength of the hexagonal unit cell of the surrounding GAL, while R is the radius of the perforations, both in units of the graphene lattice constant, $a = 2.46$ Å. The width W of the waveguide is defined via $N \equiv W/w$, where w is the width of the enlarged GAL unit cell, as illustrated in the lower panel of

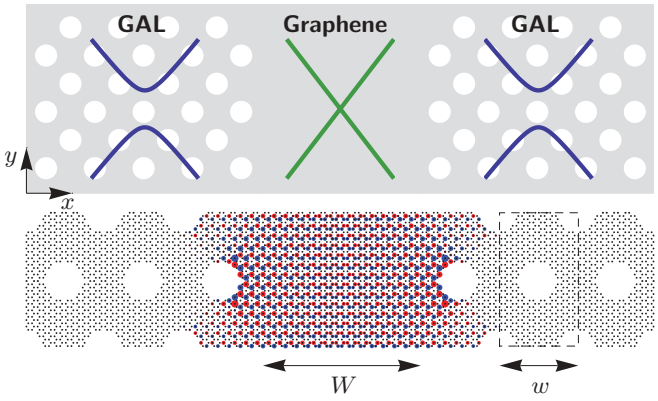

FIG. 1. (Color online) Upper panel: conceptual illustration of a graphene antidot lattice (GAL) waveguide. A central region of pristine graphene is surrounded by GAL regions, the band gaps of which confine states to the waveguide region. Translational symmetry is assumed in the y direction, which is along the longitudinal direction of the waveguide. Lower panel: geometry of a $\{7,3\}_2^{zz}$ GAL waveguide. Black dots show the location of carbon atoms. Bloch boundary conditions are imposed on all boundaries. The dashed lines illustrate the enlarged GAL unit cell, the width of which we denote by w. The lowest-energy waveguide mode at the Γ point, calculated via the tight-binding model, is illustrated with circles, the size of which shows the absolute value $|\psi(x,y)|$ of the (real-valued) eigenstate, while the color indicates the sign.

Fig. 1. The width of the waveguide is of course somewhat more ambiguous than in the case of GNRs, as we have no sharp edge defining the precise boundary between the region of pristine graphene and the surrounding antidot lattice. For denoting the geometries we simply take W as the distance between the nearest edges of the two bordering antidot lattice unit cells. However, as we discuss below, the effective waveguide width is slightly larger than this. The width w of the enlarged GAL unit cell depends on the orientation of the waveguide with respect to the graphene lattice, which we indicate with the superscript, with zz (ac) denoting a waveguide with the longitudinal direction along the zigzag (armchair) orientation of the graphene lattice. Note that in both cases we choose the orientation of the GAL such that the superlattice basis vectors lie parallel to carbon-carbon bonds, to ensure that a band gap always exists for the GAL.[23] The lower panel of Fig. 1 illustrates the geometry of a $\{7,3\}_2^{zz}$ waveguide. For simplicity we restrict the width of the waveguide to be an integer multiple of the width of the GAL unit cell. This is merely for computational convenience, and as we will demonstrate in this paper simple scaling laws exist to predict the properties of more general widths of the waveguide.

In this paper, two different methods will be employed to determine the waveguiding properties of GAL waveguides. We first consider a model based on the Dirac approximation, including the influence of the GAL barriers via a position-dependent mass term. We will show that this model admits analytical solutions in certain limits, which is highly beneficial for determining the general dependence of the waveguide properties on the various structural parameters. Furthermore, these results demonstrate clearly the unique properties of graphene waveguiding compared to quantum-well structures defined in ordinary 2DEGs. To include the atomistic details of the structures we also consider a tight-binding model, which we use to calculate the transmission properties of the waveguides, taking into account potential structural disorder.

II. DIRAC MODEL

A. Analytical derivation

We first consider a simple model of a GAL waveguide based on a Dirac model of graphene. For graphene nanoribbons, the exact edge geometry can be included in a Dirac model via the boundary conditions of the spinor components in each valley.[9,24] However, in our case, no atomically defined boundary exists between the central region and the bordering GAL regions and we thus adopt a model wherein the band gap E_g of the confining GALs is included via a position-dependent mass term. We introduce dimensionless coordinates $(\chi,\gamma) = 2/W \times (x,y)$ and dimensionless energies $\epsilon = E/E_0$, with $E_0 = 2\hbar v_F/W \simeq 1.278\,\text{eV nm}\times W^{-1}$, assuming a Fermi velocity $v_F = 10^6$ m/s of graphene. In these units, the eigenvalue problem for the spinor eigenstates reads

$$\begin{bmatrix} m(\chi) & -i(\partial_\chi - i\partial_\gamma) \\ -i(\partial_\chi + i\partial_\gamma) & -m(\chi) \end{bmatrix} \begin{bmatrix} \phi_A(\chi,\gamma) \\ \phi_B(\chi,\gamma) \end{bmatrix} = \epsilon \begin{bmatrix} \phi_A(\chi,\gamma) \\ \phi_B(\chi,\gamma) \end{bmatrix}, \tag{1}$$

where the dimensionless mass term $m(\chi) = \delta = E_g/(2E_0)$ for $|\chi| > 1$ and zero otherwise. This equation has been derived from the Dirac Hamiltonian H_K, which emerges as a linearization of a TB model of graphene near the K point. We will discuss the differences between the two inequivalent K and K' valleys of graphene below. Note that the sign of the mass term is arbitrary and that changing it has no physical significance but merely results in an interchange of the two spinor components. We stress, however, that the sign should be the same on both sides of the central waveguiding region. The Hamiltonian commutes with the y component of the momentum operator, and we thus take spinor components of the form $\phi_A(\chi,\gamma) = f(\chi)e^{i\kappa\gamma}$ and $\phi_B(\chi,\gamma) = g(\chi)e^{i\kappa\gamma}$, where $\kappa = kW/2$ is the dimensionless Bloch wave vector along the longitudinal direction of the waveguide. As the mass term is piecewise constant, the equations for the spinor components can be decoupled in each region of the waveguide structure. We look for bound states and thus take $\epsilon^2 < \delta^2$. The normalizable solutions for the first spinor component thus read $f(\chi) = A_\pm e^{\pm\beta\chi}$ for $|\chi| > 1$ and $f(\chi) = B\cos(\alpha\chi) + C\sin(\alpha\chi)$ for $|\chi| < 1$ while the second component is given via $g(\chi) = i(\kappa - \partial_\chi)f(\chi)/[\epsilon + m(\chi)]$. Here, we have defined $\alpha = \sqrt{\epsilon^2 - \kappa^2}$ and $\beta = \sqrt{\delta^2 + \kappa^2 - \epsilon^2}$. The requirement of continuity of both spinor components at the boundaries of the central waveguide region leads to a transcendental equation for the energies, $\sqrt{\delta^2 - \alpha^2} = \alpha\tan 2\alpha$, regardless of which valley is considered (see below). The solution of the problem is thus closely reminiscent of that of an ordinary one-dimensional square-well potential, albeit with the crucial difference that for graphene $E \propto \alpha$ rather than $E \propto \alpha^2$, as a consequence of the linear dispersion relation of graphene. Also, we note that, contrary to the case of the Schrödinger equation, the derivative of the eigenstate spinors need not be continuous at the boundary.

B. Infinite mass limit

The standard textbook graphical solution suggests that there are N bound states in the waveguide if $(N-1)\pi/2 < \delta < N\pi/2$. In general, the energies and spinor components of these states will need to be determined by numerical solution of the transcendental equation. However, in the limit of an infinite mass term, $\delta \to \infty$, the problem admits an analytical solution for the energies:

$$\epsilon_{\rm ns}^{\infty}(\kappa) = s\sqrt{\kappa^2 + \frac{\pi^2}{4}\left(n+\frac{1}{2}\right)^2}, \quad n = 0,1,2\ldots, \qquad (2)$$

or, reverting to ordinary units,

$$E_{\rm ns}^{\infty}(k) = s\sqrt{E_b^2(k) + \frac{\hbar^2 v_F^2 \pi^2}{W^2}\left(n+\frac{1}{2}\right)^2}, \qquad (3)$$

where $E_b(k) = \hbar v_F k$ is the bulk graphene dispersion relation and $s = \pm 1$. The dispersion relations of the waveguide modes thus resemble those of gapped graphene[25] with a mass term of $\Delta_{\rm eff} = (\hbar v_F \pi / W)(n+\frac{1}{2})$. Series expansion of the transcendental equation for the energies in the case of a finite mass term reveals that $\alpha \simeq \pi/2(n+1/2)[1+1/(2\delta)]^{-1}$, so the results in the infinite mass limit are expected to be valid when $E_g \gg 2\hbar v_F/W \simeq 1.278$ eV nm$\times W^{-1}$. Including the leading-order correction, the energies are given as

$$E_{\rm ns}^{(1)}(k) = E_{\rm ns}^{\infty}(k) - s\frac{2\hbar^2 v_F^2 \pi^2 \left(n+\frac{1}{2}\right)^2}{W^2\sqrt{k^2W^2 + \pi^2\left(n+\frac{1}{2}\right)^2}} \times \frac{1}{E_g}. \qquad (4)$$

The eigenstate spinors in the infinite mass limit are most easily determined by using the boundary conditions derived by Berry,[26] which set a phase relationship between the spinor components at the edge of the waveguide. The spinor components for $\kappa = 0$ and $\epsilon > 0$ can then be derived as

$$f_n(\chi) = \begin{cases} \cos\left(\pi/2\left[n+\frac{1}{2}\right]\chi\right) & \text{for } n \text{ zero or even} \\ \sin\left(\pi/2\left[n+\frac{1}{2}\right]\chi\right) & \text{for } n \text{ odd} \end{cases}, \qquad (5)$$

while

$$g_n(\chi) = \begin{cases} i\sin\left(\pi/2\left[n+\frac{1}{2}\right]\chi\right) & \text{for } n \text{ zero or even} \\ -i\cos(\pi/2[n+\frac{1}{2}]\chi) & \text{for } n \text{ odd} \end{cases}, \qquad (6)$$

for $|\chi| < 1$. Here, we have omitted normalization constants. We note that, because of the particle-hole symmetry of graphene, the eigenstates should be normalized separately on each sublattice.[27] The spinors for the $\epsilon < 0$ eigenstates are given by exchanging f_n and g_n. Interestingly, and in stark contrast to an ordinary infinite square-well potential, this shows that in the limit of infinite mass the charge density is evenly distributed within the waveguide, for states with vanishing wave vectors. We find that this holds true also in the more general case of a finite mass term, the main difference being that in this case the spinors extend slightly into the mass regions. Including a nonzero wave vector, the charge density is localized predominantly on either the edges or the middle of the waveguide.

The derivation above takes as its starting point a linearization of graphene near the K valley. The Dirac Hamiltonian near the inequivalent K' valley is such that the energy spectrum of the waveguide is the same for both valleys, while the eigenstate spinors are related by an interchange of the spinor components, i.e., $\phi_A^{K'} = \phi_B^K$ and $\phi_B^{K'} = \phi_A^K$. We also note that to obtain the full wave function, a Bloch phase factor of $e^{i\mathbf{K}\cdot\mathbf{r}}$ or $e^{i\mathbf{K}'\cdot\mathbf{r}}$ should be added to the spinors, with $\mathbf{K}$ and $\mathbf{K}'$ depending on the orientation of the graphene lattice. We will return to this point below, when we compare the results of the Dirac approximation with those obtained with a tight-binding model.

III. TIGHT-BINDING MODEL

To include the atomistic details of the waveguide structures, and to clarify the validity of the results derived in the Dirac approximation, we employ a nearest-neighbor tight-binding approximation. This will also allow us to assess the significance of the orientation of the waveguide with respect to the graphene lattice. The TB model is parametrized via a hopping term $t = -3$ eV between π orbitals, the on-site energy of which we set to zero. We ignore nonorthogonality of the π orbitals. Figure 1 illustrates the geometry used for the TB model in the case of a $\{7,3\}_2^{zz}$ GAL waveguide. We use periodic boundary conditions along the x axis as well as the y axis. We have ensured that the results are converged with respect to the number of GAL unit cells included around the waveguide. The band gap of the GAL is quite well developed even with just a few rows of antidots,[28] so including three GAL unit cells on each side of the waveguide usually yields converged results.

IV. RESULTS

A. Dispersion relations

In Fig. 2, we show the band structure of a $\{7,3\}_5^{zz}$ GAL waveguide calculated using the TB model as well as the Dirac

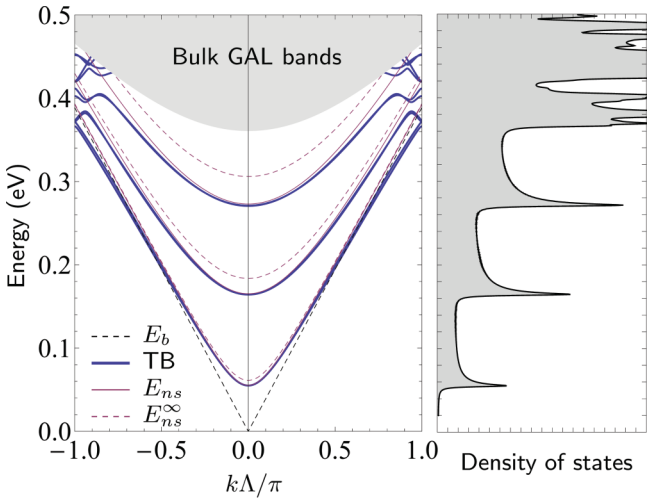

FIG. 2. (Color online) Left: band structure of the $\{7,3\}_5^{zz}$ GAL waveguide. The band structures are shown for the tight-binding model as well as the analytical infinite mass-limit results $E_{\rm ns}^{\infty}$ and numerical solution of the transcendental equation of the Dirac approximation $E_{\rm ns}$. The shaded gray area shows the projected bands of the surrounding GAL regions. For comparison, the bulk graphene band structure E_b is also shown. Note that Λ denotes the lattice constant of the waveguide. Right: corresponding density of states for the TB model. Note the Van Hove singularities characteristic of one-dimensional structures.

approximation. Only electron ($E > 0$) bands are shown. Both the TB and the Dirac model exhibit perfect electron-hole symmetry, so hole ($E < 0$) bands simply follow from a sign change. For the Dirac results we take the effective width of the waveguide to be $W_{\text{eff}} = (N + \frac{1}{2})w$, slightly larger than the definition used for denoting the waveguide geometries. Note that the wave vector is shown relative to the lattice constant of the GAL waveguide, which is $\Lambda = 3La$ for the zigzag orientation and $\Lambda = \sqrt{3}La$ for the armchair orientation. In the figure, the shaded gray region illustrates the projected bands of the GAL, which define the region below which localized waveguide states are expected to appear. This particular waveguide structure supports several localized states. Higher-lying band gaps also appear in the GAL, and we have confirmed that localized waveguide modes are also supported in these gaps. It is worth stressing that localized waveguide modes exist for all wave vectors in the first Brillouin zone. This is in contrast to the case of waveguides defined via electrostatic gating, where guided modes generally exist only for a limited range of wave vectors.[29] The dispersions of the waveguide states agree very well between the TB and the Dirac model, as long as the wave vector is not too near the Brillouin zone edges. The largest deviations between the two models occur for energies close to the projected bands of the GAL, where coupling between the waveguide and the GAL states is pronounced. We note that the analytical result obtained in the infinite mass limit E_{ns}^{∞} is a very good approximation of the lowest waveguide mode. Including the first-order correction to E_{ns}^{∞} leads to near-perfect agreement with the full solution of the transcendental equation. Note that, as illustrated in the derivation of the Dirac result, the waveguide dispersion relation quite closely resembles that of gapped graphene, which in turn is approximately the same as bulk graphene for wave vectors $k \gg \Delta_{\text{eff}}/(\hbar v_F)$. This is evident in the figure, where for comparison we also include the bulk graphene dispersion relation. The density of states (DOS) calculated using the TB model is shown in the right panel of Fig. 2. As expected from the Dirac approximation, the DOS closely resembles one-dimensional gapped graphene, i.e., $g(E) \propto \Theta(E - \Delta_{\text{eff}})E/(\hbar v_F\sqrt{E^2 - \Delta_{\text{eff}}^2})$ with the Van Hove singularities characteristic of one-dimensionality clearly evident in the figure.

B. Band gaps and effective masses

In Fig. 3(a), we show the energy of the lowest localized waveguide state at the Γ point as a function of the width of a $\{7,3\}_N^{(\text{zz,ac})}$ waveguide. Results are shown for the TB model as well as the analytical results obtained in the Dirac equation approach. Note that, due to electron-hole symmetry, the band gap is twice this value. While the solution derived from the Dirac equation does not distinguish between zigzag and armchair orientation of the waveguide, the TB model predicts that there are some differences between the two cases. To illustrate this, we show results obtained for waveguides oriented along the zigzag (ZZ) and armchair (AC) directions, respectively. The inset of the figure illustrates that both ZZ and AC orientations exhibit a clear $1/W$ dependence of the energies, as predicted from the Dirac approximation, provided the waveguide is sufficiently wide. We note that

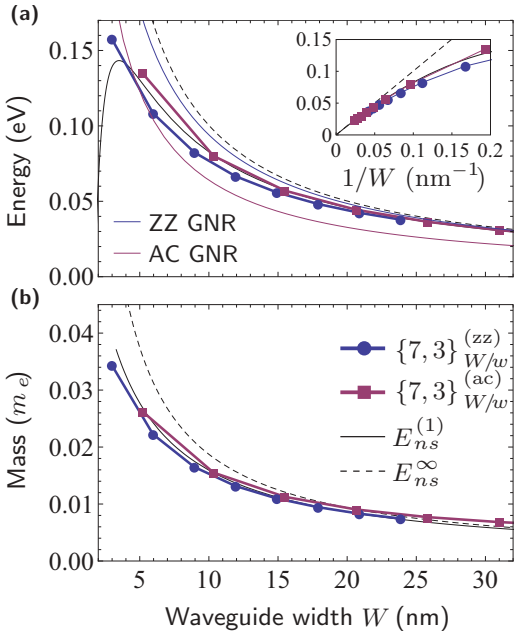

FIG. 3. (Color online) (a) Energy of the lowest localized waveguide state at the Γ point, for the $\{7,3\}_N$ family of GAL waveguides. The energy is shown as a function of the width of the waveguide. Results are shown for TB models (points) of waveguides oriented along the zigzag (ZZ) and armchair (AC) directions, respectively, as well as the analytical results obtained via the Dirac model in the infinite mass limit and including the first-order correction (black lines). See the legend in panel (b). Inset: $1/W$ dependence of the energy for wide waveguides. For comparison, the thin colored lines show the energies for ZZ and AC GNRs, if certain edge dependencies are ignored (see text). (b) Corresponding effective masses in units of the free-electron mass m_e. In both panels, note the close resemblance of the results obtained for AC and ZZ oriented waveguides.

while differences do exist between AC and ZZ orientations these are rather small and could be attributed to a slightly different effective width of the waveguides in the two cases, due to the $\pi/6$ difference in the orientation of the surrounding GAL with respect to the waveguide. Indeed, results of the Dirac approximation fit both orientations quite well, especially when including the first-order correction. The results of the Dirac model can be made to fit even better if we take into account the fact that the effective width of the waveguide is likely to be somewhat larger than the definition we have used (see Fig. 1). Indeed, introducing the same effective width in the Dirac model as we did for Fig. 2 results in even better agreement with TB results.

The absence of a well-defined edge means that the dependence of the properties of the guided modes on the width of the waveguide is much simpler than is the case for GNRs. In particular, GAL waveguides are always semiconducting, whereas in a nearest-neighbor TB model armchair GNRs alternate between metallic and semiconducting behavior depending on the exact width of the ribbon, while zigzag GNRs display dispersionless midgap states, localized on the edges.[9] In Fig. 3(a), we show the energies for ZZ and AC GNRs, calculated via the TB model. We stress that the ZZ GNRs also contain dispersionless edge states at the Dirac point energy. Furthermore, AC GNRs are metallic for widths

$W = (3p - 1)a$, with p being an integer.[8] To compare with the waveguide results, we have included only semiconducting AC GNRs in the figure. With these modifications, there is quite good agreement between the energies of GNRs and the GAL waveguide structures. GAL waveguides thus resemble ribbons without the particulars resulting from edge effects. As such, we speculate that the electronic properties of GAL waveguides may be easier to control experimentally.

In Fig. 3(b), we show the effective mass of the lowest waveguide state at the Γ point as a function of the width. From the analytical Dirac results in the limit of an infinite mass term, we find an effective mass $m_{\text{eff}}^{\infty} = \hbar\pi(n + \frac{1}{2})/(v_F W)$. Again, we note that there is excellent agreement between the results obtained in the Dirac approximation and those from a TB model, for both orientations of the waveguide. Including the first-order correction, results from the Dirac model are in near-perfect agreement with the TB model. While electrons in pristine graphene have vanishing effective masses, the appearance of an effective mass term in the waveguide structures results in nonzero albeit still very small effective electron masses, which tend to zero in the limit of infinitely wide waveguides.

C. Eigenstates

To further compare the AC and ZZ waveguide orientations, we show in Fig. 4(a) the eigenstates corresponding to the lowest (positive) energy of $\{7,3\}_5^{(zz)}$ and $\{7,3\}_3^{(ac)}$ GAL waveguides, calculated at the Γ point. Note that these have approximately the same waveguide widths. The lower panels in the figure show the absolute square of the wave function, with the color indicating the sublattice. These results demonstrate a crucial difference between the AC and ZZ orientations, namely, that while for the AC waveguide the wave function is distributed evenly across the two sublattices the ZZ waveguide exhibits pseudo-spin-polarization, with the wave functions of the two sublattices localized predominantly on opposite edges of the waveguide. We note that the lowest energy is doubly degenerate and that the second eigenstate (not shown) has the opposite pseudo-spin-distribution. The upper panels in the figure show the integrated probability density, $\rho(x) \equiv \int |\psi(x,y)|^2 dy$, along the transversal direction of the waveguide, with color indicating the sublattice. Note that, despite the lack of a clearly defined edge, the probability densities very closely resembles those of GNRs.[9] The black lines in the upper panels show the total probability density, if a broadening of the order of the graphene lattice constant is included in order to account for the spatial extent of the π orbitals. As predicted from the Dirac equation approach above, these results illustrate how the charge density is nearly uniformly distributed across the entire waveguide also for the higher-lying states shown in Fig. 4(b). This is in stark contrast to gate defined waveguides, which have wave functions more reminiscent of ordinary standing wave solutions.[29] In agreement with the Dirac results, we find that the uniform distribution only occurs at the Γ point. For nonzero wave vectors the density becomes localized predominantly at the edges of the waveguide for the lowest state, as illustrated with dashed lines in the figure for $k\Lambda = \pi/2$. In contrast to this,

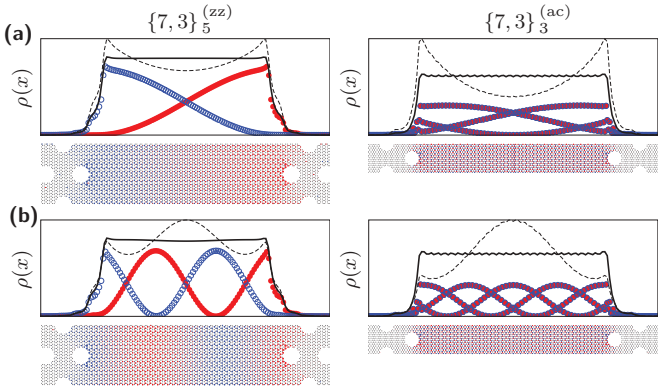

FIG. 4. (Color online) Wave functions of the localized waveguide modes corresponding to the (a) lowest and the (b) second-lowest (positive) energy at the Γ point of a (left) $\{7,3\}_5^{(zz)}$ and a (right) $\{7,3\}_3^{(ac)}$ GAL waveguide. The lower panels in each case show the geometry, with carbon atoms indicated with black dots. Note that the actual computational cell includes additional GAL unit cells on each side of the central region. Superimposed on top of the geometry is the wave function, with the size of the circles indicating the absolute square of the π-orbital coefficient, while the color indicates the sublattice. The upper panels show the integrated probability density, $\rho(x) \equiv \int |\psi(x,y)|^2 dy$. Red and blue circles indicate the densities on each sublattice. The black line shows the total density, when including a small broadening term. The dashed line shows the corresponding density at nonzero wave vectors, $k\Lambda = \pi/2$. Note the rapid oscillations of the integrated density of the AC waveguide.

the densities of the second-lowest states tend to localize in the center of the waveguide as the wave vector is increased.

To compare the wave functions with the spinor components derived via the Dirac equation, we first note that both the K and the K' points of graphene are folded onto the Γ point of the waveguide structure. We thus expect the eigenstates to resemble linear combinations of the eigenstates in both valleys. The differences between the zigzag and armchair waveguides emerge due to the Bloch phase factors $e^{i\mathbf{K}\cdot\mathbf{r}}$ and $e^{i\mathbf{K}'\cdot\mathbf{r}}$, which differ depending on the orientation of the graphene lattice. For the zigzag orientation, the integrated probability density $\rho(x)$ becomes a simple linear combination of the eigenstates belonging to each valley, $\rho_A(x) \propto |f_K(x) + f_{K'}(x)|^2$ and $\rho_B(x) \propto |g_K(x) + g_{K'}(x)|^2$. Using the expressions for the spinor components derived above, we find $\rho(x) \propto 1 \pm \sin(2\pi[n + \frac{1}{2}]x/W)$, with the sign depending on the sublattice, which is in excellent agreement with the TB results. In contrast to this, because of the mixing of the valleys the probability densities of the armchair orientation exhibit a rapidly oscillating term, with a period $2\pi/\Delta K$.[27] These rapid oscillations are clearly evident in the right panels of Fig. 4. As shown in the figure, these rapid oscillations are quickly washed out if a small amount of broadening is included. In this case, we recover the nearly uniform charge distribution within the waveguide predicted from the Dirac results. Finally, we note that the differences between armchair and zigzag oriented GAL waveguides are very similar to those seen between GNRs with armchair and zigzag edges.[9] In the case of GNRs, though, the difference emerges due to different boundary conditions at the edge of the ribbon, which are not present in the case of GAL waveguides.

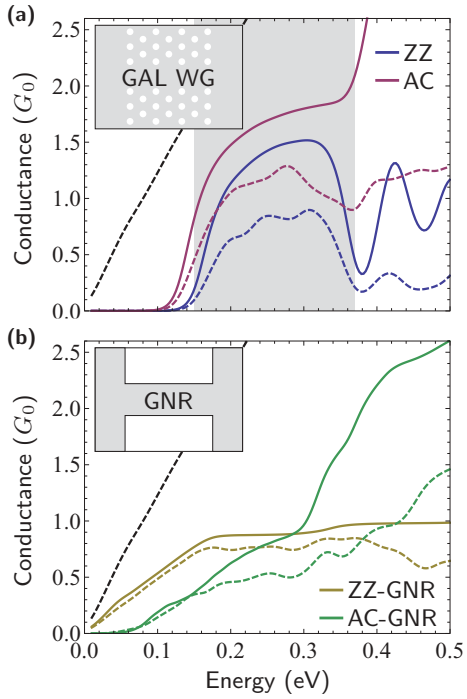

FIG. 5. (Color online) Insets: schematic transport setups for (a) a GAL waveguide and (b) a GNR, each connecting two semi-infinite graphene leads. Conductances for pristine (solid lines) and disordered systems (dashed lines) are shown for (a) GAL waveguides and (b) GNRs, in units of the conductance quantum G_0. The straight black dashed lines show the graphene conductance. In the disordered systems, edge atoms have been randomly removed with a 5% probability. The lengths of the waveguides and GNRs are $L = 89$ nm. The shaded area in panel (a) indicates the energy range of the confined waveguide mode.

D. Conductance

Because the GAL waveguides have no clearly defined edge, one might wonder whether the guiding properties of the waveguides would be relatively robust to disorder. Indeed, the crucial ingredient is the existence of a band gap in the surrounding GAL. As this gap essentially occurs due to an averaging of the effect of the individual holes,[30] the emergence of a gap should be relatively robust to disorder. A thorough investigation of disorder is beyond the scope of this paper, but as a preliminary study we model disorder by randomly removing atoms at the edges of the holes in the GAL. We consider a disordered GAL waveguide sandwiched between semi-infinite pristine graphene leads as illustrated in the inset of Fig. 5(a). For comparison we also consider the analogous system with the two graphene leads connected with a GNR having the same width as the corresponding waveguide ($W = 4.5$ nm for ZZ, $W = 6.0$ nm for AC), as illustrated in the inset of Fig. 5(b). We calculate the transmission through the waveguide and GNR using a recursive Green's-function method[31] with the lead self-energies determined using an iterative procedure.[32] The transmission is averaged over 100 values of the transverse wave vector, and we further average over ten samples with different realizations of the random disorder. To smear out the rapid oscillations that occur due to interference between transmitted and reflected waves at the boundaries between the GAL waveguide and the graphene leads, we calculate the conductance at a finite temperature of $T = 100$ K. We consider a relatively high level of disorder, for which edge atoms are removed with a 5% probability. In Fig. 5(a), we show the conductance of disordered $\{7,3\}_1^{(zz,ac)}$ GAL waveguides of length $L = 89$ nm (dashed lines). For comparison, we also include the conductance of the pristine waveguides (solid lines). The shaded area indicates the energy range for the confined waveguide mode. In Fig. 5(b), we show the corresponding results for ZZ and AC GNRs.

Focusing first on the conductances for the pristine systems (solid lines), we observe that the ZZ and AC oriented GAL waveguides have a similar conductance in the energy range of the waveguide mode. The high conductances $G \sim 1.5\,G_0$ show that there is a relatively good electronic coupling between the GAL waveguide and the graphene leads. The metallic ZZ GNR is conducting at all energies, but the conductance saturates at a value close to unity. In the energy range of the waveguide mode, the GAL waveguides thus have a higher conductance than both of the GNRs. Turning to the results for the disordered systems we observe that the GAL waveguides retain relatively high conductances. The ZZ and AC orientations show comparable reductions in the conductance due to disorder. The ZZ GNR is less affected by disorder, while the AC GNR conductance is significantly reduced except at the lowest energies. We conclude that the GAL waveguides appear to be relatively robust against structural disorder and in general have higher conductances than the corresponding GNR systems.

E. Waveguide bends

As mentioned earlier, the waveguides introduced in this paper are closely analogous to photonic crystal waveguides. In such structures, light can be guided through bends in the waveguide with very little radiation loss.[19] Relying on this analogy, we expect GAL waveguides to show a similar

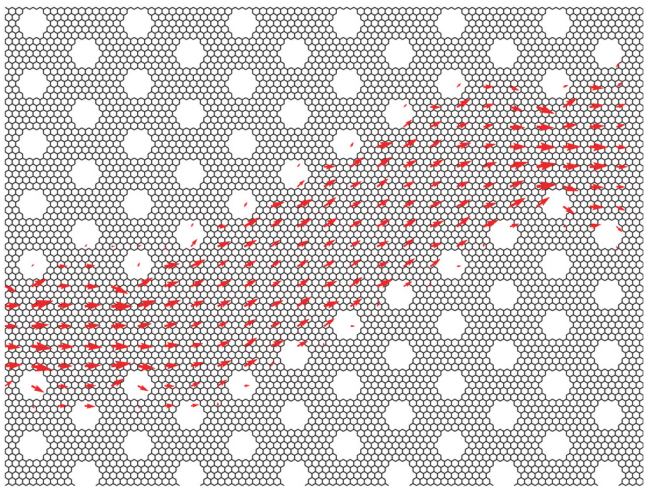

FIG. 6. (Color online) Bond current through a "kinked" $\{5,2\}_1^{(zz)}$ GAL waveguide. The current is calculated at energy $E = 0.25$ eV with a transmission of $\mathcal{T} = 1.9$. The current is highly confined to the waveguide region and no additional reflections are observed due to the kinks.

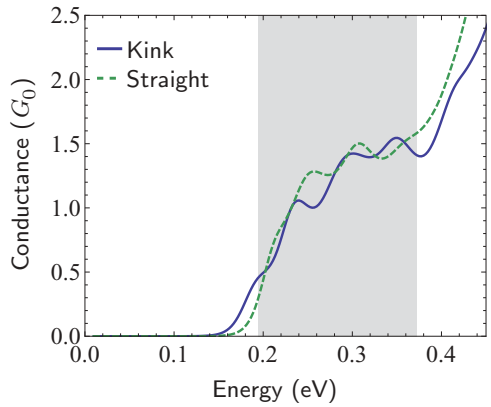

FIG. 7. (Color online) Conductances of the "kinked" waveguide shown in Fig. 6 (straight line) and of a straight waveguide of similar length (dashed line). The shaded area indicates the energy range of the confined waveguide mode of the straight waveguide. Note the nearly identical conductances of the two systems.

robustness to kinks along the waveguide. To illustrate the localization of the electronic state and the guiding properties of the GAL waveguide we show the local current through the waveguide in Fig. 6. Similar to the results of Fig. 5, the waveguide structure is connected on both sides to semi-infinite bulk graphene leads, not included in the figure. The left going bond current (per unit energy) in the presence of an infinitesimal bias voltage is calculated from the left scattering state spectral function $A_{L,ij}$ and the hopping matrix elements H_{ij} from the TB Hamiltonian. Between atom i and j the local current is $A_{L,ij}\,H_{ij}$.[33] To visualize the current on the given scale the current running away from each atom was calculated and averaged over an applied mesh. The illustrated average current thus cannot be assigned to the individual atoms anymore, which is the reason why current appears to occur within the holes in the figure. Since the k-averaged transmission only changes slightly from the Γ-point result, we use the Γ-point scattering states. Figure 6 clearly illustrates the confinement of the current to the waveguide region and the robustness against kinks.

To further illustrate the strong guiding properties of GAL waveguides, we show in Fig. 7 the conductance of the waveguide bend illustrated in Fig. 6. A similar method was used as that for the results of Fig. 5. For comparison, we also show the corresponding conductance through a waveguide generated by omitting the kink in Fig. 6 and instead having the waveguide run straight through. These results show that, while there are small differences between the two structures in the oscillations of the conductance, overall the introduction of a kink has almost no consequence on the conductance through the GAL waveguide. Very low reflection loss is thus introduced by the kink, despite the fact that the waveguide alternates between zigzag and armchair orientations. We note that we have found similar results for slightly different waveguide structures.

V. DISCUSSION AND SUMMARY

The GAL waveguide systems studied in this paper represent idealized structures, which may be challenging to realize experimentally due to the small hole sizes. However, the applicability of the Dirac model allows for simulations of arbitrarily large structures. Moreover, the Dirac model can equally well be applied to other gapped graphene systems, where the band gap is not induced through periodic holes, but, e.g., via periodically absorbed hydrogen.[20] Although the Dirac and TB models applied in this work are very simple, previous studies of pure GALs have shown that both the Dirac and TB models reproduce the trends obtained from more accurate density-functional theory calculations.[34] In any case, the concept of a GAL waveguide depends only on the existence of a band gap in the GAL region and not on the specific details, and we believe our simplified models capture the correct physics.

In summary, we have introduced GAL waveguides. The band structures of GAL waveguides have been modeled with the Dirac model including a mass term, which is shown to be in excellent agreement with an atomistic tight-binding model. We have shown that GAL waveguides support modes which are highly confined to the waveguide region and are robust against structural disorder and kinks in the waveguide. In transport calculations, we find that GAL waveguides have higher conductances than corresponding graphene nanoribbons. A further advantage of the surrounding GAL may be that it will mechanically stabilize the structure and be able to carry some of the generated Joule heat away from the device. GAL waveguides may thus be an attractable way of realizing electronic wires in integrated graphene circuits.

ACKNOWLEDGMENTS

The work by J.G.P. is financially supported by the Danish Council for Independent Research, FTP Grants No. 11-105204 and No. 11-120941. T.M. acknowledges support from the Danish Council for Independent Research, FTP Grants No. 11-104592 and No. 11-120938. The Center for Nanostructured Graphene is sponsored by the Danish National Research Foundation.

[1] K. S. Novoselov, A. K. Geim, S. V. Morozov, D. Jiang, Y. Zhang, S. V. Dubonos, I. V. Grigorieva, and A. A. Firsov, Science **306**, 666 (2004).
[2] A. H. Castro Neto, F. Guinea, N. M. R. Peres, K. S. Novoselov, and A. K. Geim, Rev. Mod. Phys. **81**, 109 (2009).
[3] S. V. Morozov, K. S. Novoselov, M. I. Katsnelson, F. Schedin, D. C. Elias, J. A. Jaszczak, and A. K. Geim, Phys. Rev. Lett. **100**, 016602 (2008).
[4] A. K. Geim and K. S. Novoselov, Nat. Mater. **6**, 183 (2007).
[5] Y.-M. Lin, C. Dimitrakopoulos, K. A. Jenkins, D. B. Farmer, H.-Y. Chiu, A. Grill, and P. Avouris, Science **327**, 662 (2010).
[6] S. Bae *et al.*, Nat. Nanotech. **5**, 574 (2010).
[7] A. R. Botello-Méndez, E. Cruz-Silva, J. M. Romo-Herrera, F. López-Urías, M. Terrones, B. G. Sumpter, H. Terrones, J.-C. Charlier, and V. Meunierz, Nano Lett. **11**, 3058 (2011).
[8] K. Nakada, M. Fujita, G. Dresselhaus, and M. S. Dresselhaus, Phys. Rev. B **54**, 17954 (1996).
[9] L. Brey and H. A. Fertig, Phys. Rev. B **73**, 235411 (2006).

[10]J. Lahiri, Y. Lin, P. Bozkurt, I. I. Oleynik, and M. Batzill, Nat. Nanotechnol. **5**, 326 (2010).
[11]M. I. Katsnelson, K. S. Novoselov, and A. K. Geim, Nat. Phys. **2**, 620 (2006).
[12]J. R. Williams, T. Low, M. S. Lundstrom, and C. M. Marcus, Nat. Nanotech. **6**, 222 (2011).
[13]G. W. Semenoff, Phys. Rev. Lett. **53**, 2449 (1984).
[14]T. G. Pedersen, C. Flindt, J. Pedersen, N. A. Mortensen, A.-P. Jauho, and K. Pedersen, Phys. Rev. Lett. **100**, 136804 (2008).
[15]J. Eroms and D. Weiss, New J. Phys. **11**, 095021 (2009).
[16]M. Begliarbekov, O. Sul, J. Santanello, N. Ai, X. Zhang, E.-H. Yang, and S. Strauf, Nano Lett. **11**, 1254 (2011).
[17]M. Kim, N. S. Safron, E. Han, M. S. Arnold, and P. Gopalan, Nano Lett. **10**, 1125 (2010).
[18]J. Bai, X. Zhong, S. Jiang, Y. Huang, and X. Duan, Nat. Nanotech. **5**, 190 (2010).
[19]A. Chutinan and S. Noda, Phys. Rev. B **62**, 4488 (2000).
[20]R. Balog *et al.*, Nat. Mater. **9**, 315 (2010).
[21]A. Lopez-Bezanilla and S. Roche, Phys. Rev. B **86**, 165420 (2012).
[22]R. Quhe *et al.*, NPG Asia Materials **4**, e6 (2012).
[23]R. Petersen, T. G. Pedersen, and A.-P. Jauho, ACS Nano **5**, 523 (2011).
[24]A. R. Akhmerov and C. W. J. Beenakker, Phys. Rev. B **77**, 085423 (2008).
[25]T. G. Pedersen, A.-P. Jauho, and K. Pedersen, Phys. Rev. B **79**, 113406 (2009).
[26]M. V. Berry, Proc. R. Soc. London A **413**, 183 (1987).
[27]L. Brey and H. A. Fertig, Phys. Rev. B **73**, 195408 (2006).
[28]T. Gunst, T. Markussen, A.-P. Jauho, and M. Brandbyge, Phys. Rev. B **84**, 155449 (2011).
[29]F.-M. Zhang, Y. He, and X. Chen, Appl. Phys. Lett. **94**, 212105 (2009).
[30]J. Pedersen, C. Flindt, N. A. Mortensen, and A.-P. Jauho, Phys. Rev. B **77**, 045325 (2008).
[31]T. Markussen, R. Rurali, M. Brandbyge, and A.-P. Jauho, Phys. Rev. B **74**, 245313 (2006).
[32]M. P. L. Sacho, J. M. L. Sancho, and J. Rubio, J. Phys. F **14**, 1205 (1984).
[33]T. N. Todorov, J. Phys.: Condens. Matter **14**, 3049 (2002).
[34]J. A. Fürst, J. G. Pedersen, C. Flindt, N. A. Mortensen, M. Brandbyge, T. G. Pedersen, and A.-P. Jauho, New J. Phys. **11**, 095020 (2009).

Paper V

Jesper T. Rasmussen, Tue Gunst, Peter Bøggild, Antti-Pekka Jauho and Mads Brandbyge

Electronic and transport properties of kinked graphene

Beilstein Journal of Nanotechnology **4**, 103-110 (2013)

Beilstein Journal of Nanotechnology

Electronic and transport properties of kinked graphene

Jesper Toft Rasmussen, Tue Gunst, Peter Bøggild, Antti-Pekka Jauho and Mads Brandbyge*

Full Research Paper

Open Access

Address:
Center for Nanostructured Graphene (CNG), Department of Micro- and Nanotechnology (DTU Nanotech), Technical University of Denmark, DK-2800 Kongens Lyngby, Denmark

Email:
Mads Brandbyge* - mads.brandbyge@nanotech.dtu.dk

* Corresponding author

Keywords:
adsorption and reactivity; curvature effects; DFT calculations; electronic transport; graphene nanoribbons; graphene nanostructuring

Beilstein J. Nanotechnol. **2013,** *4,* 103–110.
doi:10.3762/bjnano.4.12

Received: 13 December 2012
Accepted: 31 January 2013
Published: 15 February 2013

This article is part of the Thematic Series "Physics, chemistry and biology of functional nanostructures".

Guest Editors: P. Ziemann and T. Schimmel

Abstract

Local curvature, or bending, of a graphene sheet is known to increase the chemical reactivity presenting an opportunity for templated chemical functionalisation. Using first-principles calculations based on density functional theory (DFT), we investigate the reaction barrier reduction for the adsorption of atomic hydrogen at linear bends in graphene. We find a significant barrier lowering (≈15%) for realistic radii of curvature (≈20 Å) and that adsorption along the linear bend leads to a stable linear kink. We compute the electronic transport properties of individual and multiple kink lines, and demonstrate how these act as efficient barriers for electron transport. In particular, two parallel kink lines form a graphene pseudo-nanoribbon structure with a semimetallic/semiconducting electronic structure closely related to the corresponding isolated ribbons; the ribbon band gap translates into a transport gap for electronic transport across the kink lines. We finally consider pseudo-ribbon-based heterostructures and propose that such structures present a novel approach for band gap engineering in nanostructured graphene.

Introduction

Nanostructures based on graphene have an enormous potential for applications. Especially in future electronic devices compatible with and extending silicon technology, due to the outstanding electronic transport properties of graphene [1]. However, it is crucial to modify the semimetallic electronic structure of graphene to exploit its full potential for many electronic applications: a band gap can be introduced by nanostructuring graphene.

A common approach towards engineering the electronic structure is to form quasi-1D graphene in the form of nanoribbons (GNR) [2]. The electronic structure of GNRs depends on width,

direction and edge structure – all parameters that to some degree can be controlled. GNRs can be formed by etching [2], by unzipping carbon nanotubes (CNTs) [3], or ultimately be grown with atomic-scale precision by using self-assembly of precursor molecules on metal substrates [4]. However, for electronic applications this approach requires a structure-preserving means of releasing and transferring the structures to an insulating substrate. Bonding of H or other species to graphene with large coverage opens an insulating band gap at the adsorption sites due to sp^3 hybridisation [5]. Periodically ordered clusters of adsorbed hydrogen can be formed on graphene in patterns dictated by the Moiré lattice mismatch between graphene and the metal substrate, which opens a semiconducting band gap [6]. Finally, regular perforations, known as a graphene antidot lattice (GAL) [7], or a nanoscale mesh of holes [8-10] can have neck widths [10,11] down to 5 nm corresponding to band gaps of the order of 1 eV [2].

Graphene consists entirely of surface atoms and is thus exceedingly sensitive to the surroundings. In particular, the van der Waals (vdW) interaction with the substrate is of importance. The substrate interactions, which make graphene cling to small features, may be exploited by manufacturing nanostructures in the substrate. Periodic steps in a Cu substrate has been used to induce "wrinkles" or ripples in graphene with period and height on the order of 10 nm [12]. Recently, Hicks et al. [13] demonstrated how arrays of 1D large band gap, semiconducting graphene nanoribbons corresponding to a width of ≈1.4 nm can be formed in graphene on a step-patterned SiC substrate. The substrate interactions can clamp a graphene sheet while partly suspended across small holes, so that a pressure difference between the in- and outside leads to the formation of bubbles or "blisters" in the sheet [14]. Also, linear folds, where the graphene sheet is bulging up from the substrate, have been induced for graphene suspended over trenches by using heat treatment [15]. Thus, the sheet can obtain significant bends at certain places induced by the substrate interaction, substrate nanostructuring, and subsequent treatments [16]. Calculations by Low et al. [17] showed how a sharp step of height 1 nm in a SiC substrate, comparable to experimental values [13], can induce a linear bend in the graphene sheet with a radius of curvature down to around 1 nm.

The ability to accurately control sharp local curvatures of graphene presents opportunities for strain-assisted modification of the local electronic structure and chemical reactivity in the graphene sheet, and may open a route to band gap engineered devices [13,18-21]. Very recently, Wu et al. [21] showed how graphene on a Si substrate decorated with SiO_2 nanoparticles induced local regions of strain and increased reactivity in a selective manner. Atomic hydrogen or other chemical species do not easily react with flat graphene when dosed from a single side [22]. However, at positions where there is a substantial local bending, rippling or strain of the graphene sheet the reactivity changes significantly [5,23]. So far there have been only a few theoretical studies of the atomic geometry of hydrogenated ripple structures in unsupported, strain-induced, graphene ripples [24-26]. However, to the best of our knowledge, no studies have addressed the reactivity of bends or the transport through hydrogenated ripples, or discussed the possibility of stabilising nonplanar structures by hydrogenation.

In this paper we consider the reactivity of linear bends in a graphene sheet, and the electronic transport properties of kinks resulting from the hydrogenation of bends. Our starting point is the generic graphene structure shown in Figure 1a, which is inspired by the experimental observation of trench formation [15]. The bulging of this structure results from shortening the distance between two separated, clamped regions in the sheet. The remaining sections of the paper are organised as follows: Section "System setup" describes our computational method and setup. In the subsequent section we present our results. First, we describe the adsorption barriers for the reaction with single atomic H on the graphene bend at positions with different local curvature (positions I–VIII in Figure 1a). Then we show how a linear bend transforms into a kink when decorated by H

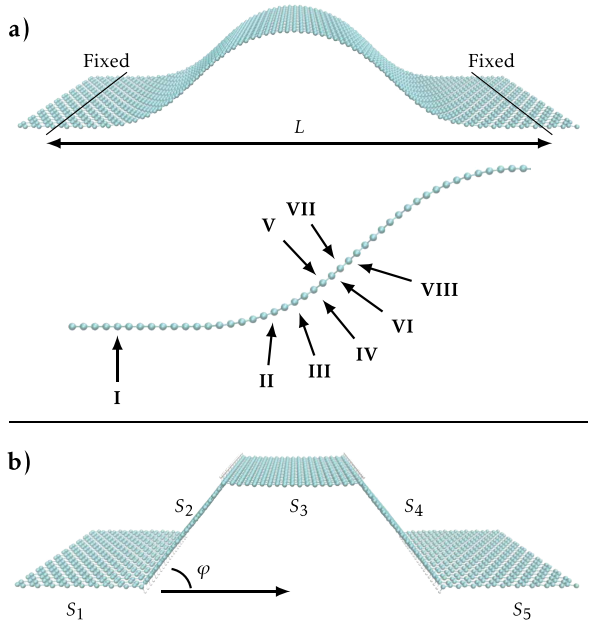

Figure 1: (a) Smooth ripple-like structure where the first and last six rows of carbon-dimers are surface-clamped regions with a separation of L = 90 Å. Atomic hydrogen is adsorbed at positions I–VIII. (b) The resulting kinked graphene structure after hydrogen is adsorbed in lines at the most reactive position (II) corresponding to the smallest local radius of curvature. The four kinks divide the structure into five sections, S_1–S_5.

along the most reactive (most curved) line (Figure 1b), and we present the electronic transmission through a single kink in the subsection "Single kink". The kink acts as an effective barrier with its transmission depending on the kink-angle, φ. In the subsection "Two kinks" we study how two parallel kinks lead to the formation of a pseudo-ribbon-type electronic structure. Finally, in subsection "Multiple kinks" we demonstrate the opening of a transport gap for multikink systems, such as the one shown in Figure 1b.

System setup

The bend we consider in Figure 1a is created along the armchair direction by fixing the first and last six rows of carbon atoms and shortening the separation L, while the rest of the atoms are allowed to relax. A separation of L = 90 Å is chosen in order to obtain realistic curvatures [17]. We first assessed the reactivity of the structure at positions with different local curvature, see positions I–VIII in Figure 1a. Subsequently we relaxed the structure where lines of hydrogen (Figure 1b) have been placed at the points of lowest radius of curvature, i.e., the points of highest local reactivity. This particular system is meant to illustrate the potential of the hydrogen adsorption mechanism, and to gain insight into the modification of the electronic properties due to the hydrogen lines. In a corresponding experimental setup we can imagine placing graphene across a trench, which allows hydrogen adsorption on either side of the sheet.

The atomic and electronic structure calculations are based on density functional theory (DFT) using the SIESTA [27] code, and the PBE-GGA exchange-correlation [28] functional. We employ periodic boundary conditions (PBC) in the direction along the bend with a cell-width of four carbon dimers, and 10 Monkhorst–Pack k-points. We use a mesh cut-off of 500 Ry throughout. When calculating reactivity in the form of reduced reaction barriers the unit-cell is chosen so that the distance between single hydrogen atoms is larger than 8.5 Å. This ensures low hydrogen–hydrogen interaction, which is known to impact reaction barriers [29]. In the total energy calculations of relaxed atomic geometries and reaction barriers, we also use PBC transverse to the bend (5 k-points). We use a TZP basis-set for hydrogen and a SZ basis for carbon, except in the reaction barrier calculations where we compare calculations using a DZP and SZP basis for the four carbon atoms nearest to the hydrogen. In the barrier determinations we furthermore use spin-polarised calculations because of unpaired electrons. For the relaxed geometries a force tolerance of 0.01 eV/Å is used, and the final energies are corrected for basis-set-superposition errors (BSSE) [30].

Based on the computed atomic and electronic structures we subsequently use the TranSIESTA [31] method to calculate the electronic conductance per unit-cell width transverse to the bend. To this end we attach semi-infinite flat graphene electrodes to each side of the selected kinks, i.e., replace sections S_1 and S_2 in Figure 1b by semi-infinite electrodes in order to calculate the transmission through the single kink separating S_1 and S_2. In the conductance calculations we employ a dense transverse k-point grid of 400 points.

Results and Discussion

Adsorption barrier

Adsorption of hydrogen on graphene involves a reaction barrier that needs to be overcome before the single hydrogen atom sticks to the graphene sheet. Several investigations based on DFT calculations show that atomic hydrogen adsorbs on-top on flat graphene with a barrier about 0.2 eV and binding energy in the range of 0.7–1.0 eV [22,32-34]. Thus a minimum kinetic energy for the first hydrogen to react [32,33] is required, in an out-of-equilibrium situation such as in an atomic beam [34]. Casolo et al. [35] calculated the reaction barrier and adsorption energy for multiple hydrogen atoms on flat graphene. In agreement with other studies they found decreased barriers to sticking for the second H atom, compared to the barrier for adsorbing a single H atom on a clean surface [36].

Here, we first focus on the trends in the change in adsorption barrier as a function of the local curvature of the graphene sheet. To this end we have considered atomic hydrogen absorption at the on-top carbon positions at points with different curvature on the bent structure, see Figure 1a (positions I–VIII). The barrier is determined by calculating the total energy for each position of hydrogen above graphene as the hydrogen is moved successively closer to the graphene. Following the adsorption investigations on flat graphene by Ivanovskaya et al. [37] we perform, in each step, a relaxation of the hydrogen-bonded carbon atom and its three nearest neighbours. Using the method described above we obtain a reaction barrier of 0.22 eV on locally flat graphene. This is comparable to results obtained by several groups using DZP or plane wave basis sets and the PW91 functional [22,29,32,33]. We find that a SZP basis set for the relaxed carbon atoms yields a reduced barrier height of 0.18 eV (both basis sets with orbital range corresponding to an energy shift of 0.01 eV). Hence, we use the SZP basis in the following reaction-barrier calculations in order to lower the computation time.

For the positions (I-VIII) we obtain the reaction barrier for adsorption of hydrogen as a function of the local radius of curvature (RoC) shown in Figure 2. The second least curved position (VIII), resulting in a large RoC, reduces the barrier by roughly 3% compared to flat graphene (position I). The most curved position (II) in our considered structure has a minimum

RoC of ≈20 Å resulting in a barrier reduction of roughly 16%. For comparison, this RoC roughly corresponds to the radius of a (25,25) nanotube. Experiments by Ruffieux et al. [38] compare hydrogen adsorption on C_{60} molecules, CNTs, and graphite to show that reactivity is increased with curvature. In our case we find that the local electronic density of states changes little for the atoms on the pristine bent graphene sheet (as in Figure 1a). Thus, we conclude that the lowering of the adsorption barrier for the moderate RoC of about 20 Å is mainly due to the mechanical strain in the bend shifting the carbon atoms out of the graphene plane in the direction of the hydrogen. We note that an additional increase in reactivity may result from the change in electronic structure for highly bent graphene. Thus, we expect an increase in reactivity for the graphene with a linear bend, and a simple Arrhenius estimate using our data yields a factor of 3–4 at room temperature (300 K). We have also performed calculations using the less rigorous DFTB method [39] and obtained results in agreement with the trend in reaction-barrier reduction obtained above.

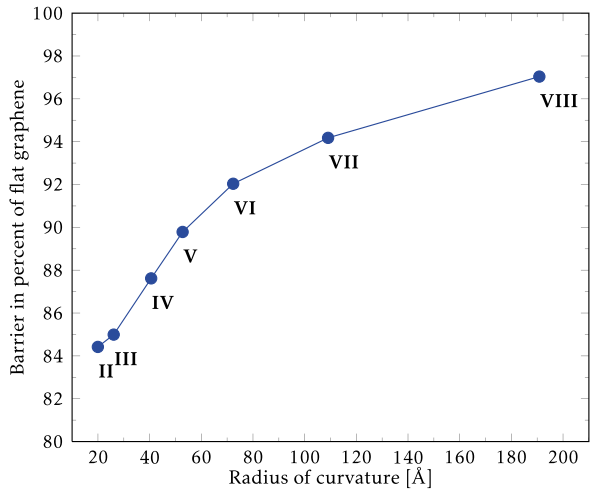

Figure 2: Calculated reaction barriers for hydrogenation of bent graphene as a function of the local radius of curvature (II–VIII in Figure 1a). Flat graphene (position I) has an infinite radius of curvature and is used to normalise the barriers. Calculations are spin-polarised and allow for atomic relaxation.

We may understand the reaction barrier and its change with curvature by considering the changes in carbon bond lengths. The barrier is due to the fact that the reacting carbon atom has to be pulled out of the graphene plane, stretching the strong carbon–carbon bonds, when reacting with the incoming hydrogen atom. When the graphene sheet is curved the carbon atom is already slightly out of the plane, and thus the energy required to pull the atom further out of plane is decreased compared to flat graphene. The ortho- and para-locations in the graphene hexagon have been shown to be the preferred locations for hydrogen adsorption in studies of flat graphene [22,29,40]. With this in mind as well as the curvature-related reduction of reaction barriers, we conclude that the considered system allows the adsorption of hydrogen atoms in single lines along armchair-edges. The kink in the atomic structure due to the sp^3-binding of a single H makes the graphene curve even more in its vicinity, which in turn, preferentially lowers the barrier for absorption of a H along the linear bend. This suggests a mechanism in which the hydrogen adsorption is propagating and leads to the decoration of the entire linear bend turning it into a kink line. It may be viewed as analogous to crack-formation mechanisms, where the breaking of a bond increases the stress on neighbouring bonds; only in this case, the graphene is hydrogenated rather than broken or destroyed.

Single kink

Next, we examine the energetic and transport properties of kink-lines in the armchair direction. We first consider a single kink with angle φ, e.g., between sections S_1 and S_2 in Figure 1b. The kink-angle φ is varied in the range 0°…90°, while the three nearest unit cells on each side of the kink are allowed to relax. The total energy per H is shown as a function of φ in the inset of Figure 3, showing a minimum energy for φ ≈ 50°. This angle roughly corresponds to the angle in an sp^3 configuration where 2φ = 109.5°. The adsorption of H causes local changes in the geometry, i.e., only the carbon atoms very close to the kink are moved, while the remaining structure remains unperturbed. For this reason, the adsorption of hydrogen atoms can be considered as a process that locally pins the bend.

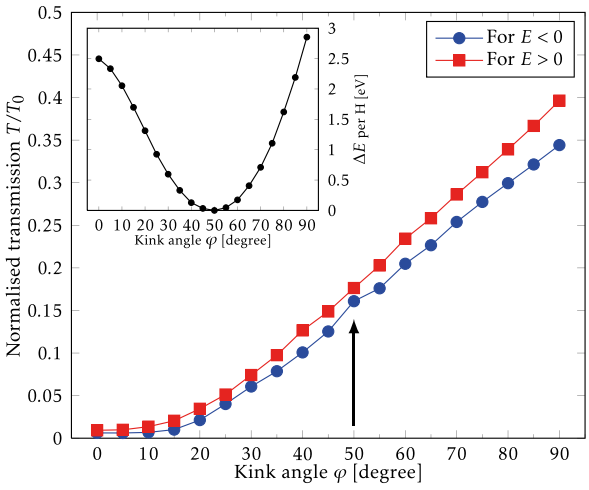

Figure 3: Electronic transmission through a single kink normalised by the transmission of pristine graphene (T_0) as a function of the kink angle, φ, for electrons ($E > 0$) and holes ($E < 0$). The arrow indicates the normalised transmission at the equilibrium angle determined from the total energy calculations shown in the inset.

The electron transmission per unit-cell width is linear in energy for pristine graphene in a energy range around the charge neutrality point ($E = 0$), e.g., $T_0 \propto E$. We find similarly that the calculated kink-transmission curves are also linear, and therefore we express the results for the transmissions in terms of the roughly energy-independent ratio $T/T_0 = \text{const}$. The kink breaks the electron–hole symmetry, and we fit $E > 0$ and $E < 0$ separately, as shown in Figure 3. Larger kink angles result in an increase in the overall transmission, which may be attributed to a better π-orbital overlap across the kink. For the equilibrium angle, φ = 50°, the ratio T/T_0 is close to 0.17 in both regions (indicated by the arrow in Figure 3), corresponding to a transmission reduction of 83%. Thus, we see that the hydrogen-induced kinks in graphene can be used to form effective electron barriers. We now turn to the effect of multiple barriers and periodic kink structures in order to examine resonant tunnelling phenomena and band gap formation.

Two kinks

Band-structure calculations show that periodic nanoscale rippling of the graphene is not sufficient to create a band gap [24] due to the low scattering by the elastic deformation [17]. In contrast, periodic arrangements of adsorbed hydrogen can indeed induce a semiconducting band gap [24,26]. The electronic band structures of hydrogen lines on flat graphene have been examined by Chernozatonskii et al. [25,26], and recently also for nanoscale-rippled graphene [24]. Here we show how two parallel kinks lead to a local electronic structure that resembles that of an isolated GNR between the kinks. Such structures could be produced experimentally by using the techniques described by Pan et al. [12]. Hydrogen-terminated armchair GNRs are semiconducting but have a small energy gap when the width in atomic lines is $N = 3L - 1$, where L is an integer [41]. In Figure 4 we compare the electronic bandstructure for armchair GNRs (aGNRs) (left panel) to the electronic transmission through two kinks separated by the corresponding aGNR width (right panel). In the present case the initial width (or, kink separation) is $N = 17$ atomic lines of carbon, which shows a semimetallic behaviour in the transmission spectrum with a small transport gap. In accordance with isolated aGNRs the next two widths $N = 18$, 19 are semiconducting, while the last investigated width $N = 20$ is semimetallic again (not shown). The close correspondence between the electronic band structure for the GNR and the transmission gap for the double-kink system allows us to consider the structure between two kinks as a pseudo-ribbon.

For the semiconducting pseudo-ribbons transport gaps surrounded by van Hove-type 1D behaviour are seen in the transmission functions (Figure 4, right panel). The transport gaps, $E_{\text{gap}} = 0.4$ eV and $E_{\text{gap}} = 0.5$ eV, are in reasonable agreement with the power-law scaling of E_{gap} with width found for aGNRs [41]. We note that the pseudo-ribbon breaks the electron–hole symmetry: For the $N = 18$ case a larger van Hove resonance is seen at the valence band edge, while for $N = 19$ a larger resonance is seen at the conduction band edge. There are small transmission values within the electronic band gap due to leakage through the barriers, which we expect to introduce shifts in the energies between the real and pseudo aGNR.

Multiple kinks

In order to illustrate the behaviour of systems with more kinks we consider a system consisting of four hydrogen-induced kinks, as illustrated in Figure 1b and Figure 5. The sections S_1/S_5 are now replaced by left/right infinite-lead structures, and the "top" S_3 pseudo-ribbon is connected to the leads via the "side" S_2, S_4 pseudo-ribbons. We keep S_2, S_3 identical for simplicity and determine the transmission across the kinks (in the z-direction in Figure 5), which is experimentally more feasible. We now investigate how the different sections influ-

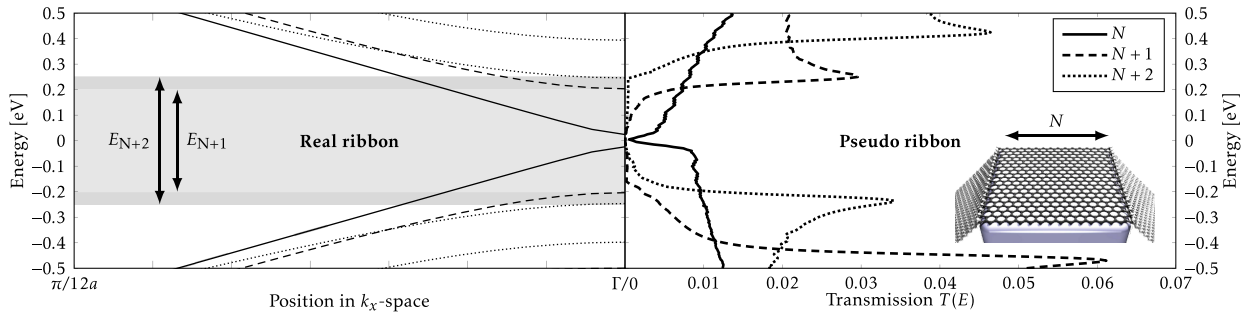

Figure 4: (Left) Band structures for H-passivated armchair ribbons with varying width, N. The ribbons are a zero-gap semiconductor, a semiconductor with band gap $E_{N+1} = 0.4$ eV, and a semiconductor with band gap $E_{N+2} = 0.5$ eV for widths N, $N + 1$, $N + 2$, respectively. All widths are based on the number of carbon atom lines $N = 17$. The band gaps are indicated by arrows and are highlighted. (Right) The electronic transmission functions for the corresponding pseudo-ribbons, i.e., across two parallel kinks of varied separation as shown in the inset.

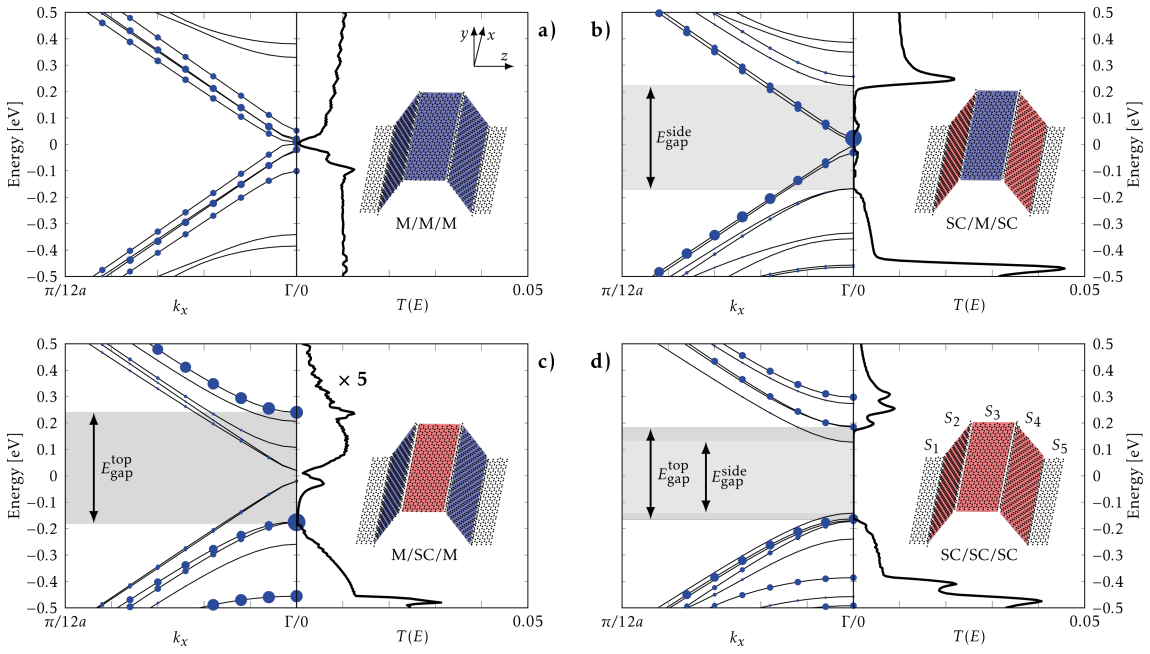

Figure 5: Projected band structure and transmission through structures with multiple kinks. The top (section S_3) and connecting pseudo-ribbons (sections S_2/S_4) are varied in width, changing their electronic properties. The projected band structure along the pseudo-ribbons (i.e., k_x) is shown by using filled circles with radii proportional to the weight on section S_3. Semimetallic (M) pseudo-ribbons corresponding to N = 17 are shown in blue, while semiconducting (SC) ribbons of width N + 1 are shown in red. Band gaps of the top sections E_{gap}^{top} and connecting sections E_{gap}^{side} are highlighted. These are E_{gap}^{side} = 0.39 eV (b), E_{gap}^{top} = 0.42 eV (c), and E_{gap}^{top} = 0.35 eV, E_{gap}^{side} = 0.27 eV (d). The transmission $T(E)$ (per simple transverse unitcell) is determined across all kinks in the z-direction, and transmission gaps comparable to the band gaps are observed in subfigures b and d.

ence the total transport for the four possible combinations of semiconducting (SC) and semimetallic (M), corresponding to the pseudo-ribbon widths N, N + 1 used in Figure 4.

In order to analyse the transmission we single out the band structure projected on to the top section, S_3 (excluding carbon and hydrogen atoms at the kink), in the band structure along the pseudo-ribbon direction. The weight on S_3 is represented by a circle of radius R_{nk},

$$R_{nk} \propto \sum_{i \in S_3} \left|\Psi\left(n, k_x, i\right)\right|^2. \qquad (1)$$

Here Ψ is the wave function at k_x (k_z = 0) with n (i) being the band (orbital) index. The obtained projected band structures are shown in the left parts of each subfigure in Figure 5. Generally, some bands have no weight (no circles), while others have significant weight indicating that there is little mixing between the orbitals from section S_3 and other sections.

In Figure 5a and Figure 5b we consider pseudo-ribbons with semimetallic top regions, namely S_2/S_3/S_4 being M/M/M and SC/M/SC, respectively. For the all-metal pseudo-ribbons, M/M/M, an almost energy-independent transmission function is seen with a transmission close to that of the metallic double-kink in the previous subsection. The SC/M/SC structure shows a transport gap similar to that of the single SC pseudo-ribbon with van Hove resonances, while the S_3-projected band structure reveals isolated metallic states within the gap. We note that the transmission at the resonances for the SC/M/SC structure is larger than the corresponding M/M/M transmission. For the case of semiconducting top pseudo-ribbons in Figure 5c and Figure 5d, we note that M/SC/M show a greatly reduced transport gap compared to the single pseudo-ribbon case (also, note the scaling of the transmission axis), while the SC/SC/SC structure shows a complete extinction of the transmission in the electronic gap, as expected. Generally, we find that the main behaviour of the transmission is controlled by the connecting sections S_2, S_4, i.e., there is a good correspondence between the side section band gaps E_{gap}^{side} and the transmission gaps.

Conclusion

The presented investigations show that linear kink-line structures may form in graphene by reacting with atomic hydrogen along a linear bend in the sheet. The adsorption barrier is lowered in the close vicinity of the bend, which can be exploited to form the kink. In particular, we have shown that a radius of curvature of ≈20 Å reduces the hydrogen adsorption barrier by roughly 16% compared to H adsorption on pristine

graphene. The calculations suggest that once a single hydrogen atom has been adsorbed, the induced local kink and resulting increase in local curvature makes it easier for the following H to adsorb, thus creating a propagating kink formation. A full line of hydrogen atoms pins the structure and divides the electronic systems into different regions. We have shown that the electronic transmission through a single kink is reduced by 83% compared to pristine graphene, meaning that the kink-line acts as an efficient barrier for electron motion. We have demonstrated how two close-by parallel kinks form a pseudo graphene nanoribbon with similar behaviour of the electronic structure to that for isolated nanoribbons. The transmission function displays transport gap features corresponding to the isolated nanoribbon band gaps.

The present work thus suggests that it may be feasible to template functional electronic nanostructures by using the conformation of graphene, e.g., to the substrate, and that this in turn induce changes in local reactivity. Our work clearly calls for extensions in a number of directions. First of all more calculations are needed in order to investigate the kink-line propagation reaction proposed by our results. To this end it is important to include a realistic description of the actual substrate. It is also interesting to consider other adsorbate species, possibly introducing doping of the pseudo-ribbons and electronic gating. Finally, decoration and pinning of the edges of other geometries such as “bubbles” or “blisters” is of interest, e.g., in order to produce GAL-like structures [7] without perforating the graphene sheet. Calculations have shown how the adsorption of hydrogen is correlated over a length scale involving several of the unit cells employed in this work [22,35,42,43]. Thus the adatom–adatom interaction will play a significant role in the kink-line propagation along the step and will be addressed in a future study.

Acknowledgements

We appreciate helpful discussion with Dr. H. Sevinçli. We thank the Danish Center for Scientific Computing (DCSC) for providing computer resources. The Center for Nanostructured Graphene is sponsored by the Danish National Research Foundation. JTR and MB thank the Lundbeck foundation for support (R95-A10510).

References

1. Novoselov, K. S.; Fal'ko, V. I.; Colombo, L.; Gellert, P. R.; Schwab, M. G.; Kim, K. *Nature* **2012,** *490,* 192–200. doi:10.1038/nature11458
2. Han, M. Y.; Özyilmaz, B.; Zhang, Y.; Kim, P. *Phys. Rev. Lett.* **2007,** *98,* 206805. doi:10.1103/PhysRevLett.98.206805
3. Xie, L.; Wang, H.; Jin, C.; Wang, X.; Jiao, L.; Suenaga, K.; Dai, H. *J. Am. Chem. Soc.* **2011,** *133,* 10394–10397. doi:10.1021/ja203860a
4. Cai, J.; Ruffieux, P.; Jaafar, R.; Bieri, M.; Braun, T.; Blankenburg, S.; Muoth, M.; Seitsonen, A. P.; Saleh, M.; Feng, X.; Müllen, K.; Fasel, R. *Nature* **2010,** *466,* 470–473. doi:10.1038/nature09211
5. Elias, D. C.; Nair, R. R.; Mohiuddin, T. M. G.; Morozov, S. V.; Blake, P.; Halsall, M. P.; Ferrari, A. C.; Boukhvalov, D. W.; Katsnelson, M. I.; Geim, A. K.; Novoselov, K. S. *Science* **2009,** *323,* 610–613. doi:10.1126/science.1167130
6. Balog, R.; Jørgensen, B.; Nilsson, L.; Andersen, M.; Rienks, E.; Bianchi, M.; Fanetti, M.; Lægsgaard, E.; Baraldi, A.; Lizzit, S.; Sljivancanin, Z.; Besenbacher, F.; Hammer, B.; Pedersen, T. G.; Hofmann, P.; Hornekær, L. *Nat. Mater.* **2010,** *9,* 315–319. doi:10.1038/NMAT2710
7. Pedersen, T. G.; Flindt, C.; Pedersen, J.; Mortensen, N. A.; Jauho, A.-P.; Pedersen, K. *Phys. Rev. Lett.* **2008,** *100,* 136804. doi:10.1103/PhysRevLett.100.136804
8. Kim, M.; Safron, N. S.; Han, E.; Arnold, M. S.; Gopalan, P. *Nano Lett.* **2010,** *10,* 1125–1131. doi:10.1021/nl9032318
9. Liang, X.; Jung, Y.-S.; Wu, S.; Ismach, A.; Olynick, D. L.; Cabrini, S.; Bokor, J. *Nano Lett.* **2010,** *10,* 2454–2460. doi:10.1021/nl100750v
10. Bai, J.; Zhong, X.; Jiang, S.; Huang, Y.; Duan, X. *Nat. Nanotechnol.* **2010,** *5,* 190–194. doi:10.1038/NNANO.2010.8
11. Shimizu, T.; Nakamura, J.; Tada, K.; Yagi, Y.; Haruyama, J. *Appl. Phys. Lett.* **2012,** *100,* 023104. doi:10.1063/1.3675547
12. Pan, Z.; Liu, N.; Fu, L.; Liu, Z. *J. Am. Chem. Soc.* **2011,** *133,* 17578–17581. doi:10.1021/ja207517u
13. Hicks, J.; Tejeda, A.; Taleb-Ibrahimi, A.; Nevius, M. S.; Wang, F.; Shepperd, K.; Palmer, J.; Bertran, F.; Le Fèvre, P.; Kunc, J.; de Heer, W. A.; Berger, C.; Conrad, E. H. *Nat. Phys.* **2013,** *9,* 49–54. doi:10.1038/nphys2487
14. Bunch, J. S.; Dunn, M. L. *Solid State Commun.* **2012,** *152,* 1359–1364. doi:10.1016/j.ssc.2012.04.029
15. Bao, W.; Miao, F.; Chen, Z.; Zhang, H.; Jang, W.; Dames, C.; Lau, C. N. *Nat. Nanotechnol.* **2009,** *4,* 562–566. doi:10.1038/nnano.2009.191
16. Neek-Amal, M.; Peeters, F. M. *Phys. Rev. B* **2012,** *85,* 195445. doi:10.1103/PhysRevB.85.195445
17. Low, T.; Perebeinos, V.; Tersoff, J.; Avouris, P. *Phys. Rev. Lett.* **2012,** *108,* 096601. doi:10.1103/PhysRevLett.108.096601
18. Levy, N.; Burke, S. A.; Meaker, K. L.; Panlasigui, M.; Zettl, A.; Guinea, F.; Castro Neto, A. H.; Crommie, M. F. *Science* **2010,** *329,* 544–547. doi:10.1126/science.1191700
19. Guinea, F.; Katsnelson, M. I.; Geim, A. K. *Nat. Phys.* **2010,** *6,* 30–33. doi:10.1038/NPHYS1420
20. Ortolani, L.; Cadelano, E.; Veronese, G. P.; Degli Esposti Boschi, C.; Snoeck, E.; Colombo, L.; Morandi, V. *Nano Lett.* **2012,** *12,* 5207–5212. doi:10.1021/nl3023737
21. Wu, Q.; Wu, Y.; Hao, Y.; Geng, J.; Charlton, M.; Chen, S.; Ren, Y.; Ji, H.; Li, H.; Boukhvalov, D. W.; Piner, R. D.; Bielawski, C. W.; Ruoff, R. *Chem. Commun.* **2013,** *49,* 677–679. doi:10.1039/C2CC36747E
22. Hornekær, L.; Rauls, E.; Xu, W.; Šljivančanin, Ž.; Otero, R.; Stensgaard, I.; Lægsgaard, E.; Hammer, B.; Besenbacher, F. *Phys. Rev. Lett.* **2006,** *97,* 186102. doi:10.1103/PhysRevLett.97.186102
23. Srivastava, D.; Brenner, D. W.; Schall, J. D.; Ausman, K. D.; Yu, M.; Ruoff, R. S. *J. Phys. Chem. B* **1999,** *103,* 4330–4337. doi:10.1021/jp990882s
24. Wang, Z. F.; Zhang, Y.; Liu, F. *Phys. Rev. B* **2011,** *83,* 041403(R). doi:10.1103/PhysRevB.83.041403

25. Chernozatonskii, L. A.; Sorokin, P. B. *J. Phys. Chem. C* **2010,** *114,* 3225–3229. doi:10.1021/jp9100653
26. Chernozatonskii, L. A.; Sorokin, P. B.; Brüning, J. W. *Appl. Phys. Lett.* **2007,** *91,* 183103. doi:10.1063/1.2800889
27. Soler, J. M.; Artacho, E.; Gale, J. D.; García, A.; Junquera, J.; Ordejón, P.; Sánchez-Portal, D. *J. Phys.: Condens. Matter* **2002,** *14,* 2745–2779. doi:10.1088/0953-8984/14/11/302
28. Perdew, J. P.; Burke, K.; Ernzerhof, M. *Phys. Rev. Lett.* **1996,** *77,* 3865–3868. doi:10.1103/PhysRevLett.77.3865
29. Kerwin, J.; Jackson, B. *J. Chem. Phys.* **2008,** *128,* 084702. doi:10.1063/1.2868771
30. We note that our correction is not a proper BSSE correction, since we only calculate the energy of a relaxed (bent) graphene sheet (as in Figure 1a) with nearby hydrogen ghost atoms, instead of the graphene structure relaxed in the presence of hydrogen. Our analyses show that this simpler approach underestimates the found reaction barriers by a few tens of meV.
31. Brandbyge, M.; Mozos, J.-L.; Ordejón, P.; Taylor, J.; Stokbro, K. *Phys. Rev. B* **2002,** *65,* 165401. doi:10.1103/PhysRevB.65.165401
32. Jeloaica, L.; Sidis, V. *Chem. Phys. Lett.* **1999,** *300,* 157–162. doi:10.1016/S0009-2614(98)01337-2
33. Sha, X.; Jackson, B. *Surf. Sci.* **2002,** *496,* 318–330. doi:10.1016/S0039-6028(01)01602-8
34. Xia, Y.; Li, Z.; Kreuzer, H. J. *Surf. Sci.* **2011,** *605,* L70–L73. doi:10.1016/j.susc.2011.07.009
35. Casolo, S.; Løvvik, O. M.; Martinazzo, R.; Tantardini, G. F. *J. Chem. Phys.* **2009,** *130,* 054704. doi:10.1063/1.3072333
36. Šljivančanin, Z.; Rauls, E.; Hornekær, L.; Xu, W.; Besenbacher, F.; Hammer, B. *J. Chem. Phys.* **2009,** *131,* 084706. doi:10.1063/1.3187941
37. Ivanovskaya, V. V.; Zobelli, A.; Teillet-Billy, D.; Rougeau, N.; Sidis, V.; Briddon, P. R. *Eur. Phys. J. B* **2010,** *76,* 481–486. doi:10.1140/epjb/e2010-00238-7
38. Ruffieux, P.; Gröning, O.; Bielmann, M.; Mauron, P.; Schlapbach, L.; Gröning, P. *Phys. Rev. B* **2002,** *66,* 245416. doi:10.1103/PhysRevB.66.245416
39. Aradi, B.; Hourahine, B.; Frauenheim, T. *J. Phys. Chem. A* **2007,** *111,* 5678–5684. doi:10.1021/jp070186p
40. Šljivančanin, Z.; Andersen, M.; Hornekær, L.; Hammer, B. *Phys. Rev. B* **2011,** *83,* 205426. doi:10.1103/PhysRevB.83.205426
41. Barone, V.; Hod, O.; Scuseria, G. E. *Nano Lett.* **2006,** *6,* 2748–2754. doi:10.1021/nl0617033
42. Buchs, G.; Krasheninnikov, A.; Ruffieux, P.; Gröning, P.; Foster, A. S.; Nieminen, R. M.; Gröning, O. *New J. Phys.* **2007,** *9,* 275. doi:10.1088/1367-2630/9/8/275
43. Boukhvalov, D.; Katsnelson, M.; Lichtenstein, A. I. *Phys. Rev. B* **2008,** *77,* 035427. doi:10.1103/PhysRevB.77.035427

License and Terms

The definitive version of this article is the electronic one which can be found at:
doi:10.3762/bjnano.4.12

Paper VI

Tue Gunst, Jing-Tao Lü, Per Hedegård and Mads Brandbyge

Phonon excitation and instabilities in biased graphene nanoconstrictions

Phys. Rev. B, Rapid Comm., **88**, 161401(R) (2013)

PHYSICAL REVIEW B **88**, 161401(R) (2013)

Phonon excitation and instabilities in biased graphene nanoconstrictions

Tue Gunst,[1,*] Jing-Tao Lü,[1,2,†] Per Hedegård,[2] and Mads Brandbyge[1]

[1]*Department of Micro- and Nanotechnology (DTU Nanotech), Center for Nanostructured Graphene (CNG), Technical University of Denmark, DK-2800 Kgs. Lyngby, Denmark*

[2]*Niels Bohr Institute, Nano-Science Center, University of Copenhagen, Universitetsparken 5, 2100 Copenhagen Ø, Denmark*

(Received 9 May 2013; published 11 October 2013)

We investigate how a high current density perturbs the phonons in a biased graphene nanoconstriction coupled to semi-infinite electrodes. The coupling to electrode phonons, electrode electrons under bias, Joule heating, and current-induced forces is evaluated using first principles density functional theory and nonequilibrium Green's function calculations. We observe a strongly nonlinear heating of the phonons with bias and breakdown of the harmonic approximation when the Fermi level is tuned close to a resonance in the electronic structure of the constriction. This behavior is traced back to the presence of negatively damped phonons driven by the current. The effects may limit the stability and capacity of graphene nanoconstrictions to carry high currents.

DOI: 10.1103/PhysRevB.88.161401 PACS number(s): 63.22.Rc, 72.80.Vp, 72.10.Di, 46.32.+x

Graphene has emerged as a highly attractive material for future electronic devices.[1,2] It can sustain current densities six orders of magnitude larger than copper and is foreseen to be a versatile material with numerous applications in nanoelectronics, spintronics, and nanoelectromechanics.[3] In graphene nanoconstrictions (GNCs) the current is passed through a short ribbon[4,5] at the narrowest point. Constrictions and nanoribbons provide semiconducting interconnects in graphene nanocircuitry,[6,7] and is a central building block of graphene-based nanoelectronics. Related structures include graphene antidot lattices,[8,9] which can be viewed as a periodic network of constrictions. Current state-of-the-art experiments indicate that these may be "sculpted" in monolayer graphene with close to atomic precision to a width of a few benzene rings.[10]

Clearly, for GNCs of this size the current density can locally be very high, and it is important to address their stability and performance under bias.[11] Experimental results for electron transport,[12,13] local heating by Raman spectroscopy,[14–16] and infrared emission,[17] have been published for GNCs. Recently, it has been argued that several current-induced forces and excitation mechanisms driven by these, besides Joule heating, can play a role in the stability of nanoconductors.[18–21] In particular, energy nonconservative "wind"/"waterwheel" forces may transfer energy to the phonons in parallel with the well-known Joule heating. However, it is not easy to directly infer these mechanisms from experiments in most cases. On the other hand for graphene, the structural response to a high bias can be studied by *in situ* transmission electron microscopy, making graphene nanoconductors a good test bed for current-induced phenomena.[22–24] In particular, a gate electrode can be used to control Fermi level and electronic states involved in the transport, and thereby the current-induced excitation.

In this Rapid Communication, we calculate the current-induced phonon excitation in a small hydrogen-passivated GNC (Fig. 1) using parameters obtained from density functional theory (DFT). We find a highly nonlinear heating of the GNC due to the deterministic current-induced forces, as opposed to the Joule heating by random forces. In particular, for certain phonon modes in the GNC the nonequilibrium electronic friction force turns into an amplification for voltages beyond a threshold voltage. These amplified modes will dominate the dynamics and lead to a breakdown of the harmonic approximation beyond the voltage threshold.[20,21] The nonequilibrium negative friction was theoretically predicted for low conductance tunneling transport through asymmetric molecules[21,25] driven by population inversion between *two* molecular states. Here the highly conducting GNC displays negative friction at finite bias due to a more generic mechanism, which we trace back to a different coupling to the electronic states involved in the phonon emission and absorption processes.

In Fig. 1(b) we see how the electron transmission of the GNC for energies around the charge neutral Fermi energy ($E_F = 0$) is dominated by two resonance peaks originating from states presenting localized current along the edges (first peak) and through the center (second peak) of the GNC, respectively. Resonances occur due to the diffraction barrier at abrupt interfaces in graphene.[13,26] The calculated localized voltage drop and high current across the GNC is shown in Figs. 2(a) and 2(b). By employing a gate voltage (V_g) we may tune E_F to a highly conducting peak and consider the phonon excitation close to the resonance. We will focus on the constriction gated to the second peak which is mostly unaffected by the boundary conditions in the electrodes (k-point sampling),[27] and exhibits little dependence on the applied bias (V_a) [cf. Fig. 2(c)].

To address the phonon excitation in the presence of current we employ the semiclassical generalized Langevin equation (SCLE).[19,20,28,29] The SCLE describes the Joule heating, current-induced forces, and coupling to electrode phonons in the same formalism. For the mass-scaled ion displacements (Q) the SCLE reads

$$\ddot{Q}(t) = -K\,Q(t) - \int^{t} \Pi^{r}(t-t')Q(t')dt' + f(t). \quad (1)$$

Here K is the force constant matrix. The couplings to the electron and phonon baths are described by the retarded phonon self-energies $\Pi^r = \Pi^r_e + \Pi^r_{\rm ph}$, and the random noise force, $f(t)$, accounts for the Joule heating.[28] We consider the retarded self-energy due to the interaction between the

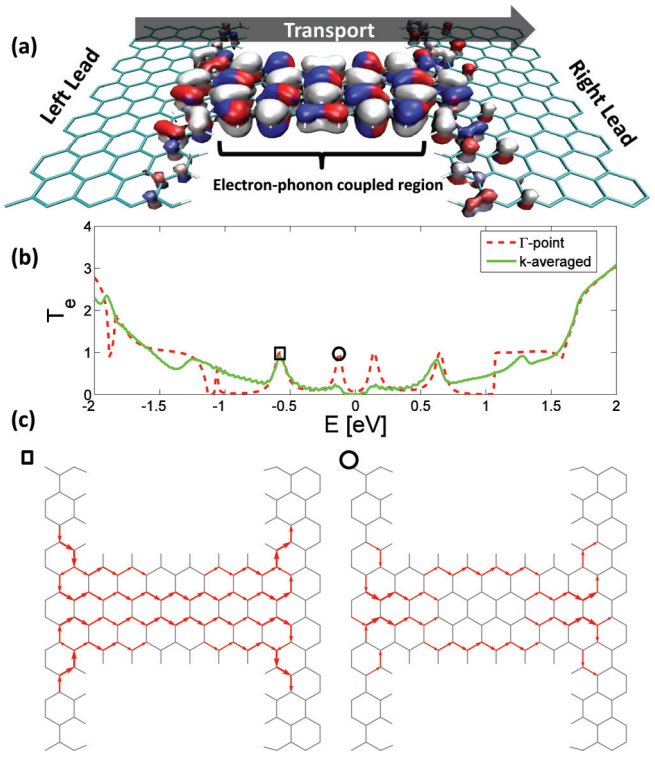

FIG. 1. (Color online) (a) Transport setup illustrating the hydrogen passivated GNC between two semi-infinite graphene leads. The left eigenchannel at zero bias and $E \approx -0.58$ eV (colored according to phase, red-white-blue from $-\pi$ to π). (b) Γ point and the k-averaged transmission function ($E = 0$ corresponds to the Dirac point). (c) Bond currents at the two peaks (Γ) marked in the transmission plot ($E \approx -0.12$ eV and $E \approx -0.58$ eV).

phonons and the electronic current,

$$\Pi_e^r(\omega) = i\pi\,\mathrm{Re}\,\Lambda(\omega) - \pi\,\mathrm{Im}\,\Lambda(\omega) + \pi\mathcal{H}\{\mathrm{Re}\,\Lambda(\omega')\}(\omega) + i\pi\mathcal{H}\{\mathrm{Im}\,\Lambda(\omega')\}(\omega), \quad (2)$$

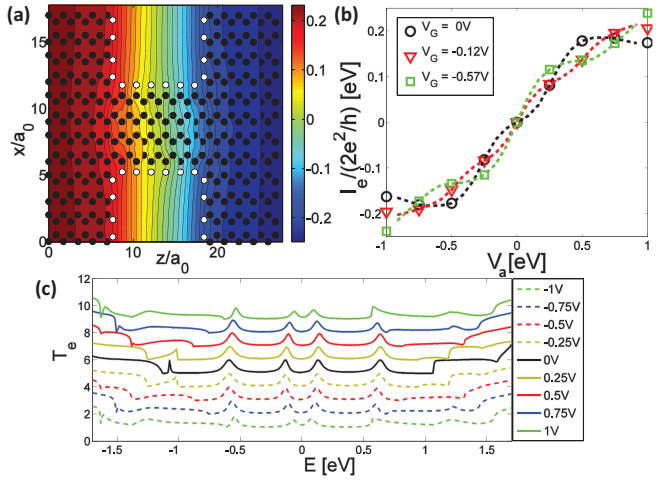

FIG. 2. (Color online) (a) Real space potential drop ($V_a = 0.5$ eV) integrated along the out-of-plane direction (in the region with nonvanishing electronic density). (b) IV characteristics for the GNC gated to different chemical potentials. Gating to a peak lowers the resistance at low V_a. (c) Transmission curves (shifted vertically) for different applied bias ($E_F = 0$).

which is given by the interaction-weighted electron-hole pair density of states, Λ, and its Hilbert transform ($\mathcal{H}$).[30] The four terms in this expression yield the electronic friction, nonconservative wind, renormalization, and Berry forces in nonequilibrium conditions, respectively.[19] Especially for the nonequilibrium electron system, $\Lambda = \sum_{\alpha,\beta}\Lambda^{\alpha\beta}$, with contributions from left/right leads ($\alpha = L, R$),

$$\Lambda^{\alpha\beta}(\omega) \equiv 2\int \frac{d\epsilon}{4\pi^2}\mathrm{Tr}[\mathbf{M}^k\mathbf{A}_\alpha(\epsilon+\omega)\mathbf{M}^l\mathbf{A}_\beta(\epsilon)] \times [n_F(\epsilon+\omega-\mu_\alpha) - n_F(\epsilon-\mu_\beta)]. \quad (3)$$

Here $\mathbf{M}^k$ is the coupling to phonon mode k, $\mathbf{A}_\alpha$ is the electronic spectral density for states originating from lead α with chemical potential μ_α, and n_F is the Fermi distribution. The spectral density for the noise, f, including the Joule heating, is given by

$$S_f(\omega) = -\pi\sum_{\alpha,\beta}\Lambda^{\alpha\beta}(\omega)\coth\left(\frac{\omega-(\mu_\alpha-\mu_\beta)}{2k_BT}\right).$$

Importantly, we include the full electronic and phononic structures of the graphene electrodes, and go beyond the constant/wide-band approximation (WBA) for the electronic structure. This is essential for our results of the phonon excitation when the graphene system is gated close to electronic resonance. We determine all parameters entering the SCLE above in the presence of current using first principles DFT and nonequilibrium Green's functions (DFT-NEGF).[27,31–33] We restrict the el-ph interaction to the GNC region where the current density is high, and evaluate the electronic spectrum at finite bias, but neglect the small voltage dependence of K and $\mathbf{M}^k$.

We note that the GNC device region in the present calculation encompasses a basis of 1336 orbitals for the electronic subsystem [matrix size in Eq. (3)]. Thus in order to efficiently compute Λ in Eq. (3) beyond WBA we first limited the basis. We employed an expansion of the retarded Green's function and $\mathbf{A}_\alpha$ in the eigenspace of $\mathbf{H} + \Sigma_0(E_F)$, $\mathbf{H}$ being the electronic Hamiltonian and $\Sigma_0(E_F)$ the lead self-energies, which vary slowly with energy.[34] We have found it sufficient to limit this basis to 200 states within the interval $[-7,6]$ eV around E_F. Secondly, we computed Λ by parallel execution over the ω and V_a parameters. The phonon self-energies describing the semi-infinite graphene leads was calculated on the basis on a zero-bias finite difference calculation. Detailed information is given in the Supplemental Material.[35]

From Eq. (1) we can obtain the nonequilibrium retarded phonon Green's function,

$$D^r(\omega) = [D^a(\omega)]^\dagger = [(\omega+i\eta)^2 - K - \Pi^r(\omega)]^{-1}, \quad (4)$$

and the excitation in terms of the average kinetic energy of the phonons,

$$E_{\mathrm{kin}} = \int_{-\infty}^{\infty}\frac{d\omega}{2\pi}\omega^2\mathrm{Tr}[D^r(\omega)S_f(\omega)D^a(\omega)]. \quad (5)$$

The phonon density of states (DOS) is given by $-2/\pi\omega\,\mathrm{Im}[D^r(\omega)]$. The DOS is affected both by the coupling to electrons, in particular giving rise to nonequilibrium forces, as well as coupling to the electrode phonons. In Fig. 3(a) we show the phonon DOS at applied bias of $V_a = 0$ and

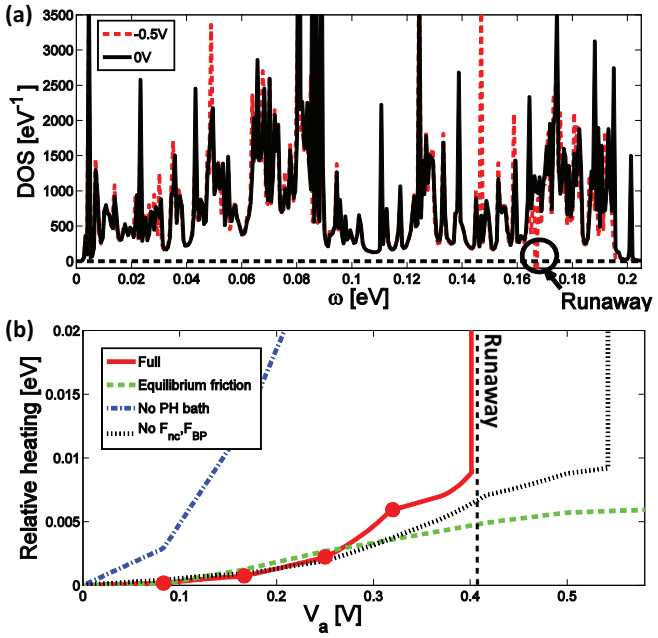

FIG. 3. (Color online) (a) Dashed (full) lines show the phonon DOS of the GNC with (without) electronic current. An unstable "runaway" mode appears for an applied bias of $V_a \approx \pm 0.5$ V as a negative DOS peak. (b) Heating (change in average kinetic energy per atom due to current) of the GNC at 300 K. Full line: Result including all current-induced forces. Dashed line: only fluctuating force (Joule heating) and zero-bias electronic friction. Dot-dashed line: The wide-band approximation without coupling to the electrode phonon bath. Dotted line: Full calculation neglecting the nonconservative wind and Berry-phase forces.

$V_a = 0.5$ V. Most importantly, the DOS becomes negative at a particular phonon frequency ($\omega \approx 170$ meV), corresponding to a negatively damped mode, denoted "runaway". From Eq. (5) the runaway gives rise to a divergence in the current-induced change of E_{kin}(heating) of the GNC at $V_a \approx 0.4$ V [see Fig. 3(b)]. This signifies an instability in the harmonic approximation, where the high excitation is likely to lead to dramatic effects such as contact disruption.[18]

The instability can be traced back to the bias dependent electronic friction, and disappears when this is kept at its zero-bias value. We further note that for V_a above ~ 0.3 V the deterministic current-induced forces lead to a qualitatively different heating compared to that of Joule heating only. Figure 3(b) furthermore shows how the damping due to electrode phonons is crucial: The heating increases by an order of magnitude if the electrode-phonon bath is neglected. Moreover, if we neglect the damping due to the phonon bath we observe runaway starting already at $V_a \approx 0.15$ V, increasing to more than 15 runaway modes at $V_a \approx 0.4$ V, both due to the effects of negative friction and nonconservative forces.[18] The nonconservative wind and Berry-phase forces are found to be on the same order of magnitude for the runaway mode. Even though they do not themselves lead to the first runaway condition they lower the runaway threshold.

We will now in detail analyze the origin of the runaway. We focus on the modes contributing to the phonon DOS peak around the runaway, $\omega_0 \approx 170$ meV. They can be found as

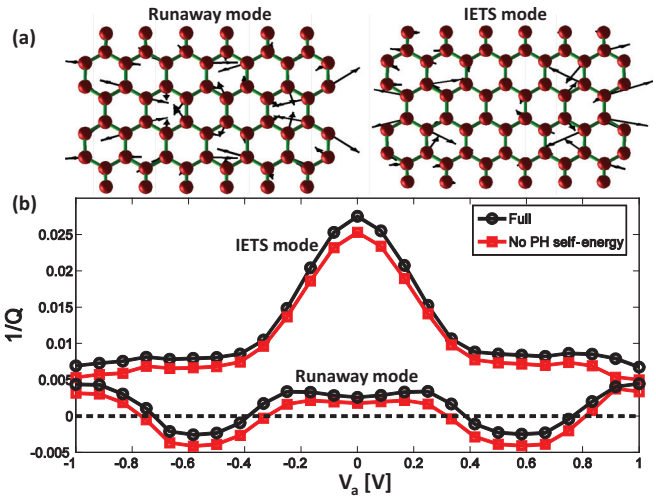

FIG. 4. (Color online) (a) Two degenerate modes ("runaway"/"IETS") at $V_a = 0.4$ V with $\omega_0 \approx 170$ meV. The runaway mode breaks the left-right symmetry due to the coupling to the nonequilibrium electrons and becomes unstable at finite bias. The IETS yields the largest inelastic signal in the current. (b) Inverse Q factor (loss) as a function of bias for the modes.

the eigenvectors of $K + \mathrm{Re}\,\Pi^r(\omega_0)$. The two main modes are displayed in Fig. 4. The "IETS mode" exhibits the largest inelastic tunnel spectroscopy signal (IETS) in the electronic current and largest noise $S_{f,ii}(\omega_i)$, while the "runaway mode" is the first mode that turns unstable with increasing V_a. In Fig. 4 we show the inverse quality factor $1/Q = -2\frac{\mathrm{Im}(\omega)}{\mathrm{Re}(\omega)} = 1/Q_{\mathrm{ph}} + 1/Q_{\mathrm{el}}(V_a)$ (energy loss/period) for the two modes as a function of V_a. The Q_{ph} factor is relatively big, especially for the runaway mode, due to low phonon DOS around ω_0. The runaway corresponds to amplification $1/Q < 0$, while $1/Q > 0$ remains for the IETS mode despite a strong decrease with bias.

It is instructive to view the runaway in terms of phonon absorption/emission processes in a simple master equation for the phonon number N,

$$\dot{N} = \mathcal{B}(N+1) - \mathcal{A}N, \tag{6}$$

where $\mathcal{A}(\mathcal{B})$ are the rates for absorption (emission). From Fermi's golden rule we find the emission,

$$\mathcal{B} = -2\pi \sum_{\alpha\beta} n_B(\hbar\omega_0 + \mu_\alpha - \mu_\beta)\Lambda^{\beta\alpha}(\omega_0),$$

and $\mathcal{A}$ is obtained by a replacement $\omega \to -\omega$. Only a single scattering state $|\psi_{L/R}\rangle$ contributes to $\mathcal{A}$ and $\mathcal{B}$. Expressed in the single flux-normalized eigenchannel, and assuming $k_B T \ll \hbar\omega_0 < eV_a$, we have

$$\begin{aligned} \mathcal{B} &\approx \int_{\mu_R+\hbar\omega_0}^{\mu_L} |\langle\psi_L(\epsilon)|\mathbf{M}|\psi_R(\epsilon-\hbar\omega_0)\rangle|^2 \frac{d\epsilon}{2\pi}, \\ \mathcal{A} &\approx \int_{\mu_R-\hbar\omega_0}^{\mu_L} |\langle\psi_L(\epsilon)|\mathbf{M}|\psi_R(\epsilon+\hbar\omega_0)\rangle|^2 \frac{d\epsilon}{2\pi}. \end{aligned} \tag{7}$$

Here we did not include the intraelectrode terms ($\Lambda^{LL/RR}$) in $\mathcal{A}$ since these vary only slightly with V_a for the runaway mode. The phonon absorption rate decreases while the emission rate increases as the bias exceeds the mode frequency [see

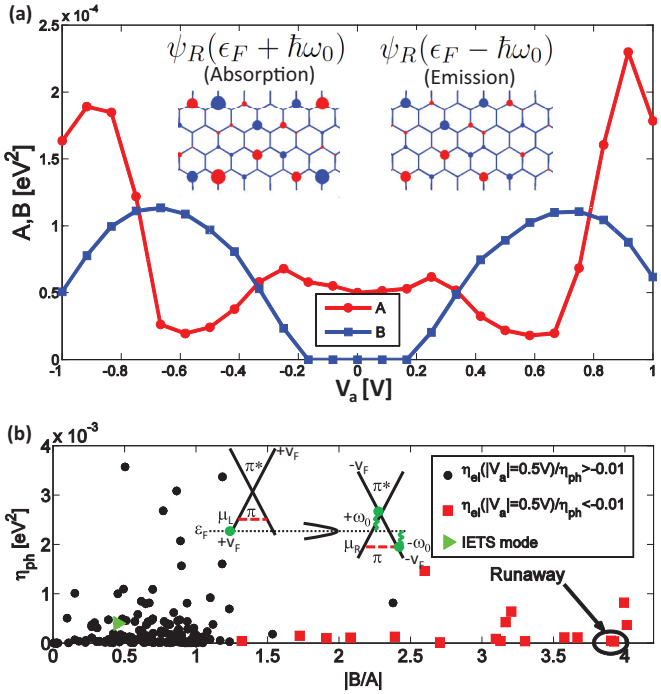

FIG. 5. (Color online) Nonequilibrium friction mechanism. (a) Phonon absorption/emission ($\mathcal{A}/\mathcal{B}$) rates for the runaway mode. Note that $\mathcal{B}=0$ for $V_a<\omega_0$. When $V_a>\pm 0.4$V emission exceeds absorption, $\mathcal{B}>\mathcal{A}$. Inset: at resonance scattering states giving the main contribution to the interaction integrals. The radius shows the absolute value $|\psi(x,y)|$ of the eigenstate, while the color indicates the sign of the real part. (b) Runaway occurs for the mode with the largest emission and lowest phonon friction ($\eta_{\rm ph}$). Squares indicate modes with a significant electron friction ($\eta_{\rm el}$). These modes all have $\mathcal{A}$,$\mathcal{B}$ coefficients with the same behavior as the first runaway mode. Inset: resonance between two graphene leads at certain filling (red dashed line) and bias voltage. An incoming scattering state (left green dot) at resonance (dashed line) can either absorb ($+\omega_0$) to a state with lower DOS close to the π-π^* crossing or change to a state with higher DOS by emission ($-\omega_0$).

Fig. 5(a)]. The electronic friction is given by the difference $\mathcal{A}-\mathcal{B}=-2\pi\sum_{\alpha\beta}\Lambda^{\alpha\beta}(\omega)$. This difference manifests itself in how the Q factor varies with bias for the runaway mode. The state symmetry changes significantly with energy [Fig. 1(c)]. Thus we expect that a given phonon will yield very different emission and absorption matrix elements due to the symmetry. The symmetry of the scattering state $\psi_L^*(E_F)$ is almost unchanged from going *up* in energy (absorption) [see $\psi_R(E_F+\omega_0)$ in the inset of Fig. 5(a)], while the symmetry of $\psi_R(E_F-\omega_0)$ differs significantly from this. In particular, the el-ph matrix element of the runaway mode yields very low absorption and high emission due to the selective symmetry of this phonon mode. The large phonon frequencies and linear DOS of graphene strengthens this symmetry breaking. The negative electronic friction is found for several modes and seems to be a generic phenomena in graphene nanostructures.

In Fig. 5(b) we illustrate how each mode shows up in a parameter space of the phonon friction and $\mathcal{B}/\mathcal{A}$. The dominating runaway mode shows up at high $\mathcal{B}/\mathcal{A}$ and low phonon friction. The other modes with a nonvanishing negative electron friction are also displayed. All these modes have $\mathcal{A}$,$\mathcal{B}$ coefficients with the same generic behavior as the first runaway mode [Fig. 5(a)]. In the general case where one has a resonance between graphene leads [inset of Fig. 5(b)], the wave incoming at resonance will absorb to an eigenstate close to the Dirac crossing. Hence it will have low DOS and a dissimilar phase. On the contrary emission leads to an eigenstate with larger DOS and similar phase. This holds true for states dominated by the interlead contributions. Compared to the runaway mode the IETS mode has low emission-absorption ratio due to high intraelectrode terms $\Lambda^{LL/RR}$ and a higher phonon damping.

We conclude that negative friction can appear for certain phonons in realistic systems such as graphene nanoconstrictions in the presence of electrical current. The negative friction effect is here rooted in the high phonon energies which lead to markedly different symmetry of the electronic states involved in emission and absorption and thus different matrix elements and rates. Therefore, it is a generic nonequilibrium effect. Two-dimensional systems like graphene, where a gate can be applied, make an exciting test bed for probing effects of electronic current on the atomic scale.

We thank the Danish Center for Scientific Computing (DCSC) for providing computer resources. The Center for Nanostructured Graphene (CNG) is sponsored by the Danish National Research Foundation.

*tue.gunst@nanotech.dtu.dk

†Present address: School of Physics, Huazhong University of Science and Technology, Wuhan, China; jtlu@mail.hust.edu.cn

[1] K. S. Novoselov, A. K. Geim, S. V. Morozov, D. Jiang, Y. Zhang, S. V. Dubonos, I. V. Grigorieva, and A. A. Firsov, Science **306**, 666 (2004).

[2] A. H. Castro Neto, F. Guinea, N. M. R. Peres, K. S. Novoselov, and A. K. Geim, Rev. Mod. Phys. **81**, 109 (2009).

[3] A. K. Geim, Science **324**, 1530 (2009).

[4] K. Nakada, M. Fujita, G. Dresselhaus, and M. S. Dresselhaus, Phys. Rev. B **54**, 17954 (1996).

[5] L. Brey and H. A. Fertig, Phys. Rev. B **73**, 235411 (2006).

[6] D. A. Areshkin and C. T. White, Nano Lett. **7**, 3253 (2007).

[7] A. R. Botello-Mendez, E. Cruz-Silva, J. M. Romo-Herrera, F. Lopez-Urias, M. Terrones, B. G. Sumpter, H. Terrones, J.-C. Charlier, and V. Meunier, Nano Lett. **11**, 3058 (2011).

[8] J. Bai, X. Zhong, S. Jiang, Y. Huang, and X. Duan, Nat. Nanotech. **5**, 190 (2010).

[9] T. G. Pedersen, C. Flindt, J. Pedersen, N. A. Mortensen, A. P. Jauho, and K. Pedersen, Phys. Rev. Lett. **100**, 136804 (2008).

[10] Q. Xu, M.-Y. Wu, G. F. Schneider, L. Houben, S. K. Malladi, C. Dekker, E. Yucelen, R. E. Dunin-Borkowski, and H. W. Zandbergen, ACS Nano **7**, 1566 (2013).

[11] F. Börrnert, A. Barreiro, D. Wolf, M. I. Katsnelson, B. Büchner, L. M. K. Vandersypen, and M. H. Rümmeli, Nano Lett. **12**, 4455 (2012).

[12]N. Tombros, A. Veligura, J. Junesch, M. H. D. Guimares, I. J. Vera-Marun, H. T. Jonkman, and B. J. v. Wees, Nat. Phys. **7**, 697 (2011).

[13]P. Darancet, V. Olevano, and D. Mayou, Phys. Rev. Lett. **102**, 136803 (2009).

[14]D.-H. Chae, B. Krauss, K. von Klitzing, and J. H. Smet, Nano Lett. **10**, 466 (2009).

[15]S. Berciaud, M. Y. Han, K. F. Mak, L. E. Brus, P. Kim, and T. F. Heinz, Phys. Rev. Lett. **104**, 227401 (2010).

[16]I. Jo, I.-K. Hsu, Y. J. Lee, M. M. Sadeghi, S. Kim, S. Cronin, E. Tutuc, S. K. Banerjee, Z. Yao, and L. Shi, Nano Lett. **11**, 85 (2010).

[17]M. Freitag, H.-Y. Chiu, M. Steiner, V. Perebeinos, and P. Avouris, Nat. Nanotech. **5**, 497 (2010).

[18]D. Dundas, E. J. McEniry, and T. N. Todorov, Nat. Nanotech. **4**, 99 (2009).

[19]J.-T. Lü, M. Brandbyge, P. Hedegård, T. N. Todorov, and D. Dundas, Phys. Rev. B **85**, 245444 (2012).

[20]N. Bode, S. V. Kusminskiy, R. Egger, and F. von Oppen, Phys. Rev. Lett. **107**, 036804 (2011).

[21]J.-T. Lü, P. Hedegård, and M. Brandbyge, Phys. Rev. Lett. **107**, 046801 (2011).

[22]X. Jia, M. Hofmann, V. Meunier, B. G. Sumpter, J. Campos-Delgado, J. M. Romo-Herrera, H. Son, Y.-P. Hsieh, A. Reina, J. Kong, M. Terrones, and M. S. Dresselhaus, Science **323**, 1701 (2009).

[23]A. Barreiro, F. Börrnert, M. H. Rümmeli, B. Büchner, and L. M. K. Vandersypen, Nano Lett. **12**, 1873 (2012).

[24]M. Engelund, J. A. Fürst, A. P. Jauho, and M. Brandbyge, Phys. Rev. Lett. **104**, 036807 (2010).

[25]D. A. Ryndyk, M. Hartung, and G. Cuniberti, Phys. Rev. B **73**, 045420 (2006).

[26]S. Ihnatsenka and G. Kirczenow, Phys. Rev. B **85**, 121407 (2012).

[27]M. Brandbyge, J.-L. Mozos, P. Ordejon, J. Taylor, and K. Stokbro, Phys. Rev. B **65**, 165401 (2002).

[28]J.-T. Lü, M. Brandbyge, and P. Hedegård, Nano Lett. **10**, 1657 (2010).

[29]J.-T. Lü, T. Gunst, P. Hedegård, and M. Brandbyge, Beilstein J. Nanotechnol. **2**, 814 (2011).

[30]The Hilbert transform is defined as $\mathcal{H}\{g(x')\}(x) = \frac{1}{\pi}\mathcal{P}\int \frac{g(x')}{x'-x}dx'$.

[31]J. M. Soler, E. Artacho, J. D. Gale, A. Garca, J. Junquera, P. Ordejn, and D. Snchez-Portal, J. Phys.: Condens. Matter **14**, 2745 (2002).

[32]T. Frederiksen, M. Paulsson, M. Brandbyge, and A.-P. Jauho, Phys. Rev. B **75**, 205413 (2007).

[33]We used single-zeta-polarized localized pseudoatomic orbitals in the basis set for both hydrogen and carbon. Exchange-correlation effects were handled within generalized gradient approximation Perdew-Burke-Ernzerhof and a grid cutoff of 210 Ry was applied. The Brillouin zone was sampled with a [5 1 2] Monkhorst-Pack grid, with the x axis as the transverse direction and the z axis as the transport direction. The system was relaxed until all forces were smaller than 0.005 eV/Ang. We used 150 points along the bias contour with a broadening of 0.01 eV.

[34]R. Egger and A. O. Gogolin, Phys. Rev. B **77**, 113405 (2008).

[35]See Supplemental Material at http://link.aps.org/supplemental/10.1103/PhysRevB.88.161401 for detailed information on the electron and phonon DFT-NEGF modelling.

Supplementary note on nonequilibrium modeling

Tue Gunst,[1,*] Jing-Tao Lü,[1,2,†] Per Hedegård,[2] and Mads Brandbyge[1]

[1]*Department of Micro- and Nanotechnology (DTU Nanotech), Center for Nanostructured Graphene (CNG), Technical University of Denmark, DK-2800 Kgs. Lyngby, Denmark*

[2]*Niels Bohr Institute, Nano-Science Center, University of Copenhagen, Universitetsparken 5, 2100 Copenhagen Ø, Denmark*

(Dated: September 23, 2013)

DFT-NEGF CALCULATIONS

The first-principles calculations were performed with the SIESTA/TransSIESTA code[1, 2]. The generalized gradient approximation (GGA-PBE) was used for exchange and correlations. To accurately describe the phonon modes we use a single-ζ polarized basis set and a mesh-cutoff of 210 Ry. Similar settings were previously used to accurately describe phonon modes of carbon nanotubes [3]. With these parameters the optimal nearest neighbor distance of graphene is approximately 1.46 Å. The potential drop was applied between the semi-infinite leads as implemented in the TranSIESTA method[2]. Several of the current-induced forces give rise to changes in the phonon frequencies. Especially we observe a significant change in phonon frequencies due to the phonon and electron damping forces. However, we do neglect the additional correction in phonon frequencies due to the potential drop when performing the initial finite difference evaluation of the force constants. This would be a minor, computational expensive, change to include as compared to the additional forces due to the electronic current. The influence of the electronic current on the phonon distribution is evaluated as a perturbation to the equilibrium distribution (to second order in the electron-phonon coupling). The treatment is equivalent to the first Born approximation applied in the lowest order expansion. This is a current-conserving approximation that reduce computational demands, and at the same time agrees with the results of self-consistent approximations, for a range of realistic devices[4]. A self-consistent scheme could induce a further shift in phonon frequencies than obtained by the lowest order renormalization.

ELECTRON-PHONON CALCULATIONS

The calculation of phonon modes and electron-phonon coupling inside the constriction was performed within the finite difference approximation as implemented in the Inelastica package[4] at zero bias. When the voltage drop is localized over a few atomic bonds or a tunnel barrier, the voltage dependence of the electron-phonon coupling could play an important role[5]. In our case the voltage drop is locally small since it is spread over the entire constriction region (cf. Fig. 2). The phonon NEGF calculations were performed by calculating the force constants of a super cell, e.i. repeating the unit cell in the transverse direction. In the transport direction semi-infinite graphene leads were used by calculating

the surface Green's function for both electrons (at finite bias) and phonons (at zero bias) by an iterative procedure[6]. The phonon transmission for both graphene and the constriction is illustrated in Fig. 1 and compared to that obtained with the widely used empirical Brenner potential[7]. For the ab initio calculation a cutoff radius smaller than the lead dimension was

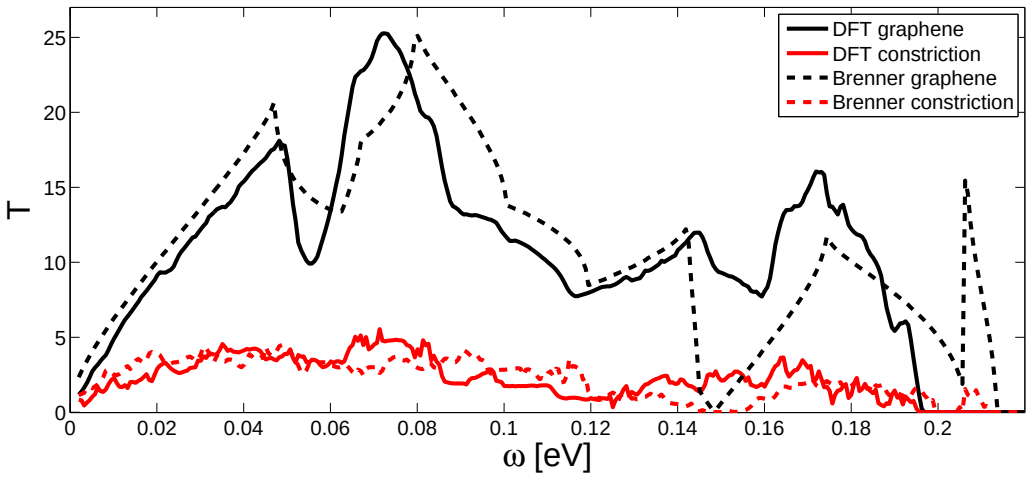

FIG. 1. (Color online) Phonon transmission as a function of frequency across ideal graphene and the graphene nanoconstriction. The result from the DFT calculations are compared to that of the empirical Brenner potential.

used to apply Green's function techniques. The momentum conservation was imposed by adjusting the diagonal elements of the dynamical matrix to secure physical transmissions also at acoustic frequencies. No changes in the symmetrized result were observed when increasing the cutoff radii. The figure highlights the importance of using ab initio approaches in the description of especially optical phonon modes. In the context of current-induced heating it is these high frequency phonon modes that are excited the most. The phonon bath self-energies describe the finite life-time of a device phonon, and a finite phonon transmission reduces the accumulated heat in the device. This is illustrated in Fig.3B of the main text, where the heating with (full red line) and without (dot-dashed blue line) phonon baths to absorb part of the excess energy are shown. The heating with the phonon baths (full red line) is a result of the competition between heat accumulation and energy transfer to the leads.

We further elaborate on the definition of the phonon self-energy of the open system. In

the above calculation we averaged the transmission over 43 transverse k-points

$$\mathcal{T}_{ph}(\omega) = \frac{1}{N_k}\sum_{i=1}^{N_k} \mathrm{Tr}\left[\mathbf{D}^r(\omega,k_i)\mathbf{\Gamma}_R(\omega,k_i)\mathbf{D}^a(\omega,k_i)\mathbf{\Gamma}_L(\omega,k_i)\right]. \quad (1)$$

where $\mathbf{\Gamma}_{L,R} = i[\mathbf{\Pi}^r_{L,R} - \mathbf{\Pi}^a_{L,R}]$ gives the coupling to the electrodes and N_k is the number of sampled k-points. This corresponds to a sequence of constrictions repeated in the transverse direction, resembling a line of holes a kin to a single line of antidots[8]. In the paper we want to address the damping of a single constriction connected to graphene leads. Therefore, we propagate the self-energy to the device region. In this region we construct a k-averaged/real-space self-energy describing the damping of a single constriction connected to infinite graphene leads[9]. In Fig. 2 we compare the transmission between these two different setups. It is clear from the figure that the transmission and phonon damping to some

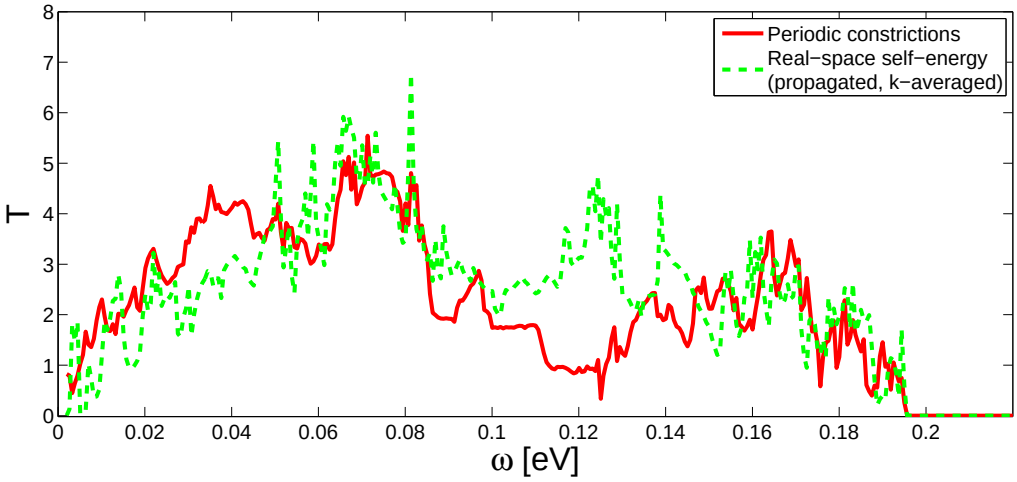

FIG. 2. (Color online) Phonon transmission across the graphene nanoconstriction. We compare two different phonon baths: The one from periodic boundary conditions in the transverse direction and that from a real-space self-energy resembling the graphene nanoconstriction. The real-space phonon self-energy was obtained by propagating to the constriction part and performing the k-averaging. In both transmission calculations 43 transverse k-points were used.

extend is different for the two different configurations.

* Tue.Gunst@nanotech.dtu.dk

† jtlu@mail.hust.edu.cn, now at School of Physics, Huazhong University of Science and Technology, Wuhan, China.

[1] J. M. Soler, E. Artacho, J. D. Gale, A. Garca, J. Junquera, P. Ordejn, and D. Snchez-Portal, J. Phys.: Condens. Matter **14**, 2745 (2002).

[2] M. Brandbyge, J.-L. Mozos, P. Ordejn, J. Taylor, and K. Stokbro, Phys. Rev. B **65**, 165401 (2002).

[3] N. Mingo, D. A. Stewart, D. A. Broido, and D. Srivastava, Physical Review B **77**, 033418 (2008).

[4] T. Frederiksen, M. Paulsson, M. Brandbyge, and A.-P. Jauho, Phys. Rev. B **75**, 205413 (2007).

[5] S. Ulstrup, T. Frederiksen, and M. Brandbyge, Physical Review B **86**, 245417 (2012).

[6] M. P. L. Sancho, J. M. L. Sancho, and J. Rubio, Journal of Physics F: Metal Physics **14**, 1205 (1984).

[7] D. W. Brenner, Phys. Rev. B **42**, 9458 (1990).

[8] T. Gunst, T. Markussen, A.-P. Jauho, and M. Brandbyge, Physical Review B **84**, 155449 (2011).

[9] W. Zhang, N. Mingo, and T. S. Fisher, Physical Review B **76**, 195429 (2007).